DOI: 10.14750/ME.2026.030

University of Miskolc
Faculty of Earth Science and Engineering
Mikoviny Samuel Doctoral School of
Earth Sciences

Research on the Reverse Flotation of Waste Printed Circuit Boards

Doctoral (PhD) dissertation

by

Alaa Abbadi

Scientific supervisor:

Dr. Ljudmilla Bokányi
Honorary Professor

Co-scientific supervisor:

Dr. Rácz Ádám
Associate Professor

MIKOVINY SAMUEL DOCTORAL SCHOOL OF EARTH SCIENCES

Head of the Doctoral School

Prof. Dr. Péter Szűcs
Professor, Doctor of Science

Miskolc, 2025

DOI: 10.14750/ME.2026.030

Supervisor's Recommendation for

Alaa Abbadi

for his doctoral dissertation titled

"**Research on the Reverse Flotation of Waste Printed Circuit Boards**"

Alaa Abbadi graduated from An-Najah National University, Nablus, Palestine, with B.Sc. diploma in Civil Engineering in 2015. Between 2015 and 2018 he worked in field of municipal waste management.

In 2018 he won Stipendium Hungaricum scholarship and enrolled for M.Sc. Environmental Engineering Program at University of Miskolc, from where graduated in 2020 with diploma "With Honour". During his study he already showed serious interest in research, and was involved into departmental research projects, and submitted Student Scientific Work. His achievements embraced the followings:

Silver honorary medal for outstanding academic achievements, 2020
Student Scientific Research Conference, University of Miskolc
First place research award and Best presentation award, 2019.

His excellent M.Sc. thesis contained the results of his research work and titled as "Experimental investigation of hydrodynamic cavitation for the sake of sewage sludge treatment", advisors: Dr. Ljudmilla Bokányi and Dr. József Faitli.

Later, during his gap year he contacted me with the decision he made to come back to our Institute for PhD study under my scientific supervision, in the research topic "Finely dispersed solid wastes selective recycling from aqueous environment by physical-chemical separation techniques". He won PhD Stipendium Hungaricum scholarship for this aim as well. I have decided to share his scientific supervision with Dr. Ádám Rácz colleague in course of comminution issue needed for his research.

His first scientific steps in field of flotation were devoted to natural talc flotation within an international EIT R&D project „MineTAL" carried out under my leadership. He obtained very valuable results, published several papers and participated in conferences. Nevertheless, he decided to turn into flotation recycling waste printed circuit boards, and I support this idea. His original approach was to float the non-metals which are naturally hydrophobic, and not the metals as it was generally researched. He obtained numerous findings in course of his research: along with the technological or techno-economical, there are very important fundamental findings as well.

During this period of his doctoral study he has carried out a huge amount of various experiments, measurements, calculations, and, definitely, considerations. Alaa Abbadi is an outstandingly hard-working and dynamic researcher with excellent analytical and synthetizing abilities. He is absolutely self-reliant, autonomous, gifted experimentalist and researcher.

He successfully passed the departmental discussion (pre-defense) of his dissertation on the 31st of October, 2025. I do recommend dissertation of Alaa Abbadi for the PhD public defense, in case it will be successful, the awarding him doctoral (PhD) degree.

Miskolc 20th November, 2025

Dr. Ljudmilla BOKÁNYI PhD, CSc
Honorary Professor
Scientific Supervisor

DOI: 10.14750/ME.2026.030

Table of contents

DOI: 10.14750/ME.2026.030

DOI: 10.14750/ME.2026.030

DOI: 10.14750/ME.2026.030

List of Figures

DOI: 10.14750/ME.2026.030

DOI: 10.14750/ME.2026.030

List of Tables

DOI: 10.14750/ME.2026.030

List of Symbols and Abbreviations

AAS	Atomic absorption spectroscopy
AI	Aggregation index
BFRs	Brominated flame retardants
CEM-1	Cotton paper and epoxy
CEM-2	Cotton paper and epoxy
CEM-3	Woven glass and epoxy
CEM-4	Woven glass and epoxy
CEM-5	Woven glass and polyester
CPUs	Central processing units
DTPA	Diethylenetriaminepenta acetate
ECs	Electronic components
ED	Electrodeposited
EDS	Energy dispersive spectrometry
EDTA	Ethylene diaminetetramaide
EEE	Electrical and electronic equipment
ENT	Degree of entrainment
e-waste	Electronic waste
FR-2	Phenolic cotton paper
FR-3	Cotton paper and epoxy
FR-4	Woven glass and epoxy
FR-5	Woven glass and epoxy
FR-6	Matte glass and polyester
G-10	Woven glass and epoxy
ICP-OES	Inductively coupled plasma optical emission spectrometry
ICs	Integrated circuits
MIBC	Methyl isobutyl carbinol
MLCCs	Multilayer ceramic capacitors
MPs	Metallic particles
N	Impeller speed
NMPs	Nonmetallic particles

DOI: 10.14750/ME.2026.030

PAHs	Polycyclic aromatic hydrocarbons
PBDEs	Polybrominated diphenyl ethers
PCBs	Printed circuit boards
PE	Polyethylene
PP	Polypropylene
PS	Polystyrene
PSD	Particle size distribution
PTFE	Polytetrafluoroethylene
PVC	Polyvinyl chloride
PWBs	Printed wiring boards
Q_a	Aeration rate
RA	Rolled annealed
RAM	Random-access memory
S.E.	Separation efficiency
SEM	Scanning electron microscopy
Sr	Standard deviation of the estimate
WPCBs	Waste printed circuit boards
X	Solids concentration
XPS	X-ray photoelectron spectroscopy

DOI: 10.14750/ME.2026.030

Chapter 1: Introduction

The rapid proliferation of consumer electronics has fueled an unprecedented rise in electronic waste (e-waste), now one of the fastest-growing waste streams globally [1]. In 2022 alone, e-waste generation surged to 62 million metric tonnes, yet only a fraction was formally recycled, leaving vast quantities improperly managed [2]. This surge presents both a crisis and an opportunity: while e-waste contains hazardous substances, it is also an urban mine rich in valuable metals, making efficient recycling a necessity. Beyond resource recovery, effective recycling mitigates environmental and health risks, reduces energy consumption, and supports a circular economy by decreasing reliance on primary raw materials [3–8].

Within the e-waste stream, waste printed circuit boards (WPCBs) are among the most valuable yet complex types of waste. Printed circuit boards (PCBs) form the backbone of nearly all electrical and electronic equipment (EEE), with their global production expanding rapidly due to increasing electronic demand and rapid obsolescence [9, 10]. While WPCBs constitute only 3–7% of e-waste mass, they hold high metal content (30–50 wt.%), including copper concentrations exceeding 20% and significant quantities of precious metals [11–15]. Recycling high-grade WPCBs can be highly lucrative; modeled economic assessments have estimated net present values of up to 63 million euros under favorable recovery and market conditions [16]. However, improper disposal and informal recycling introduce hazardous substances, posing severe environmental and health risks [17]. These factors emphasize the need for efficient recycling strategies that maximize resource recovery while minimizing ecological impact.

The complexity of WPCBs necessitates a multi-stage recycling approach, typically involving disassembly, mechanical pretreatment, and metallurgical recovery through pyrometallurgy, hydrometallurgy, or biohydrometallurgy [18]. Direct metallurgical processing is possible but often inefficient and environmentally problematic without prior mechanical pretreatment, as non-valuable components increase energy and reagent consumption while contributing to waste and emissions [19]. Mechanical processing plays a critical role in liberating metals and concentrating valuable fractions; yet, it inevitably generates fine particles that pose challenges for conventional physical separation methods, potentially leading to significant metal losses [20]. To address this limitation, froth flotation has emerged as a complementary approach, working alongside mechanical processing to improve the recovery of fine metallic fractions while maintaining low energy consumption [19]. **Figure 1. 1** presents a simplified flowchart

DOI: 10.14750/ME.2026.030

comparing the direct metallurgical approach bypassing mechanical pretreatment and an alternative route incorporating mechanical preprocessing prior to metallurgical recovery.

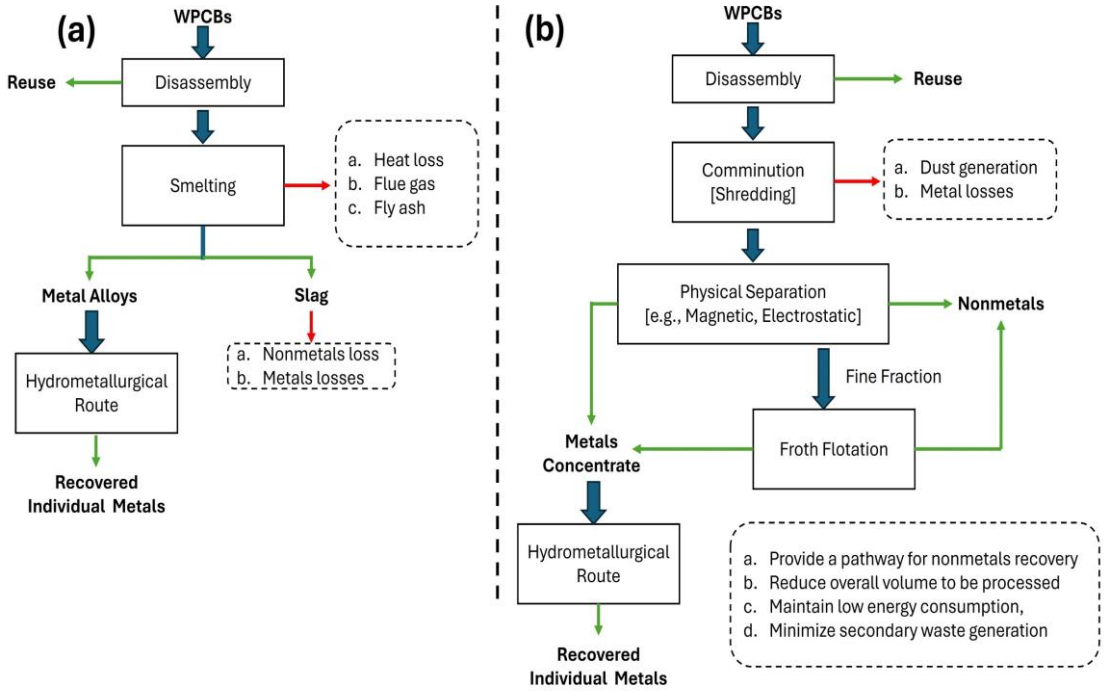

Figure 1. 1: Simplified process flowsheets illustrating (a) an integrated pyro-hydrometallurgical processing route without mechanical pretreatment and (b) an integrated metallurgical processing route incorporating mechanical pretreatment for the recycling of WPCBs (adapted from Das et al. [20]).

Froth flotation, a physicochemical separation process that exploits differences in surface properties, has been a cornerstone of mineral beneficiation for over a century [21, 22]. Its versatility extends beyond traditional mineral processing, with applications in paper recycling, wastewater treatment, and, more recently, WPCB recycling [18]. The process relies on the selective attachment of hydrophobic particles to air bubbles, enabling their recovery in the overflow, while hydrophilic particles remain in the liquid phase [23]. Given its three-phase nature (solid, liquid, and gas), froth flotation is inherently complex and influenced by multiple chemical and physical parameters, including particle size, shape, surface chemistry, pulp composition, and froth stability, all of which directly impact recovery and selectivity [22, 24]. Flotation can be conducted via direct flotation, where the target material reports to the froth phase, or reverse flotation, which selectively floats unwanted materials, enriching the desired fraction in the underflow [25].

While long established in mineral processing, its application to WPCB recycling remains at the research stage. Early studies explored flotation for enriching metal fractions in comminuted

WPCBs, with Ogunniyi and Vermaak [26] introducing reverse flotation to concentrate metallic components by floating nonmetallic materials as waste overflow. The heterogeneous composition of WPCBs, consisting of metals, polymers, ceramics, and fiberglass, presents both challenges and opportunities for flotation-based separation [27]. However, the inherent hydrophobic nature of nonmetallic components has been leveraged to facilitate their separation, enabling bulk metallic enrichment [28].

Recent research has demonstrated increasing interest in WPCB flotation, with studies exploring the optimization of process parameters, reagent selection, and surface modification techniques [26, 29–31]. However, despite these advancements, flotation remains confined to laboratory scale, with no industrial applications to date. While the potential of WPCB flotation is evident, its transition to practical implementation is hindered by critical knowledge gaps and unresolved challenges.

Knowledge gaps span multiple interconnected aspects of WPCB flotation systems. These include the unquantified effects of grinding environments on flotation feed preparation, the overlooked role of pulp particle aggregation in pulping challenges, and the complex interplay between flotation hydrodynamics, pulp solids concentration, and flotation performance. Furthermore, the rheological properties of WPCB pulps remain inadequately characterized as both a challenge and a potential process control parameter, with a lack of prior work on targeted pretreatment strategies to mitigate these effects at industrially relevant conditions.

The primary aim of this PhD dissertation is to address key knowledge gaps in WPCB flotation to improve process efficiency and scalability. This research identifies critical factors governing flotation performance, with the aim of informing scalable solutions based on laboratory investigation and practical relevance.

To achieve this, the dissertation begins by establishing the research context in **Chapter 1**. **Chapter 2** then presents a literature review, delving into the challenges specific to WPCB processing and flotation, which leads to the identification of key research gaps and the formulation of objectives. **Chapter 3** outlines the materials, reagents, and experimental methodologies employed. Subsequently, **Chapter 4** characterizes the mechanically processed WPCB feed, focusing on particle properties crucial for flotation. **Chapter 5** addresses the challenges of particle aggregation during pulping, investigating the role of intense agitation in mitigating these issues. **Chapter 6** examines reverse flotation performance under varying conditions, exploring rheological constraints and metal recovery dynamics. **Chapter 7**

DOI: 10.14750/ME.2026.030

investigates strategies for mitigating rheological challenges to enhance flotation performance at elevated solids concentrations. Finally, **Chapter 8** concludes with the major findings of the dissertation and outlines potential directions for future research.

DOI: 10.14750/ME.2026.030

Chapter 2: Literature Review

2.1. Waste Printed Circuit Boards

Printed circuit boards (PCBs) are fundamental components of modern electronic devices, serving as the backbone of nearly all electrical and electronic equipment [9]. They provide mechanical support and establish electrical connections among electronic components, enabling the seamless operation of devices [10]. Often referred to as printed wiring boards [20], PCBs are integral to a wide range of applications, including random access memory, motherboards, and network interface cards in computers, as well as televisions, mobile phones, and household appliances [32].

The global production of PCBs has grown substantially, with global production increasing by 8.7% annually, while regions like Southeast Asia and China have experienced even higher growth rates of 10.8% and 14.4%, respectively [33, 34]. By 2021, the PCB market size surpassed USD 75 billion, and China emerged as a leading contributor, producing nearly 40% of the world's PCBs [33, 35]. This rapid growth in PCB manufacturing, coupled with accelerating technological advancement and shortened device lifecycles, has led to a significant increase in waste printed circuit boards (WPCBs).

WPCBs account for approximately 3–7% of the total mass of e-waste and represent a high-value fraction due to their rich composition of copper (averaging over 20%), precious metals such as gold, silver, and palladium, and other recyclable metals [11–14]. In 2020, an estimated 1.2 million tonnes of WPCB were generated, with 34% undergoing environmentally sound recycling, which is substantially higher than the 17% recycling rate for e-waste as a whole [36].

Globally, WPCB generation has reached an annual accumulation of 1.5–2 million tonnes [37]. This trend is largely fueled by the rapid obsolescence of electronic devices, which contributes to their frequent replacement [33]. **Table 2. 1** presents the main sources of PCB and their respective weight contributions.

The significance of WPCBs lies in their dual impact on economic and environmental fronts. Economically, WPCBs are a valuable recycling resource due to their high metal content (30–50 wt.%) [15]. Fully recycling high-grade WPCBs can generate considerable economic benefits, with estimates of a net present value reaching 63 million euros for high-grade ones [16]. Environmentally, however, improper disposal or informal recycling of WPCBs poses significant risks due to hazardous substances such as lead, mercury, cadmium, and brominated

flame retardants (BFRs) [17]. This combination of economic potential and environmental concerns makes WPCBs a critical focus within e-waste management strategies, emphasizing their role in sustainable resource recovery and pollution mitigation efforts.

Table 2. 1: Sources of PCB and their respective weight contributions.

Equipment type	Share of PCB	
	(wt.%)[a]	(wt.%)[b]
Refrigerator	0.5	N.R*
Air conditioner	2.7	N.R
Washing machine	1.7	N.R
Printer	7.4	4.7
LCD TV	11.6	10.6
Notebook PC	13.7	N.R
Desktop PC	9.4	19.2
Stereo	11.1	5.2
Radio	10.4	6.4
Telephone	12.6	7.1
Mobile phone	30.3	N.R
DVD player/recorder	14	3.9

[a] Oguchi et al. [38]; [b] Yuan et al. [39]; * Not Reported

2.1.1. PCB structure, types, and composition

The continuous evolution in the design, performance, and functionality of EEEs has driven significant advancements in PCBs. As a result, PCBs have undergone substantial modifications, leading to highly heterogeneous materials with varying properties and compositions. This heterogeneity is a direct outcome of efforts to enhance the efficiency, durability, and adaptability of PCBs to meet the demands of modern technology. Consequently, understanding the structure and composition of PCBs is critical for identifying the challenges associated with their recycling. Such insights are essential for developing efficient and environmentally sustainable recycling strategies.

The manufacturing materials used to make PCBs are determined by their application [40]. The key components of PCBs are (i) the base, which is a thin, rigid, or flexible board of insulating material that holds all conductors and components; (ii) the conductors, which are typically high-purity copper thin strips in appropriate shapes securely bonded to the base material; and (iii) the components attached to the substrate, such as chips, connectors, and capacitors [41].

DOI: 10.14750/ME.2026.030

a) Base material

The fundamental component of a PCB unit is the substrate, which acts as both a mechanical support and a medium for connecting circuit tracks. PCB laminates are typically constructed from polytetrafluoroethylene reinforced with fiberglass, such as FR-2 (phenolic cotton paper), FR-3 (cotton paper and epoxy), FR-4 (woven glass and epoxy), FR-5 (woven glass and epoxy), FR-6 (matte glass and polyester), G-10 (woven glass and epoxy), CEM-1 (cotton paper and epoxy), CEM-2 (cotton paper and epoxy), CEM-3 (woven glass and epoxy), CEM-4 (woven glass and epoxy), and CEM-5 (woven glass and polyester). Common matrix insulating materials include epoxy, polyimide, and triazine polymers. In general, a resin polymer contains embedded fiberglass as reinforcement. One of the most prevalent laminate materials used in electronics is FR-4, which consists of woven fiberglass cloth impregnated with epoxy resin (**Figure 2. 1**) [42, 43].

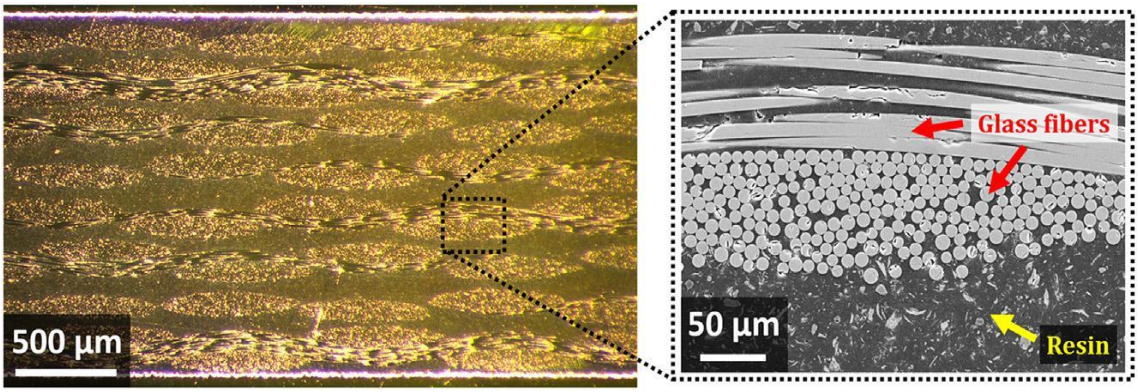

Figure 2. 1*:* Optical depiction of fiber bundles encapsulated within an epoxy matrix alongside an enlarged SEM image of a standard fiber-reinforced FR-4 laminate [44].

All PCB base materials share three fundamental components: (1) the resin system with additives, (2) reinforcement materials, and (3) the conductive layer. The combined properties of these components define the overall characteristics of the substrate [45]. Epoxy resins dominate PCB production, offering a balance of mechanical, electrical, and physical properties while being cost-effective compared to high-performance resins like phenolic or polyester [43]. Woven fiberglass cloths are the preferred reinforcement material, providing an optimal combination of mechanical strength and electrical performance [46].

b) Conductive materials

Copper is widely used in the production of PCBs due to its high conductivity, accessibility, and cost-effectiveness. There are different types of copper foil used in the PCB industry, each with its own advantages and disadvantages. The primary purpose of copper layers is to ensure

electrical conductivity between the different layers of the PCB and the electronic components [47].

The two most commonly used types of copper foil are electrodeposited (ED) and rolled annealed (RA). The main difference between them lies in their grain structures. ED copper has a vertical grain formation, which makes it prone to cracking when stress concentrates in the valleys between sharp surface peaks. Fractures can easily spread along boundaries. On the other hand, the RA copper has a horizontal grain structure and a smoother surface, resulting in fewer stress points. However, once a crack starts, it needs to traverse multiple grain boundaries to completely fracture the copper structure [47].

c) Electronic components

Items that use electricity are called electronic components (ECs). These components come in different shapes, sizes, and functions, depending on their specific uses. Some key types include integrated circuits (ICs), central processing units (CPUs), resistors, tantalum capacitors, multilayer ceramic capacitors (MLCCs), and random-access memory (RAM). These components are mounted onto PCBs, which have conductive paths made by etching copper sheets onto an insulating base [46]. Attaching electronic components to PCBs involves various methods, which can be divided into two main approaches:

- Attachment methods (such as screwing, inserting, soldering, tying, wrapping, and applying coatings or plating); and
- inclusion methods (such as embedding, encapsulating, mixing alloys, and embedding within a compound).

Broadly speaking, components that are attached using screws, clips, or rivets, or by inserting, wrapping, or embedding, can be easily removed. On the other hand, components that are secured by coating, tying, soldering, or encapsulating are more difficult to remove. Components that are combined through alloying and embedding are permanently fixed and cannot be separated mechanically [48, 49].

d) PCB types

Based on structure and alignment, there are three basic forms of PCB construction: single-sided, double-sided, and multilayered [50]. Single-sided means that wiring is available only on one side of the insulating substrate. These boards are typically used in the case of simple circuitry [51]. When the number of components on a single-sided board becomes too large, a

DOI: 10.14750/ME.2026.030

double-sided board can be employed. Double-sided PCBs have wiring patterns on both sides of the insulating material, i.e., the circuit pattern is available both on the component side and the solder side [14]. Multilayer PCBs have one or more conductor layers (usually power planes) buried inside, in addition to having a conductor layer on each outside surface. The inner layers are connected to each other and to the outer layers by plated through-holes or vias. Multilayer PCBs are the type of choice for nearly all digital applications, ranging from personal computers to supercomputers. The number of layers ranges from 3 to as many as 50 in special applications [52]. **Figure 2. 2** shows the layers and components found in typical multilayer PCBs.

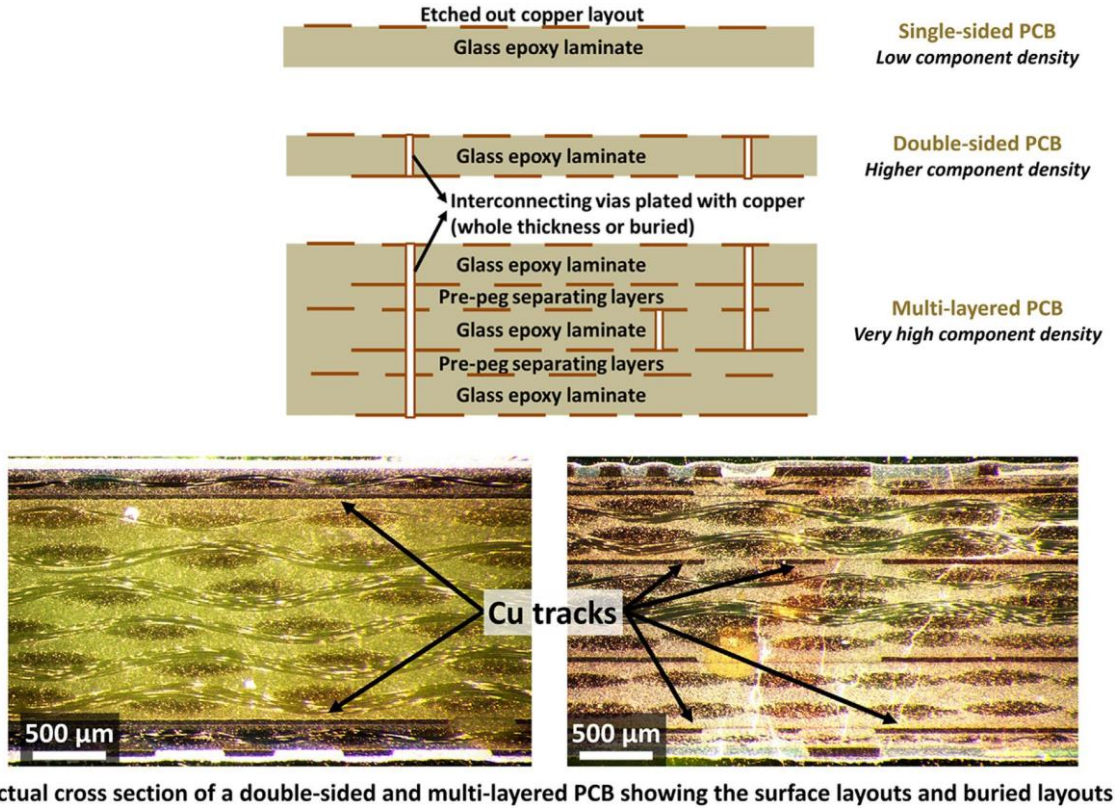

Figure 2. 2: Schematics of single, double, and multilayered printed circuit boards along with a cross-sectional image of the real double-sided and multilayered PCBs [44].

e) PCB composition and value

PCBs are complex mixtures of materials, comprising up to 60 different elements, including both valuable and hazardous substances [53]. These elements are broadly categorized into three groups: metals, nonmetals, and organic materials. Generally, each category contributes approximately one-third to the total PCB mass, although some studies estimate the composition as roughly 40% metals, 30% plastics (organic materials), and 30% fiberglass (nonmetals) [48, 54, 55]. **Table 2. 2** provides a detailed breakdown of these materials alongside a comparison with typical ore bodies, drawing on data from various studies.

DOI: 10.14750/ME.2026.030

Table 2. 2: PCB material composition.

Materials	(source)[a]	(source)[b]	(source)[c]	(source)[d]	Typical ore (source)[a, c, d]
Metals					
Cu (%)	10–26.8	6–31	3–37.9	12–19	0.5–3
Fe (%)	1.22–8	0.7–15.2		0–11	30–60
Al (%)	2–4.8	1.3–11.7	0.3–13.5	2–8	20–24
Sn (%)	1–5.28	0.7–7.4	0.6–8.4		0.5
Pb (%)	0.99–4.19	0.8–6.7	0.8–15.5		3
Ni (%)	0.28–2.35	0.2–5.4	0.0–5.4		1
Zn (%)	0.16–2.17	0.2–2.2	0.1–5.9		2.5
Sb (%)	0.06–0.4	0.2–0.4			
Au (ppm)	80–1000	9–2050	0–1500	29–1120	0.5–10
Ag (ppm)	110-3300	110–5700	0–3800	100–5200	5–10
Pd (ppm)	10-294	3–4000	0–680	33–220	1–10
Pt (ppm)	5–30	5–40			
Co (ppm)		1–4000			
Ceramics					
SiO_2	15–41	15–30			
Al_2O_3	6–7	6–9.4			
Alkali-earth oxides	6–10	6			
Titanates-micas	3	3			
Plastics					
PE		10–16			
PP		4.8			
PS		4.8			
Epoxy		4.8			
PVC		2.4			
PTFE		2.4			
Nylon		0.9			

[a] Goodship et al. [40]; [b] Kaya [18]; [c] Vucinic et al. [56]; [d] Holuszko et al. [57]

Plastics, which constitute a significant portion of WPCBs, are primarily composed of styrene-based polymers such as polystyrene (PS) and epoxy resins. Additionally, other polymers like polyethylene (PE), polypropylene (PP), polyvinyl chloride (PVC), and polytetrafluoroethylene (PTFE) are frequently used. These plastics represent complex, high-performance materials that offer versatility but pose recycling challenges. A variety of recycling techniques, including depolymerization, thermal treatment, solvent dissolution, and mechanical recycling, are employed to recover and reuse these materials [1].

The remarkable enrichment of several metals in WPCBs, with concentrations equal to or even surpassing those found in natural ore deposits, is shown in **Table 2. 2**. Metals such as copper, tin, lead, and nickel, alongside precious metals, are present in substantial amounts, emphasizing the resource potential of WPCB recycling. Notably, a study by Arshadi et al. [58] revealed that the average economic value of WPCBs is approximately 140 times greater than the average

value of the top ten natural ores, underscoring their economic significance. However, direct comparisons between WPCBs and mined ore resources can be challenging due to their distinct compositions. While mining ores typically consist of low metal concentrations mixed with various elements, WPCBs represent a complex mixture of plastics, metals, ceramics, and other materials. This complexity not only complicates processing but also makes it difficult to establish a refining process adaptable to the diverse categories of WPCBs [1].

The economic potential of WPCBs is further complicated by the considerable variability in their metal content. This variation can be attributed to several factors, including the type of PCB, its intended application, year of production, and specific design specifications [15]. For instance, cell phone PCBs, which require superior connectivity, contain significantly higher concentrations of precious metals (e.g., silver at 2100 ppm) compared to TV PCBs (e.g., silver at 48 ppm) [15].

Additionally, studies by Ogunniyi et al. [59] and Bizzo et al. [60] analyzed trends in the metallic composition of PCBs over extended periods, spanning 15 years (1991–2006) and 21 years (1993–2014), respectively. Both studies noted a decline in precious metal content, such as gold and silver, in more recent PCBs. For instance, gold concentrations, which were reported to exceed 1000 ppm in the early 1990s, have been shown in more recent studies to vary between approximately 420 ppm and as low as 29 ppm. Conversely, the concentrations of base metals like copper, nickel, tin, lead, zinc, and aluminum remained relatively consistent over the same periods.

The high economic attractiveness of WPCBs is primarily driven by their precious metal content. Based on gold concentration, WPCBs can be categorized into low (less than 100 ppm), medium (100–400 ppm), and high (over 400 ppm) value groups [61]. Different values of WPCBs require distinct processing methods to focus on recovering specific metals. Low-value WPCBs are generally treated to extract copper and iron, whereas high-value WPCBs are processed to recover valuable metals such as copper, gold, silver, palladium, and platinum.

Forecasts indicate that by 2030, approximately 58 tonnes of gold will be recycled from WPCBs, representing an economic value of about $11.3 billion [62]. Given that the gold content of WPCBs is approximately 0.023%, its potential value is estimated at $5620 per tonne [63]. Furthermore, a study utilizing a weighted sum model to evaluate the trade-offs between energy-saving potential, economic value, and ecotoxicity demonstrated that gold recovery holds the highest priority when equal weights are assigned to these three sustainability criteria [64].

2.2. WPCB Recycling

WPCBs have garnered significant attention due to their dual role as a valuable resource and a potential environmental and health hazard. Recycling WPCBs typically involves three primary stages. The first is disassembly, which entails selectively disassembling reusable components and hazardous substances, either manually or through automated or semi-automated processes. This is followed by upgrading, where mechanical and physical processing techniques are applied to prepare materials for refinement. The end-processing stage utilizes metallurgical methods, such as pyrometallurgy, hydrometallurgy, electrometallurgy, or biohydrometallurgy, to purify and recover valuable metals.

2.2.1. Disassembly

Disassembly is the first step in WPCB recycling, enabling the separation of ECs for reuse or subsequent processing [34]. Proper disassembly ensures that valuable metals in ECs are recovered effectively and prevents these components from entering the main recycling stream, where extraction efficiency would significantly decrease [65–67].

Disassembly methods can be broadly categorized into selective and simultaneous approaches. Selective disassembly involves identifying and removing individual components manually or semi-automatically for reuse or remanufacturing, whereas simultaneous disassembly removes all components at once, often using thermal processing. However, simultaneous disassembly is resource-intensive and increases the risk of damaging components [68, 69].

In informal recycling practices, particularly in developing countries, manual disassembly using basic tools remains prevalent. This often includes hazardous practices such as burning or melting, which release toxic fumes with well-documented health and environmental consequences [68]. Conversely, developed countries increasingly rely on mechanical disassembly processes to mitigate these risks. Fully automated systems employ vision-based technologies to identify and sort reusable or hazardous components, while semi-automatic methods use heating combined with mechanical forces like vibration or shearing to remove components more efficiently [70, 71].

2.2.2. Mechanical processing

Mechanical processing methods constitute a pivotal upgrading stage in WPCB recycling, primarily focusing on the liberation and separation of metals and nonmetals [1, 10]. The separation mechanisms exploit various physical characteristics of metals, including density,

electrical conductivity, and magnetic susceptibility [72]. Common methods include density separation [73–75], magnetic separation [76], gravity separation [73, 77], pneumatic separation [78, 79], electrostatic separation, and eddy current separation [80–82].

As a pretreatment step, mechanical processing can enhance the extraction efficiency of downstream metallurgical processes, such as pyrometallurgy, hydrometallurgy, and biohydrometallurgy, by improving metal recovery rates and reducing the overall volume of material to be processed [83]. This reduction decreases the energy demands of energy-intensive refining processes, contributing to their economic and environmental feasibility. Moreover, physical methods preserve the integrity of nonmetallic fractions, supporting their reuse and promoting circular economy principles [84].

Despite its advantages, such as simplicity, lower energy consumption, and relatively low initial investment, mechanical processing faces notable limitations. These include inefficiencies in separating metals from nonmetals [1], challenges in recovering metals from comminution fines [85], and loss of metals in the form of dust during comminution [18]. Such shortcomings affect the overall effectiveness and economic viability of WPCB recycling, highlighting the need for process optimization [86].

2.2.3. Pyrometallurgical processing

Pyrometallurgical processing is one of the most dominant industrial approaches for WPCB recycling, currently treating over 70% of WPCBs through various high-temperature operations ranging from 500 to 2000°C [87, 88]. Common processes include smelting, incineration, roasting, sintering, and plasma arc furnace operations. These techniques primarily target the recovery of non-ferrous and precious metals [89].

One of the notable advantages of pyrometallurgy is its versatility, as it can process WPCBs regardless of their size, shape, or composition. This flexibility makes it suitable for large-scale industrial applications [20]. Additionally, the organic content of WPCBs, such as plastics and flammable components, partially serves as a reducing agent and fuel during smelting, thereby lowering external energy requirements [90]. For example, facilities like the Umicore plant utilize WPCB fractions combined with coke as a reductant and fuel source, while the Rönnskar smelter employs pulverized WPCBs as an alternative energy input [88].

Despite its industrial success, pyrometallurgical processing has several drawbacks. The method is highly energy-intensive, contributing to high operational costs. It also generates significant

quantities of slag, which encapsulates metals like aluminum and copper, reducing their recovery efficiency [91]. The presence of ceramics and fiberglass in WPCBs exacerbates this issue, as these components act as slag-forming agents, further trapping valuable metals [1]. Additionally, hazardous emissions, including heavy metal fumes, particulate matter, dioxins, and greenhouse gases, pose serious environmental and health risks [1, 89]. Emission control systems are essential to mitigate these effects, particularly for WPCBs containing PVC or brominated flame retardants [89].

The economic aspects of pyrometallurgical processing present a mixed picture. While the process demonstrates economic efficiency in precious metal recovery, it requires higher initial capital investment compared to hydrometallurgical alternatives [91]. Furthermore, the complexity of WPCB materials poses challenges in process control, and the selective recovery of individual metals and high purity requirements necessitate subsequent hydrometallurgical or electrochemical refining steps [1, 90].

Recent assessments emphasize that although pyrometallurgical technology can handle large volumes of e-waste regardless of form, its high energy demands and challenges in achieving efficient metal value separation raise concerns about its long-term sustainability [20]. Additionally, the process generates significant greenhouse gases and hazardous emissions, while the recovery of certain valuable metals remains problematic. This has driven research into the potential of mechanical pretreatment as a means to enhance metal recovery efficiency and mitigate slag formation. Such approaches are increasingly relevant given the growing complexity of WPCBs and their progressively lower metal content [92, 93].

2.2.4. Hydrometallurgical processing

Hydrometallurgy is an extractive method that utilizes aqueous solutions to dissolve and recover metals from various sources, including WPCBs [94]. This process primarily involves the dissolution of metals using strong chemical lixiviants, followed by metal recovery through various purification techniques [89, 91].

The process typically begins with a leaching stage, where metals are solubilized using various reagents. Common lixiviants include mineral acids (sulfuric acid, hydrochloric acid, nitric acid, and aqua regia), ammonia, ammonium salts, and chlorides [1, 95]. For precious metals such as gold, silver, and platinum, specialized leaching agents like thiourea, thiosulfate, and cyanides are employed [96, 97].

Following the leaching stage, metal recovery from solution is achieved through various techniques, including electrorefining, precipitation, cementation, absorption, ion exchange, and solvent extraction [98–100]. This systematic approach enables the production of high-purity metals, particularly precious metals such as gold and silver [89].

Compared to pyrometallurgical processing, hydrometallurgical methods offer several distinct advantages. The process demonstrates higher efficiency, cost-effectiveness, and predictability while requiring less energy and operating at lower temperatures. It also provides superior metal selectivity, generates minimal emissions, and eliminates slag formation. [83, 97]. Additionally, the process offers easier control over reactions and presents fewer environmental hazards than pyrometallurgical approaches [10].

Despite these advantages, hydrometallurgical processing has notable drawbacks. The method requires large volumes of chemicals, often resulting in hazardous liquid and solid wastes that demand careful disposal [55, 91]. The process can be slow and time-consuming due to leaching kinetics, necessitating fine particle sizes and mechanical pretreatment to enhance efficiency [10, 83]. While capital costs are generally lower than pyrometallurgical alternatives, the investment in chemical procurement and waste treatment infrastructure remains significant [1]. Additionally, the use of toxic and flammable reagents, coupled with the high investment costs, presents challenges to its widespread adoption [1].

2.2.5. Biometallurgical processing

Biometallurgy, also known as biohydrometallurgy, represents an innovative approach that harnesses microorganisms to enhance metal solubilization from WPCBs under mild ambient temperatures and atmospheric pressure [101]. The process primarily encompasses two main areas: bioleaching and biosorption [89], where various microorganisms facilitate metal recovery through multiple mechanisms, including bio-oxidation, bio-reduction, bioaccumulation, biosorption, and bio-precipitation [102]. Key microorganisms utilized in bioleaching include autotrophic acidophilic bacteria such as *Acidithiobacillus ferrooxidans*, *Acidithiobacillus thiooxidans*, and *Leptospirillum ferrooxidans*, as well as fungi like *Aspergillus niger* and *Penicillium spp.* [89, 103].

The process employs diverse microorganisms, with acidophilic bacteria and filamentous fungi being predominant for base metal recovery. Autotrophic bacteria such as *Acidithiobacillus spp.*, *Sulfolobus spp.*, and *Leptospirillum spp.* have demonstrated effectiveness in extracting base metals through both contact and non-contact bioleaching mechanisms [102]. Fungi,

particularly *Aspergillus niger* and *Aspergillus tubingensis*, have shown promising results, with studies reporting extraction efficiencies of up to 100% for zinc, 80% for nickel, and 86% for copper over a 30-day period [104]. Notable success has also been achieved in precious metal recovery, as demonstrated by Kumar et al. [105].

The effectiveness of biometallurgical processing is heavily dependent on proper pretreatment of WPCBs, particularly regarding particle size reduction. Research indicates optimal bioleaching occurs with particles smaller than 1 mm, as finer particles enhance the interaction between metallic and nonmetallic components [103]. To achieve this, mechanical pretreatment methods are typically preferred for their lower environmental impact compared to chemical options [103, 106].

Despite its numerous advantages, including lower investment costs, reduced environmental impact, and minimal energy consumption compared to conventional pyrometallurgical and hydrometallurgical routes, biometallurgy faces several significant challenges [107]. The process is characterized by extended recovery periods and requires fine powders necessitating size reduction operations [108]. Additionally, the sensitivity of microorganisms to environmental conditions poses challenges in maintaining consistent performance, as factors such as water purity, operating temperatures, and geographic location can significantly impact process outcomes [109]. Moreover, microorganisms are also highly sensitive to toxic metals, which can inhibit their metabolic processes and reduce overall efficiency. The scalability of laboratory successes to industrial applications remains a significant hurdle, primarily due to the slow kinetics and challenges in treating high pulp density materials [91].

2.2.6. Summary of processing approaches

The various end-processing recycling approaches for WPCBs, including pyrometallurgical, hydrometallurgical, and biometallurgical processing, each present distinct advantages and limitations, as summarized in **Table A. 1** (**Appendix I**). The growing complexity of WPCBs and their decreasing metal content necessitate an integrated approach that maximizes recovery efficiency and economic viability.

Mechanical processing as a pretreatment step plays a fundamental role across all recycling methods. Although pyrometallurgical processing can handle raw WPCBs without pretreatment, incorporating mechanical processing offers several crucial benefits: it reduces the formation of slag that can trap valuable metals, decreases the energy requirements of subsequent thermal treatments, and enables more efficient recovery of metals from increasingly complex WPCB

compositions. For hydrometallurgical and biometallurgical processes, mechanical pretreatment is essential, as it enhances leaching kinetics through increased surface area and improved metal liberation, ultimately leading to higher recovery rates and reduced chemical consumption through higher concentration gradients.

The effectiveness of mechanical pretreatment hinges primarily on the comminution step, which serves as the cornerstone of size reduction and liberation. This critical stage determines the success of subsequent separation processes and influences the overall efficiency of metal recovery in downstream operations. Understanding the comminution process is, therefore, crucial for developing more effective and sustainable WPCB recycling strategies.

2.3. Comminution of WPCBs

The complexity of WPCB comminution exceeds that of conventional mineral processing, as these materials present intricate multilayer structures comprising tightly fused laminates, substrates, and solders [74]. These components exhibit diverse mechanical properties at room temperature, which influence their behavior during comminution [110]. For instance, a higher metal content in boards tends to enhance mechanical performance [111]. Key properties such as tensile strength, bending strength, and impact toughness play varying roles depending on the type of size reduction machine and the forces it exerts [112, 113].

Comminution machinery that utilizes shearing, shredding, and cutting stresses has proven particularly effective for processing WPCBs due to their predominantly non-brittle composition [114]. Cutting mills and rotary shears have shown effective performance in liberating WPCB components. However, these methods face challenges such as rapid wear of machine parts, limited selectivity in material separation, and high maintenance costs [115]. In contrast, high-intensity impact mills are highly effective at disrupting the intricate structures of WPCBs, significantly enhancing liberation but are often associated with excessive generation of fines [116, 117].

2.3.1. Liberation

The liberation characteristics of WPCBs differ fundamentally from those of mineral ores, as no specific size range ensures optimal liberation. Instead, different types of elements are released across varying size ranges [114]. The effectiveness of liberation is governed by both process parameters (equipment type, operating conditions, and loading) and inherent WPCB properties (mechanical strength, thermal stability, and material composition) [18]. As detailed

in **Table A. 2** (**Appendix I**), various mechanical comminution machinery has been employed in WPCB pretreatment, yielding different liberation outcomes.

Studies have extensively examined liberation outcomes using different comminution approaches. Zhang and Forssberg [49, 118] demonstrated that metallic particles in PC WPCBs achieve near-complete liberation when their particle size is reduced to below 2 mm using a hammer mill. Similarly, Duan et al. [119] and Ogunniyi et al. [59] showed that swing hammer mills equipped with internal sieves under 0.5 mm could achieve complete liberation of WPCBs from PCs, cell phones, and switchboards. Notably, studies by Li et al. [120], Guo et al. [79], and Quan et al. [114] consistently showed approximate complete metal liberation below 0.59-0.42 mm across different comminution methods.

Component-specific liberation behaviors vary significantly. While slots achieve complete liberation at relatively coarse fractions (<2 mm) due to their disengaging mechanism, PWBs and ICs exhibit coupled liberation modes that prevent complete separation above 0.125 mm [119, 121]. Advanced microscopic analyses by Ogunniyi et al. [59] revealed that even at fine fractions below 0.075 mm, where quantitative assessments suggested 99.48% liberation, SEM and EDS analyses detected persistent composite particles, particularly residual solder-attached copper traces.

2.3.2. Fines and dust generation

Given the unique structural and mechanical properties of WPCBs, characterized by their high strength and tenacity, and the requirement for metal liberation to typically occur within size ranges below 0.5–1 mm, achieving such fine size reduction inevitably generates significant amounts of fines and dust during crushing and pulverization [116, 122].

The term "fines" or "comminution fines" in the context of WPCB recycling refers to particle size fractions that exhibit notably low separation efficiency when subjected to physical separation methods. Various studies have highlighted the challenges associated with these fine fractions. For instance, Li et al. [120, 123] reported that particle sizes below 0.3 mm were unsuitable for corona electrostatic separation due to reduced recovery, with optimal separation observed between 0.6 and 1.2 mm. Similarly, Wen et al. [121] found that high-tension electrostatic separators struggled to effectively process size fractions of 0.074–0.5 mm, and for particles below 0.074 mm, metal reclamation became nearly impossible with traditional methods. Suponik et al. [124] further confirmed the reduced efficiency of electrostatic separators when processing particles below 0.125 mm.

A similar trend is observed with other gravity separation techniques. Yoo et al. [125] demonstrated that zig-zag classifiers achieved about 95% separation of metallic components from WPCB particles larger than 0.6 mm, but this efficiency dropped significantly to 60% for particles smaller than 0.6 mm. Nie et al. [126] noted a sharp decline in metal recovery and grade for WPCB particles below 0.125 mm when using a shaking table. For fine size fractions below 0.1 mm, conventional gravity separators struggle to capture metallic values effectively. While specialized equipment like centrifugal gravity separators, such as Knelson and Falcon, operating at high G-forces can potentially handle these fines, their limited feeding capacity poses practical constraints for industrial applications [127].

The processing of fines becomes increasingly critical when considering their substantial yield and notable metal content, as highlighted in various studies. Zhihai et al. [128] investigated the size distribution of crushed mixed WPCBs using a hammer mill with a 2.2 mm internal mesh sieve and found that fines below 0.25 mm constituted 45–54 wt.% of the total output across different operating conditions. Similarly, Li et al. [123], using a two-step crushing process for mobile phone WPCBs involving a rotary shear shredder followed by a hammer mill with 1 mm screen holes, reported that particles below 0.3 mm accounted for nearly 50% of the total particle weight.

Eswaraiah et al. [129] examined PC WPCB crushing discharge and noted that size fractions below 0.25 mm made up approximately 20% of the total yield, containing about 6% of the total feed's metal content. Guo et al. [79] observed comparable results, with particles below 0.25 mm comprising around 20% of the yield and 12% of the total metal content, including 3% copper, 0.5% aluminum, 0.3% iron, 14 mg/kg gold, and 10 mg/kg silver. Nekouei et al. [130] reported similar findings for PC WPCBs comminuted to sizes below 0.212 mm.

Dinç et al. [127] demonstrated the high metal content of fines generated through a two-step comminution of PC WPCBs, employing a rotary shear shredder with a 2 mm sieve followed by a hammer mill with a 0.5 mm sieve. Their results showed that fines below 0.3 mm accounted for 34.3% of the total sample weight and contained 27% of the total metal distribution, including 10.4% copper, 26 mg/kg gold, and 98 mg/kg silver.

In addition to the significance of fines in WPCB comminution, the generation of dust also demands attention due to its distinct characteristics and implications for material recovery. Dust generation during comminution varies significantly across studies and processing conditions. For instance, Silvas et al. [131] reported 6 wt.% dust losses during WPCB processing using a

cutting mill with a 6 mm bottom sieve followed by a hammer mill with a 1 mm grid. This was markedly lower compared to Moraes et al. [132] (25 wt.%) and Yamane et al. [133] (29 wt.%). These variations were attributed to differences in both WPCB types and processing parameters, particularly bottom sieve sizes. Further supporting this variability, Bachér et al. [116, 134] demonstrated that dust generation was influenced not only by the manufacturing year of mobile phone WPCBs but also by the choice of comminution equipment, with hammer mills generating more dust (2.9 wt.%) compared to cutting mills (1.1 wt.%).

The characterization of dust has revealed distinct findings regarding both size distribution and metal content. Wang et al. [73, 135] analyzed dust samples collected from a typical PCB recycling plant in Anhui Province, China, and found that 76 wt.% of the dust was below 0.25 mm, with 51.15 wt.% falling below 0.075 mm. This dust, composed of 73.1 wt.% organic matter, also contained recoverable metals such as aluminum (46.5 kg), iron (45.5 kg), copper (26.7 kg), lead (10.6 kg), manganese (8.6 kg), and zinc (7.6 kg) per tonne of processed dust.

Furthermore, Bachér et al. [116, 134] highlighted the metal enrichment of dust generated from mobile phone WPCBs, identifying high concentrations of base metals and neodymium. This reflects the brittleness of components such as loudspeakers and small motors containing neodymium magnets, which pulverize easily during comminution. Precious metals like gold, palladium, and platinum were also found in notable quantities in the dust, with gold concentrations ranging from 401 to 415 mg/kg, palladium between 119 and 129 mg/kg, and platinum between 1.7 and 4.9 mg/kg. These elevated precious metal concentrations were attributed to the surface-mounted nature of gold-plated connectors and palladium-containing components, making them particularly susceptible to grinding during comminution.

2.3.3. A summary of WPCB comminution challenges

To summarize, mechanical processing is increasingly recognized as a fundamental pretreatment step across all recycling approaches, with the comminution stage playing a pivotal role in the success of subsequent separation processes. Although comminution disrupts the complex multilayer structures of WPCBs and facilitates metal liberation, it does not achieve complete liberation, as composite particles persist even in fine size ranges. Moreover, comminution generates fines and dust, which, while constituting a small fraction of the overall throughput, pose challenges for conventional physical separation methods. These fractions can lead to considerable metal losses, with precious metals like gold experiencing losses of up to 20%. The dual presence of valuable and harmful elements in these fractions, coupled with their

impact on the efficiency of conventional separation techniques, highlights the need for alternative separation methods. Froth flotation emerges as a promising solution to address this critical gap and enhance WPCB recycling efficiency. However, effective flotation requires careful consideration of both particle size distribution and liberation characteristics. This raises fundamental questions about the optimal grinding approach to achieve the specific size and liberation requirements for successful WPCB flotation, an aspect that remains unexplored in current literature.

2.4. Froth Flotation in WPCB Separation

Froth flotation is a physicochemical separation process that exploits differences in the surface properties of materials. Originally developed over a century ago for mineral beneficiation, it has since become an indispensable technique in mineral processing and has been successfully adapted for use in paper recycling and wastewater treatment, highlighting its versatility and adaptability [18, 21, 22].

The fundamental principle of froth flotation relies on the selective attachment of hydrophobic particles to air bubbles, leading to their recovery in the overflow, while hydrophilic particles remain dispersed in the liquid phase [136]. This selectivity is governed by the wettability behavior of particles, which is fundamentally defined by surface energy. Surface energy, analogous to liquid surface tension, is divided into dispersive (nonpolar) and specific (polar) components. Techniques such as contact angle measurements and inverse gas chromatography are employed to calculate surface energy and assess the work of adhesion to water. This enables predictions about whether a material is hydrophilic or hydrophobic [23, 137, 138].

Froth flotation is a complex system involving three phases (solids, water, and air) and the interplay of numerous chemical and physical variables. Chemical variables primarily control the transition between hydrophilic and hydrophobic states, while physical variables encompass both material-specific properties (such as particle size and liberation) and operational parameters (such as air flow rate and bubble size) [22, 24].

A multitude of factors influence flotation response, including particle size, shape, surface roughness, surface chemistry, pulp chemistry, and froth stability [139]. Surface-active reagents play critical roles in modifying system behavior. Frothers regulate bubble formation and froth stability, while collectors selectively enhance the hydrophobicity of target solids via physisorption or chemisorption. The performance of collectors depends on proper reagent dosage, pH control, and conditioning time [136, 140].

DOI: 10.14750/ME.2026.030

The flotation process encompasses three primary mechanisms by which particles are recovered from the pulp to the overflow product: (1) selective attachment to air bubbles, referred to as "true flotation"; (2) entrainment in water carried through the froth; and (3) physical entrapment between particles in the froth attached to air bubbles ("aggregation") [24]. The mass transfer dynamics within a flotation cell involve multiple pathways (**Figure 2. 3**). Hydrophobic particles are transported to the froth from the pulp via true flotation (1) and are subsequently transferred to the overflow (2). Simultaneously, entrainment processes transfer both hydrophobic and hydrophilic particles to the froth (3) and overflow (4). Drainage mechanisms return detached and entrained particles to the pulp (5) [141]. While true flotation serves as the primary recovery mechanism for hydrophobic particles, separation efficiency is significantly influenced by entrainment and physical entrapment. Unlike true flotation's selective nature, both hydrophobic and hydrophilic particles can be recovered through entrainment and entrapment, making froth phase stability control crucial for achieving effective separation [24].

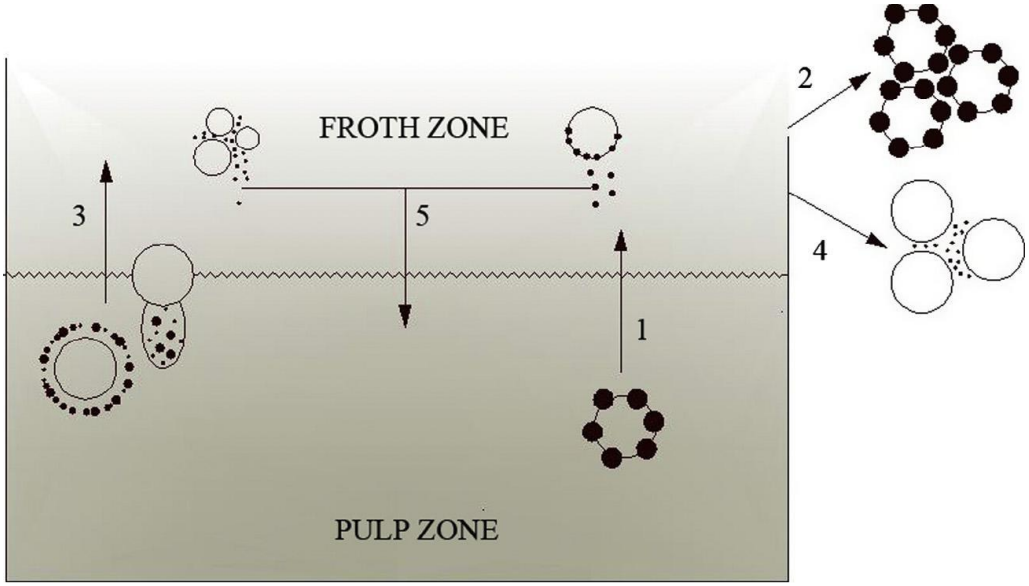

Figure 2. 3: Pathways of mass transfer dynamics in a flotation cell [141].

Froth flotation can be implemented through two primary approaches: direct flotation, which involves floating the target material into the overflow product while leaving the gangue in the underflow, and reverse flotation, where the gangue materials are floated into the overflow, concentrating the desired materials in the underflow [25]. These approaches are selected based on the specific material characteristics and desired separation outcomes.

While froth flotation has long been established in mineral processing, its application in WPCB recycling is relatively recent. The earliest work by Das et al. [142] utilized flotation alongside tabling to enhance the metal content in targeted streams. Shortly thereafter, Ogunniyi and

Vermaak [26] investigated froth flotation for WPCB comminution fines (<0.075 mm), introducing reverse flotation as a promising method to recover metal content by floating nonmetallic components as waste overflow, thereby concentrating the metallic fraction in the underflow.

The inherent complexity of WPCBs, comprising metals, alloys, ceramics, and plastics, presents both unique challenges and opportunities for selective separation via flotation [143]. This technique has proven particularly effective for pulverized WPCBs, leveraging the intrinsic hydrophobic nature of nonmetallic components to facilitate their separation and achieve bulk metallic enrichment [27]. Recent research has focused on optimizing flotation parameters for WPCBs, including the effects of particle size, shape, and surface properties. Studies have also examined chemical conditions, such as reagent selection and dosage, and physical conditions, including cell hydrodynamics, to improve flotation efficiency [28–31, 50, 144, 145]. Furthermore, integrating pretreatment techniques to modify the surface properties of WPCB components has emerged as a promising trend, enhancing their flotation response [146, 147].

2.4.1. Flotation behavior of the WPCB components

The heterogeneous composition of WPCBs presents unique challenges for selective separation via flotation. WPCBs typically contain 40% metallic particles, while the remaining 60% consists of nonmetallic components, including plastics, ceramics, resin matrix, and fiberglass reinforcements. These distinct material classes exhibit diverse surface properties that significantly affect their flotation behavior.

a) Nonmetallic particles (NMPs)

Plastics constitute a significant portion of the NMP fraction, including thermoset resins (epoxies, phenol formaldehyde), vinyl polymers (PVC), and engineering thermoplastics (ABS) [148]. These materials typically exhibit natural hydrophobicity, with water contact angles ranging from 76.5° for PET to 96.8° for PE, indicating favorable flotation behavior [18]. However, their flotation response varies with polymer chemistry, plasticizers, degree of polymerization, crystallinity, and surface structure [140]. The presence of additives such as lubricants, flame retardants, and stabilizers can introduce hydrophilic sites that modify surface properties [149].

Mechanical processing significantly influences NMP flotation behavior. Comminution creates fresh surfaces through polymer chain rupture, generating free radicals that readily react with

oxygen to form hydrophilic functional groups (–OH, =O) [140]. These newly formed surfaces typically demonstrate reduced hydrophobicity compared to original intact surfaces [149].

The flotation characteristics of fiberglass reinforcements are primarily determined by their resin impregnation [150]. Studies by Nie et al. [151] demonstrated that residual resin coating on fiberglass bundles enables bubble attachment and subsequent flotation. Kumar et al. [152] corroborated these findings through surface energy analysis, showing that while liberated fiberglass exhibits hydrophilic behavior, residual resin imparts hydrophobicity. EDS analysis revealed significant surface carbon content (49.42%) from resin impregnation, while FTIR spectroscopy identified hydrophobic alkyl and aromatic groups alongside polar functional groups capable of collector adsorption [58, 153].

Contact angle measurements for NMPs vary across studies, with mobile phone PCBs showing values of 77.31-81.70° [151, 153], while arcade machine PCBs exhibited lower angles (25.66-60.43°) [154]. These variations largely stem from differences in PCB laminate composition and surface characteristics [155]. Given the predominant hydrophobicity of NMPs, reverse flotation schemes have emerged as the preferred approach, where NMPs are floated while metals are concentrated in the underflow. This approach leverages the natural floatability of plastics and the hydrophobic characteristics imparted to resin-coated fiberglass, facilitating effective separation.

b) Metallic particles (MPs)

When exposed to aqueous environments, metals and their alloys develop complex surface reaction products whose properties, including solubility and thickness, significantly influence their suspension behavior and flotation response. The formation and extent of surface passivation are heavily dependent on solution conditions, particularly pH and oxidation-reduction potential, even in pure water systems [156].

Studies on pure metal surfaces have revealed a range of wettability characteristics. Contact angle measurements by Somlyai-Sipos and Baumli [157] demonstrated partial wetting characteristics for silver, gold, copper, iron, nickel, and titanium substrates, with angles ranging from 57° to 73°, suggesting a correlation with atomic radius. Further investigations by Hornyák [158] showed that properly prepared and polished copper and aluminum surfaces maintain relatively stable contact angles (80-82° and 83-85°, respectively) across pH 2-10. These studies highlight how surface preparation, roughness, oxidation, and the adsorption of airborne contaminants contribute to the hydrophobic or hydrophilic nature of metals. While pure metals

may display hydrophobic tendencies under specific conditions, their wetting behavior is far from uniform and varies based on surface state and environmental interactions [159].

The flotation behavior of MPs in WPCBs introduces additional complexity. Unlike pure metals, WPCB metallic fractions consist of engineering alloys and compounds tailored for stability and functionality in electronic applications [160]. X-ray photoelectron spectroscopy (XPS) analysis by Han et al. [153] revealed the presence of various metal compounds, including copper(II) oxide, copper-methionine, and aluminum-copper. These compounds, especially when oxidized during prolonged use, exhibit high surface energy, rendering them hydrophilic in flotation systems [160]. This hydrophilic tendency, coupled with the engineered inertness of alloys, differentiates the flotation characteristics of WPCB metals from those of minerals or pure metals commonly studied in flotation research.

Studies have shown that despite their inherent hydrophilicity, MPs can achieve floatability through collector interactions, with their high surface energies facilitating collector chemisorption [50, 161]. While research has demonstrated successful flotation of pure metals and their compounds using various collectors, attempts to concentrate WPCB metals in the froth phase have proven to be complex, often involving surface oxidation and low alloy affinity [50].

2.4.2. Important variables affecting WPCB flotation

a) Particle size

Particle size is a critical variable influencing flotation performance. In conventional mineral flotation, overflow recovery typically follows an "elephant curve," with optimal performance occurring in the 0.015–0.100 mm range [162]. Plastic flotation, on the other hand, generally involves larger particle sizes, with effective recovery achieved for particles between 2.0 and 6.0 mm, whereas particles smaller than 0.05 mm tend to float unselectively regardless of surface properties [139, 140]. In the reverse flotation of WPCBs, several studies have explored size ranges up to 1.5 mm and reported acceptable separation efficiency [143, 163, 164]. Nevertheless, questions persist regarding the suitability of using flotation at these sizes given the availability of simpler physical separation methods and metal liberation considerations.

In flotation of WPCBs, the relationship between particle size and separation efficiency presents unique characteristics for both NMPs and MPs. Contact angle measurements for NMPs of varying particle sizes (0.045-1.0 mm) show minimal differences, with angles ranging from 77.48° to 79.22° [165]. However, finer NMPs exhibit higher natural floatability, with overflow

recovery increasing as particle size decreases. Without frother addition, recovery ranged from 1.93% for 0.5-1.0 mm particles to 84.04% for particles below 0.045 mm. At a frother dosage of 300 g/t, recovery improved dramatically, reaching 99.78% for the finest size fraction, indicating that finer particles require lower reagent dosages to achieve maximum recovery [165].

For MPs, particle size affects flotation performance, including underflow recovery and grade. Studies have shown that reducing feed size below 0.25 mm decreases the metals recovery and grade in the underflow. This trend, observed by Ellamparuthy et al. [166] and corroborated by Sarvar et al. [29], Barnwal et al. [30], He and Duan [167], and Zhu et al. [168], highlights the trade-off between metal recovery and particle size, which impacts the flotation separation efficiency of WPCBs.

Notably, despite metals being the target component in WPCB reverse flotation, research has predominantly focused on understanding NMP flotation mechanisms and phenomena. MPs' flotation behavior, in contrast, has been characterized primarily by recovery and grade metrics, with limited attention to the fundamental mechanisms underlying their flotation. This knowledge gap is significant, as the unintended reporting of MPs into the froth reduces underflow recovery, negatively affecting overall separation efficiency. Understanding the role of particle size in metallic particle flotation behavior is crucial for optimizing the process and improving separation performance.

b) Particle shape

Particle shape, determined during the comminution stage, plays a role in the flotation process by influencing surface floatability [169, 170]. These attributes directly affect the efficiency of particle-bubble attachment and detachment mechanisms [170].

Post-comminution particle shapes include angular, rounded, flaky, and elongated particles, each exhibiting distinct flotation behaviors. Elongated and flaky particles resist detachment from bubbles more than spherical ones due to larger contact areas, while angular particles with sharp edges facilitate attachment by readily rupturing the bubble-particle liquid film. Irregular particles, having larger surface areas, adsorb more flotation reagents, affecting the three-phase contact line stability [170]. Shape variation influences entrainment, with high-aspect-ratio and lamellar particles showing increased entrainment due to higher drag forces [171–174]. Particle shape also impacts pulp rheology, as irregular particles create greater inter-particle friction than spherical ones at equal volume fractions, demonstrated by the lower viscosity of spherical

ferrosilicon compared to irregular magnetite suspensions in dense medium separation [175, 176].

In WPCB processing, the choice of comminution equipment directly influences particle shape through different mechanical stress mechanisms. The resulting shapes vary significantly among WPCB components due to heterogeneity in their material composition and mechanical properties, ranging from ductile metals to brittle ceramics and polymers [74]. Post-comminution, MPs tend to be spherical [177], rounded [178], needle-shaped [124], or irregular forms [164], with finer-sized MPs showing enhanced floatability due to their irregular, elongated, flat shapes [26, 179, 180]. Conversely, NMPs are more commonly elongated [144], flaky [124], or angular [30], shapes that intrinsically affect their floatability and interaction with bubbles.

c) Solids percentage in the pulp

The solids percentage in the pulp significantly influences flotation performance by affecting bubble loading, froth stability, particle suspension, collision efficiency, flotation kinetics, and separation selectivity [181–184]. While conventional mineral flotation typically operates at 10-40 wt.% solids (11-20 vol.%), WPCB flotation achieves optimal performance at notably lower solids concentrations [24, 185]. Studies have indicated peak metallic recovery at 4 wt.% for 0.25-0.5 mm particles [186], 6-10 wt.% for particles below 0.25 mm [167], and 8 wt.% for particles below 0.075 mm [26].

This preference for lower pulp densities in WPCB flotation, similar to practices in plastic flotation, arises from the negative effects of higher solid percentages. Increased pulp density restricts particle-bubble mobility, inflates froth, and intensifies particle friction, which raises the likelihood of coarse particles detaching from bubble surfaces [186]. For example, in reagent-free flotation of sub-0.212 mm particles, both extreme conditions, low (3 wt.% ≈ 2.8 vol.%) and relatively high (10 wt.% ≈ 9 vol.%) densities, negatively impacted recovery due to insufficient frothing and the formation of unstable, viscous pulp, respectively [30].

d) Impeller speed and aeration rate

Impeller speed and aeration rate are interdependent parameters that fundamentally control flotation cell hydrodynamics, with the impeller providing energy input and aeration supplying essential air bubbles for separation [187]. At the macroscopic level, higher impeller speeds enhance solid suspension and pulp circulation [188], while proper aeration ensures optimal

bubble dispersion patterns [189]. Microscopically, increased agitation and airflow generate microturbulence and shear, promoting bubble-particle collisions [187, 188].

The process requires careful optimization to balance insufficient and excessive conditions. While reduced agitation and aeration limit particle-bubble contact, excessive levels can destabilize froth and increase unwanted hydrophilic particle overflow recovery through entrainment [190]. The optimal parameters depend on cell design, feed characteristics, and whether grade or recovery is prioritized [191].

In WPCB flotation, operational regimes differ significantly from conventional mineral flotation. Impeller speeds typically range from 1 to 4 m/s, and aeration rates from 0.5 to 2.5 L/min, compared to 5–7 m/s and 1.8–5.4 L/min, respectively, in mineral systems [28, 50, 147, 168, 178]. Experimental studies highlight that higher agitation intensities and air flows, while effective in mineral flotation, can be detrimental in WPCB flotation, disrupting bubble-particle attachments and preventing stable froth formation [50, 167]. This aligns WPCB flotation more closely with plastics flotation, which operates under lower turbulence [139, 192–194].

e) Pulp pH

Pulp pH plays a pivotal role in flotation by affecting surfactant hydrolysis, surface charge of species, and solution ionization. These factors influence the adsorption of surface-active agents at the solid-water interface and overall process selectivity [195, 196]. Studies on reagent-free WPCB flotation have shown stable natural pH levels, with Ogunniyi [50] reporting a pH of 8 for mixed WPCBs and Estrada-Ruiz et al. [197] observing a pH of 7.0 for arcade machine WPCBs. This suggests that variations in feed material can impact baseline conditions.

Research by Han et al. [153] on surface charge characteristics revealed that nonmetal WPCB particles exhibit a negative zeta potential at neutral pH, with decreasing absolute values under acidic conditions and a point of zero charge near pH 3.05. Comprehensive studies on the effects of pH on flotation performance were conducted by Zhu et al. [198], who demonstrated a complex relationship where separation performance varied significantly across the pH spectrum. Their findings identified an optimal pH range of 6-8, during which silicon recovery to the underflow (associated with fiberglass) remained low at approximately 10%, while achieving high copper selectivity, resulting in an underflow product containing 75% copper. Outside this range, particularly at extreme pH values (2 and 12), the process exhibited a loss of separation selectivity [198].

f) Collectors and frothers

The flotation of WPCBs has gained attention as an environmentally friendly process, with the potential to operate under reagent-free conditions [30, 197]. While reagent-free flotation demonstrates high metal recovery in the underflow, low separation efficiency persists due to inadequate nonmetal removal. Collectors enhance separation by conferring hydrophobicity through adsorption and facilitating bubble-particle attachment by generating attractive hydrophobic forces that overcome repulsive interactions [24]. Hydrocarbon-based collectors containing alkanes and aromatics, such as diesel oil, laurylamine, and kerosene, have demonstrated effectiveness in interacting with hydrophobic sites on NMPs [28, 144, 147, 167].

However, collector usage presents challenges, as demonstrated by Zhu et al. [198] and Chen et al. [186], where increasing collector dosage improved metallic underflow grade but reduced overall metal recovery due to co-flotation with NMPs. Studies with kerosene revealed similar issues, with SEM and EDS analyses showing enhanced floatability of incompletely liberated metallic particles through metal-organic complex formation [167].

The role of frothers has been shown to be more significant than collectors in WPCB flotation due to the inherent hydrophobicity of NMPs [178]. Frothers enhance flotation by stabilizing the froth phase, regulating bubble size, and facilitating bubble-particle transfer [199, 200]. Das et al. [178] demonstrated that increasing methyl isobutyl carbinol (MIBC) frother dosage from 0 to 150 g/t improved overflow product yield (27% to 58.2%) and underflow metallic grade (21% to 79.4%). However, excessive frother dosage led to decreased copper recovery (95.9% to 83.1%) due to unwanted entrainment and entrapment of metallic particles [178].

2.5. Aggregation/Dispersion in WPCB Flotation System

A commonly reported challenge in the reverse flotation of WPCB particles is the poor dispersion within the flotation pulp, largely resulting from the aggregation of NMPs as reported in the work of He and Duan [167], Vidyadhar and Das [143], Dai et al. [147], and Das et al. [178]. This phenomenon presents a fundamental obstacle to effective separation, as froth flotation inherently depends on the proper dispersion of particles within the pulp to facilitate selective bubble-particle attachment [201]. Therefore, enhancing dispersion is essential to optimize the flotation performance [202, 203].

These surface interactions govern interfacial phenomena, such as bubble-particle attachment, the adsorption of flotation reagents, and the aggregation of particles [204]. Such surface

interactions are predominantly controlled by multiple forces, including van der Waals forces, electric double-layer forces, hydrophobic forces, and other surface-related forces, all of which are intrinsically linked to the bulk and surface properties of the interacting materials [204].

In conventional mineral processing systems, the interactions between mineral particles in aqueous media have been extensively studied due to their profound impact on particle aggregation and subsequent flotation efficiency [204]. These investigations have revealed several significant aspects of particle interactions. For instance, the homocoagulation of valuable minerals can enhance flotation performance by increasing effective particle size, thereby improving bubble-particle collision and attachment probabilities, which is particularly beneficial for fine particles that typically present flotation challenges [205]. Additionally, the homocoagulation of hydrophilic fine gangue minerals can effectively mitigate entrainment issues by increasing particle size [141]. However, heterocoagulation between valuable and gangue minerals, commonly manifested as slime coating, can detrimentally affect flotation performance by reducing the surface hydrophobicity of valuable minerals and compromising concentrate grades [206–208].

While these principles have been extensively examined in the context of mineral processing, the analogous phenomena in WPCB flotation, particularly their impact on flotation performance and separation efficiency, remain underexplored.

2.5.1. WPCBs nonmetallic particle interactions

A significant step in understanding the behavior of WPCB nonmetallic particles during flotation lies in analyzing their interfacial interactions. The following insights are derived from the work of Han et al. [153], which provides a detailed investigation into the free energy of interaction and its implications for particle aggregation.

The surface energy of particles plays a pivotal role in determining the intensity of interactions between particles and water, bubbles, reagents, and other particles. To explore why WPCB nonmetallic particles are prone to aggregation in water, Han et al. [153] calculated the particle surface energy, offering a foundation for studying interparticle interactions.

Young's equation describes the relationship between the solid surface energy γ_S, liquid surface energy γ_L, free interaction energy γ_{SL}, and the equilibrium contact angle (θ) in solid-liquid-gas three-phase systems. This relationship is expressed in **Eq. (2. 1)**.

$$\gamma_S = \gamma_L(1 + \cos\,\theta) \qquad \textbf{Eq. (2. 1)}$$

DOI: 10.14750/ME.2026.030

Surface energy of NMPs was determined through surface tension and contact angle measurements using deionized water, ethanol, and glycerin. The surface tensions of these liquids were 71.80 mJ/m^2, 47.70 mJ/m^2, and 64.20 mJ/m^2, respectively. Nonmetallic materials were pressed into sheets, and their contact angles with the liquids were measured as 81.70° (deionized water), 39.38° (ethanol), and 61.94° (glycerin).

Based on these measurements, the surface energy of the nonmetallic particles was calculated to be 37.01 mJ/m^2. Importantly, the van der Waals component constituted the majority of the surface energy, with nonpolar components making up 94.60% of the total. This indicated that the NMPs predominantly exhibit nonpolar, low-energy surfaces, which are less likely to be wetted by water.

To further analyze interparticle interactions, Han et al. [153] applied the extended Derjaguin–Landau–Verwey–Overbeek (EDLVO) theory. According to this theory, the primary forces governing particle interactions include electrostatic forces, van der Waals forces, hydrophobic attraction, and hydration repulsion. For particles with low-energy surfaces, the hydrated film formed is thin, resulting in weak hydration repulsion forces. Zeta potential measurements showed that the particle surface in a neutral solution is negatively charged (-33.68 mV), leading to electrostatic repulsion between particles. Consequently, the attractive interactions between particles are primarily governed by hydrophobic and van der Waals forces.

The free energy of interaction between particles in water was calculated using the following relationship, **Eq. (2. 2**):

$$\Delta G = \Delta G^{EL} + \Delta G^{LW} + \Delta G^{AB} \qquad \textbf{Eq. (2. 2)}$$

In this expression, ΔG^{EL} primarily representing the electrostatic repulsion force as discussed earlier, does not contribute to particle aggregation. When $\Delta G^{LW} > 0$, the van der Waals force between particles is repulsive, and when $\Delta G^{LW} < 0$, it becomes attractive. Similarly, $\Delta G^{AB} > 0$ indicates hydration repulsion between particles, while $\Delta G^{AB} < 0$ signifies hydrophobic attraction.

The calculated values were $\Delta G^{LW} = -3.12$ mJ/m^2 and $\Delta G^{AB} = -52.28$ mJ/m^2, indicating that hydrophobic attraction is the dominant interaction force between particles, significantly outweighing the contribution of van der Waals forces. These findings underscore that the

hydrophobic attraction between nonmetallic particles is the primary driver of their aggregation in water. This behavior is similar to plastic flotation, where the large hydrophobic attraction, driven by the AB Gibbs function, is the predominant interparticle force [209].

2.5.2. Bridging laboratory-industrial gaps in WPCB flotation

In the current body of research on the reverse flotation of WPCBs, there exists a notable mismatch between academic research approaches and industrial demands. This disparity is particularly evident in how researchers have addressed the poor dispersion characteristics of WPCB flotation systems. For instance, Ogunniyi et al. [50] adopted a pulping procedure in which a paste of the WPCB sample was first formed, introduced into the flotation cell, and subsequently diluted with water. This method was necessary because the WPCB particles tended to float when poured on water or displace water when submerged. While effective for laboratory-scale experiments, this approach fails to provide a scalable solution to the pulping challenge.

Ultrasonic treatment has been employed in several studies to improve dispersion, either during the pulping stage before aeration or during aeration itself, as demonstrated by Nekouei et al. [74], Wang et al. [210], and Chen et al. [186]. Although ultrasonic pretreatment shows promise in laboratory settings, the application of this technique at an industrial scale faces significant hurdles due to high energy demands and operational limitations [208].

Another common approach in the literature has been the use of intense agitation pretreatment for pulping and dispersion of WPCB particles in aqueous media [86, 127, 168, 180, 211, 212]. While intense agitation has proven beneficial as a pretreatment step in other applications, such as coal flotation, where it reduces slime coating through surface cleaning and improves flotation performance [213, 214], the role of energy input during the agitation pretreatment stage has been largely disregarded in WPCB flotation research. This oversight is significant, as energy input has been demonstrated to influence reagent adsorption, slurry rheology, flotation kinetics, and the aggregation and breakup behaviors of particles [203, 215].

The industrial-academic disparity is further exemplified by the solids concentration used in research studies, typically ranging from 4 to 10 wt.%. While operating at low solids concentrations is common in mineral flotation plants processing problematic ores to mitigate negative rheological impacts [216, 217], this approach inevitably reduces flotation productivity [208]. This issue is even more critical in WPCB flotation, where the solids concentrations are substantially lower than in mineral flotation. Scaling up these conditions to industrial levels

worsens the productivity challenges and raises questions about the feasibility of applying laboratory-scale findings in practical settings.

Notably, the rheological behavior of solid slurries serves as a key indicator of inter-particle interaction and aggregation levels, making it a valuable processing control parameter [217]. Research has demonstrated that yield stress and viscosity effectively indicate the degree of particle aggregation or dispersion [176, 217]. In flotation pulps, interparticle interaction forces, including hard-sphere interaction, electrostatic interaction, steric interaction, and van der Waals attractions, significantly influence rheological properties [176]. These interactions can be either DLVO or non-DLVO in nature, depending on the complexity of particle surfaces [218]. Despite this understanding, rheological considerations have been overlooked as a control parameter in WPCB flotation research.

While the use of rheology modifiers (dispersants) has shown promise in addressing the adverse rheological effects in problematic ores with clay minerals, WPCB flotation research has thus far explored only a limited array of such approaches. Existing studies have primarily focused on a narrow set of chemical agents, including tannic acid [153] and alkaline immersion methods [147], the latter of which poses practical challenges for industrial-scale adoption. Importantly, a comprehensive investigation into correlating these or other potential pretreatment strategies with rheological parameters and their subsequent impact on WPCB flotation performance remains notably absent. This represents a knowledge gap that limits the translation of rheological understanding into practical process optimization strategies for WPCB flotation systems.

These gaps, ranging from unscalable dispersion techniques to unexamined rheological constraints and unrealistic solids loadings, underscore a broader disconnect between academic experimentation and industrial flotation demands. Addressing these neglected factors is essential for advancing WPCB flotation from laboratory feasibility to industrial applicability.

2.6. Research Gaps and Objectives

The following research gaps have been identified from the analysis of current literature on WPCB flotation:

- Effective WPCB mechanical processing aims to maximize metal recovery at the coarsest possible size, balancing overgrinding, which increases metal losses to fines and dust, and inadequate liberation, which reduces separation efficiency. These limitations leave valuable

non-liberated or physically unrecovered metals in the post-separation fraction, justifying additional processing. While flotation offers a promising solution, its success depends on achieving optimal particle size and liberation through grinding. The impact of the grinding environment, wet versus dry, on size reduction progression, discharge size distribution, and liberation characteristics remains unexplored.

- Upon introduction to water, the hydrophobic nature of WPCB nonmetallic particles leads to aggregation, creating pulping challenges that hinder particle dispersion and subsequently affect flotation performance. While intense agitation is commonly employed to facilitate pulping, the extent to which energy input influences effective dispersion and aggregation mitigation remains unexplored.
- The flotation performance of reverse flotation in WPCB systems remains poorly understood, particularly the interplay between nonmetal rejection to the overflow and metallic particle retention in the underflow. Existing studies focus on bulk metal recovery and grade metrics, overlooking metal-specific flotation behavior and the mechanisms driving metal losses, especially under varying cell hydrodynamics and pulp solids concentrations.
- The rheological behavior of WPCB flotation pulps, influenced by hydrophobic interparticle interactions, has not been examined as a process control parameter. Although its significance in mineral flotation is well established, the connection between pulp rheology and flotation performance in WPCB systems remains poorly understood.
- Despite the clear rheological effects exhibited by WPCB flotation pulps, particularly under elevated solids conditions, no prior work has sought to mitigate these effects through targeted pretreatment strategies.

The primary objective of this PhD dissertation is to develop a focused understanding of WPCB flotation, with particular emphasis on the role of the grinding environment, pulp characteristics, and metallic particle flotation behavior. Ultimately, this work aims to establish an industrially scalable approach that optimizes flotation performance and efficiency.

Based on the foregoing discourse, the specific objectives of this PhD investigation are to:

- Evaluate the influence of the grinding environment (wet vs. dry) on discharge size distribution and liberation in WPCB processing to determine optimal conditions for downstream flotation performance;

DOI: 10.14750/ME.2026.030

- Investigate the challenges associated with WPCB particle pulping, including aggregation and dispersion behavior, and examine their impact on metal losses during flotation;
- Assess the role of intense agitation in mitigating aggregation and dispersion issues by analyzing the effect of stirring speed as a proxy for energy input on pulp dispersion and flotation outcomes;
- Investigate the effects of impeller speed, aeration rate, and pulp solids concentration on the reverse flotation performance of WPCB, focusing on nonmetal removal to the overflow and metallic particle retention in the underflow;
- Analyze the flotation behavior of individual metallic constituents under varying flotation conditions to identify the process variables and material factors influencing their distinct flotation responses, including trade-offs in process optimization;
- Examine the rheological properties of WPCB flotation pulps across a range of solids concentrations to understand their impact on flotation performance, particularly regarding overflow yield and metal recovery;
- Characterize the main mechanisms responsible for metal losses to the overflow through size-based analysis and flotation kinetics modeling.
- Evaluate the effectiveness of physical pretreatment through ultrafine removal under elevated WPCB solids loading by assessing its impact on pulp rheology and its implications for flotation performance;
- Investigate chemical pretreatment using alkaline-assisted grinding as a strategy to mitigate rheological challenges, focusing on its effects on nonmetal chemistry, surface properties, grinding behavior, and subsequent flotation performance at elevated solids concentrations.

DOI: 10.14750/ME.2026.030

Chapter 3: Experimental

This chapter presents the materials and the experimental procedures, building on the research objectives from the previous chapter. The chapter is divided into sections detailing the materials used, the methodologies implemented, and the analytical techniques applied.

3.1. WPCBs Sample

A representative batch of populated and unpopulated WPCBs was obtained from an e-waste processing facility (Metalex 2001 Kft., Budapest) for this research. The sample comprised mixed-value boards originating from various electronic sources, including personal computers, servers, switchboards, and household appliances. The majority of the boards were multilayer and double-sided types, with a smaller fraction consisting of single-sided boards.

The manufacturing period of most boards was unknown, except for a subset of unpopulated, high-layer-count WPCBs produced in 2010 with an FR-4 structure. Notably, the sample did not contain liquid crystal displays or batteries, which are typically classified as hazardous components.

Structurally, the WPCBs were expected to feature a copper-clad laminate core, fabricated by compressing epoxy or phenolic resin-impregnated fiberglass or cellulose layers into a solid sheet, with copper foil adhered to one or both sides. The most commonly used substrate materials include FR-4, a multilayer epoxy/fiberglass composite widely employed in consumer electronics, and FR-2, a phenolic/fiberglass variant often found in larger electronic products.

3.2. Chemicals and Reagents

Several chemicals and reagents were utilized throughout the experimental procedures. Aerofroth 70 (supplied by Eurotalc-plant, Slovakia), an alcohol- and glycol-based frother, was used as a frothing agent. Sodium hydroxide (98.0% grade, VWR International Kft.) and hydrochloric acid (37.57% grade, Acidum-2 Kft.) were used as pH regulators. Additionally, n-heptane (99.8% grade, Avantor Chemicals) served as the nonpolar phase in the two-liquid flotation (liquid-liquid extraction) experiments. Ethanol (99.98% grade, ES Lab Magyarország Kft.) was employed in density measurements.

DOI: 10.14750/ME.2026.030

3.3. Mechanical Processing and Grinding

3.3.1. Mechanical processing

The applied mechanical processing of WPCBs followed a multi-stage approach to achieve effective pretreatment and material upgrading, i.e., the liberation and separation of metallic and nonmetallic components, as illustrated in **Figure 3. 1**.

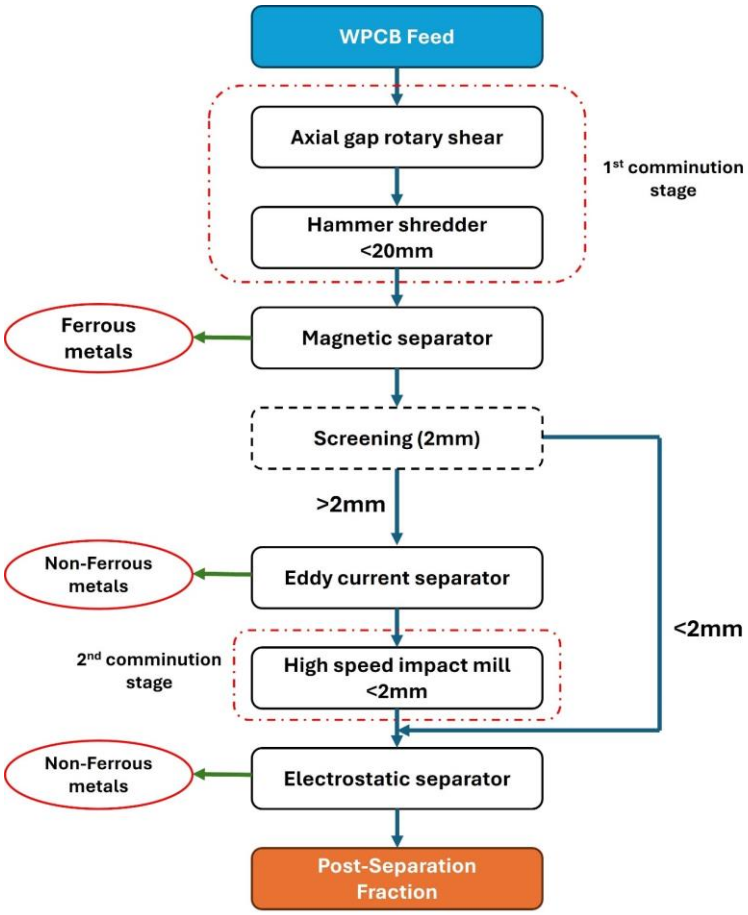

Figure 3. 1: Flowchart of mechanical processing as a pretreatment/upgrading stage for WPCB.

The comminution of WPCBs was carried out in two stages. In the first stage, an axial gap rotary shear with low (~0.5 m/s) circumferential speed rotors was used to comminute WPCB panels into sizes suitable for feeding into a modified hammer shredder. The hammer shredder, a converted mineral crusher equipped with a straight anvil, reinforced sieve, and heavier hammers, was operated with a 20 mm internal screen. In the second stage, a high-speed impact mill with a tip speed of 80 m/s and an internal screen of 2 mm was employed.

Following size reduction, the processed material was separated into several size fractions via dry screening. Metallic materials were separated through a sequence of physical separation stages, with settings adjusted according to unpublished findings from Dr. Csőke, Faculty of

DOI: 10.14750/ME.2026.030

Earth and Environmental Sciences and Engineering, University of Miskolc. The specific equipment configurations and operational parameters for the magnetic, eddy current, and electrostatic separation stages are provided in **Appendix II**.

3.3.2. Grinding tests

Following the characterization of the post-separation fraction, additional grinding was introduced to further refine the material's properties from both a particle size distribution and liberation perspective. This step was implemented to enhance the effectiveness of subsequent processing via flotation, as discussed in the following chapters.

Grinding tests were carried out using a laboratory-scale tumbling mill with a diameter of 19 cm and a length of 18 cm. Both wet- and dry-grinding experiments were conducted, utilizing alloy steel balls as the grinding media, which had a density of 7.62 g·cm^{-3}. The total mass of the grinding balls was 6.1 kg, corresponding to a 26.16% fill rate of the mill's volume. A feed sample of 220 g was used in each test, achieving a fractional powder filling of 9.15%. The specifications of the ball mill and the experimental parameters applied in these grinding tests are summarized in **Table 3. 1**.

Table 3. 1: Ball mill characteristics and experimental conditions.

Mill	Inner diameter, cm	19
	Length, mm	18
	Volume, L	5.1
	Operational speed, rpm	75
	Critical speed, rpm	97
	Grinding time, min	60
Media charge	Materials	Alloy steel
	Mass of balls, kg	6.1
	Density, g/cm^3	7.62
	Fractional ball filling, % (J)	26.16
	Powder-ball loading ratio (U)	0.875
	Ball diameter, mm	45, 30, 25
Material	Sample	WPCB particles
	Top size, mm	<1.0
	Density, g/cm^3	0.79
	Powder weight, g	220
	Fractional powder filling, % (f_c)	9.15
	Solid concentration, wt. % (wet grinding)	70
Calculation formula	$J = \frac{\text{Mass of balls/Ball density}}{\text{Mill volume}} \times \frac{1.0}{0.6}$	$U = \frac{f_c}{0.4\ \text{J}}$
	$f_c = \frac{\text{Powder weight/Powder density}}{\text{Mill volume}} \times \frac{1.0}{0.6}$	

Calculation formulas are based on Bu et al. [219]

DOI: 10.14750/ME.2026.030

The selection of grinding time (60 minutes) was based on a preliminary time-based grinding study, detailed in **Appendix II**. After each grinding test, the grinding media were removed, and the ground material was collected in a container for further analysis.

3.3.3. Characterization

a) Particle size distribution

Particle size distribution (PSD) was measured using sieve analysis (Retsch AS200, DIN/ISO 3310-2) or dynamic image analysis (Camsizer X2), depending on the processing stage. Following the first comminution stage using the hammer shredder, a ~900 g quartered sample was classified into eight size fractions (>12.5, 8.0–12.5, 5.0–8.0, 3.15–5.0, 2.0–3.15, 1.0–2.0, 0.5–1.0, and <0.5 mm). After the second comminution stage using the impact mill, a ~500 g quartered sample was classified into seven fractions (>2.0, 1.0–2.0, 0.5–1.0, 0.25–0.5, 0.125–0.25, and <0.125 mm). Post-grinding samples were split using a rotary splitter (Haver RPT, Germany). Wet grinding discharge was dried before splitting. Camsizer X2 (Retsch Technology, Haan, Germany), which utilizes dynamic image analysis (DIA; ISO 13322-2), was used to characterize particle size and shape.

b) Determination of liberation degree

The liberation degree was determined using size-dependent methods adapted from Sarvar et al. [29] and Gonçalves et al. [220].

For particles >2 mm, a visual inspection approach was applied using spread subsamples. For particles <2 mm, optical microscopy and SEM–EDS analysis were employed across multiple size fractions to quantify liberated vs. locked metal particles using the particle-counting method, where the degree of liberation of the target metals was quantified using **Eq. (3. 1)**.

$$\text{Liberation Degree} = \frac{N_{free}}{N_{free} + N_{locked}} \qquad \textbf{Eq. (3. 1)}$$

In this method, 'N_{free}' represents the number of fully liberated metal particles, while 'N_{locked}' denotes the number of particles still interlocked with nonmetallic particles.

Detailed sample preparation and imaging procedures are provided in **Appendix II**.

DOI: 10.14750/ME.2026.030

c) Metallic particles shape characterization

While the results from Camsizer X2 provided an overall shape characterization of the sample, the predominantly nonmetallic composition of the sample necessitated a separate analysis for metallic particles. To achieve this, microscope-acquired optical micrographs were utilized for metallic particle shape characterization. The ImageJ software (v. 1.54g, National Institutes of Health, USA) was employed to process and analyze the images. Key parameters, including circularity and aspect ratio, were evaluated for each particle. The resulting data were processed to provide a characterization of metallic particle shape, offering a comprehensive understanding of their geometrical properties and potential implications for subsequent flotation separation processes.

d) Determination of chemical composition

The elemental composition of the samples was determined using inductively coupled plasma optical emission spectrometry (ICP-OES), a widely employed technique for quantifying elemental concentrations. The analyses were conducted by KISANALITIKA Laboratory Services Ltd, Sajóbábony.

To ensure analytical accuracy and representative sampling, detailed sample preparation protocols were applied. These procedures are described in **Appendix II**.

3.4. Aggregation/Dispersion Challenges and the Role of Intense Agitation

3.4.1. Flotation feed preparation

The preparation of flotation feed was determined based on the results of grinding tests conducted under dry and wet environments (**Section 4.3**), with the dry grinding environment selected for further processing. The cut-off size for the flotation feed was set at 0.25 mm. To achieve this, the discharge from the dry grinding stage was subjected to screening at 0.25 mm after a grinding duration of 60 minutes.

From a sampling perspective, it is essential to clarify that the flotation feed sample, consisting of particles below 0.25 mm, was collected after batch grinding, which was conducted in 220 g batches and repeated 20 times. The collected sample was then subjected to splitting and recombination to obtain subsamples of 150 g, which were subsequently used for batch flotation tests.

DOI: 10.14750/ME.2026.030

3.4.2. Flotation process

The flotation tests were carried out using a 1L KHD Humboldt Wedag lab mechanical flotation cell. The conditioning strategy tested is illustrated in **Figure 3. 2**.

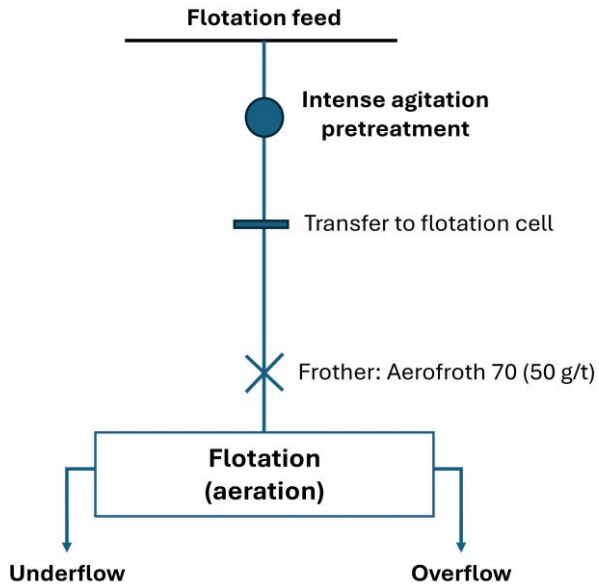

Figure 3. 2: The flowsheet for the flotation experiments.

For intense agitation pretreatment, the sample was dispersed in deionized water at 10 wt.% (6.1 vol.%) solids and stirred at four different stirring speeds: 500 rpm (1.3 m/s), 1000 rpm (2.6 m/s tip speed), 1500 rpm (3.9 m/s), and 2000 rpm (5.2 m/s). This setup consisted of a four-baffle agitated tank with a four-bladed radial impeller, as shown in **Figure 3. 3.** The 50 mm diameter impeller was positioned 30 mm from the tank bottom. After 15 minutes of stirring, the slurry was transferred to the flotation cell, where the frother was added and conditioned for 2 minutes.

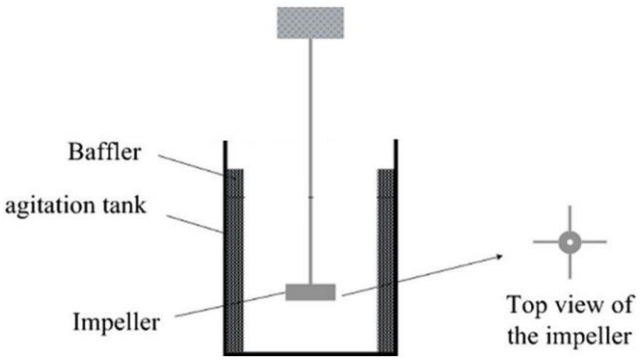

Figure 3. 3: Schematic of the intense agitation setup.

The reagent dosage, impeller speed, and airflow rate were consistent across all flotation experiments, set at 50 g/t frother, 1375 rpm impeller speed, and 2 L/min airflow rate. Following the approach recommended by Ogunniyi and Vermaak [26], each experimental condition was

DOI: 10.14750/ME.2026.030

conducted in duplicate, with all overflow yields confirmed to be reproducible within 5-10%. After each flotation experiment, the overflow and underflow products were collected and dried in an oven for 24 hours at 105°C. Finally, representative dry samples were prepared for chemical analysis to calculate grades and recoveries.

3.4.3. Characterization

a) Zeta potential measurements

To investigate the impact of intense agitation on the surface characteristics of nonmetals, zeta potential measurements were conducted using a Zeta Potential Analyzer (ZetaPlus, Brookhaven, USA). Samples were extracted from each conditioning strategy and allowed to settle for 5 minutes. After settling, the upper portion of the suspension was carefully transferred into a plastic cuvette for analysis. To ensure reproducibility and statistical significance, each sample was analyzed in triplicate, with 10 consecutive measurements taken per replicate, and the average value reported as the final zeta potential.

b) Indicators

To analyze the effect of the conditioning strategy on particle size distribution, a sample was taken immediately after the agitation step for each conditioning strategy and analyzed by wet sieving. Wet sieving measurements were conducted in triplicate to assess aggregation behavior and the effectiveness of different dispersion methods. To quantify deviations from the dry-basis PSD, an aggregation index (AI) was calculated by comparing the PSDs obtained from wet sieving after each conditioning stage to the PSD from dry sieving measurement. The AI, defined by **Eq. (3. 2**), provides a numerical representation of the degree of aggregation.

$$\mathrm{AI} = \frac{1}{n}\sum_{i=1}^{n}\left|\frac{\mathrm{wet}_i - \mathrm{dry}_i}{\mathrm{dry}_i}\right| \times 100 \qquad \textbf{Eq. (3. 2)}$$

In this context, n is the number of size fractions, wet i is the percentage distribution for a given conditioning strategy based on wet sieving, and dry i is the percentage distribution from dry sieving. Lower AI values indicate better performance, signifying a closer match to the dry distribution and, consequently, better dispersion of WPCB particles in water.

Separation efficiency (S.E., **Eq. (3. 3**)) [221] for each test was calculated.

$$S.E.(\%) = \frac{c(f-t)(c-f)(100-t)}{f(c-t)^2(100-f)} \times 100 \qquad \textbf{Eq. (3. 3)}$$

Where f, c, and t represent the grades of metal in the feed, concentrate, and tailings, respectively, a higher S.E. value signifies improved separation efficiency of the process.

3.5. Reverse Flotation of WPCBs: Flotation Performance and Pulp Properties

3.5.1. Flotation process

The WPCB flotation feed (prepared as in **Section 3.4.1**), following a reverse flotation scheme, underwent an intense agitation pretreatment (following conditions based on **Section 5.4**). Following this pretreatment, the suspension was transferred to the flotation cell (1L KHD Humboldt Wedag lab mechanical flotation cell) and adjusted to the desired solid concentration. The frother was then added at a concentration of 50 g/t and conditioned for 2 minutes prior to aeration. The froth depth was maintained at 25 ± 2 mm by adding makeup water to the cell. The froth was scraped every 5 seconds, and the quantity of make-up water added to the cell was carefully measured. Subsequently, each froth product, comprising both water and solids, was subjected to a process involving weighing, drying, and re-weighing to ascertain the amount of water retrieved. The determination of water recovery is based on the ratio of the weight of water recovered in concentrate to the weight of water originally present in the feed pulp.

3.5.2. Design of experiment

A three-factor, three-level factorial experimental design was employed to characterize the relationship between key cell hydrodynamics and flotation performance. The factors investigated were impeller speed (N, rpm), air flow rate (Qa, L/min), and solids concentration in the pulp (X, wt.%), as these influence cell variables including bubble size, pulp viscosity, and turbulent energy dissipation that govern mechanical flotation [50]. A complete replicated factorial experiment would have required 27 flotation tests; however, a Box-Behnken experimental design was implemented that reduced the number of experimental trials to 15 while still enabling modeling of main effects and interactions. The selection of level values for each variable was based on preliminary experimentation.

3.5.3. Rheology measurements

Rheology measurements were performed using an Anton Paar MCR102 rotational rheometer (Anton Paar, Austria). The experimental setup consisted of a 27 mm diameter cup and a vane rotor with a diameter of 24 mm. For each measurement, a 40 mL slurry sample, collected from the flotation cell after frother addition, was poured into the cup. The gap between the rotor and the bottom of the cup was set to 5 mm. Prior to data acquisition, the slurry was then pre-sheared

DOI: 10.14750/ME.2026.030

at a constant shear rate of 300 s^{-1} for 30 seconds, followed by a 5-second resting period to stabilize the sample before initiating the measurement. Rheograms were generated across a shear rate range from 0.1 to 350 s^{-1}. To ensure the reliability and repeatability of the results, all tests were conducted in triplicate under controlled conditions at a temperature of 25°C.

3.5.4. Flotation kinetics

During the kinetic flotation tests, the froth product was collected at 0.5-, 1-, 2- and 4-min intervals. The start time (t=0) for each test was taken as the moment the froth first overflowed into the collection tray. For this investigation, four well-established kinetic models were selected and tested, as outlined in **Table 3. 2**. These models were chosen due to their demonstrated success in numerous previous studies [151, 165, 222]. The models evaluated include the classical first-order model, the Klimpel (rectangular distribution) model, the Kelsall model, and the Gamma distribution model.

Table 3. 2: The four flotation kinetic models tested in this research.

Model	Equation	
Classical model	$R = \mathrm{RI}\left(1 - e^{-kt}\right)$	**Eq. (3. 4)**
Kelsall model	$R = \theta\left(1 - e^{-k_s t}\right) + (1-\theta)\left(1 - e^{-k_f t}\right)$	**Eq. (3. 5)**
Klimpel model	$R = RI\left[1 - \frac{1}{kt}\left(1 - e^{-kt}\right)\right]$	**Eq. (3. 6)**
Gamma model	$R = RI\left[1 - \left(\frac{\lambda}{\lambda + t}\right)^{P}\right]$	**Eq. (3. 7)**

The meaning and implications of the kinetic model parameters are detailed in **Appendix II**.

The flotation kinetics parameters were determined through non-linear regression with constrained optimization using MATLAB's optimization toolbox [223]. The optimal model fit was assessed using the non-linear correlation coefficient and the standard deviation of the estimate (Sr) [223]:

$$S_r = \sqrt{\frac{\sum_i^n \left(R_{i,cal} - R_{i,exp}\right)^2}{n - m}} \qquad \textbf{Eq. (3. 8)}$$

In this equation, n represents the number of data points, m denotes the number of model parameters, $R_{i,cal}$ is the calculated recovery at time i, and $R_{i,exp}$ is the experimental recovery at time i.

DOI: 10.14750/ME.2026.030

3.5.5. Hydrophobicity test - two-liquid flotation

Two-liquid flotation is a separation method used to evaluate the hydrophobicity/hydrophilicity of fine particles [224–226]. For the two-liquid flotation tests, a mixture of 375 mL of distilled water and 125 mL of n-heptane was prepared in a 1000 mL beaker and mechanically agitated at 1000 ± 20 rpm for 5 minutes to condition the two immiscible liquid phases. Subsequently, 20 g of the <0.075 mm WPCB flotation feed sample was introduced into the stirred liquid mixture and agitated for 15 more minutes. Agitation was then stopped, allowing 5 minutes of settling time for the particles to migrate and partition into their preferred liquid phase based on surface hydrophobicity/hydrophilicity. After clear phase separation, the upper nonpolar n-heptane phase containing the hydrophobic particle fraction was carefully collected using a pipette. The remaining aqueous phase with the hydrophilic particles was filtered, and both fractions were dried at 105°C before weighing to determine the floated and sunk masses, respectively. This experiment was performed in quadruplicate for reproducibility.

3.5.6. Entrainment

The degree of entrainment (ENT_i) is defined as the ratio between the mass of a species of size i per unit mass of water in the concentrate (recovered through entrainment) and the mass of the same species size per unit mass of water in the pulp [227].

$$ENT_i = \frac{(\text{mass of free gangue particles per unit mass of water})_{\text{concentrate}}}{(\text{mass of free gangue particles per unit mass of water})_{\text{tailings}}} \qquad \textbf{Eq. (3. 9)}$$

The degree of entrainment is closely related to particle size, with coarse particles showing a low degree of entrainment (ENT_i approaching 0), while fine particles tend to exhibit a high degree of entrainment (ENT_i approaching 1). It is generally recognized that particles smaller than 0.05 mm are more readily recovered through entrainment [174].

To determine the contributions of entrainment, the method of Ross [228] was be used. The calculation procedure, including relevant equations and assumptions, is provided in **Appendix II**.

3.6. Mitigating Rheological Challenges in the Flotation of WPCB

3.6.1. Ultrafine removal

To investigate the impact of ultrafine particles on WPCB pulp rheology and flotation performance, a physical pretreatment strategy involving the targeted removal of the <0.032

DOI: 10.14750/ME.2026.030

mm fraction was implemented. The flotation feed samples, which consisted of particles below 0.25 mm and had been prepared via dry grinding and screening as described in **Section 3.4.1**, underwent an additional screening step using a 0.032 mm sieve. The oversized material (0.032-0.250 mm) was collected and then used as the flotation feed for the corresponding experimental conditions.

3.6.2. Grinding under alkaline conditions

The grinding approach implemented in this research follows the methodology outlined in **Section 3.3.2**, with respect to ball mill characteristics and experimental conditions, as detailed in **Table 3. 1**. Alkaline conditioning was integrated into the grinding process by introducing the appropriate chemicals directly into the mill alongside the WPCB sample.

For wet grinding, the process commenced by loading the grinding media and WPCB sample into the mill. A slurry was prepared at 70% pulp density (by weight of solids in water), and the pH was adjusted to values between 7 and 12 using a sodium hydroxide (NaOH) solution. In the case of dry grinding, NaOH was added in its supplied form at dosage levels of 0.1%, 0.5%, and 1% by weight of the sample.

Following each grinding test, the grinding media were removed, and the ground material was collected for analysis. PSD was determined using Camsizer X2, as described in **Section 3.3.3**. The experimental grinding conditions are summarized in **Table 3. 3**.

Table 3. 3: Designations of experimental ball mill grinding conditions.

Grinding condition	Designation	Description
Wet	GW1	Standard wet grinding
	GW2	Added water is adjusted to pH 8
	GW3	Added water is adjusted to pH 9
	GW4	Added water is adjusted to pH 10
	GW5	Added water is adjusted to pH 11
	GW6	Added water is adjusted to pH 12
Dry	GD1	Standard dry grinding
	GD2	Added sodium hydroxide at 0.1 wt.%
	GD3	Added sodium hydroxide at 0.5 wt.%
	GD4	Added sodium hydroxide at 1 wt.%

3.6.3. Flotation process

Flotation tests were conducted using a 1L KHD Humboldt Wedag laboratory mechanical flotation cell, set at an impeller speed of 1375 rpm and an aeration rate of 2 L/min. After intense agitation pretreatment, the slurry was transferred to the flotation cell, where the slurry was

adjusted to 14 wt.% solids (8.7 vol.%), and the pH was adjusted to 7 using NaOH and HCl as pH regulators. Aerofroth 70 frother (50 g/t) was then added, and the slurry was conditioned for an additional 2 minutes before aeration was initiated. Each experimental condition was conducted in duplicate.

3.6.4. FTIR analysis

The stretching and bending vibrations of chemical bonds in the nonmetallic components of WPCBs were analyzed after grinding, both with and without alkaline conditions. Measurements were performed using a JASCO FT-IR 4200 Fourier Transform Infrared Spectrometer in reflection mode with a diamond ATR. Infrared transmission spectra were recorded over a range of 400–4000 cm^{-1} with a resolution of 4 cm^{-1}. The resulting spectra are plotted as a function of wavenumber and transmittance.

3.6.5. Rheology measurements

Rheological measurements of the flotation slurries were conducted according to the procedure outlined in **Section 3.5.3**. Measurements were performed on pulp samples obtained from flotation feeds that underwent specific pretreatment strategies: the physical removal of ultrafine particles and chemical modification through alkaline-assisted grinding. In each case, samples were collected from the flotation cell after the addition of the frother.

3.6.6. Metal leaching assessment

Given the alkaline nature of the grinding process, which can potentially induce metal leaching, an investigation was conducted to evaluate the leaching behavior under both dry and wet grinding environments. The specific conditions selected for this research corresponded to those that demonstrated optimal flotation performance for WPCBs. For wet grinding, the process liquid and solid discharges were separated via filtration upon completion of grinding. For dry grinding, due to the absence of a liquid medium during the process, the process liquid was collected post-flotation conditioning after solid separation through filtration. All grinding experiments were performed in triplicate to ensure the repeatability of results. The obtained supernatant liquids were then chemically analyzed using atomic absorption spectroscopy (AAS) for the presence of metal ions to evaluate potential leaching behavior.

DOI: 10.14750/ME.2026.030

Chapter 4: WPCB Mechanical Processing and Grinding

4.1. Introduction

Efficient metal recovery from WPCBs requires a systematic mechanical processing approach centered on selective comminution and staged separation. By prioritizing controlled crushing, screening, and physical separation, this method maximizes metal recovery at coarser size fractions, minimizing unnecessary over-grinding and improving downstream processing efficiency. Unlike previous studies, which often grind WPCBs directly to fine sizes for flotation, this work evaluates and characterizes the post-separation fraction, a stream more representative of industrial-scale processing. This approach offers a realistic assessment of flotation's role within an integrated process flowsheet.

This chapter presents the results and discussion of the characterization investigations conducted on the WPCB sample after mechanical pretreatment and in preparation for flotation separation. Key aspects include particle size distribution, particle shape analysis, and liberation degree assessment. These analyses offer critical insights into the physical and morphological properties of the processed material, forming the basis for understanding its behavior in subsequent flotation experiments.

4.2. Mechanical Processing

4.2.1. Particle size distribution and material loss

The particle size distribution of the WPCB sample after the first and second comminution stages is presented in **Figure 4. 1.** The initial stage of comminution was carried out using a hammer shredder equipped with a 20 mm internal screen. At this stage, the median particle size (X_{50}), representing the size at which 50% of the material is finer, was determined to be 7.1 mm. The proportion of fines generated was relatively low, with only about 5% of the sample having a particle size below 0.5 mm.

Following the second comminution stage, conducted using a high-speed impact mill with a 2 mm internal screen, a significant reduction in particle size was observed. The X_{50} value decreased to 0.75 mm, while the fraction of fines (<0.5 mm) increased considerably, reaching approximately 40% of the sample. This demonstrates the effectiveness of the high-speed impact mill in achieving significant size reduction, a necessary step for liberation and subsequent separation processes.

DOI: 10.14750/ME.2026.030

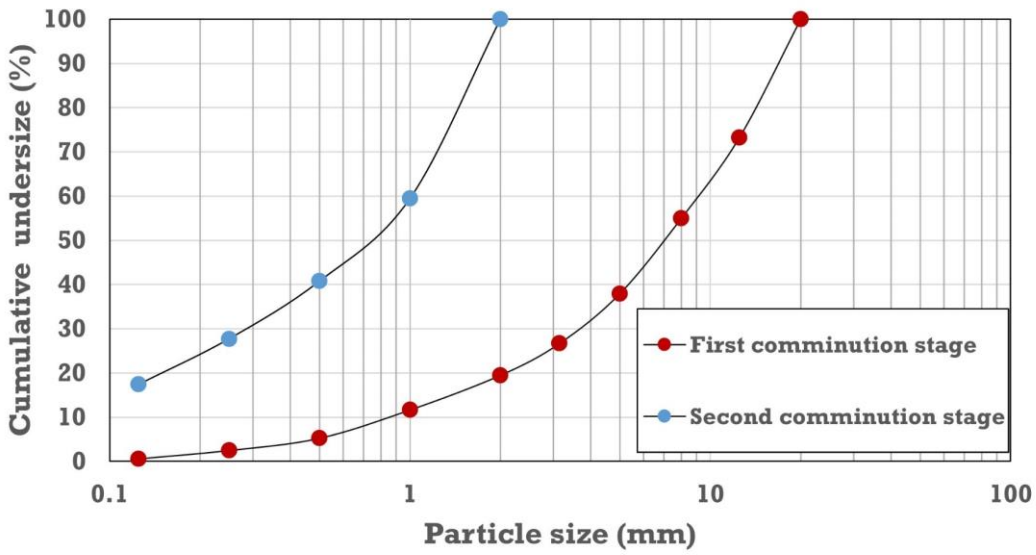

Figure 4. 1: Particle size distribution of the WPCB sample after the first and second comminution stages.

The overall material loss during the two-stage comminution process was approximately 7 wt.%. This loss is notably lower than those reported in previous studies with a single stage of comminution, such as Moraes [132], who observed a 25 wt.% loss using a hammer mill with a 4 mm internal sieve, and Yamane [133], who reported a 29 wt.% loss with a 2 mm internal sieve. The results are, however, highly comparable to the 6 wt.% loss reported by Silvas et al. [131], who employed a combination of knife and hammer mills with 6 mm and 1 mm internal sieves, respectively.

The findings further emphasize the importance of employing a stepwise comminution approach, as it allows for better control over the discharge of fine fractions and minimizes losses due to dust generation. This approach ensures that the overall efficiency of the comminution process is enhanced, providing optimal results for subsequent material recovery processes.

4.2.2. Liberation assessment and physical separation results

The approach used for liberation assessment is described in **Appendix II (Section B.2)**. The material characterization following comminution was conducted across various size fractions to evaluate the extent of liberation, with representative images of the fractions produced after splitting and spreading for assessment presented in **Figure C. 1** (**Appendix III**).

For the coarsest size fractions (>8 mm), the material primarily consisted of locked circuit board pieces interlocked with metals, exfoliated fiberglass fragments, free plastics, and a limited

DOI: 10.14750/ME.2026.030

presence of free metals, including stainless steel, aluminum, and small bundles of copper wire. In the intermediate size fractions (2 mm < x < 5 mm), a higher degree of liberation was observed, with more liberated fiberglass and free metals, such as steel pieces, individual copper wires, and aluminum fragments. However, some locked board pieces were still present. The finest size fractions (<2 mm), obtained by combining the material below 2 mm from both comminution stages, were also analyzed.

The degree of liberation was assessed based on counting the number of liberated (unlocked) and locked metal particles, with the results summarized in **Table 4. 1**. A clear trend toward higher liberation degrees was observed in the finest size fractions, with the <0.25 mm fraction achieving a liberation degree of 71%. However, contrary to findings in the literature, such as those reported by Zhang and Forssberg [49, 118], where near-complete liberation is observed for fractions below 1 mm, significant interlocking between metals and nonmetals persisted in the 1.0-2.0 mm and 0.5-1.0 mm fractions, with liberation degrees of only 42% and 51%, respectively (**Figure C. 2**, **Appendix III**). While aluminum pieces demonstrated complete liberation across all size fractions, copper fragments exhibited a tendency to remain locked.

Table 4. 1: Metal particles analyzed with the optical microscope and the calculated degree of metal liberation.

Particle size (mm)	Unlocked	Locked	Degree of liberation (%)
1.00-2.00	28	39	42
0.50-1.00	42	41	51
0.25-0.50	75	42	64
<0.25	55	23	71

The observed liberation degrees align with broader literature findings, which indicate that finer size fractions generally exhibit higher degrees of liberation. However, liberation degrees for specific size fractions vary significantly across studies, primarily due to study-specific operational parameters, including equipment type, operating conditions, and loading. Bachér et al. [116] highlighted variations in liberation resulting from differences in crusher type and rotational speed, while Otsuki et al. [229] demonstrated the impact of feed rate. Additionally, feed material composition plays a crucial role, as evidenced by Bachér et al. [134], who examined WPCBs from different production periods, and Koyanaka et al. [230], who compared liberation trends between WPCBs from PCs and TVs.

DOI: 10.14750/ME.2026.030

Following comminution and liberation assessment, the separation of metallic values was performed through a sequence of physical separation techniques, as described in **Section 3.3.1**. The process flowchart and results are presented in **Figure 4. 2**.

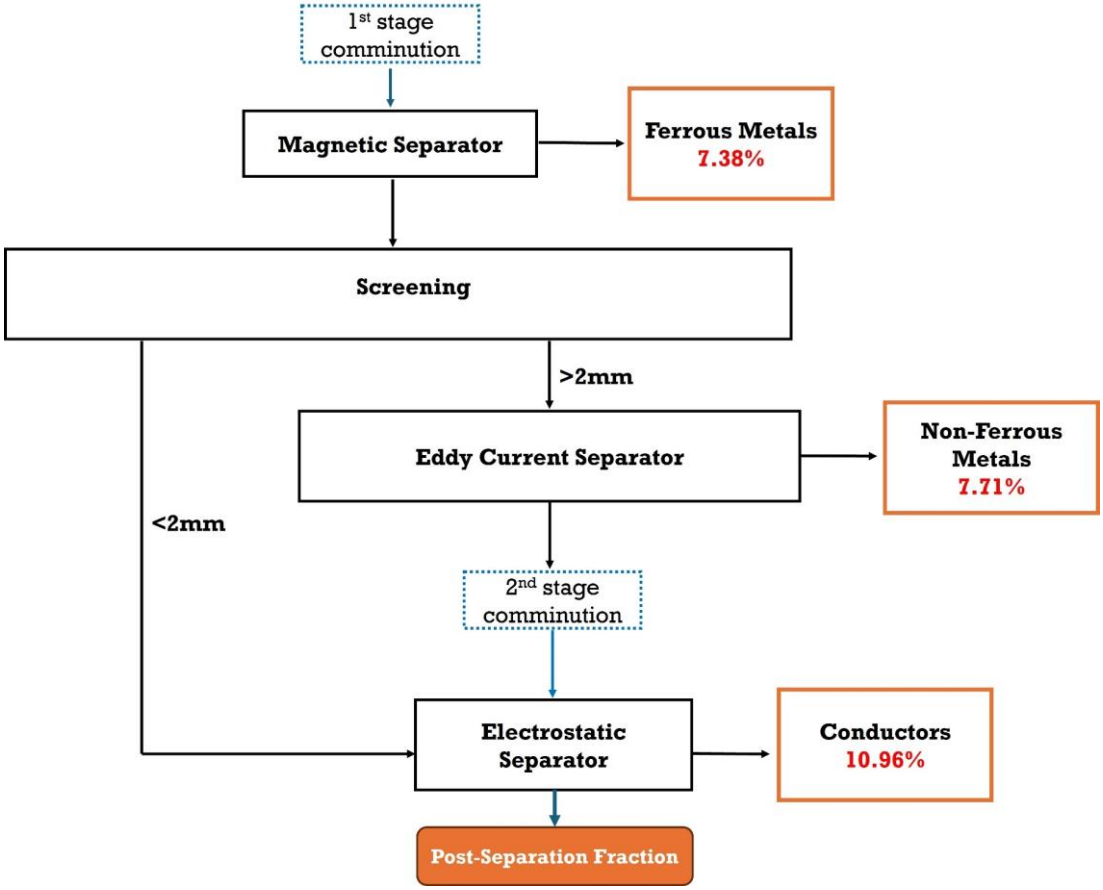

Figure 4. 2: Process flowchart and results of multi-stage physical separation of WPCB comminution products.

Magnetic separation yielded an overall magnetic material of 7.38%. The highest yields were observed in the 2.0-3.15 mm (10.48%) and 1.0-2.0 mm (11.68%) size fractions, while yields dropped significantly for fractions above 12.5 mm and below 0.5 mm, reaching as low as 2.69% and 3.4%, respectively.

Subsequent eddy current separation of the >2 mm non-magnetic fraction resulted in an overall yield of 7.71%. The >12.5 mm fraction exhibited the highest yield (~22%), but this fraction predominantly contained locked board fragments. The 8.0-12.5 mm fraction showed improved concentrations of conductive materials, including crumbled aluminum pieces, while the finer 3.15-5.0 mm and 2.0-3.15 mm fractions demonstrated higher concentrations of liberated copper foils, wires, and occasional fiberglass.

DOI: 10.14750/ME.2026.030

The electrostatic separation stage yielded an overall conductive material concentrate of 10.96%. The yield decreased with decreasing particle size, with values of 57.40%, 38.67%, and 16.91% for the 1-2 mm, 0.5-1 mm, and <0.5 mm fractions, respectively. This trend aligns with findings in the literature [129, 229, 231, 232], where metals tend to concentrate in coarser fractions post-comminution due to their ductility, limiting further fragmentation. Furthermore, electrostatic separation is known to exhibit reduced efficiency for <0.5 mm particles [120, 121, 123].

This trend was further validated through true particle density measurements of the separation products (**Figure 4. 3**). The density of conductive materials increased from 4.17 g/cm³ (1.0–2.0 mm) to 4.53 g/cm³ (0.5–1.0 mm) and 4.79 g/cm³ (<0.5 mm). Meanwhile, non-conductive fractions exhibited lower densities, with 1.41 g/cm³ for the 1.0–2.0 mm fraction, suggesting minimal metal losses. However, densities for the 0.5–1.0 mm (1.79 g/cm³) and <0.5 mm (1.98 g/cm³) non-conductive fractions were slightly higher, indicating the potential presence of residual metals.

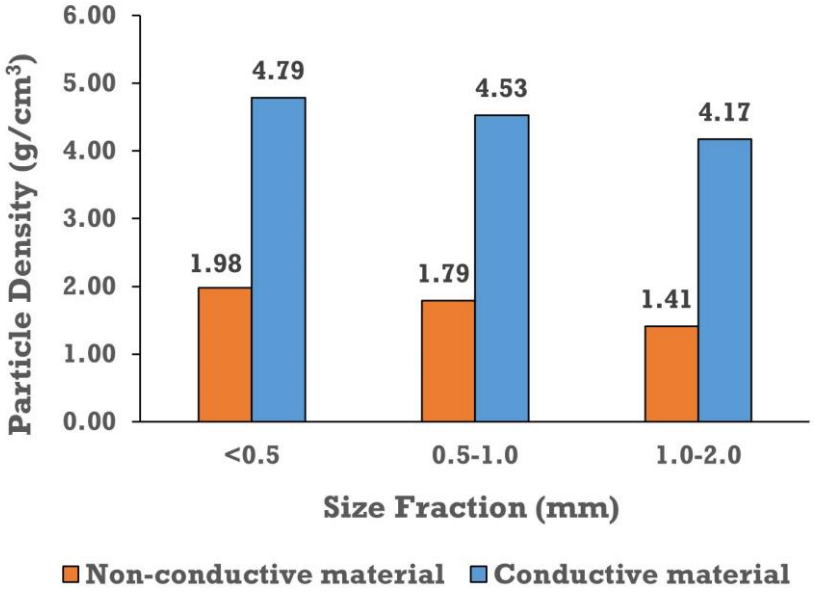

Figure 4. 3: Particle density of electrostatic separation products across size fractions.

4.2.3. Metal content and value in WPCB post-separation fraction

The limited degree of metal liberation observed during comminution, coupled with the declining efficiency of physical separation methods at finer particle sizes, suggests that the post-separation fraction may still contain considerable metal content. This is further supported by the particle density trends observed in the electrostatic separation products, which indicate

DOI: 10.14750/ME.2026.030

that metal-containing particles persist in the non-conductive fraction, particularly at size ranges below 0.5 mm.

The chemical analysis results, presented in **Table 4. 2**, confirm the presence of considerable metal content across all size fractions. Notably, the <0.5 mm fraction exhibited the highest overall metal content at 3.93%, followed by the 0.5–1.0 mm fraction at 3.01%. Meanwhile, the 1.0–2.0 mm fraction contained the lowest metal content at 1.41%, with no detectable precious metals in this fraction. These findings align with those reported by Suponik et al. [124], who observed similar trends in the post-electrostatic separation residues, where metal content ranged from 1.99% to 5.51% depending on operational conditions. The authors attributed the persistence of metals in the separated fractions to incomplete liberation of metallic particles, the reduced separation efficiency of finer size fractions, and particle aggregation on the drum and electrode surfaces, where size fractions below 0.125 mm destabilized the separation process.

Table 4. 2: Metal content of post-separation fraction per size (Results are based on the chemical analysis of the size fractions and their mass distribution.)

Metal	Unit	Size fraction (mm)		
		1.0-2.0	**0.5-1.0**	**<0.5**
Copper	%	0.30	1.90	2.50
Iron	%	0.06	0.40	0.60
Nickel	%	0.09	0.30	0.20
Lead	%	0.50	0.10	0.10
Zinc	%	0.46	0.30	0.50
Silver	mg/kg	<0.1	100	255
Gold	mg/kg	<0.1	16	85
Total content (%)		1.41	3.01	3.93

Despite the notable metal content across all size fractions, reprocessing the entire post-separation fraction is not a viable approach due to the high energy demands associated with additional processing stages such as grinding. The feasibility of further processing must also consider the mass distribution of the residue and the fact that the majority of the economic value in WPCBs stems from their precious metal content, as highlighted by Cui and Anderson [233], who reported that precious metals can account for over 50% of the total market value of WPCBs. Based on these considerations, the <1.0 mm size fractions were selected for further processing, as they combine relatively high metal content with a manageable mass distribution, constituting 61 wt.% of the post-separation fraction.

DOI: 10.14750/ME.2026.030

To assess the economic viability of recovering metals from the selected fraction, an estimation of the market value of the contained metals was performed. For this calculation, metal prices as of March 1st, 2025, obtained from Dailymetalprice [234], were used (**Table 4. 3**). The results indicate that the estimated market value of the selected WPCB fraction is approximately $6,701 per metric tonne. More than 92% of this value originates from gold, despite its much lower concentration compared to base metals such as copper, iron, lead, zinc, and nickel.

Table 4. 3: Market value of WPCB post-separation fraction selected fraction (<1.0 mm).

Metal	Price per unit (USD)	Unit	composition (%)	Value in USD per tonne
Gold	102.95	g	0.006	6,177
Silver	1.15	g	0.02	230
Copper	10.40	kg	2.3	239
Iron	0.1	kg	0.53	1
Lead	2.0	kg	0.1	2
Zinc	2.9	kg	0.43	12
Nickel	16.55	kg	0.24	40
Total value per tonne (USD)				6,701

These findings reinforce the role of flotation as an integral component of mechanical pretreatment for WPCBs, extending its utility beyond the beneficiation of comminution fines. It encompasses the broader post-separation fraction, where factors such as metallic content, particularly of precious metals, and mass distribution become critical in determining which size fractions warrant further beneficiation. This perspective expands the application of flotation and better aligns it with practical large-scale recovery strategies. Consequently, the next phase of this work will involve subjecting the post-separation fraction smaller than 1.0 mm to controlled grinding before flotation separation.

4.3. Grinding

Particle size and liberation characteristics are critical factors influencing flotation performance, as they directly affect the efficiency of particle-bubble interactions, reagent adsorptions, and subsequent separation outcomes [24, 235, 236]. The selected fraction of the WPCB post-separation fraction was evaluated to assess its suitability for flotation.

DOI: 10.14750/ME.2026.030

The PSD analysis of the selected fraction shows an X_{80} size of 0.72 mm, indicating a relatively coarse material that could hinder flotation efficiency. From a liberation perspective, data presented in **Table 4. 1** confirm a low degree of liberation, with substantial interlocking between metallic and nonmetallic components. The overall degree of liberation stands at 62%, which likely represents a conservative estimate, as preferential separation of liberated metallic particles during earlier physical separation stages may have reduced the actual liberation within this fraction.

Given the state of the selected fraction of the WPCB post-separation fraction, further grinding is essential to achieve an optimal size distribution and ensure a higher degree of liberation. The target cut-off size for grinding is set at 0.25 mm, based on flotation performance and liberation considerations. Nie et al. [165] demonstrated that nonmetal flotation overflow yields significantly improve when particles are below 0.25 mm, reaching 67.43% without frother addition, compared to only 6.8% for coarser particles. With the addition of a frother, these yields further increase to 80.35% and 32.52%, respectively. Additionally, complete liberation of metals has been reported in size fractions below 0.25 mm when grinding WPCB material with a top size of 0.5-1.0 mm [147, 164, 167].

The choice of grinding environment, dry or wet, was considered, with each approach offering distinct advantages and limitations. Wet grinding, traditionally favored in mineral processing, provides superior grinding efficiency, favorable slurry rheology for material transport, and compatibility with downstream flotation processes. The aqueous medium also eliminates dust collection requirements and allows for immediate surface treatment with reagents during grinding, enhancing process effectiveness [237, 238]. However, growing concerns over water scarcity have renewed interest in dry grinding, which offers benefits such as reduced grinding media wear and potential advantages for specific downstream processes [239, 240]. Despite these benefits, dry grinding typically consumes 20-25% more energy, faces challenges in pneumatic transport, and requires robust noise and dust management systems [241].

4.3.1. Assessment of bulk particle size distribution and shape

Figure 4. 4 presents the particle size distribution for wet and dry grinding, measured using Camsizer X2 and expressed as a cumulative distribution based on volume over the $x_{c,\,min}$ diameter. The results reveal distinct differences in grinding efficiency between the two environments. Dry grinding demonstrated moderately superior size reduction efficiency, achieving an X_{80} particle size of 0.33 mm compared to 0.37 mm for wet grinding. This

DOI: 10.14750/ME.2026.030

advantage extends to the production of the target size fraction (<0.25 mm), with dry grinding yielding 69% undersize material compared to 60% for wet grinding. However, dry grinding also generated a higher proportion of fines (<0.032 mm) at 23%, compared to 16% for wet grinding.

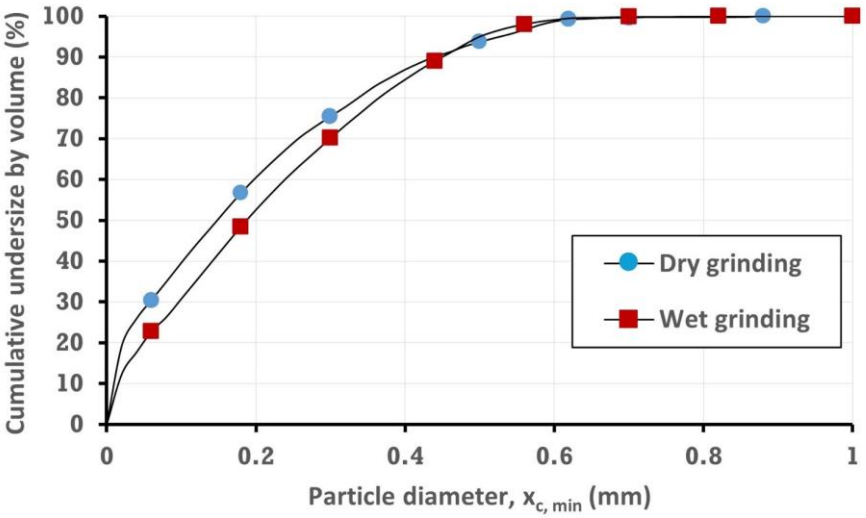

Figure 4. 4: Cumulative undersize based on volume for wet and dry grinding by dynamic image analyses (Camsizer X2).

The observed differences in PSD can be attributed to variations in effective breakage energy and pulp rheology between the two grinding environments. It has been demonstrated that in water (wet grinding), approximately 20% less energy than in air (dry grinding) is effectively transferred to the particles for breakage [242].

This energy dissipation leads to lower breakage efficiency in wet conditions. Nevertheless, under the applied 70 wt.% solids concentration, wet grinding is expected to achieve its highest breakage efficiency, as further dilution would only reduce the imparted breakage energy [219, 243]. Beyond energy considerations, differences in pulp rheology significantly impact the grinding behavior, as the captured mass of particles influences the stress mechanisms governing size reduction [241]. To understand this phenomenon, it is essential to consider both the stress mechanism during grinding and the material-specific characteristics of WPCBs.

According to the stress model, the efficiency of size reduction depends on the stress intensity (SI), defined as the ratio of stress energy (SE) imparted by grinding balls to the mass of particles (m_A) being stressed ($SI = SE/m_A$) [244, 245]. Three stress scenarios can occur: (a) single-particle stressing, where one particle absorbs the entire energy; (b) multi-particle stressing, where particles are stressed individually but with varying intensities; and (c) particle bed

DOI: 10.14750/ME.2026.030

stressing, where a mass of particles collectively absorbs the energy, reducing stress per particle [245].

For WPCBs, the hydrophobic nature of nonmetal components alters this conventional stress mechanism. During wet grinding, hydrophobic attraction forces promote particle aggregation, increasing m_A and reducing SI, effectively following particle bed stressing. This aggregation, observed immediately upon introducing the liquid medium, diminishes grinding efficiency. In contrast, dry grinding prevents such aggregation, particularly among coarse particles, enabling more effective individual particle stressing.

In addition to particle size distribution, the Camsizer X2 was used to assess the bulk shape characteristics of the ground material. Three key shape parameters, aspect ratio, sphericity, and convexity, were analyzed and visualized in **Figure 4. 5** against the particle size ($x_{c,\ min}$, diameter). Given that the processed sample is predominantly composed of nonmetallic materials (>96%), the shape characterization primarily reflects the state of the nonmetal components.

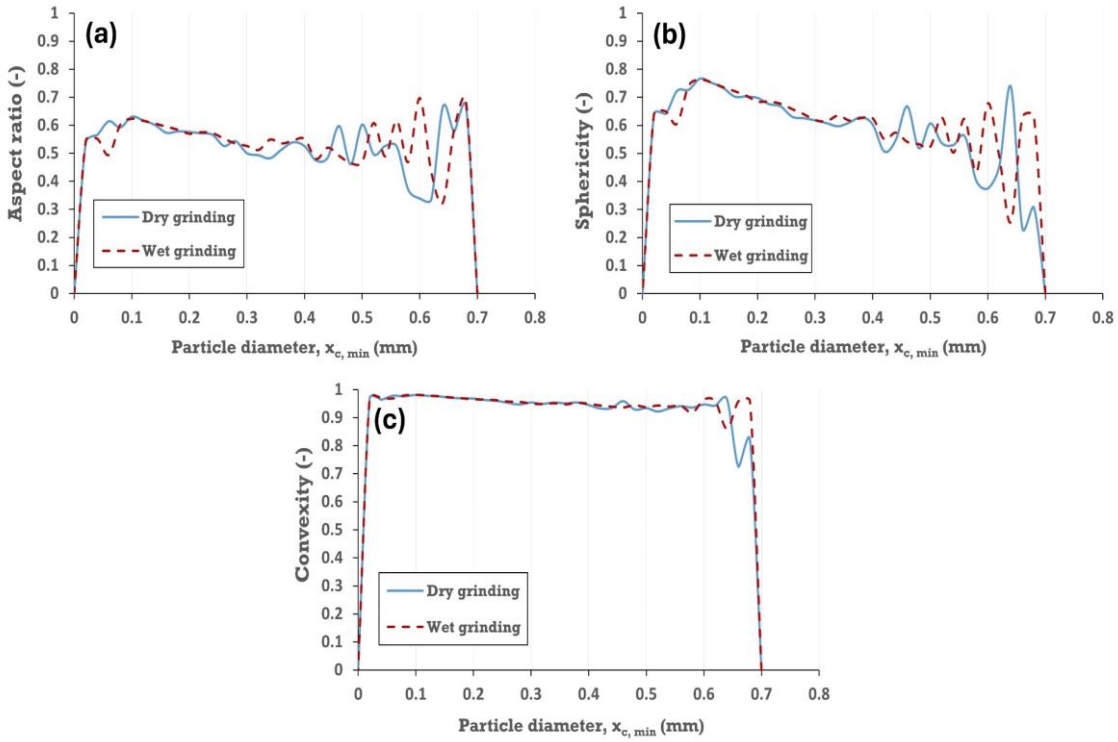

Figure 4. 5: Shape factors (a) aspect ratio, (b) sphericity, and (c) convexity plotted against particle size ($x_{c,\ min}$, diameter) for wet and dry grinding.

As expected, similar trends were observed for both dry and wet grinding environments across all three shape factors. This consistency arises from the fact that particle morphology is primarily dictated by the mechanical stresses applied during fracture, which remain unchanged

DOI: 10.14750/ME.2026.030

between dry and wet grinding in a ball mill. A closer examination of the trends reveals that both aspect ratio (**Figure 4. 5a**) and sphericity (**Figure 4. 5b**) increase with decreasing particle size before showing a slight decline below 0.1 mm. In contrast, convexity (**Figure 4. 5c**) remains relatively stable across all particle sizes, with an average value of 0.95.

For the target size fraction (<0.25 mm), the average aspect ratio, sphericity, and convexity were 0.58, 0.70, and 0.97, respectively. These shape descriptors suggest that the nonmetal particles can be characterized as elongated, moderately angular fragments with relatively smooth outer surfaces. The combination of moderate sphericity and high convexity suggests that the particles have well-defined edges but do not exhibit excessive surface complexity. This morphology is consistent with the grinding of laminated materials such as WPCBs, where the composite structure of resin and fiberglass layers fractures along preferential planes, producing elongated fragments with relatively smooth edges.

4.3.2. Liberation and shape analysis of metallic particles

The results of metallic particle analysis of the flotation feed size range below 0.25 are presented in **Table 4. 4**. The results, obtained from both dry and wet grinding, indicate a high degree of liberation across all size fractions, with dry grinding showing a modest advantage. Notably, liberation efficiency increases with decreasing particle size, reaching near-complete liberation below 0.075 mm.

Table 4. 4: Analyzed metal particles and their calculated degrees of liberation.

Grinding enviro.	Particle size (mm)	Copper		Others		Degree of liberation (%)		
		Lib.	Lok.	Lib.	Lok.	Copper	Other	Total
Dry	0.125-0.25	246	43	110	15	85	88	86
	0.075-0.125	157	16	62	7	91	90	91
	<0.075	59	3	48	1	95	98	96
Wet	0.125-0.25	218	54	88	19	80	82	81
	0.075-0.125	94	13	36	4	88	90	88
	<0.075	18	1	24	2	95	92	93

Despite the overall high liberation observed, distinct variations exist among different metal types, as illustrated in **Figure 4. 6**. Copper, although generally well liberated (**Figure 4. 6b**), still exhibits instances of interlocking with nonmetallic components, particularly in coarser fractions. For example, **Figure 4. 6c** depicts copper wires remaining attached to solder mask residues, signifying incomplete liberation. In contrast, aluminum particles demonstrated a significantly higher liberation degree across all studied fractions and were observed to be

DOI: 10.14750/ME.2026.030

completely liberated even in coarser size classes (**Figure 4. 6d**). Solder particles similar to copper exhibited partial intergrowth with nonmetallic components, as exemplified by a lead-free solder alloy particle in **Figure 4. 6e**.

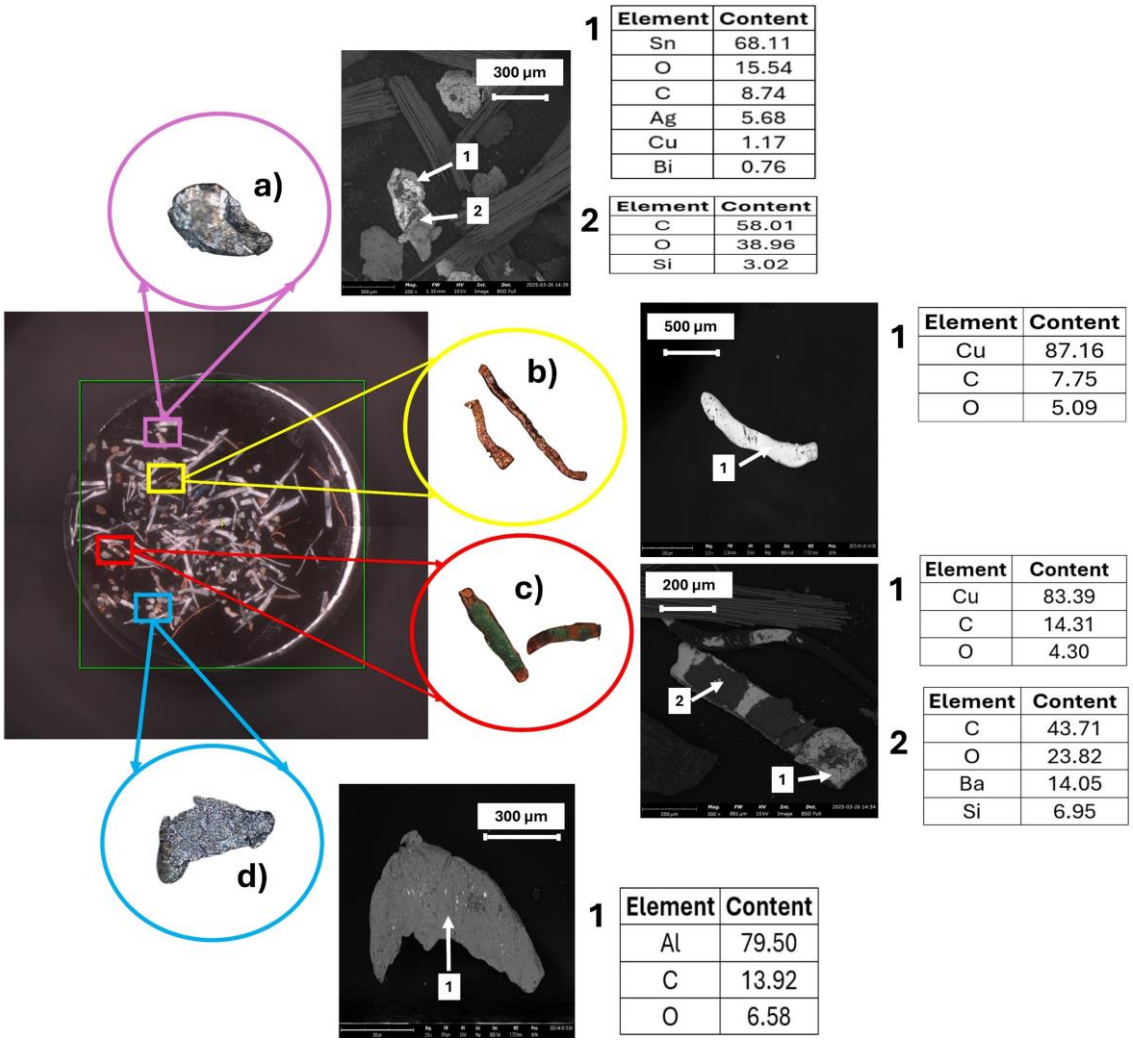

Figure 4. 6: Selected representations of liberation patterns of metallic particles in the 0.125–0.250 mm size fraction. Images were acquired using a digital microscope and SEM, with elemental characterization by EDS. (a) Solder particle intergrown with nonmetallic substrate, (b) Liberated copper particles, (c) Partially liberated copper wire attached to solder mask, (d) Fully liberated aluminum particles.

These differences can be attributed to the distinct structural roles of metals within WPCBs. Copper is predominantly embedded within internal conductive layers or tracks laminated between fiberglass-reinforced epoxy sheets. This structural embedding complicates its mechanical separation and often results in residual attachment to insulating substrates. On the other hand, aluminum is commonly present in discrete components such as capacitors and heat sinks, which are more readily liberated during size reduction. Solder alloys, typically found at interconnection points, are inherently associated with both metallic and polymeric substrates, leading to partial intergrowth and variable liberation outcomes.

DOI: 10.14750/ME.2026.030

Additional complexity arises from the occurrence of alloyed particles, as shown in **Figure 4. 7**, which includes solder and brass particles. These materials retain their alloyed structure post-grinding, limiting the extent to which individual elemental constituents can be separated mechanically. For instance, in solder particles, elements such as lead and silver remain in fixed stoichiometric ratios, preventing their physical separation via comminution alone.

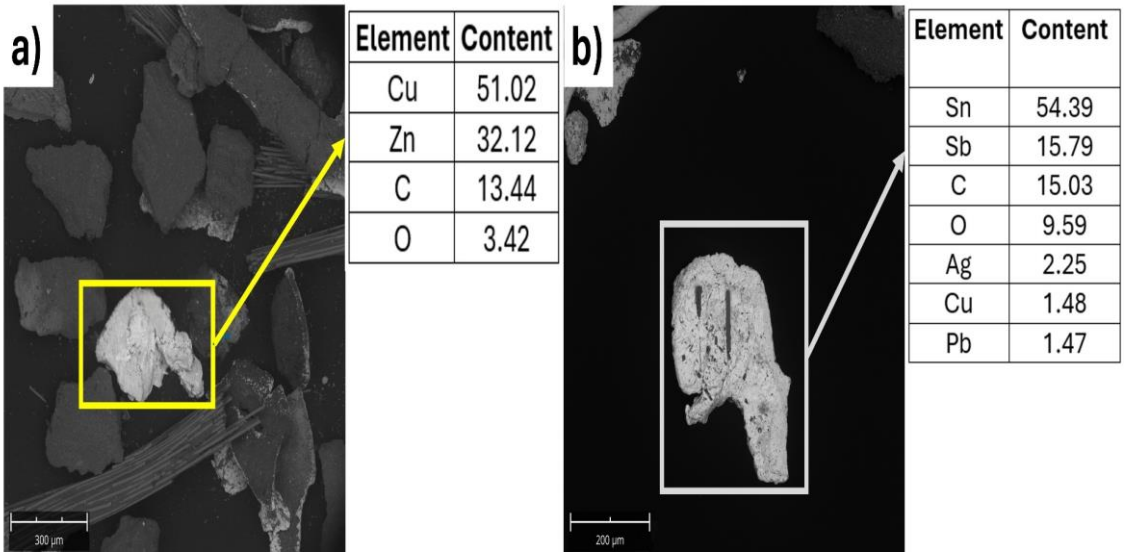

Element	Content
Cu	51.02
Zn	32.12
C	13.44
O	3.42

Element	Content
Sn	54.39
Sb	15.79
C	15.03
O	9.59
Ag	2.25
Cu	1.48
Pb	1.47

Figure 4. 7: Selected SEM-EDS images showing alloyed metallic particles identified in the processed WPCB sample. Elemental analysis confirmed (a) solder alloy, primarily composed of Sn and Sb, and (b) brass particle, consisting of a Cu-Zn alloy.

Precious metals also display distinct distribution patterns. Gold appears predominantly as discrete, localized particles, often associated with copper-nickel substrates (**Figure 4. 8**). This reflects its targeted use in high-value applications such as connector pins and contacts [246]. Conversely, silver tends to occur more diffusely, distributed across multiple locations and potentially associated with a wider range of components, including switches, solders, and contacts [10]. EDS elemental mapping (**Appendix III**, **Figure C. 3**) confirms this dispersed pattern. Such differences in occurrence and distribution patterns bear direct implications for the selectivity and efficiency of downstream recovery methods, particularly flotation.

DOI: 10.14750/ME.2026.030

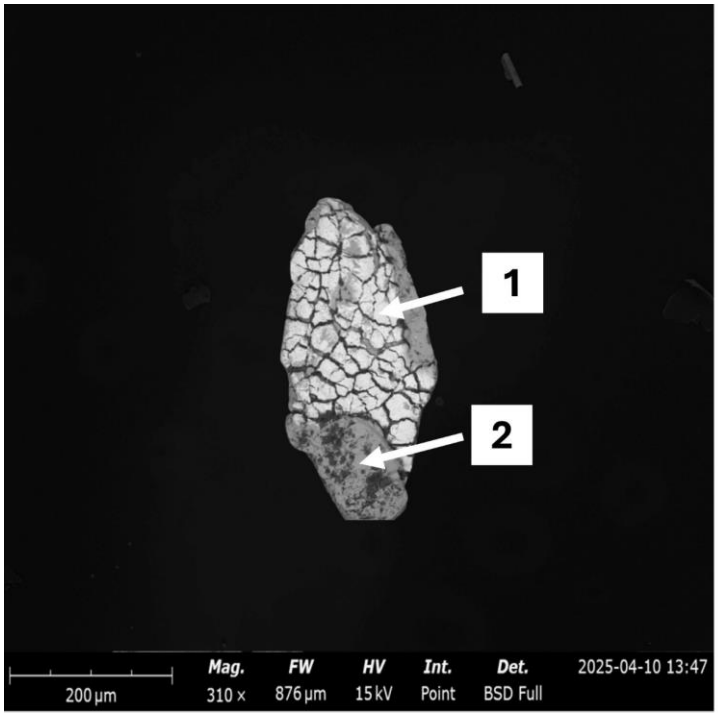

1

Element	Content
Au	92.38
Ni	4.20
C	2.87
O	0.55

2

Element	Content
Cu	67.64
C	27.05
O	4.39
Ni	0.93

Figure 4. 8: SEM-EDS image showing a gold-coated copper-nickel particle.

The shape of metallic particles in the flotation feed (<0.25 mm) was evaluated using optical micrographs. These images were processed and analyzed with ImageJ software to extract key shape descriptors across different size fractions. **Table 4. 5** summarizes the number of particles analyzed and the corresponding average values of circularity and solidity for each size class.

Table 4. 5: Average shape parameters of metallic particles in the flotation feed, categorized by size fraction.

Size fraction (mm)	No. of particles	Circularity (-)	Solidity (-)
0.125-0.25	154	0.41	0.84
0.075-0.125	138	0.44	0.84
<0.075	61	0.48	0.87

The results reveal consistent trends: circularity increased from 0.41 to 0.48 as particle size decreased, reflecting a gradual shift toward less elongated morphologies in finer fractions. Meanwhile, solidity remained relatively stable (0.84–0.87), indicating minimal surface complexity and smooth perimeters. Collectively, these descriptors suggest that metallic particles are moderately elongated but retain well-defined edges. Examples of metallic particle morphology observed in the flotation feed are presented in **Figure 4. 9**.

DOI: 10.14750/ME.2026.030

Figure 4. 9: Diverse morphology of metallic particles observed in the flotation feed.

4.3.3. WPCB flotation feed

Following the comparative analysis of wet and dry grinding environments, dry grinding was selected as the preferred method for preparing WPCB flotation feed. Dry grinding demonstrated superior size reduction efficiency, achieving a finer discharge and yielding a higher proportion of the target size fraction (<0.25 mm). Although both environments produced comparable results in terms of metal liberation degree and shape characteristics, dry grinding provided a distinct operational advantage. It effectively minimized particle aggregation, a phenomenon particularly pronounced in wet grinding due to the hydrophobic nature of WPCB nonmetallic components. Such aggregation not only reduced grinding efficiency but also posed significant challenges during subsequent screening.

Having established dry grinding as the preferred method for preparing the flotation feed, attention must now be directed to the subsequent screening stage, which is essential for isolating the target flotation feed (<0.25 mm). While dynamic image analysis (Camsizer X2) provided particle size distribution data, the morphological complexity of the ground material, characterized by elongated particles (**Sections 4.3.1 and 4.3.2**), introduces discrepancies between image-derived PSD and sieve analysis results (**Figure 4. 10**).

As evidenced in **Figure 4. 10**, sieve analysis appears to overestimate the intermediate size fraction (0.075–0.125 mm; 21.99 vs. 16.36 in image analysis) while underestimating both the coarse (0.125–0.25 mm; 30.40% vs. 34.54%) and fine fractions (<0.075 mm; 47.61% vs. 49.10%). Such deviation arises from the tendency of elongated-shaped particles to align horizontally or bridge sieve openings. Consequently, particles that would otherwise be classified as finer by image analysis may be retained in coarser fractions during screening. Despite these limitations, sieve analysis remains the practical basis for screening and

DOI: 10.14750/ME.2026.030

classification for the grinding discharge. Therefore, for all subsequent experimental work, the particle size distribution derived from sieve analysis will serve as the basis for isolating and classifying the <0.25 mm flotation feed.

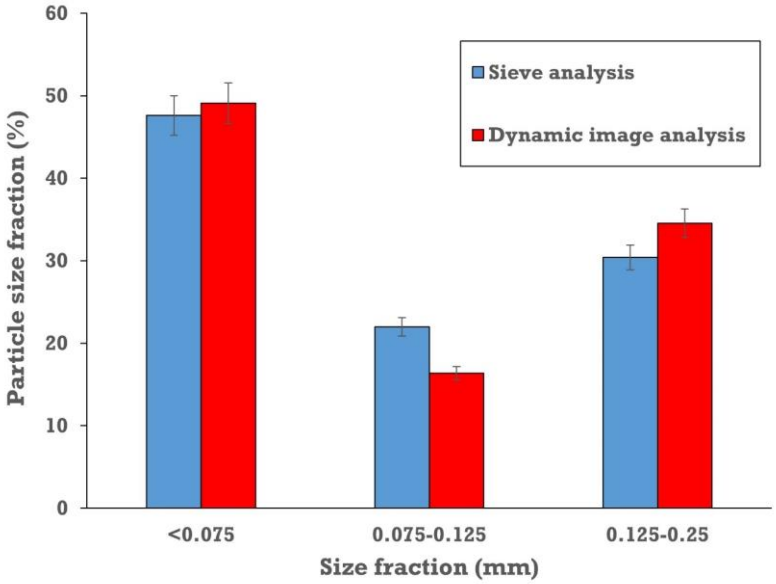

Figure 4. 10: Comparison of particle size distribution of flotation feed: dynamic image analysis vs. sieve analysis.

Following screening by sieve analysis, the metal distribution across size fractions was analyzed using chemical assay. **Figure 4. 11** depicts the distribution of key metals in the flotation feed, revealing that metal distribution varies considerably across size ranges. Copper and zinc exhibit a pronounced concentration in the coarse fraction, accounting for approximately 75% and 61% of their total content, respectively. Nickel and lead are more evenly distributed, though they still show a slight preference for the coarser sizes. On the other hand, metals such as gold, silver, and iron are predominantly concentrated in the fine fraction, with 56%, 60%, and 66% of their respective contents observed below 0.075 mm. These trends are consistent with findings reported by Barnwal and Dhawan [247] and Guo et al. [79], who observed similar distribution patterns in ground WPCBs with particle sizes below 0.3 mm.

These metal distribution patterns correspond to the liberation behavior and particle shape characteristics of the metals, reflecting the distinct structural roles each metal plays within the WPCB matrix. Copper, primarily used as conductive pathways, such as wires and tracks, occurs in relatively thick layers (>0.035 mm) and exhibits high ductility. These factors contribute to its preferential accumulation in coarser particle fractions after grinding [248]. Conversely, gold, typically applied as an extremely thin surface coating layer (0.05–2.54 μm), is far more prone to fragmentation [248]. As illustrated in **Figure 4. 8**, a typical gold-coated

DOI: 10.14750/ME.2026.030

copper-nickel particle shows a severely cracked gold coating. This indicates that such thin layers easily fragment under mechanical stress, consequently reporting to finer size fractions. In summary, the distribution of metals across size fractions is governed by their embedded structural functions, which in turn influence how they break, disperse, and concentrate during grinding.

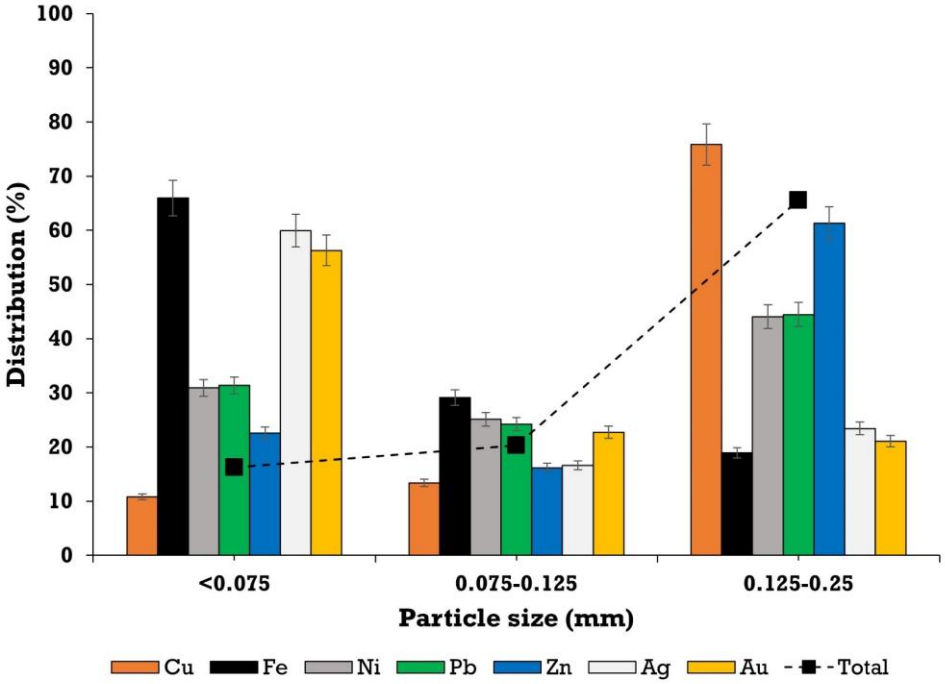

Figure 4. 11: The distribution of metals in size fractions expressed as the percentage of each metal's total content in the flotation feed.

4.4. Conclusions

The stepwise comminution and staged physical separation approaches prove fundamentally advantageous, minimizing material losses (7 wt.%) with controlled fines generation and enabling effective metal recovery at coarser size fractions through selective liberation. However, economically significant metal values persist in the post-separation fraction, with the <0.5 mm and 0.5-1.0 mm fractions containing 3.93% and 3.01% metal content, respectively, and an estimated market value of $6,701 per tonne dominated by gold (>92% of value). This limitation redefines flotation's role as a core process within the mechanical pretreatment stage. Rather than merely treating comminution fines, flotation must now address the broader post-separation fraction, where metal content and distribution, particularly that of precious metals, emerge as decisive factors in guiding the selection of size fractions that merit further beneficiation.

DOI: 10.14750/ME.2026.030

To enable effective flotation separation, further grinding was implemented to treat the selected fraction of the post-separation fraction (X_{80}: 0.72 mm, liberation degree: 62%), aiming to achieve an optimal size distribution and enhanced metal liberation. Comparative assessments of dry and wet grinding environments revealed notable differences in grinding performance. Dry grinding produced a finer product (X_{80}: 0.33 mm), yielding 69% of the discharge below the 0.25 mm target cut-off size compared to 60% for wet grinding (X_{80}: 0.37 mm). These differences were attributed to variations in breakage energy and pulp rheology, with wet grinding hindered by particle aggregation caused by the hydrophobic nature of WPCB nonmetal components. Both methods achieved high liberation degrees across all size fractions (0.125-0.250 mm: 86%; 0.075-0.125 mm: 91%; <0.075 mm: 96%), with dry grinding showing a modest advantage. Dry grinding was ultimately selected as the preferred approach due to its balance of optimal size distribution and enhanced liberation while avoiding complications during screening operations.

The nonmetallic components of the WPCB flotation feed are characterized by elongated, moderately angular fragments with smooth surfaces. These shape characteristics have significant implications for screening and flotation performance. Metallic particles exhibit moderate elongation, with well-defined edges and minimal surface complexity. Liberation analysis reveals metal-specific trends: copper and solder particles show persistent attachment to nonmetallic constituents, while aluminum particles demonstrate near-complete liberation. These differences reflect the structural and bonding roles of each metal within the WPCB matrix. Additionally, the distribution of metals across size fractions follows distinct patterns related to their original placement and function in the board.

The insights gained from characterizing the flotation feed, specifically regarding particle morphology, liberation states, and size-dependent metal distribution, underscore the inherent complexity of WPCBs as a flotation feed. The combined effects of incomplete liberation, alloyed particle associations, shape-driven behaviors, and the tendency of nonmetallic constituents to aggregate in aqueous media necessitate a tailored and comprehensive approach to understanding flotation behavior and optimizing process efficiency.

DOI: 10.14750/ME.2026.030

Chapter 5: Aggregation/Dispersion Challenges and the Role of Intense Agitation

5.1. Introduction

The flotation performance of WPCBs is significantly influenced by the dispersion behavior of their constituent particles. Due to their inherent hydrophobicity, nonmetallic particles in WPCBs tend to aggregate upon introduction to water, hindering effective dispersion and leading to suboptimal flotation performance. While intense agitation is often employed to enhance dispersion, the extent to which energy remains unexplored. This chapter addresses these gaps by investigating the fundamental challenges associated with WPCB particle aggregation and dispersion, alongside assessing the role of intense agitation, quantified through stirring speed, as a pretreatment strategy to enhance flotation separation.

This chapter begins by examining the challenges associated with pulping WPCB samples, including the types of aggregates formed and their contribution to metal losses during flotation. The effectiveness of intense agitation at varying stirring speeds is then assessed as a pretreatment conditioning step, focusing on its influence on particle dispersion and the interaction of WPCB nonmetals in the flotation pulp. To quantify aggregation, an aggregation index based on sieve analysis is introduced, complemented by zeta potential measurements to evaluate surface characteristics. Finally, flotation tests are conducted to determine how intense agitation at different stirring speeds impacts flotation performance.

5.2. Aggregation

The initial observation indicates that despite the true density of the WPCB flotation feed being 1.7 g/cm³, the introduction of the WPCB sample into the water for flotation pulp preparation was hindered by the aggregation phenomenon. This resulted in the formation of both completely dry aggregates and partially wetted surface aggregates where the inner particles remained dry. Consequently, their low bulk density caused them to float on the pulp surface (**Figure 5. 1**).

The particle-particle interactions leading to the immediate formation of dry and partially wetted aggregates upon adding the WPCB sample to water can be primarily attributed to the hydrophobic nature of the nonmetallic components of WPCBs. Zeta potential measurements as a function of pH (**Figure 5. 2**) revealed that the nonmetal particles have a negatively charged surface in a neutral solution, resulting in repulsive forces between them. This rules out

DOI: 10.14750/ME.2026.030

electrostatic attraction as a mechanism for nonmetal aggregation. Therefore, the predominant forces causing aggregation are the hydrophobic attraction forces [151, 153, 165]. The hydrophobic attraction between particles immersed in water is an effective interaction that arises from the high free energy of cohesion among surrounding water molecules, particularly the hydrogen-bonding network. When nonpolar surfaces approach each other, structured water at the interface is displaced, reducing the system's free energy and resulting in an apparent attractive force [249].

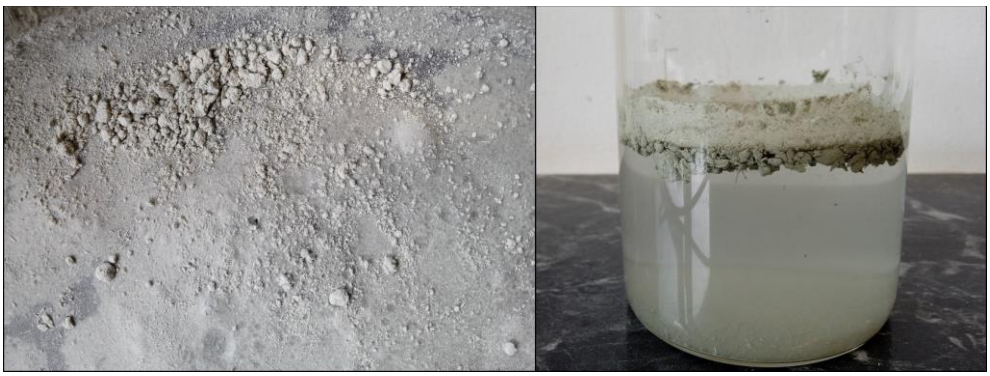

Figure 5. 1: Immediate formation of completely dry and partially wetted surface aggregates following the addition of dry WPCB powder to water.

The hydrophobicity of WPCB nonmetals stems from the organic resins used in WPCB manufacturing [151]. During production, fiberglass is impregnated with these resins, which are difficult to remove completely by comminution [163]. Consequently, the residual resin influences the surface characteristics of both the resin particles and the impregnated fiberglass [152]. The WPCB nonpolar hydrophobic surfaces tend to minimize their contact area with water, leading to an induced attractive force that causes aggregation.

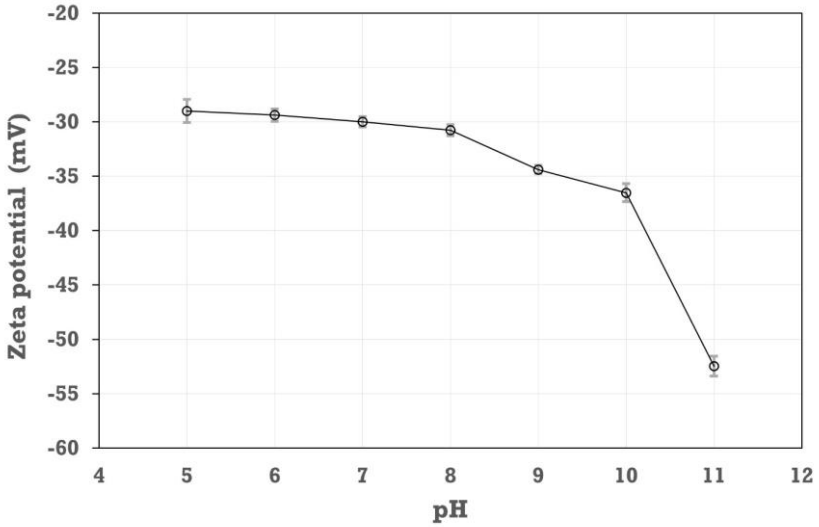

Figure 5. 2: Zeta potential of WPCB nonmetal as a function of pH.

DOI: 10.14750/ME.2026.030

The formation of nonmetal aggregates, where they can unselectively entrap metallic particles, poses a significant challenge in the flotation process, as inadequate dispersion may allow these aggregates to persist throughout the conditioning stage and remain within the pulp. This persistence increases the likelihood of their transfer to the froth zone upon flotation initiation. Evidence of this phenomenon was observed in dry-formed aggregates that accumulated on the pulp surface, as shown in **Figure 5. 3**. Microscopic examination of these recovered aggregates (**Figure 5. 4**) confirmed the presence of metallic particles, supporting the hypothesis that nonmetal aggregation contributes to unintended metal entrapment. Consequently, such aggregates may lead to increased metal losses to the overflow product, ultimately diminishing the separation efficiency.

Figure 5. 3: Dry aggregates remaining on the pulp surface during the conditioning stage.

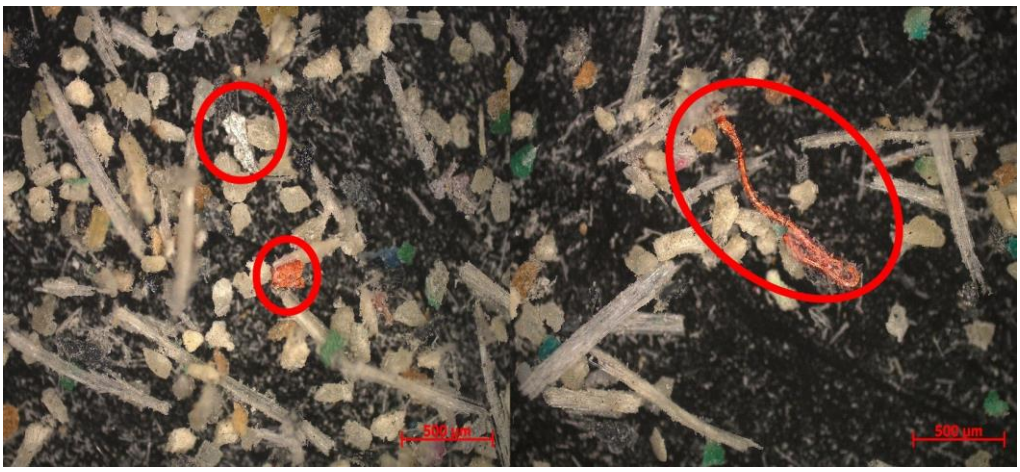

Figure 5. 4: Microscopic analysis of dry aggregates showing entrapment of metallic particles.

A similar aggregation phenomenon has been observed in the work of Vanderbruggen et al. [250], which investigated the flotation behavior of lithium metal oxides and graphite for lithium-ion battery recycling. Their study reported that when dry graphite or model black mass was introduced into water, aggregates spontaneously formed both within and on the surface of the pulp. These aggregates significantly reduced the selectivity of froth flotation, as their unselective formation led to the entrapment of nickel-manganese-cobalt oxides. This behavior closely parallels the aggregation observed in the present research, where the formation of nonmetallic WPCB aggregates poses a challenge by potentially entrapping metallic particles, thereby affecting flotation efficiency.

The equivalency between the two systems extends beyond the mere formation of aggregates; it is also rooted in the comparable hydrophobicity of the materials involved. The nonmetallic components of WPCBs in this study exhibit contact angles ranging from 77.31° to 81.70° [151, 153], while the graphite in Vanderbruggen et al. [250] work had a contact angle of 81.2° ± 4.4°. This similarity in surface wettability reinforces the underlying mechanism driving aggregation in both cases, where hydrophobic attraction between particles immersed in water leads to the spontaneous formation of aggregates, ultimately impacting separation efficiency.

5.3. Assessment of Intense Agitation Pretreatment

To analyze the aggregation behavior of the WPCB flotation feed and evaluate the effect of intense agitation on dispersion, dry and wet particle size distributions were determined using sieve analysis. While sieve analysis is not the optimal method due to the mechanical energy applied during sieving, which may disrupt pre-existing aggregates and lead to potentially misleading results, it remains a practical approach. Alternative techniques, such as laser diffraction particle size analysis, often employed for characterizing aggregation behavior in wet conditions [203, 214, 251], present inherent limitations that must be carefully considered.

One significant drawback of laser diffraction particle size analyzers is the potential for aggregate breakup due to the pump used to circulate the suspension within the flow cell. Such behavior has been reported by Patil et al. [252] in their study on the hydrophobic aggregation of ultrafine scheelite particles through shear flocculation. Additionally, the interpretation of volume-based laser diffraction results can be challenging, particularly when dealing with particles exhibiting irregular morphologies.

The nonmetallic fraction exhibits distinct shape anisotropy, particularly its elongated nature, as described in **Section 4.3.1**. This shape irregularity significantly impacts the accuracy of particle

DOI: 10.14750/ME.2026.030

size measurements. Although conversion procedures exist to reconcile laser diffraction data with sieve analysis results, these conversions inevitably introduce additional uncertainties and still fail to provide a comprehensive representation of the actual particle size distribution. Furthermore, laser diffraction analysis relies on small-volume representative sampling (5-10 mL), which introduces additional challenges in ensuring measurement accuracy.

The inherent heterogeneity and complexity of WPCB material pose significant challenges for aggregation characterization. While sieve analysis presents limitations due to energy applied, which may disrupt pre-existing aggregates, it enables the evaluation of the entire batch samples. Several assumptions underpin this approach: Dry sieving approximates a dispersed state due to the absence of water-mediated interactions; particle aggregation manifests as an upward shift in size distribution to coarser fractions (>0.125 mm); and in the absence of aggregation, wet sieving results should closely align with dry sieving. Therefore, deviations from dry sieving baselines are interpreted as aggregation indicators. While this approach has a limitation in directly differentiating between dispersed particles and aggregates within specific size fractions, correlation with flotation test outcomes remains to be verified to establish its potential as a comparative tool for assessing dispersion quality.

To assess the impact of intense agitation on particle aggregation/dispersion, **Figure 5. 5** presents the size distribution of the suspension under different stirring speeds following the agitation stage. The deviations observed between the dry and wet PSDs highlight the influence of stirring speed as a proxy for energy input in the system.

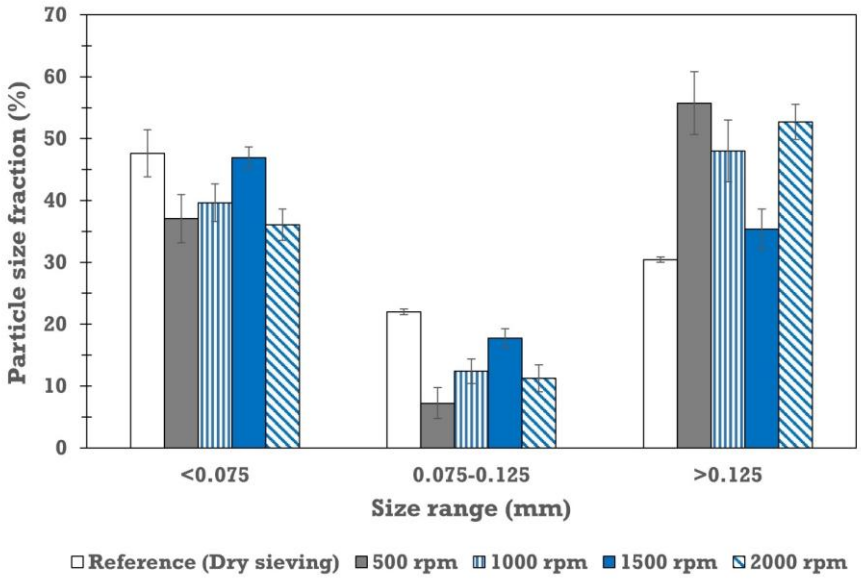

Figure 5. 5: Particle size distribution of WPCB particles after intense agitation at different stirring speeds.

DOI: 10.14750/ME.2026.030

Following intense agitation at 500 rpm, a significant shift in particle distribution is observed. The coarse fraction (>0.125 mm) increases markedly to 55.7% ± 5.1%, while the intermediate (0.075–0.125 mm) and fine (<0.075 mm) fractions decrease to 7.2% ± 2.5% and 37.1% ± 3.9%, respectively. In contrast, the dry sieving reference shows these fractions at 34.3% ± 3.8%, 19.5% ± 2.0%, and 46.2% ± 1.8%, respectively. The increase in the coarse fraction and the reduction in the fine fractions indicate poor dispersion and aggregation within the pulp (**Figure C. 4**, **Appendix III**).

While aggregation persists across all stirring speeds, its extent diminishes with increasing energy input up to an optimal point. This trend is quantified by the aggregation index (AI), described in **Section 3.4.3**, as depicted in **Figure 5. 6**. At 1500 rpm, the lowest AI value of 6.6% ± 2.5% is achieved, indicating the most effective dispersion. In contrast, 500 and 1000 rpm exhibit severe aggregation, with AI values of 48.5% ± 10.4% and 30.4% ± 10.7%, respectively. The substantial difference in AI values underscores the critical role of energy input in destabilizing hydrophobic aggregates, as supported by literature on shear flocculation in mineral processing [253–257].

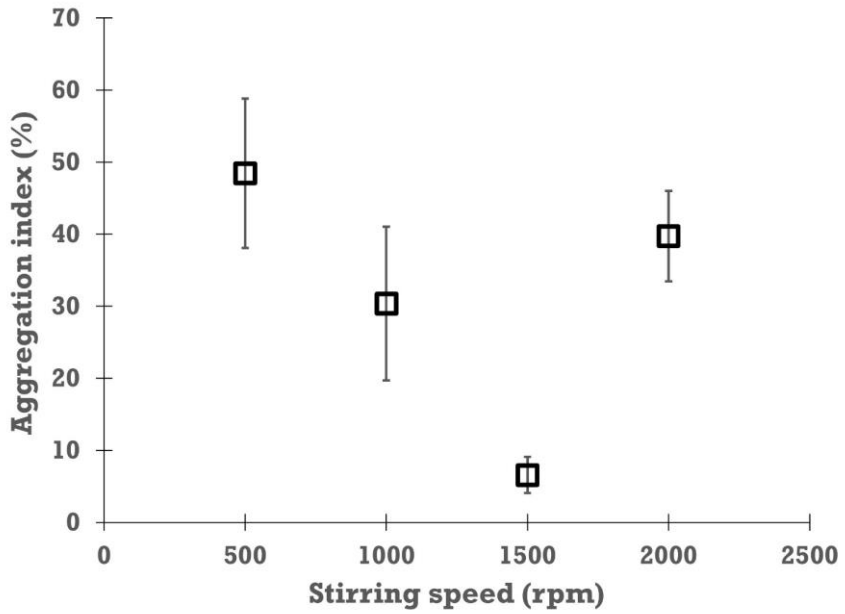

Figure 5. 6: Effect of stirring speed on aggregation index following intense agitation pretreatment.

Higher stirring speeds generate intense shear that disrupts metastable hydrophobic aggregates. The applied mechanical energy exceeds the weak interfacial forces that hold these aggregates together, forcing water penetration into particle contact zones and reducing effective hydrophobic contact, thereby enabling more uniform dispersion throughout the pulp. However,

DOI: 10.14750/ME.2026.030

beyond the optimal stirring speed, excessive energy input may not lead to further improvements and can even degrade dispersion. This is evident at 2000 rpm, where dispersion deteriorates despite the high energy input.

Notably, while 500 and 1000 rpm did not achieve effective dispersion, they also avoided foam layer formation, a phenomenon discussed in detail next. The 1500 rpm stirring speed achieved the best dispersion and minimized foam formation, resulting in a slight deviation from the reference PSD. This suggests that 1500 rpm operates within the optimal energy range, providing sufficient energy to disrupt hydrophobic interactions without inducing adverse effects.

At a stirring speed of 2000 rpm, the WPCB suspension exhibited higher aggregation and poorer dispersion compared to 1500 rpm, despite the increased energy input. This is reflected in the AI, which reached 39.8%± 6.3%, indicating a significant reversal in dispersion efficiency. This unexpected trend is primarily attributed to the formation of a stable foam layer at the pulp-air interface (**Figure 5. 7**), where WPCB nonmetallic particles adhere to air bubbles introduced through increased turbulence. A similar phenomenon was reported by Yangshuai et al. [258] in their study of flaky graphite particle systems.

Figure 5. 7: Stable foam layer at the pulp-air interface formed solely by high-speed agitation at 2000 rpm (no aeration or frother addition).

The formation of this layer at the pulp-air interface results from a complex interplay between WPCB particle characteristics and hydrodynamic conditions. Previous research has established

that WPCB pulp can generate a stable froth phase upon aeration in surfactant-free conditions through particle-mediated mechanisms [26, 30]. While conventional two-phase froth systems typically require reduced surface tension, three-phase systems can achieve stabilization through fine particles without necessitating such reductions in surface tension [26].

Foam stabilization in surfactant-free systems, as observed in mineral processing, is strongly influenced by particle size, shape, concentration, and hydrophobicity [259]. At the interface, entrapped air bubbles become coated with particles, leading to the formation of a dispersed system stabilized by particle-particle and particle-bubble interactions [199]. For hydrophobic particles, stabilization occurs when they form a closely packed monolayer around bubble surfaces, preventing bubble coalescence and reinforcing the foam lamella [26, 30]. In WPCB pulps, the fine nonmetallic particles likely enhance this stabilization mechanism due to their inherent hydrophobicity, creating a robust barrier against film rupture [199].

The hydrodynamic conditions generated at 2000 rpm play a pivotal role in this phenomenon. Increased turbulence at this high stirring speed introduces a significant quantity of air into the system, while the abundance of fine particles provides a large surface area for stabilizing bubble walls. This dynamic stabilization closely resembles froth formation, where fine particle flocculation strengthens bubble interstices, maintaining foam integrity even without surfactants.

The foam layer was collected and subjected to PSD, SEM, and chemical analyses. The PSD results confirmed that 86% of the particles in the foam were finer than 0.075 mm, while a combined 14% were coarser. This finding aligns with the proposed mechanism, where fine particles contribute to stabilization while coarser particles may be entrapped as aggregates or individual particles. More critically, microscopic images provided direct evidence of metallic particle presence within the foam layer, as shown in **Figure 5. 8**.

Chemical analysis further quantified the extent of metal entrapment in the foam, revealing notable metal concentrations: 5.7 g/kg copper, 2.2 g/kg zinc, 0.5 g/kg lead, 1 g/kg nickel, 10 g/kg iron, 212 mg/kg silver, and 22.6 mg/kg gold. These findings indicate that the foam layer can serve as a significant pathway for unintended metal losses during flotation. The persistence of this foam layer at 2000 rpm suggests that beyond an optimal stirring speed, additional energy input fails to improve dispersion and exacerbates metal losses by promoting the entrapment of metals within stabilized foam structures.

DOI: 10.14750/ME.2026.030

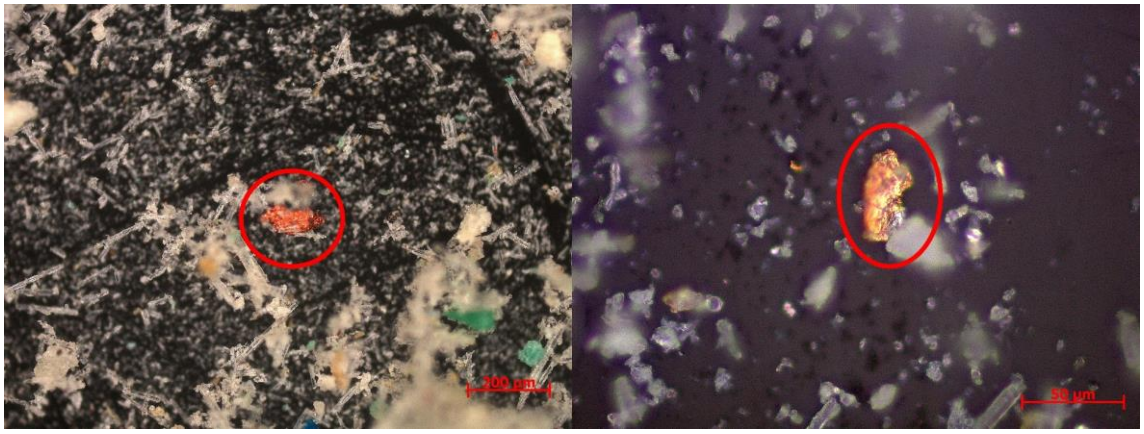

Figure 5. 8: Microscopic images of metallic particle entrapment within the foam layer.

Together, these findings highlight two distinct but interrelated pathways through which the inherent hydrophobicity of WPCB nonmetallic components could negatively influence flotation performance and contribute to potential metal losses. First, hydrophobic attraction promotes the formation of dry and partially wetted nonmetal aggregates during pulp preparation, which appear capable of entrapping metallic particles within their structure. Second, under high agitation, fine hydrophobic particles stabilize air bubbles introduced by turbulence, leading to the formation of a persistent foam layer at the pulp-air interface. This layer may physically entrap metallic particles, enabling their unintentional transport to the overflow during subsequent aeration. In both cases, hydrophobic interactions disrupt effective pulp dispersion and create conditions conducive to metal misplacement, underscoring the importance of controlling agitation intensity as a potential mitigation strategy.

Agitation time is a critical factor in intense agitation conditioning [214]. Its influence on the dispersion of WPCB particles was examined by evaluating the aggregation index at a fixed stirring speed of 1500 rpm, as illustrated in **Figure 5. 9**. When the suspension was stirred for only 5 minutes, the AI reached 70.6%, indicating a substantial degree of aggregation. However, as agitation time increased, a significant reduction in AI was observed, demonstrating improved dispersion. The most pronounced decrease occurred between 5 and 20 minutes, with the AI reaching its lowest value of 5.9% at the 20-minute mark. Beyond this point, extending the agitation time further did not result in any additional improvement in dispersion, as the AI remained unchanged even after 30 minutes of agitation.

DOI: 10.14750/ME.2026.030

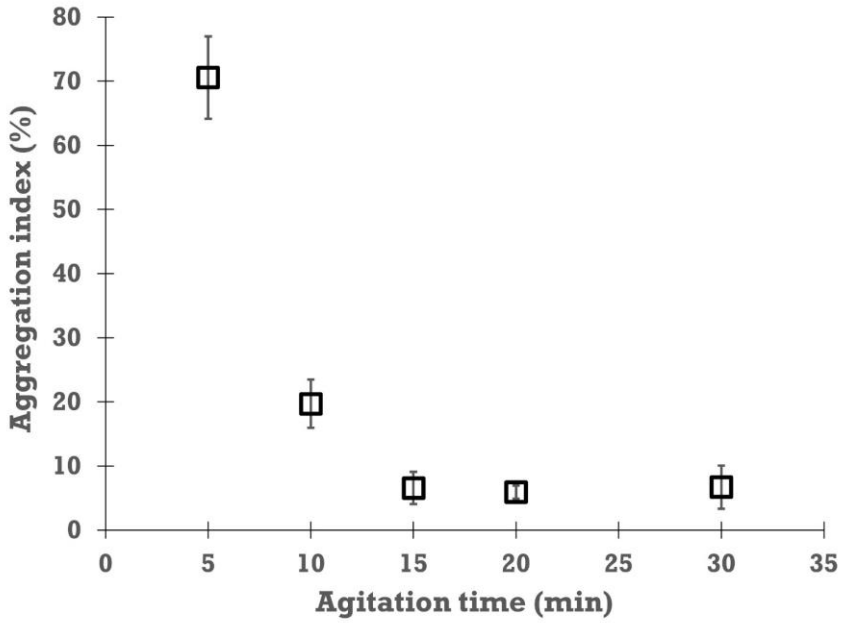

Figure 5. 9: Effect of agitation time on the aggregation index at a stirring speed of 1500 rpm.

These findings indicate that the effectiveness of the intense agitation pretreatment is governed by both stirring speed and agitation time. While increasing agitation time initially enhances dispersion, there exists an optimal duration beyond which further agitation does not contribute to additional dispersion.

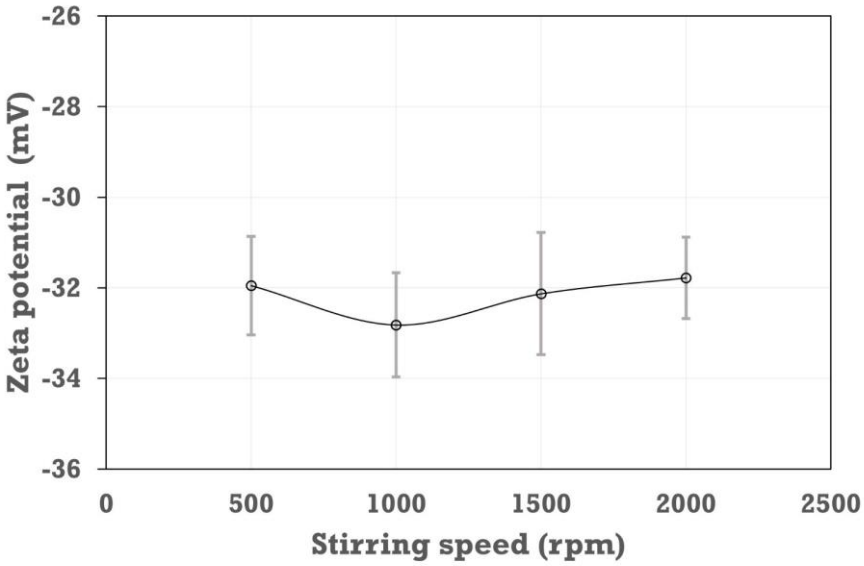

Figure 5. 10: Effect of stirring speed on zeta potential.

Having established the influence of stirring speed and conditioning time on particle dispersion, it is equally important to examine whether these mechanical pretreatment parameters affect the surface charge properties of WPCB nonmetallic particles. As shown in **Figure 5. 10**, the zeta potential remained stable across all stirring speeds, fluctuating only between −31 and −33 mV.

DOI: 10.14750/ME.2026.030

This narrow range indicates that intense agitation pretreatment does not alter the fundamental electrical properties of particle surfaces. The zeta potential values suggest that the improved dispersion results primarily from mechanical disruption of hydrophobic interactions and physical breakdown of aggregates.

5.4. Flotation Results

To examine the effect of intense agitation pretreatment on flotation performance, flotation tests were conducted at a solid concentration of 10 wt.%, an impeller stirring speed of 1375 rpm, and an air flow rate of 2 L/min. The influence of stirring speed during the 20-minute intense agitation pretreatment was assessed, and the results are presented in **Figure 5. 11**.

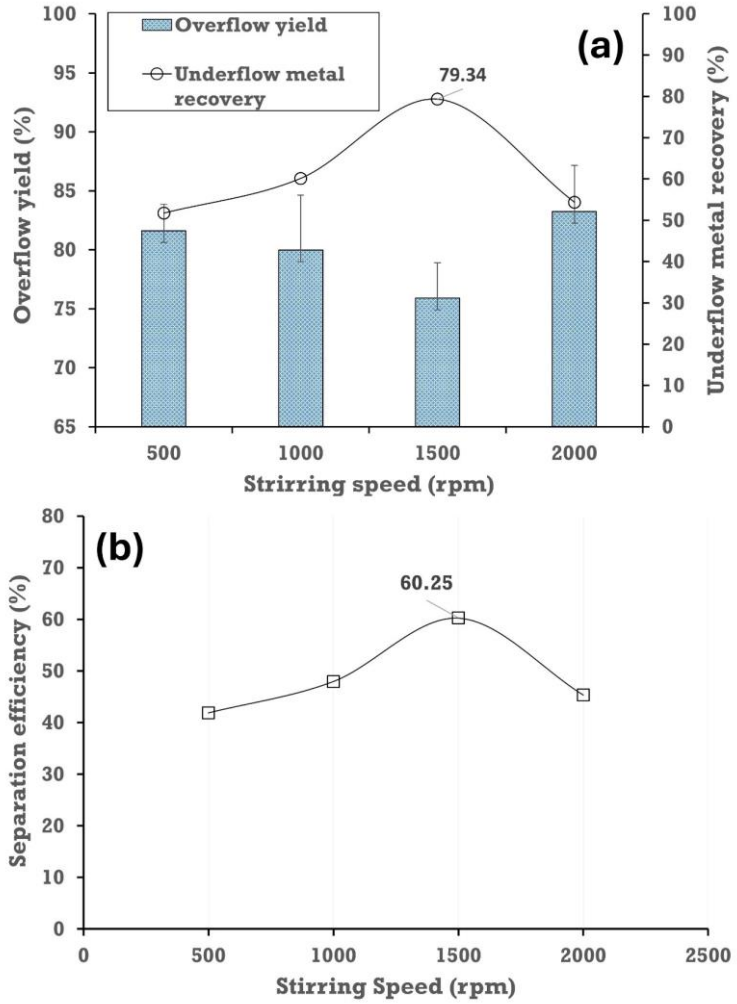

Figure 5. 11: Effect of stirring speed during intense agitation pretreatment on flotation performance: (a) overflow yield and underflow metal recovery and (b) separation efficiency.

As shown in **Figure 5. 11a**, variations in stirring speed significantly influenced both the overflow yield and the underflow metal recovery. Increasing the stirring speed from 500 to 1500 rpm resulted in a decline in overflow yield from 81.62% to 75.91%, while underflow

metal recovery improved from 51.71% to 79.34%. These trends can be directly linked to the extent of aggregation formed during the intense agitation pretreatment.

A clear relationship emerges between the degree of aggregation and flotation performance. Higher aggregation levels, such as those observed at 500 rpm, contributed to increased overflow yield, while the lowest aggregation level at 1500 rpm corresponded to the lowest overflow yield. This trend diverges from particle size-based WPCBs flotation behavior, where finer particles typically exhibit higher recovery in the overflow [165, 167]. However, in this case, aggregation increases the apparent particle size with low bulk density, as nonmetallic hydrophobic clusters entrap air pockets, forming larger, low-density structures. These aggregates exhibited enhanced buoyancy, persisting at the pulp-air interface and easily reporting to the overflow upon aeration.

Furthermore, aggregation also impacted underflow metal recovery. The unselective nature of these aggregates, which entrap metallic particles (as discussed in **Section 5.2**), explains the trend in underflow metal recovery. As dispersion improves with increased stirring speed, metal entrapment within aggregates diminishes, leading to a more selective flotation process and higher metal recovery in the underflow. A similar effect of WPCB particle aggregation on flotation selectivity has been reported, where optimal dispersion conditions yielded the highest metal recovery [147, 186]. The findings support the relevance of the aggregation index as a comparative tool, with its trends closely reflecting the observed flotation performance.

The flotation behavior following intense agitation at 2000 rpm deviates from the previously observed trends. Here, the dominant factor is not aggregation but rather the formation of a stable foam layer at the pulp-air interface, a phenomenon unique to the highest turbulence condition. Upon aeration, this foam layer reports directly to the overflow, significantly increasing the overflow yield to 83.25%. Additionally, the foam layer's ability to entrap metallic particles exacerbates metal losses, as it creates a physical barrier that prevents metals from settling into the underflow. Consequently, flotation after 2000 rpm pretreatment results in low underflow metal recovery at 54.36%.

The interplay between overflow yield and underflow metal recovery has a direct impact on the overall flotation separation efficiency, as illustrated in **Figure 5. 11b**. Although a trade-off exists between these two parameters, the results demonstrate that an optimal balance can be achieved. Intense agitation at 1500 rpm, despite yielding the lowest overflow recovery (indicating higher nonmetals in the underflow), exhibited the highest separation efficiency of

DOI: 10.14750/ME.2026.030

60% due to its enhanced selectivity upon effective dispersion. However, deviations from this optimal range, either higher or lower stirring speeds, resulted in a marked decline in separation efficiency.

While the previous discussion focused on overall metal recovery trends, a more detailed analysis of individual metals reveals distinct flotation behaviors under the same process conditions, as illustrated in **Figure 5. 12**. A key observation from the results shows marked differences in recovery under identical process conditions. For instance, following intense agitation at 1500 rpm, copper recovery reaches 85.66%, whereas iron recovery remains significantly lower at 54.28%. This variability is not unique to these two metals but extends across all metals analyzed.

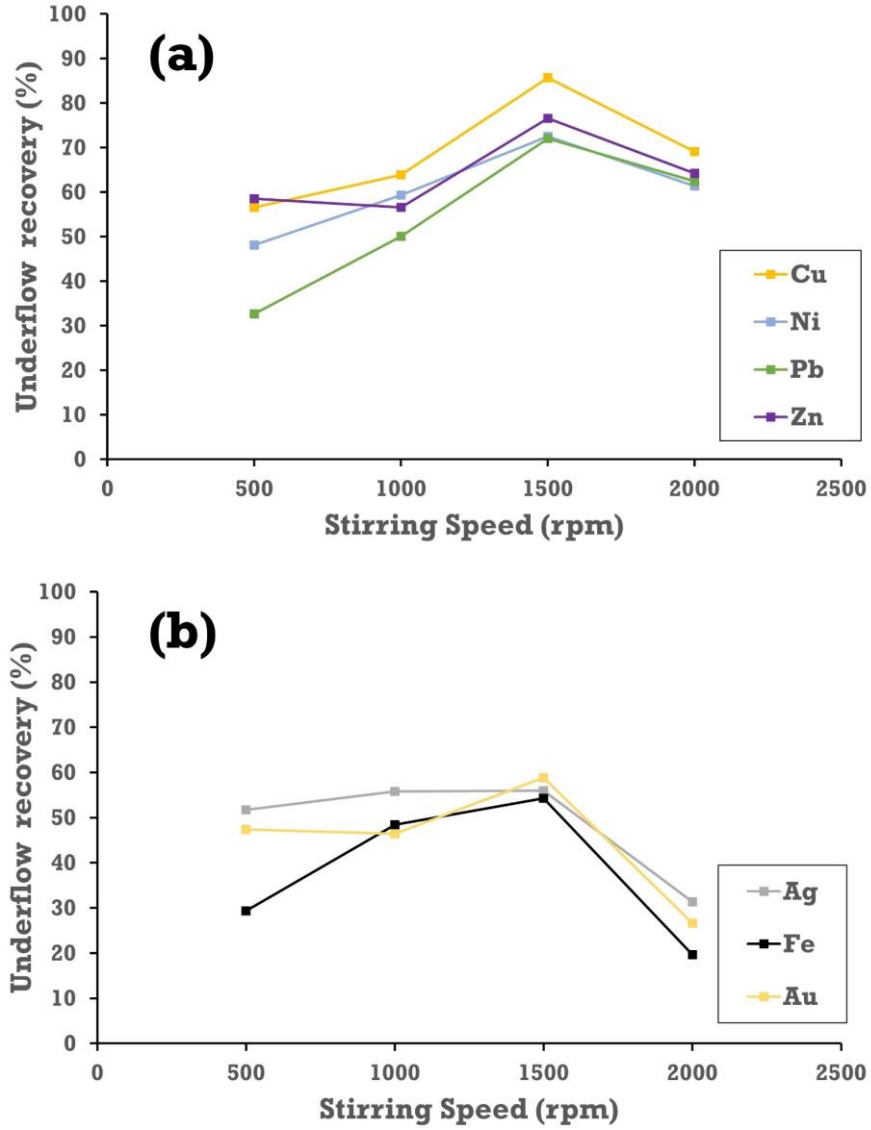

Figure 5. 12: Flotation recovery of individual metals following intense agitation pretreatment at different stirring speeds.

DOI: 10.14750/ME.2026.030

Examining the flotation performance of individual metals following different stirring speeds during intense agitation pretreatment reveals distinct recovery patterns. While all metals benefit from improved recovery as stirring speed increases from 500 to 1500 rpm, their responses are not uniform.

Metals in **Figure 5. 12a**, such as copper, nickel, lead, and zinc, exhibit a substantial increase in recovery when the stirring speed during intense agitation is raised from 1000 to 1500 rpm. Copper recovery, for example, improves from 63.91% to 85.66%, marking an increase of over 20%, with similar trends observed for nickel, lead, and zinc. Interestingly, while increasing the stirring speed to 2000 rpm leads to a decline in recovery for all metals, this group appears to be less impacted by the foam layer formation associated with excessive turbulence.

In contrast, metals in **Figure 5. 12b**, including gold, silver, and iron, show lower improvements in recovery between 1000 and 1500 rpm. Gold recovery increases by 12.42%, while iron and silver recoveries improve by only 5.85% and 1.15%, respectively. However, when stirring speed is further increased to 2000 rpm, these metals experience a sharp decline in recovery. Gold and iron, in particular, suffer substantial losses of over 30%, indicating a pronounced sensitivity to the adverse effects of foam layer formation.

The observed differences in flotation behavior stem from variations in each metal's amenability to aggregation. Although aggregation and foam layer formation are inherently random processes, certain metal characteristics, such as feed abundance and particle size distribution, play a crucial role in defining flotation outcomes. Copper, the most abundant metal in the feed, appears highly susceptible to entrapment in aggregation, as evidenced by its marked recovery improvement upon effective dispersion. Conversely, metals predominantly enriched in the <0.075 mm fraction (gold, silver, and iron) are more prone to entrapment within the foam layer at 2000 rpm, leading to severe losses.

5.5. Conclusions

The inherent hydrophobicity of WPCB nonmetallic particles resulting from residual organic resins used in manufacturing drives complex behaviors in aqueous systems. These nonpolar surfaces minimize contact with water, leading to hydrophobic attraction forces that manifest in two key pathways detrimental to flotation performance. First, spontaneous aggregation during pulp preparation forms buoyant clusters that entrap metallic particles and hinder selective separation. Second, fine hydrophobic particles stabilize air bubbles introduced by turbulence, generating a persistent, metal-laden foam layer at the pulp-air interface.

DOI: 10.14750/ME.2026.030

Intense agitation was investigated as a pretreatment strategy to enhance dispersion, with stirring speed being a critical factor. The application of intense agitation effectively and irreversibly broke up aggregates, releasing entrapped metals and significantly improving particle dispersion. Optimal conditions at 1500 rpm for 20 minutes achieved the lowest aggregation index of 5.9-6.6%, resulting in underflow metal recovery of 79.34%, a substantial improvement from 51.71% at 500 rpm. Copper recovery improved from 63.91% to 85.66% as the stirring speed increased from 1000 to 1500 rpm, with similar trends observed for nickel, lead, and zinc. However, when the stirring speed exceeded the optimal range, excessive turbulence promoted the foam formation at the pulp-air interface (AI: 39.8%). This foam layer, comprising 86% particles finer than 0.075 mm and containing significant metal concentrations (5.7 g/kg Cu, 22.6 mg/kg Au), acted as a secondary site for metal entrapment and contributed to increased losses to the overflow.

While the results establish fundamental principles for process optimization, it is important to note that industrial-scale performance may differ due to variations in hydrodynamics and scaling effects observed in larger cell sizes. Nevertheless, the research demonstrates how controlled energy input during pretreatment can maximize metal recovery while minimizing the negative effects of particle aggregation and foam formation, providing a practical framework for improving flotation separation.

DOI: 10.14750/ME.2026.030

Chapter 6: Reverse Flotation of WPCBs: Rheological Constraints, Separation and Metal Recovery Dynamics

6.1. Introduction

Flotation of WPCBs is governed by a multitude of variables, particularly cell hydrodynamics and pulp properties like solids concentration, as discussed in **Section 2.4.2**. However, the specific influence of these variables on the flotation behavior of metallic and nonmetallic constituents in reverse flotation systems is not well understood.

Results from **Chapter 5** demonstrate that significant metal losses occur to the overflow product, even under optimized pretreatment conditions. Notably, substantial variation was observed in the recovery of specific metals despite uniform flotation settings. This highlights a critical gap in existing research, which often emphasizes overall metal recovery and grade, overlooking the distinct flotation behaviors of individual metallic constituents. These behaviors, shaped by differences in liberation, composition, particle size, and morphology, require targeted investigation, especially when the goal is to optimize for economic value rather than bulk recovery.

In this chapter, impeller speed, aeration rate, and solid concentration were the flotation variables examined in the tests. The primary objective was to evaluate how these variables influence WPCB flotation performance. Furthermore, rheological properties of the pulp were assessed as a diagnostic lens to interpret flotation behavior under varying hydrodynamic conditions. Through these investigations, the research aims to offer insights into the fundamental limitations of WPCB flotation and to identify critical parameters for optimizing metal recovery.

6.2. Selection of Variable Levels for Box-Behnken Design

The selection of variable levels for the Box–Behnken experimental design was guided by preliminary flotation tests. These tests aimed to identify operational ranges that would induce meaningful variations in recovery while maintaining overall flotation performance. The experimental levels for each variable, impeller speed, aeration rate, and pulp solids concentration, in the Box-Behnken design are presented in **Table 6. 1**.

Impeller speed levels were chosen to ensure adequate suspension of particles in the pulp while avoiding excessive turbulence that could destabilize the froth. The highest impeller speed of 1500 rpm corresponded to conditions above which turbulence at the pulp–froth interface was

DOI: 10.14750/ME.2026.030

disrupting froth stability. Conversely, the lowest speed of 1250 rpm resulted in minor settling of coarse particles at the base of the flotation cell, indicating insufficient suspension.

Table 6. 1: Experimental variable levels for Box–Behnken design.

Variable	Levels	
	Low	High
Impeller speed (rpm)	1250	1500
Aeration rate (L/min)	1	3
Solid concentration (wt.%)	6	14

Aeration rates were similarly selected to support froth formation while avoiding the negative effects of over-aeration. The lower bound of 1 L/min was sufficient to generate a stable froth layer, whereas the upper limit of 3 L/min approached conditions where excessive air led to bubble coalescence and froth instability, both of which are detrimental to selective flotation. This range was therefore deemed suitable for observing the influence of aeration on flotation without introducing artifacts related to froth collapse or flooding.

In terms of pulp solids concentration, the tested range extended from 6 wt.% (3.6 vol.%) to 14 wt.% (8.7 vol.%). Below 6 wt.%, froth formation was visibly hindered, and overflow yield dropped considerably. At 18 wt.% (11.4 vol.%) concentration, the pulp became highly viscous and caused stagnation in overflow yield.

6.3. Flotation Results

The flotation test results obtained from the Box–Behnken experimental design are presented in **Table 6. 2**. These results include key flotation responses, namely, overflow yield, underflow total metal recovery, and overflow water recovery. Together, these indices provide a comprehensive evaluation of overall flotation performance under varying conditions. In addition to this bulk-level evaluation, the flotation behavior of individual metals was examined separately to gain deeper insights into their recovery patterns.

To analyze the effects of these variables, the data were fitted using Design Expert software (v. 13.0.5.0). Best-fit models were derived based on the coefficient of determination (R^2), and their statistical validity was verified through analysis of variance (ANOVA) at a 95% confidence level. Significance of regression coefficients was assessed via p-values, while a Pareto chart identified the most influential factors for each response.

DOI: 10.14750/ME.2026.030

Table 6. 2: WPCB reverse flotation test results under various conditions.

Run	N	Q_a	X	Overflow yield	Underflow total metal recovery	Water recovery
	rpm	L/min	Wt.%	%	%	%
1	1250	2	6	56.44	87.52	7.61
2	1375	1	6	63.39	74.88	8.16
3	1375	3	6	71.26	73.69	12.02
4	1500	2	6	63.65	75.46	9.24
5	1250	1	10	64.44	76.71	11.66
6	1250	3	10	70.9	62.45	15.31
7	1375	2	10	74.6	72.34	16
8	1375	2	10	73.67	71.06	16.25
9	1375	2	10	73.51	73.37	15.3
10	1500	1	10	66.02	73.04	13.17
11	1500	3	10	79.59	60.10	19.34
12	1250	2	14	59.13	78.62	22.15
13	1375	1	14	64.57	72.2	17.23
14	1375	3	14	73.1	60.57	24.94
15	1500	2	14	68.3	64.53	25.74

N is impeller speed; Q_a is the aeration rate; X is the solid concentration; Water recovery is the overall water recovery representing a fraction of water in the cell recovered into the overflow.

6.3.1. Overall flotation performance

In the following subsections, the individual and interactive effects of these variables are analyzed for the flotation responses.

a) Overflow yield

In the reverse flotation of WPCBs, the overflow yield represents the mass fraction of the feed material that reports to the froth phase and is collected as the overflow product. This process is designed to selectively remove nonmetallic constituents, resulting in the overflow predominantly containing hydrophobic polymeric materials, such as resins and fiberglass. Thus, the overflow yield serves as an indicator of how effectively unwanted nonmetals are removed.

As presented in **Table 6. 2**, overflow yield varied considerably across the experimental runs based on the applied conditions. The lowest overflow yield of 56.44% was recorded in Run #1, which had low cell hydrodynamic conditions and a pulp solids concentration of 6 wt.%. In contrast, the highest overflow yield of 79.59% was achieved in Run #11, characterized by the

DOI: 10.14750/ME.2026.030

highest cell hydrodynamics and a moderate solids concentration of 10 wt.%. However, when the solids concentration was further increased to 14 wt.% under the same hydrodynamic conditions in Run #14, the overflow yield decreased to 73.10%. This suggests a non-linear relationship between solids concentration and overflow yield.

To better understand the influence of these variables and their interactions on overflow yield, a regression model was developed. The model fitting and statistical significance were assessed through ANOVA, and a backward elimination approach was applied to retain only significant terms in the model. The ANOVA summary and regression coefficients are provided in **Table 6. 3**.

Table 6. 3: Summary of ANOVA for the regression model of the overflow yield.

Overflow yield	
Model p value	<0.0001
Lack of Fit	0.1221
R^2	0.97
Adjusted R^2	0.95
Predicted R^2	0.86
Mean	68.17
Std. Dev.	1.42

The model is statistically significant, with a p-value of 0.0001 (<0.05), confirming the adequacy of the reduced quadratic model in explaining the observed trends. Furthermore, the lack-of-fit test yielded a p-value above 0.05, indicating that the model does not suffer from significant deviation relative to experimental error. The model also demonstrated a strong fit with an R^2 value of 0.97, suggesting that 97% of the variability in overflow yield is accounted for by the model. The adjusted R^2 value of 0.95 further supports the robustness of the model, indicating that only 5% of the response variability remains unexplained. The specific regression equation and model terms are provided in **Appendix III** for reference.

The standardized effects of the independent variables and their interactions on overflow yield are illustrated in the Pareto chart (**Figure 6. 1**). This chart ranks the influence of each term based on its statistical significance, showing that the squared term of solid concentration (X^2) had the greatest effect, followed by the aeration rate (Q_a) and the squared term of impeller speed (N^2) with lower influence of linear effects and interactions of the studied flotation variables.

DOI: 10.14750/ME.2026.030

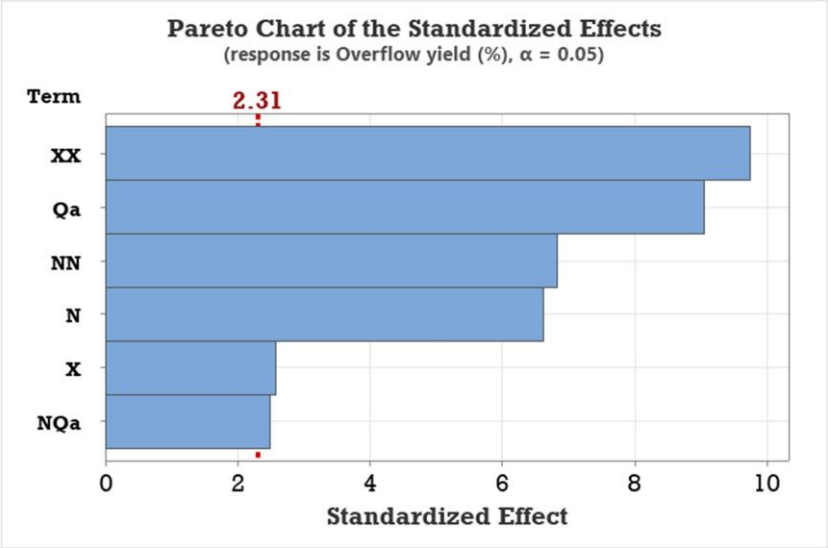

Figure 6. 1: Pareto chart of standardized effects illustrating the statistical significance of impeller speed (N), aeration rate (Qa), solids concentration (X), and their interactions on overflow yield, based on the regression model from the Box–Behnken Design.

The main effects of the variables are depicted in **Figure 6. 2**. Solid concentration exerted a particularly strong and nonlinear influence on overflow yield, displaying a pronounced quadratic trend. Yield increased with solids concentration up to the mid-level of 10 wt.%, but declined sharply at 14 wt.%. These trends suggest the presence of a process-related threshold beyond which flotation performance is hindered, likely tied to changes in pulp characteristics at higher solids concentrations.

Aeration rate demonstrated a linear positive effect on overflow yield, while impeller speed exhibited a milder quadratic influence, with yields peaking near mid-level speeds before declining. These trends align with established flotation mechanisms: increased aeration provides more bubbles for particle attachment, while moderate impeller speeds enhance collision frequency, promoting the true flotation of hydrophobic particles [141, 260]. However, excessive turbulence at higher speeds destabilizes the pulp-froth interface and promotes particle detachment, particularly of coarse particles [261]. Notably, the interaction between impeller speed and aeration rate further modulated this response, where the positive effect of impeller speed became more pronounced under higher aeration rates. These trends indicate that the highest overflow yield is achieved under conditions of high aeration rate (3 L/min), around the mid-level impeller speed (1400 rpm), and moderate pulp solids concentration (10 wt.%).

DOI: 10.14750/ME.2026.030

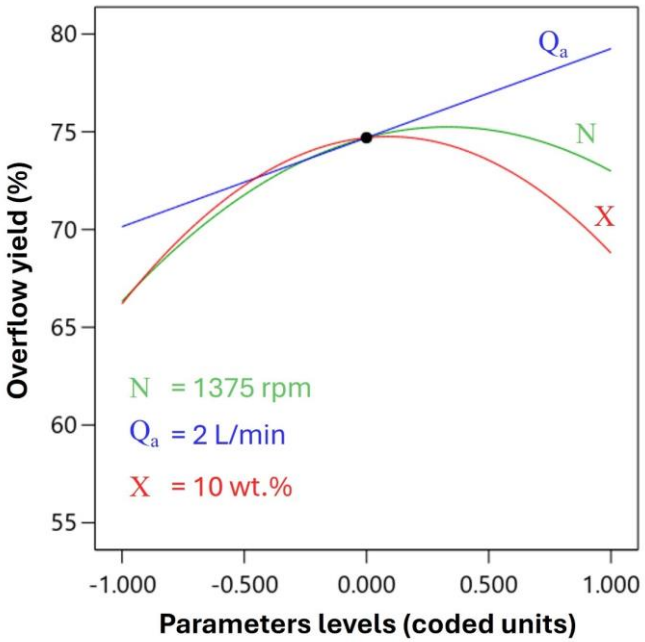

Figure 6. 2: Modeled main effects of impeller speed (N), aeration rate (Q_a), and solids concentration (X) on overflow yield, based on regression analysis of the Box–Behnken Design.

b) Underflow total metal recovery

In the reverse flotation of WPCBs, underflow total metal recovery measures the proportion of metallic constituents retained in the pulp phase relative to their original content in the feed. As presented in **Table 6. 2**, the lowest recoveries, 60.10% and 60.57%, were recorded in Runs #11 and #14, which were conducted under high cell hydrodynamics and moderate (10 wt.%) to high (14 wt.%) solids concentrations. These conditions also corresponded with some of the highest overflow yields, indicating effective rejection of nonmetallic components. In contrast, the highest recovery of 87.52% was achieved in Run #1, which featured low cell hydrodynamics and the lowest solid concentration (6 wt.%). Notably, this condition resulted in the lowest overflow yield at 56.44%, highlighting a clear trade-off between nonmetal rejection and metal retention.

The statistical significance and adequacy of the regression model for underflow metal recovery are summarized in **Table 6. 4**. The model is statistically significant, as indicated by a p-value of 0.0017 (< 0.05), and the lack of fit is not statistically significant ($p > 0.05$), supporting the model's reliability. The reduced quadratic model yielded an R^2 value of 0.80, reflecting a good correlation between the predicted and experimental data. The adjusted R^2 of 0.71 indicates that approximately 29% of the response variability remains unaccounted for. This residual variability may be attributed to unmodeled influences, such as sample heterogeneity in

DOI: 10.14750/ME.2026.030

composition, degree of liberation, particle size distribution, or the presence of secondary mechanisms not captured by the current model framework. The full regression equation is provided in **Appendix III**.

Table 6. 4: Summary of ANOVA for the regression model of the underflow total metal recovery.

Underflow total metal recovery	
Model p value	0.0017
Lack of Fit	0.0692
R^2	0.80
Adjusted R^2	0.71
Predicted R^2	0.51
Mean	71.77
Std. Dev.	3.89

The standardized effects of the independent variables on underflow metal recovery are presented in the Pareto chart **(Figure 6. 3**), whereas **Figure 6. 4** illustrates their main effects on underflow metal recovery.

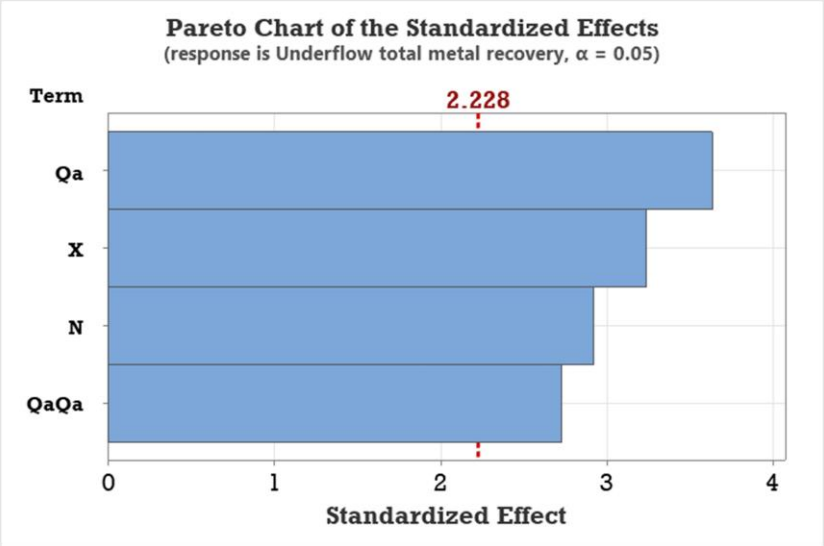

Figure 6. 3: Pareto chart of standardized effects illustrating the statistical significance of impeller speed (N), aeration rate (Qa), and solids concentration (X) and their interactions on underflow total metal recovery, based on the regression model from the Box–Behnken Design.

Underflow metal recovery demonstrates marked sensitivity to aeration rate, displaying a complex parabolic trend that enhanced recovery at moderate values (~2 L/min) but diminished it at higher rates. In comparison, impeller speed had a predominantly linear negative effect, with recovery decreasing as speed increased. Similarly, solids concentration also shows a strong negative linear relationship, with higher pulp solids resulting in reduced metal recovery.

DOI: 10.14750/ME.2026.030

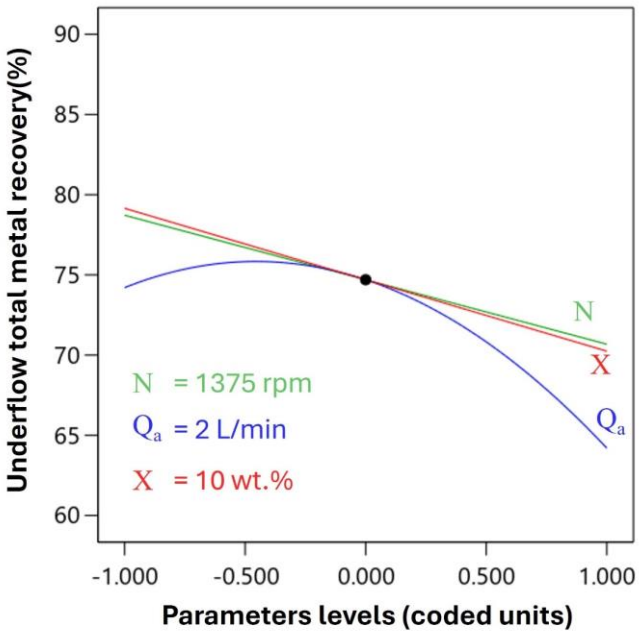

Figure 6. 4: Modeled main effects of impeller speed (N), aeration rate (Q_a), and solids concentration (X) on underflow total metal recovery, based on regression analysis of the Box–Behnken Design.

The observed underflow metal recovery behavior appears consistent with two distinct mechanisms governing metal loss to the overflow: true flotation of poorly liberated metal particles under conditions similar to those favoring overflow yield optimization and potential entrainment, particularly under elevated cell hydrodynamics that promote higher water recoveries [176, 262]. Collectively, these trends indicate that maximum underflow metal recovery is achieved under conditions of low impeller speed (1250 rpm), moderate aeration rate (1.5 L/min), and low solid concentration (6 wt.%).

c) Water recovery

In batch flotation tests, water recovery is defined as the fraction of total water in the flotation cell that reports to the concentrate (overflow). Water serves as the primary medium through which fine, hydrophilic particles become unselectively entrained into the froth phase. In direct flotation schemes, increased water recovery correlates with a decrease in concentrate grade due to enhanced gangue entrainment. However, in the context of reverse flotation of WPCBs, water recovery assumes a unique role. Since the desired metallic constituents are hydrophilic and the flotation feed is highly liberated, entrainment through water recovery to the overflow poses a potential pathway for metal losses.

The ANOVA summary for the regression model is presented in **Table 6. 5**. The model is statistically significant ($p = 0.0001$), with an insignificant lack of fit ($p > 0.05$). The linear

DOI: 10.14750/ME.2026.030

model yielded an R^2 of 0.95 and an adjusted R^2 of 0.94, indicating strong predictive accuracy with only 6% of variability unexplained. The regression equation is provided in **Appendix III**.

Table 6. 5: Summary of ANOVA for the regression model of the water recovery.

Water recovery	
Model p value	0.0001
Lack of Fit	0.1437
R^2	0.95
Adjusted R^2	0.94
Predicted R^2	0.90
Mean	15.62
Std. Dev.	1.40

The standardized effects of the variables and their interactions are illustrated in the Pareto chart (**Figure 6. 5**). Solid concentration (X) emerged as the most influential factor, followed by aeration rate (Qa) and impeller speed (N). These findings were further supported by the main effects plot (**Figure 6. 6**), which showed that each of the three variables had a linear positive relationship with water recovery. Among them, solid concentration had the steepest slope, indicating its dominant role. Interaction effects between the variables were found to be statistically insignificant.

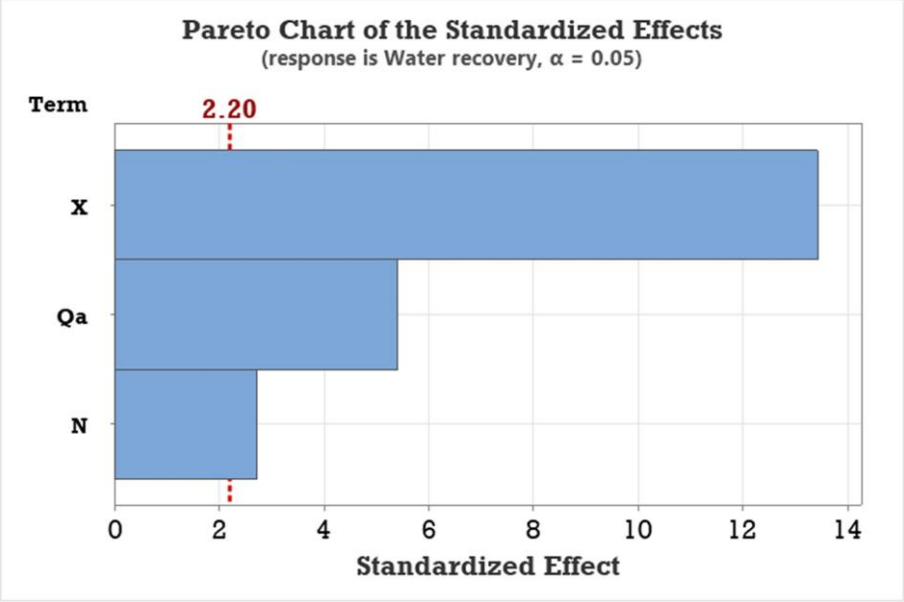

Figure 6. 5: Pareto chart of standardized effects illustrating the statistical significance of impeller speed (N), aeration rate (Qa), and solids concentration (X) on water recovery, based on the regression model from the Box–Behnken Design.

DOI: 10.14750/ME.2026.030

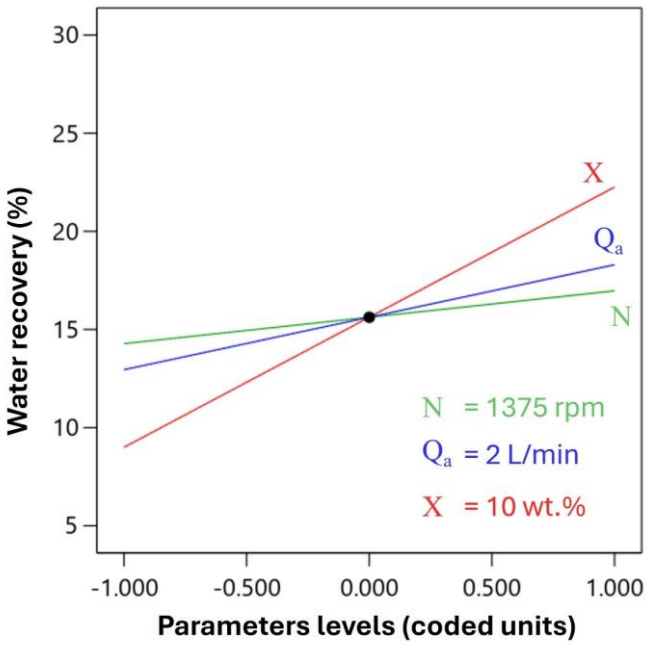

Figure 6. 6: Modeled main effects of impeller speed (N), aeration rate (Q_a), and solids concentration (X) on water recovery, based on regression analysis of the Box–Behnken Design.

6.3.2. Metal-specific flotation behavior

While the evaluation of overall metal recovery has been the predominant approach in the available literature [147, 166, 167], a more nuanced analysis would provide valuable additional insights. The complex nature of WPCBs, characterized by diverse metal types, varying content percentages, and intricate positioning and embedment patterns, strongly influences the degree of metal liberation and size distribution following mechanical processing. As such, discussions of total metal recovery and general flotation behavior, though informative, may not fully capture the underlying complexity of the process.

To move beyond generalized trends and capture the individual response behaviors of key metals, regression models were developed for the underflow recovery of each target metal. The adequacy and statistical validity of these models were evaluated using ANOVA, with the results summarized in **Table 6. 6**.

The recovery ranges demonstrated considerable variation among different metals. Copper exhibited the highest recovery with a maximum of 94% and a wide recovery range of 25%, indicative of its sensitivity to process variable adjustments. Gold also showed promising recovery that can reach up to 84%, which is critically important given its high economic value in WPCB recycling. In contrast, metals such as iron and silver showed more modest recoveries,

DOI: 10.14750/ME.2026.030

with maximum values of 63% and 66%, respectively. Nickel, zinc, and lead showed similar recovery patterns with maximum recovery values around 78% and minimum values of approximately 54%.

Table 6. 6: Summary of ANOVA for the regression models.

Metal	Min/Max Recovery (%)	Model p-value	Lack of Fit	R^2	Adjusted R^2	Significant terms	Remarks
Copper	69/94	0.0002	0.2126	0.88	0.83	N, Q_a, X, Q_a^2	—
Iron	32/63	0.0003	0.7582	0.85	0.80	N, Q_a, N^2, X^2	—
Nickel	55/79	0.0006	0.9428	0.88	0.81	N, Q_a, N^2, Q_a^2, X^2	—
Lead	53/77	0.002	0.8417	0.79	0.72	Q_a, N^2, Q_a^2, X^2	—
Zinc	53/79	0.002	0.8625	0.73	0.66	N, Q_a, Q_a^2	—
Silver	33/66	—	—	—	—	—	No statistically significant terms
Gold	54/84	0.001	0.2610	0.84	0.80	N, Q_a, X^2	

The regression models developed for metal-specific underflow recovery were statistically adequate for all metals except silver, as confirmed by ANOVA results. Notably, the set of statistically significant terms varied between metals, highlighting their distinct responses to the flotation conditions. This divergence implies that metal recovery is governed not only by process parameters but also by metal-specific factors such as liberation characteristics, particle morphology, and size distribution, which have been shown to vary between metals, reflecting the intricate positioning and embedment patterns in WPCBs.

Among the examined metals, copper recovery appears to closely resemble the total metal recovery pattern, which is attributable to copper's predominance in the feed composition, constituting more than 60 wt.% of the metal content. This similarity is evidenced by the statistically significant terms in the regression model affecting copper recovery, which closely aligns with those influencing total metal recovery. In both cases, aeration rate exerts the strongest influence with a quadratic effect, while both impeller speed and solid concentration show clear negative linear effects. Furthermore, the minimum and maximum copper recovery values closely matched those of total metal recovery, and a Pearson correlation coefficient of 0.954 between the two metrics further confirms this relationship. This alignment suggests that when total metal recovery is discussed, it predominantly reflects the flotation trend of the

DOI: 10.14750/ME.2026.030

dominant metal in the feed. Consequently, relying solely on total recovery masks the behaviors of less abundant but economically critical metals, such as gold and silver, reinforcing the importance of individual metal analysis.

A closer comparison between copper, the most abundant metal, and gold, the most economically valuable, reveals competing flotation responses under varying flotation conditions (**Figure 6. 7**). While aeration rate and impeller speed exhibited generally similar negative effects on the recovery of both metals (albeit to different degrees), solid concentration emerged as a key differentiating variable. Copper recovery responded linearly and negatively to increasing solid concentration across the entire tested range. In contrast, gold recovery followed a quadratic trend: it initially declined as solid concentration increased to the mid-level but then improved again at higher concentrations.

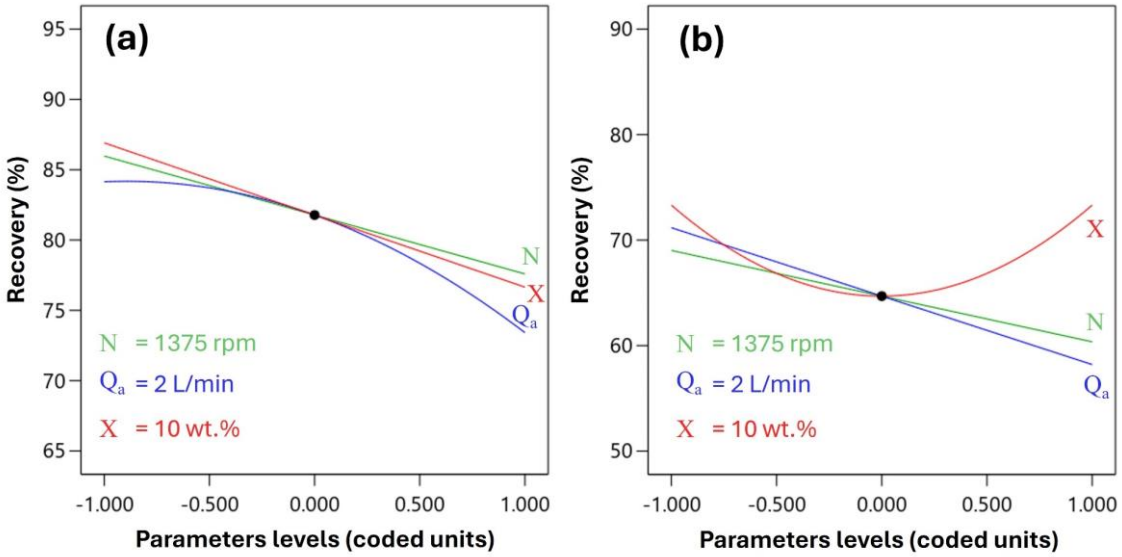

Figure 6. 7: Main effects of the variables on (a) copper recovery and (b) gold recovery.

These findings have significant implications for process optimization, as demonstrated in **Figure 6. 8**. These scenarios are based on a single rougher flotation stage, which prioritizes maximum recovery; therefore, certain trade-offs are expected. Optimizing flotation performance to maximize overflow yield and copper recovery (Scenario 1) dictates using a solid concentration of 9 wt.%, resulting in 83.7% copper recovery but only 66% gold recovery. Alternatively, optimizing for overflow yield and gold recovery (Scenario 2) requires a solid concentration of 12 wt.%, yielding 73% gold recovery but reducing copper recovery to 81%. A balanced approach attempting to maximize overflow yield along with both copper and gold recovery (Scenario 3) necessitates a solid concentration of 8 wt.%, resulting in copper and gold recoveries of 86.6% and 71.9%, respectively. However, this comes at the expense of lower

DOI: 10.14750/ME.2026.030

overflow yield and, consequently, reduced nonmetal rejection and overall separation efficiency. Moreover, such low solids concentration also limits flotation throughput, compromising process productivity.

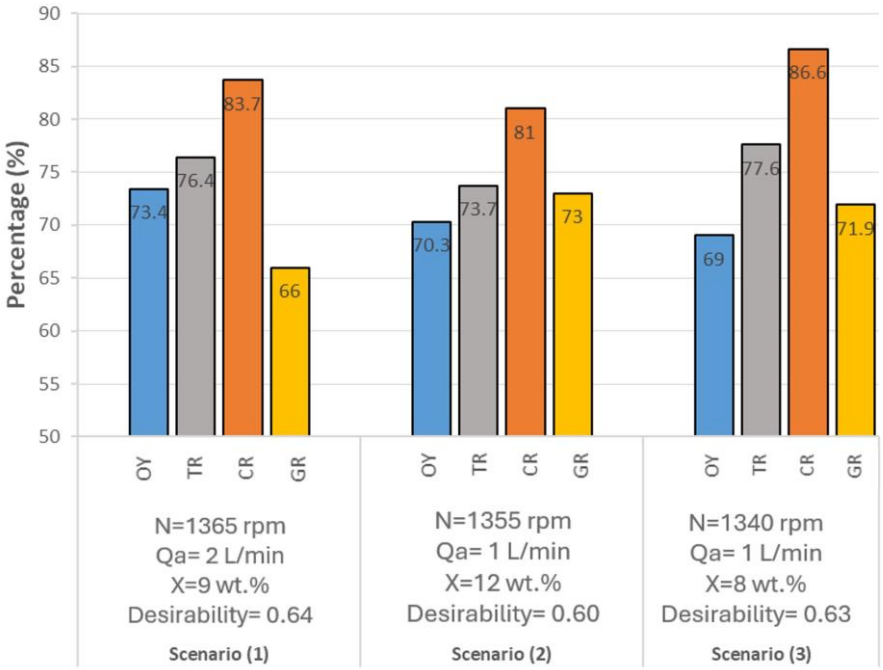

Figure 6. 8: Flotation outcomes across optimization scenarios (OY: overflow yield, TR: total recovery, CR: copper recovery, GR: gold recovery).

Economic analysis presented earlier (**Section 4.3.2**) showed that over 92% of the total market value of the selected WPCB post-separation fraction originates from gold, despite its trace concentration. This underscores that even modest improvements in gold recovery can exert a far greater economic impact than equivalent gains in bulk metal recovery. The observed narrow operating window for gold recovery therefore carries both metallurgical and financial significance. Consequently, optimization driven solely by total bulk recovery risks undervaluing process performance, since the selective retention of gold ultimately dictates the economic viability of WPCB flotation. These trade-offs are characteristic of rougher flotation operations, where the primary objective is maximizing recovery. In a continuous flotation circuit, subsequent scavenger stages would recover additional metals from the rougher tailings, while cleaner stages would upgrade the concentrate grade, potentially resolving some of the recovery-grade conflicts observed in this single-stage optimization.

In the case of silver, recovery could not be effectively modeled within the tested design space, as shown by the lack of statistical significance in the regression model and the absence of identifiable influential terms. This modeling failure indicates that silver recovery was highly

DOI: 10.14750/ME.2026.030

variable and unresponsive to changes in flotation parameters. From a flotation perspective, this implies that silver recovery cannot be effectively controlled through parameter adjustments alone. This inconsistent response aligns with silver's diffuse distribution in WPCBs. As discussed previously (**Section 4.3.2**), silver tends to occur in trace amounts across a wide range of components, including switches, solders, and contacts, rather than being concentrated in discrete phases. Elemental mapping via EDS (**Appendix III**, **Figure C. 3**) confirmed this dispersed occurrence. Such heterogeneity in distribution likely results in variable liberation characteristics, leading to unpredictable flotation behavior that cannot be adequately captured by the regression models that successfully described other metals.

6.4. Pulp Rheology

6.4.1. Effect of solid concentration

Given the significant influence of pulp solids concentration on all studied flotation responses, particularly overflow yield, and the well-established role of solids concentration in suspension rheology, rheological measurements were conducted to investigate the behavior of WPCB suspension at various solids concentrations (6–18 wt.%). The rheograms in **Figure 6. 9**, which plot shear stress against shear rate, show the effect of the increasing solids concentration in the flotation pulp.

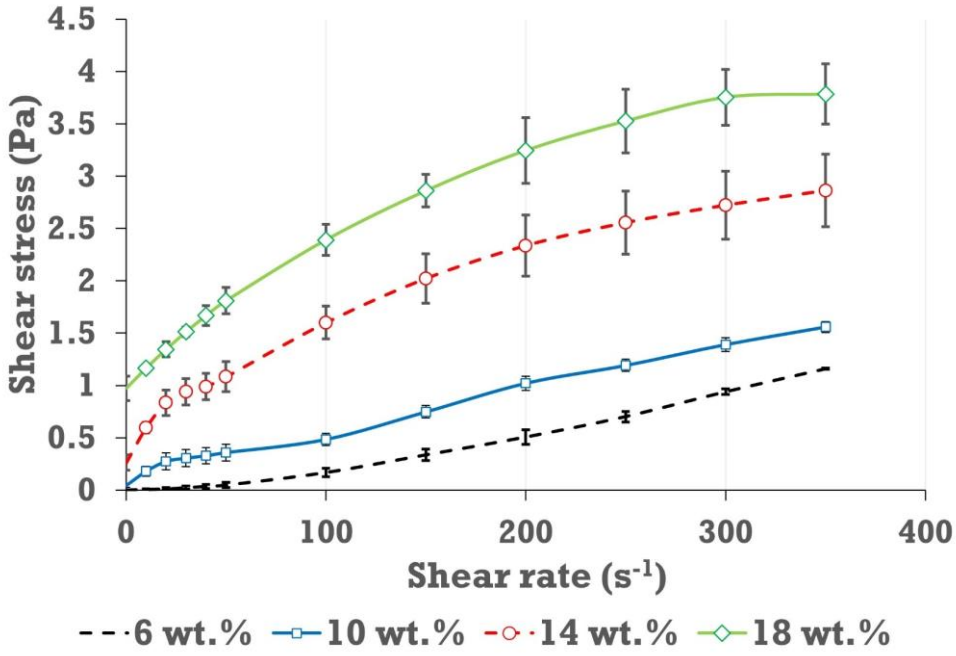

Figure 6. 9: Rheological behavior of WPCB flotation feed suspension at 6, 10, 14, and 18 wt.% solids.

DOI: 10.14750/ME.2026.030

At lower concentrations (6 wt.% and 10 wt.%), the shear stress versus shear rate curves exhibited an approximately linear trend, indicating a near-Newtonian flow response. Although slight deviations from linearity were evident, the suspensions showed only minor non-Newtonian effects in this range. However, as the solids concentration increased to 14 wt.% and 18 wt.%, the rheograms departed markedly from Newtonian behavior, displaying pronounced non-Newtonian characteristics with yield stress. This shift reflects the intensified particle–particle interactions at higher solids loading.

The apparent viscosity was calculated at a shear rate of 100 s^{-1}, a value representative of the average shear rate typically encountered in flotation cells [218, 263]. The apparent viscosities were determined to be 1.67 mPa·s at 6 wt.% (3.6 vol.%), 4.85 mPa·s at 10 wt.% (6.1 vol.%), 16.00 mPa·s at 14 wt.% (8.7 vol.%), and 23.91 mPa·s at 18 wt.% (11.4 vol.%). These results show a sharp increase in viscosity with increasing solids concentration, even within the relatively low tested range. This trend can be attributed primarily to strong interparticle interactions among nonmetallic components under hydrophobic attraction forces and, to a lesser extent, the friction expected from their dominant elongated shape [264].

Although high viscosities are often associated with high solid concentrations or problematic clay-rich slurries, even these materials exhibit relatively moderate rheological behavior at comparable volume fractions. For instance, a copper–gold ore with low clay content (X_{80} = 0.212 mm) mixed with 15 wt.% bentonite at 14 vol.% solids displayed an apparent viscosity of just 8 mPa·s [265]. Similarly, a copper–gold ore (X_{80} = 0.106 mm) containing 30 wt.% kaolinite showed an apparent viscosity of 13 mPa·s at 15 vol.% solids concentration [266]. In contrast, the WPCB slurry reached 23.91 mPa·s at only 11.4 vol.%, exceeding the values seen in these clay-rich systems. This suggests a shift towards a more constrained suspension, where interactions between particles hinder free flow. This highlights the unique rheological challenges posed by WPCB particles, even at low solid concentrations. These findings indicate that WPCB pulps exhibit a flow behavior in which even moderate solids loading can replicate the rheological penalties typically observed in much denser mineral systems. This suggests that the threshold for process control in flotation performance deterioration for WPCBs is lower than that for mineral ores, reinforcing the idea that rheology is not a peripheral property but a governing constraint in this system.

DOI: 10.14750/ME.2026.030

6.4.2. Effect on flotation performance

The rheological parameters of the WPCB slurry provide a valuable framework for understanding the observed flotation behavior, particularly the trends in overflow yield and underflow metal recovery.

a) Overflow yield

Considering the overflow yield, previous observations during variable level selection indicated a considerable drop and stagnation at 18 wt.% solids concentration. Furthermore, the overall flotation performance analysis revealed an initial increase in overflow yield as pulp solids concentration rose from 6 wt.% to an optimum around 10 wt.%, followed by a sharp decline at 14 wt.%. This relationship can be understood by examining apparent viscosity and its effect on mechanisms governing true flotation.

At 6 wt.% solids, the WPCB slurry exhibited a relatively low apparent viscosity of 1.67 mPa·s. Under such low-viscosity conditions, turbulence is insufficiently damped, a factor known to increase both particle–bubble collision and detachment probabilities in flotation systems [260]. This may account for the relatively lower overflow yield observed at this concentration, particularly with respect to nonmetallic particle overflow recovery. As the pulp viscosity increases to 4.85 mPa·s at 10 wt.% solids, the improved stability of bubble–particle aggregates likely contributes to the observed enhancement in overflow yield. This aligns with previous findings showing that higher medium viscosities, such as a glycerol–water mixture with a viscosity of 7.6 mPa·s compared to water at 0.9 mPa·s, increase the critical detachment amplitude of particles from bubbles, thereby enhancing aggregate stability [267].

However, the sharp decline in overflow yield observed at higher concentrations aligns directly with the rheological transition identified. At 14 wt.% solids, where the apparent viscosity rises sharply to 16.00 mPa·s, and even more dramatically at 18 wt.% with 23.91 mPa·s, the slurry exhibits flow characteristics that hinder the hydrodynamics of flotation. Literature indicates that high-viscosity pulps restrict gas dispersion in the flotation cell, confining turbulence to a small 'turbulent cavern' around the impeller [268, 269]. As a result, air dispersion and bubble transport are severely limited, substantially reducing nonmetal recovery to the overflow and thus diminishing overall yield. This effect becomes particularly pronounced at 18 wt.%, where the rheological properties of the pulp create conditions that effectively stagnate the flotation process.

DOI: 10.14750/ME.2026.030

Overall, the overflow yield trends align with a rheology-mediated control mechanism. Moderate viscosity stabilizes bubble–particle aggregates and enhances selective nonmetal removal, while excessive viscosity suppresses gas dispersion and froth mobility. The rheological state therefore defines a narrow operational window where the desired nonmetal rejection can be achieved before the system becomes hydrodynamically restricted.

b) Underflow metal recovery

Underflow metal recovery exhibited a decreasing linear relationship with solids concentration. This trend was initially linked to viscosity-mediated true flotation losses of poorly liberated metal particles. However, regression models indicate that overflow yield is markedly more sensitive to rheological variations than underflow metal recovery, an unexpected outcome given the metals' intergrowth patterns and surface characteristics, which would typically render them more prone to detachment under unfavorable rheology. This discrepancy suggests that additional mechanisms, beyond viscosity-driven attachment and detachment dynamics, influence metal recovery in the system. Notably, under similar overall overflow yields of 10 wt.% and 14 wt.% (Run #10 versus Run #15), metal losses at 14 wt.% were consistently higher. This indicates that factors beyond bulk mass pull, such as changes in pulp structure and froth properties, are responsible for amplifying metal losses.

A potential contributing factor to the observed decline in underflow metal recovery at higher solids concentrations is the emergence of yield stress, which increased from nearly 0 Pa at 10 wt.% to 0.35 Pa at 14 wt.%. This rise, often indicative of aggregate formation in mineral suspensions [270, 271], suggests enhanced interparticle interactions and reduced mobility at elevated solids concentrations. Although all rheological measurements were performed on pre-agitated samples, previously shown to disrupt aggregates effectively at 10 wt.%, this dispersive action appears less effective at 14 wt.%, likely due to intensified physical constraints at higher pulp solids concentrations. Such aggregates may entrap metallic particles, which may then be transported from the pulp to the froth phase due to their collectively reduced density, as detailed in **Sections 5.2 and 5.3**. However, given the relatively low magnitude of yield stress observed, this mechanism is likely secondary to other, more dominant mechanisms.

Another possible mechanism driving metal overflow loss is entrainment, which typically accounts for the transport of hydrophilic particles into the froth phase during flotation. This process is directly related to water recovery, as evidenced by **Figure 6. 10**, which shows a

DOI: 10.14750/ME.2026.030

strong correlation between water recovery and overflow metal loss (R^2 = 0.93, Pearson coefficient = 0.65).

However, several factors would conventionally limit entrainment's impact on metal recovery in this system. Over 80% of metals in the flotation feed are predominantly distributed in size fractions larger than 0.075 mm, whereas entrainment primarily affects particles finer than 0.050 mm [272]. Additionally, metals enriched in the finer fraction, such as gold, silver, and iron, possess high specific gravities (19.3, 10.5, and 7.87, respectively), which should reduce their susceptibility to entrainment due to their high settling velocities. Furthermore, entrainment operates as a nonselective process, and with the nonmetal-to-metal ratio reaching 25:1, the majority of entrained particles would theoretically consist of nonmetals.

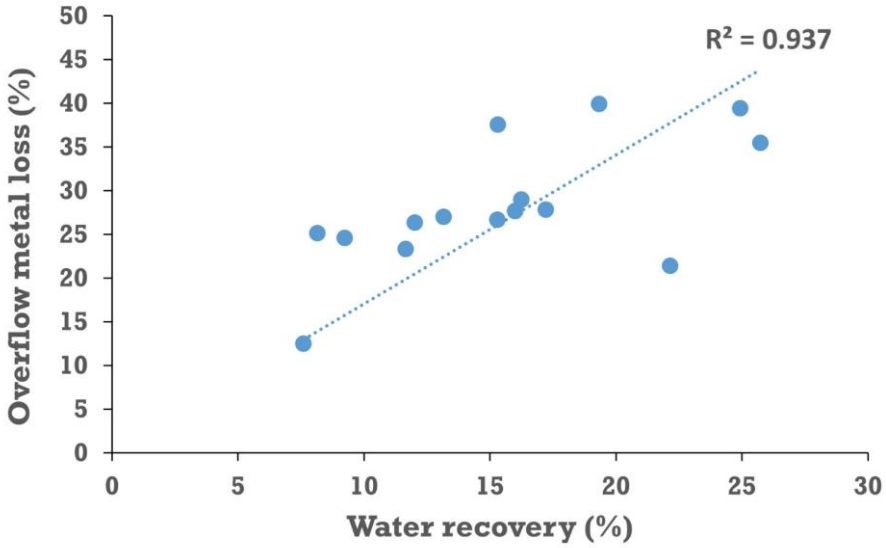

Figure 6. 10: Metal loss to the overflow versus water recovery.

The rheological measurements reveal that pulps become increasingly viscous at higher solids concentrations, significantly altering flow patterns. This change affects water drainage across the pulp–froth interface and impedes particle settling due to enhanced drag forces [273, 274]. This issue is exacerbated by the high aspect ratio of metal particles in WPCB, which increases susceptibility to entrainment because of higher drag coefficients and reduced settling velocities [172, 173]. Consequently, although conventional factors suggest minimal entrainment of metals, the unique rheological conditions and particle characteristics in this system indicate that the entrainment of fine-sized metals cannot be dismissed as a contributing mechanism to metal overflow losses.

DOI: 10.14750/ME.2026.030

These observations collectively demonstrate that the rheological regime dictates not only the rejection of nonmetal but also the dynamics of metal recovery. Elevated viscosity shifts the separation process from being governed by surface chemistry to being dictated by mechanical flow constraints. This highlights that hydrodynamic optimization alone cannot compensate for rheological degradation once the pulp enters a yield-stress regime.

6.5. Metal Losses: A Size-by-Size Analysis

Given the preceding findings and discussions, it became necessary to investigate the mechanisms responsible for metal losses to the overflow. A size-by-size analysis was therefore conducted to elucidate the role of particle size in these losses, as flotation response is strongly size-dependent. This approach provides insights into whether losses are primarily due to fine metallic particles reporting to the overflow via entrainment or due to coarse partially liberated particles being lost through true flotation, both of which are influenced by size and surface characteristics.

6.5.1. Overflow metal losses of 0.075–0.250 mm size fraction

Test Run #3 and Run #14 were repeated in duplicate, and a detailed size-by-size analysis was performed on the flotation products from each test. The analysis focused on two size fractions: 0.125–0.250 mm and 0.075–0.125 mm. The resulting data on metal losses to the overflow are presented in **Figure 6. 11**.

The results presented in **Figure 6. 11** reveal a clear size-dependent trend in metallic particle losses to the overflow. Coarse-sized metallic particles (0.125–0.250 mm) experienced significantly higher overflow losses compared to the intermediate-sized metals (0.075–0.125 mm). Increasing the pulp solids concentration from 6 wt.% to 14 wt.% led to a pronounced rise in metallic overflow losses for both size classes, with the effect being particularly severe for the coarse-sized metals. As previously discussed, in these size ranges, true flotation of poorly liberated particles is expected to constitute the dominant loss mechanism, with entrainment being negligible in these size ranges.

However, the observed metallic losses, particularly during Run #14 with high cell hydrodynamics and a high solids concentration, far exceed what would be expected from true flotation alone, with metal losses reaching 41.8% for the coarse fraction and 18.35% for the intermediate-sized fraction. These findings are inconsistent with the established high degrees

DOI: 10.14750/ME.2026.030

of metal liberation within these size ranges and contradict the unfavorable conditions for true flotation identified in earlier discussions.

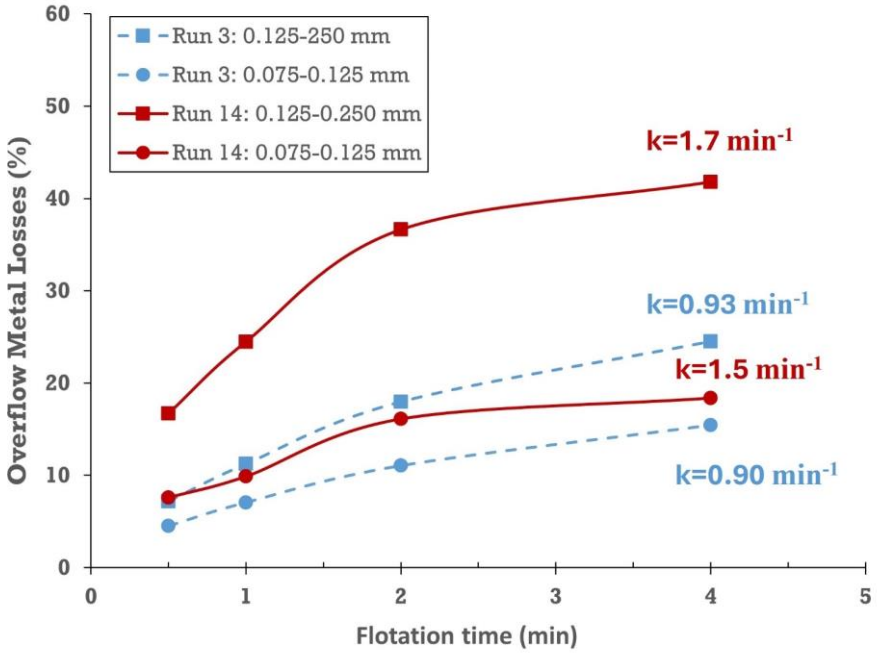

Figure 6. 11: Size-by-size metal losses to overflow at low and high solids concentrations, including rate constants from the Klimpel kinetic model. (Run #3: N= 1375 rpm, Q_a= 3 L/min, X= 6 wt.%; Run #14: N= 1375 rpm, Q_a= 3 L/min, X= 14 wt.%).

Further insights are provided by flotation kinetics analysis using the Klimpel model (detailed model fitting procedures and selection criteria can be found in **Appendix III, Figure C. 5**). The flotation rate constant derived from the model indicates that at higher pulp solids (14 wt.%), metallic particles are lost at a significantly fast rate, with approximately 60% of metal losses occurring within the first minute of flotation. Notably, the flotation rate constant for coarse-sized metals (0.125-0.250 mm) nearly doubled compared to lower solids concentrations. The dominant mechanism responsible for these losses is best described as mass-pull-driven mechanical entrapment, where metallic particles are physically carried into the froth phase due to the upward bulk transfer of naturally floatable nonmetals. However, the unexpectedly high extent and rapid rate of metal losses observed under elevated solids concentrations (particularly in Run #14) suggest that this mechanism is amplified by high pulp viscosity.

Under high solids of 14 wt.%, the pulp exhibits significantly increased apparent viscosity, which alters the flow regime within the flotation cell. These rheological conditions hinder the settling of dense metallic particles and reduce drainage within the froth. As a result, the upward movement of floatable material becomes more effective at sweeping and retaining suspended

DOI: 10.14750/ME.2026.030

non-floatable particles, such as metals in the 0.075–0.250 mm size range, which are too large to be entrained but follow the bulk drag under viscous suspension. The flat, elongated geometry of metallic particles likely exacerbates this effect, as such shapes are less prone to drain back into the pulp, increasing their susceptibility to mechanical entrapment.

In effect, viscosity acts as a mechanical facilitator of mass-pull entrapment: it suspends metallic particles within the rising pulp–froth mixture longer and enhances their probability of being physically trapped into the froth structure, accounting for the disproportionate metal losses under high-solids conditions. It also clarifies why metal losses exhibit rapid flotation-like kinetics without any surface-based interaction; what is observed is not flotation but fast mechanical entrapment under viscous bulk transport.

Microscopic examination of the overflow product confirms this, revealing fully liberated metallic particles, as shown in **Figure 6. 12**. These observations strongly indicate that, under high-solids conditions, metal losses are primarily caused by bulk-phase mechanical entrapment, which is driven by mass-pull and facilitated by high pulp viscosity.

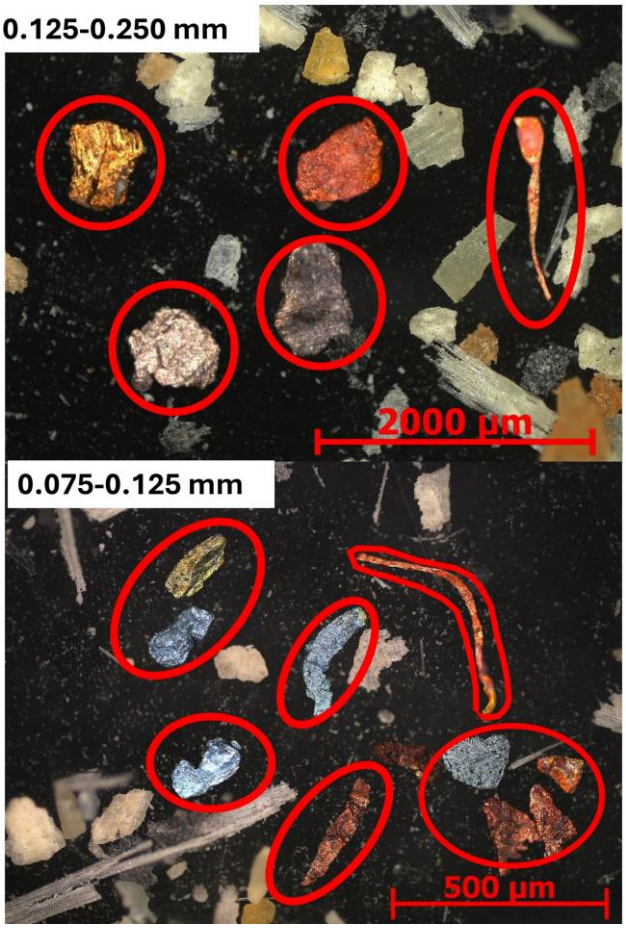

Figure 6. 12: Representative examples of entrapped, fully liberated metallic particles observed in overflow product samples at a 14 wt.% solids concentration.

DOI: 10.14750/ME.2026.030

6.5.2. Overflow metal losses of <0.075 mm size fraction

In the previous section, it was demonstrated that metallic particles in the 0.075–0.250 mm range are predominantly lost to the overflow through mechanical entrapment driven by mass-pull effects at high solids concentration. This raises an important question: do finer metallic particles below 0.075 mm exhibit a similar response even under lower pulp solids conditions, or are their losses primarily governed by entrainment? Unlike their coarser particles, fine particles (<0.075 mm) are known to behave differently within the flotation system due to their low settling rates, increased surface area, and enhanced susceptibility to following water into the froth. These differences warrant a separate analysis to determine whether the mechanisms are responsible for their overflow losses.

Following this line of inquiry, tests Run #1, Run #3, Run #12, and Run #14 were repeated in duplicate, with a detailed size-by-size analysis conducted on the flotation products, specifically targeting metals in the <0.075 mm size range. These tests were selected to represent conditions expected to maximize and minimize metal losses within the <0.075 mm size range, as well as to capture the extremes in overflow water recovery. The resulting data, presented in **Figure 6. 13**, include the temporal profiles of metal losses and corresponding flotation kinetics for the <0.075 mm size fraction, alongside water recovery trends and their kinetic behavior under each test condition.

Figure 6. 13a illustrates a wide range in metal losses to the overflow for the <0.075 mm size fraction, with values increasing markedly from 14.09% under Run #1 (low cell hydrodynamics, 6 wt.% solids concentration) to a peak of 59.72% under Run #14 (high cell hydrodynamics, 14 wt.% solids). A particularly noteworthy observation is that metal losses under Run #3 exceeded those of Run #12, despite the water recovery for Run #12 being nearly double, as seen in **Figure 6. 13b** (21% versus 11%). This indicates that within this fine size fraction, metal losses are more sensitive to cell hydrodynamics than to water recovery.

Overall, the observed metal loss is unexpectedly high. Given the low metal grade in this size fraction (approximately 1.5%) and the inherently nonselective nature of entrainment, much lower losses would typically be anticipated. However, the calculated entrainment indices (ENTi), which range from 1.9 to 8, far exceed the theoretical maximum of 1 for entrainment. This indicates the presence of additional loss mechanisms beyond simple water carryover. Supporting this observation, the flotation rate constants (k-values) for metals reporting to the

DOI: 10.14750/ME.2026.030

overflow in this fraction surpass those of water, which serves as the benchmark for the entrainment contribution of hydrophilic particles during flotation.

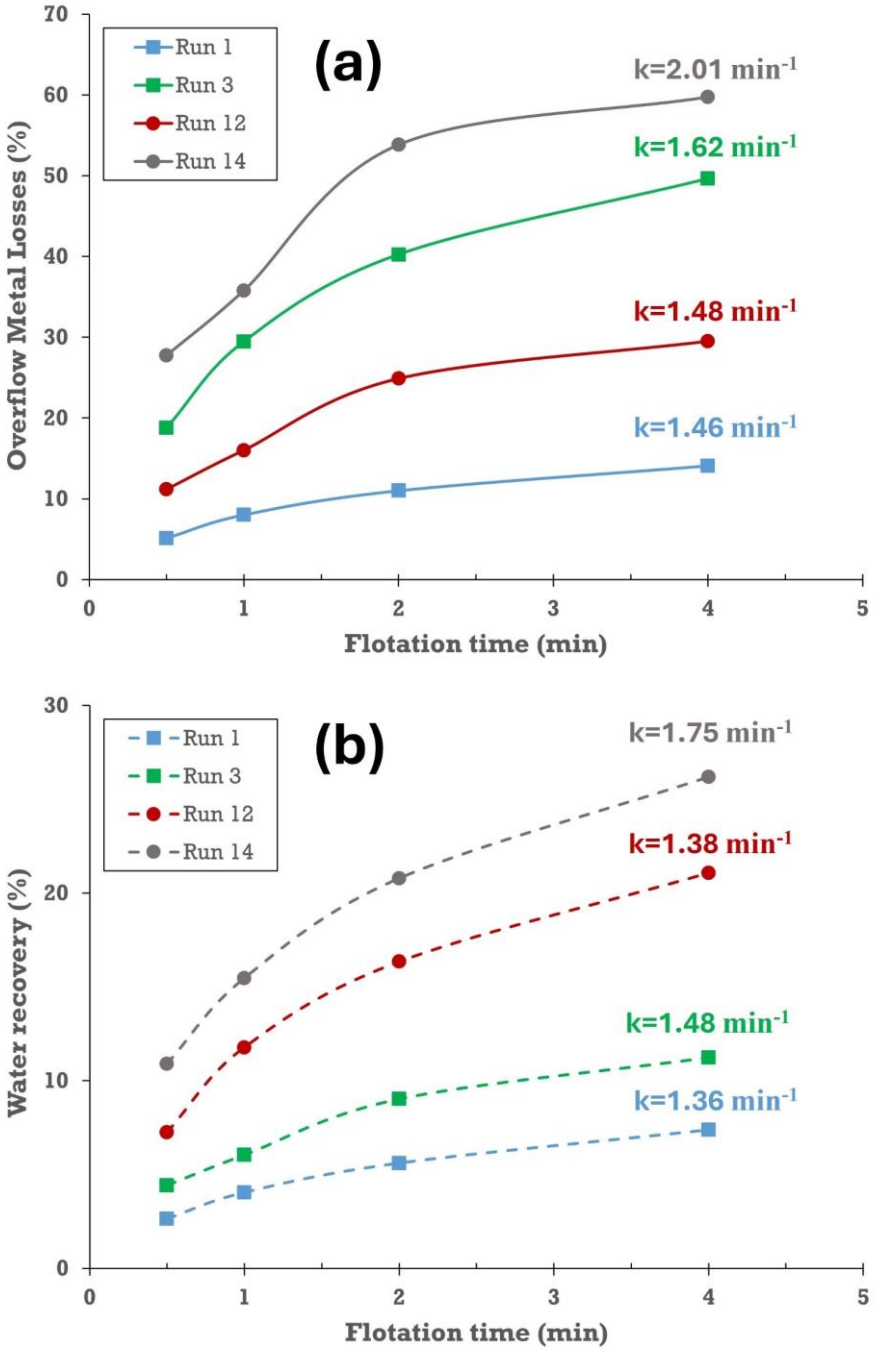

Figure 6. 13: (a) Overflow losses and kinetics of <0.075 mm metals and (b) Water recovery and kinetics under the varying flotation conditions. (Run #1: N= 1250 rpm, Q_a= 2 L/min, X= 6 wt.; Run #3: N= 1375 rpm, Q_a= 3 L/min, X= 6 wt.%; Run #12: N= 1250 rpm, Q_a= 2 L/min, X= 14 wt.; Run #14: N= 1375 rpm, Q_a= 3 L/min, X= 14 wt.%).

Further insights are provided through the application of the Kelsall model, which distinguishes between fast- and slow-floating fractions, allowing for an assessment of the relative contribution of entrainment. **Table 6. 7** summarizes the model parameters (θ, k_s, and k_f) and

DOI: 10.14750/ME.2026.030

indicates that, under high-solids conditions, the proportion of metal losses attributed to the slow-floating fraction, typically associated with entrainment, does not exceed 5% of the total. This finding aligns with earlier findings for coarser particles, where rapid losses under high-viscosity, poor-drainage conditions were linked to mass-pull-driven mechanical entrapment. Notably, this mechanism persists for fine particles even in the absence of high solids or elevated viscosity. For instance, under the most diluted condition studied (Run #1), slow-floating particles account for less than 37% of total metal loss.

Table 6. 7: Kelsall model parameters and predicted losses under selected test runs.

Run	θ	k_f (min^{-1})	k_s (min^{-1})	Fast losses (%)	Slow losses (%)
#1	0.91	1.37	0.015	8.90	5.19
#3	0.65	1.30	0.065	34.62	15.00
#12	0.71	0.85	0.005	28.17	1.35
#14	0.46	1.18	0.04	53.10	6.63

To further validate the understanding of the origin of fast-floating losses in fine-sized metals and to establish a more definitive assessment of the contribution of entrainment based on water recovery, additional investigative methods were employed.

Although the SEM-EDS-based liberation analysis presented in **Section 4.3.2** suggested that metals within the <0.075 mm fraction are nearly fully liberated, this finding may not fully reflect the complexity of the particles. As highlighted by Otsuki et al. [275], partial liberation can persist even at fine sizes, with minor inclusions of nonmetallic materials embedded within metal particles potentially escaping detection through conventional imaging techniques. Consequently, it was essential to assess the surface nature of these metal particles to better understand the extent to which true flotation might contribute to their losses in the overflow phase.

The two-liquid flotation method offered a valuable tool in this regard. This technique provides insight into particle hydrophobicity by separating the sample into a hydrophobic n-heptane phase and a hydrophilic aqueous phase. By weighing each phase and analyzing their chemical compositions, a semi-quantitative understanding of the surface affinities of the particles can be established.

The outcomes of the two-liquid flotation experiments conducted on the fine fraction (<0.075 mm) of the WPCB flotation feed are summarized in **Table 6. 8**. Upon completion of the procedure, the upper layer contains n-heptane with hydrophobic particles, while the lower layer

DOI: 10.14750/ME.2026.030

consists of hydrophilic particles (**Figure C. 6**, **Appendix III**). Results in **Table 6. 8** indicate that 2.77% of metals are present in the upper hydrophobized phase, suggesting the existence of locked metallic particles within this fraction, as supported by similar findings in previous studies, such as Ogunniyi et al. [59]. The observed standard deviation of 1.71% further highlights the variability and complexity of the material.

Table 6. 8: Distribution of metals between hydrophobic and hydrophilic phases in two-liquid flotation of WPCB flotation feed fine fraction (<0.075 mm).

Analyte	Hydrophobic phase (%)	Hydrophilic phase (%)	Standard deviation (%)
Total metals	2.77	97.23	±1.71

However, while these results support the presence of hydrophobic components, the extrapolation of such behavior to conventional froth flotation must be approached cautiously. The two-liquid method does not replicate the full complexity of flotation dynamics, particularly the role of bubble-particle interactions and turbulence within the flotation cell.

To further contextualize the contribution of entrainment, a complementary analysis was conducted following the methodology outlined by Ross [228] (see **Section 3.5.6**). **Table 6. 9** summarizes the estimated contributions of entrainment based on water recovery and presents an upper-bound estimate of the combined maximum contributions from both entrainment and true flotation. This estimate is obtained by summing the highest estimated water-driven entrainment with the maximum true flotation recovery inferred from two-liquid tests. Despite this generous upper limit, the combined mechanisms still fall significantly short of accounting for the total metal losses observed experimentally in this size fraction. Additionally, the discrepancy between the estimated and actual loss values becomes increasingly pronounced under conditions of high cell hydrodynamics.

Table 6. 9: Estimated contribution of entrainment and true flotation to fine-sized metal losses.

Run	Entrainment contribution (%)	Combined Entrainment and True Flotation (%)	Experimental losses (%)
#1	6.99	11.99	14.09
#3	9.75	14.75	49.62
#12	18.66	23.66	29.41
#14	20.12	25.12	59.64

DOI: 10.14750/ME.2026.030

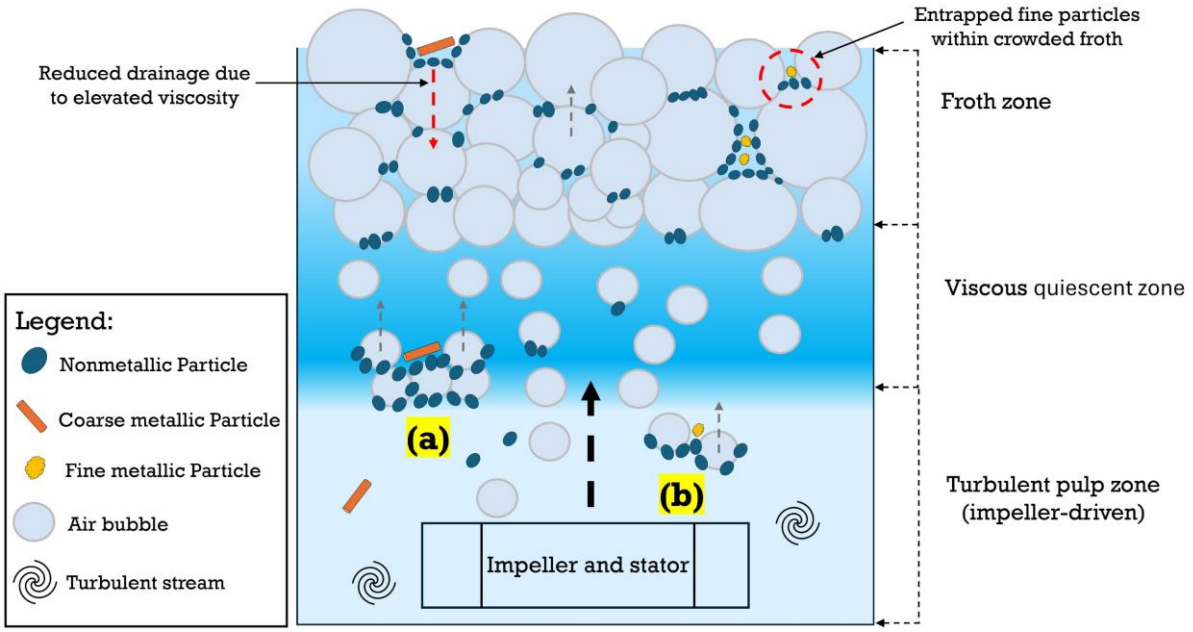

Figure 6. 14: Schematic of the dual-mechanism model for metallic particle losses during the reverse flotation of WPCBs. (a) Under high-solids, high-viscosity conditions, coarse and intermediate particles (0.075–0.250 mm) become suspended in the quiescent zone and are mechanically entrapped in the froth (viscosity-enhanced entrapment). (b) Under dilute, turbulent conditions near the impeller, fine particles (<0.075 mm) are lifted by bulk upward flow and carried into the froth, regardless of viscosity (viscosity-independent entrapment).

When viewed collectively, the findings reveal a clear pattern concerning the loss mechanisms of fine-sized metallic particles (<0.075 mm). The unexpectedly high metal losses, rapid flotation-like kinetics, and limited contributions from both entrainment and true flotation suggest the presence of a distinct mechanism. Specifically, these losses can be best explained by a viscosity-independent mechanical entrapment, in which liberated fine metallic particles are mobilized and physically swept into the froth by the bulk upward flow, especially under high cell hydrodynamics. This mechanism differs fundamentally from water-driven entrainment, as it is not governed by water flow but rather by nonselective bulk phase movement. Unlike the coarser metal particles (0.075-0.250 mm), where viscous drag under high solids is the main facilitator of mechanical entrapment, the fine particle regime exhibits this mechanical loss pathway even under dilute, low-viscosity conditions. Accordingly, a dual-mode loss model is proposed (**Figure 6. 14**): (1) viscosity-enhanced mechanical entrapment affecting coarse particles under high solids conditions, and (2) viscosity-independent mechanical entrapment dominating fine particles due to their low inertia and high mobility within the pulp phase. Both mechanisms are mass-pull driven, nonselective, and distinct from entrainment or true flotation. They highlight the critical influence of cell hydrodynamics and pulp flow behavior on the recovery of metallic particles in WPCB flotation.

6.6. Conclusions

This investigation into the reverse flotation of WPCBs reveals complex relationships between flotation variables and flotation performance. Pulp solids concentration emerges as a key factor influencing process outcomes, with its critical impact evident from preliminary variable-level selection. Initial testing showed that extreme solids loading (<6 wt.% or >14 wt.%) either hinders froth formation or induces pulp viscosity and stagnation. At low to moderate solids loading (6–10 wt.%), the interplay of cell hydrodynamics demonstrates a clear trade-off between maximizing overflow yield and underflow metal recovery. Specifically, overflow yield increases from 56.44% at 6 wt.% to 79.59% at 10 wt.%, while underflow metal recovery decreases from 87.52% at 6 wt.% to 60.10% at 10 wt.%. However, at high solids concentrations, flotation performance is significantly impaired, resulting in reduced nonmetal rejection (73.10% overflow yield) and increased metal losses (60.57% recovery).

A more nuanced analysis, moving beyond generalized trends in total metal recovery, reveals that metal-specific factors such as liberation characteristics, particle morphology, and size distribution influence individual responses to flotation conditions. While copper exhibited the highest recovery (up to 94%) with a broad recovery range of 25% and responded linearly to increasing solids concentration, gold displayed distinct quadratic behavior, achieving recoveries of 84% but requiring different optimal conditions. Process optimization scenarios illustrate these trade-offs: maximizing copper recovery necessitates 9 wt.% solids (83.7% Cu, 66% Au), while optimizing for gold demands 12 wt.% solids (73% Au, 81% Cu). This underscores the limitations of mass-based assessments when the goal is to optimize for value.

The rheological transitions observed, from Newtonian behavior at ≤10 wt.% solids to non-Newtonian, yield-stress-dominated regimes at higher concentrations, provide a critical perspective for interpreting flotation performance. The sharp apparent viscosity rise from 4.85 mPa·s at 10 wt.% to 16.00 mPa·s at 14 wt.% explains the collapse in overflow yield, as turbulent energy became confined to impeller-proximal zones, impairing bubble dispersion and nonmetal recovery. This rheological shift also increased metal losses through two distinct mass-pull-driven mechanisms: (i) viscosity-enhanced mechanical entrapment of coarse liberated metals (0.075–0.250 mm), suspended and swept into the froth by poor drainage; and (ii) viscosity-independent mechanical entrapment of fine metals (<0.075 mm), mobilized by bulk upward flow.

DOI: 10.14750/ME.2026.030

Overall, optimizing reverse flotation of WPCBs will require dynamic control of pulp solids concentration to remain within hydrodynamically favorable regimes while mitigating pulp rheological challenges to avoid metal mass-pull mechanical entrapment-induced losses and designing metal-specific flotation strategies that account for the diverse behaviors of critical metallic constituents.

DOI: 10.14750/ME.2026.030

Chapter 7: Mitigating Rheological Challenges in the Flotation of WPCB

7.1. Introduction

Despite significant advancements in metal recovery and separation efficiency from WPCBs through flotation, often using promising pretreatment strategies [147, 186, 222], a notable gap remains in current research. Existing studies have largely overlooked the critical role of pulp rheological properties, typically maintaining solids concentrations below 10 wt.%. While these dilute pulps effectively minimize adverse rheological effects by ensuring low viscosities and yield stresses, they compromise flotation throughput and productivity, posing a substantial limitation for industrial scaling [216, 217].

As demonstrated in **Chapter 6**, the reverse flotation of WPCBs is significantly influenced by the rheological characteristics of the pulp, particularly under elevated solids conditions (14 wt.%), which are considered high by WPCB flotation standards. In these conditions, increased pulp viscosity directly affects both overflow yield and underflow metal recovery, shaping the overall selectivity and efficiency of the process. Similar challenges are well-documented in the broader field of mineral processing, especially with the increased use of low-grade and complex ores, including clay-rich or fibrous materials [176]. In these systems, the required extensive fine grinding to liberate valuable components often introduces complex rheological issues that hinder efficient flotation [208].

Various strategies have been explored to mitigate these issues. One physical approach involves removing ultrafine fractions prior to flotation. Chemically, the negative rheological impact can be reduced by applying rheology modifiers, which alter surface properties and influence interparticle interactions and pulp rheology. This chapter investigates both physical and chemical strategies, with the physical approach focusing on the removal of selected ultrafine fractions before flotation. The chemical approach examines grinding under alkaline conditions, drawing upon recent findings that demonstrate the capacity of alkaline treatments to modify the surface properties of polymeric materials through specific chemical interactions, such as breaking chemical bonds in resins and plastics, thereby improving wettability [140, 147, 276, 277].

Building on the findings from the preceding chapter regarding the practical upper limit of solids concentration in WPCB flotation systems, this chapter explores the feasibility of selected physical and chemical strategies to address rheological constraints. It focuses on understanding the underlying mechanisms and evaluating their potential benefits. The outcomes contribute to

DOI: 10.14750/ME.2026.030

the development of more effective pretreatment strategies that reduce metal losses and improve flotation efficiency under challenging rheological conditions.

7.2. Physical Pretreatment: Ultrafine (<0.032 mm) Removal from Flotation Feed

7.2.1. Effect on pulp rheology

As established in **Chapter 6**, a high solids concentration of 14 wt.% in the WPCB flotation suspension increases pulp viscosity and yield stress, thereby hindering flotation performance. To address these effects, a physical pretreatment approach was evaluated that involved removing the <0.032 mm fraction from the flotation feed. This fraction constituted approximately 34 wt.% of the feed mass but contained only about 3 wt.% of the total metal, corresponding to an overall metal grade of 0.33%. Based on current market prices, the total metal value in this fraction was around USD 450 per tonne, confirming its limited economic significance.

Rheological measurements comparing the original <0.250 mm and the modified 0.032–0.250 mm flotation feeds are presented in **Figure 7. 1**. The 0.032–0.250 mm suspension exhibits a weakly non-Newtonian behavior, with a reduced yield stress of 0.10 Pa compared to the 0.35 Pa observed in the original feed. Notably, the apparent viscosity at a shear rate of 100 s^{-1} decreased significantly from 16.0 mPa·s to 5.13 mPa·s following the removal of the ultrafine fraction.

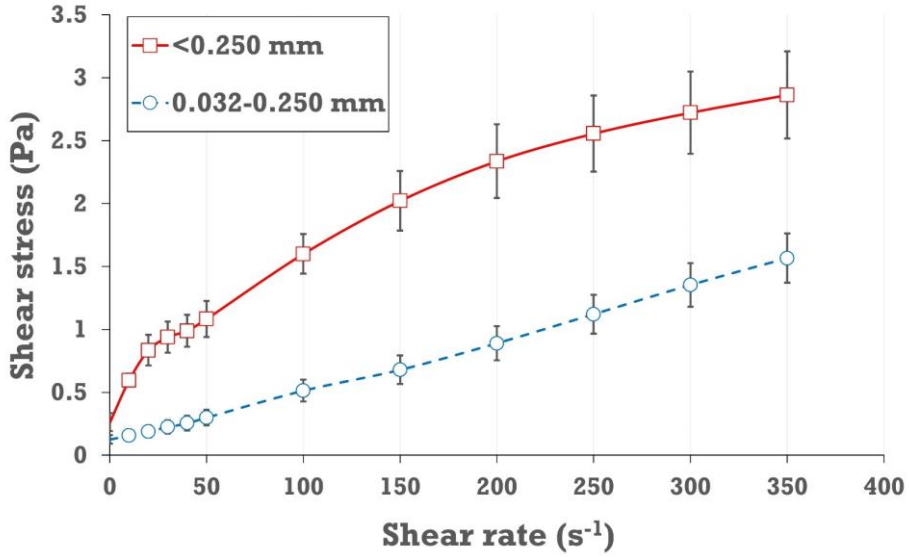

Figure 7. 1: Rheological behavior of original (<0.250 mm) and modified (0.032–0.250 mm) WPCB flotation feeds at 14 wt.% solids.

Although the removal of particles smaller than 0.032 mm increased the volumetric solids concentration from 8.7% to 10.6%, both yield stress and apparent viscosity decreased

DOI: 10.14750/ME.2026.030

significantly. This indicates that ultrafine particles disproportionately contribute to the rheological properties of WPCB suspensions. Their small size and high specific surface area facilitate the formation of dense interparticle contact networks. This observation aligns with established rheological models, which demonstrate that a decrease in particle diameter, at comparable solids loadings, results in denser structures and stronger particle-particle interactions [278]. Furthermore, the persistence of yield stress in the modified feed suggests that the aggregated structures responsible for the initial resistance to flow are not limited to the ultrafine fraction; they also involve interactions among the coarser particles.

7.2.2. Effect on flotation performance

The impact of ultrafine removal on flotation performance was assessed through comparative flotation tests conducted at 14 wt.% pulp solids, using both the original flotation feed (<0.250 mm) and the modified feed (0.032–0.250 mm). **Figure 7. 2** presents the underflow metal recovery across individual size fractions for each feed condition.

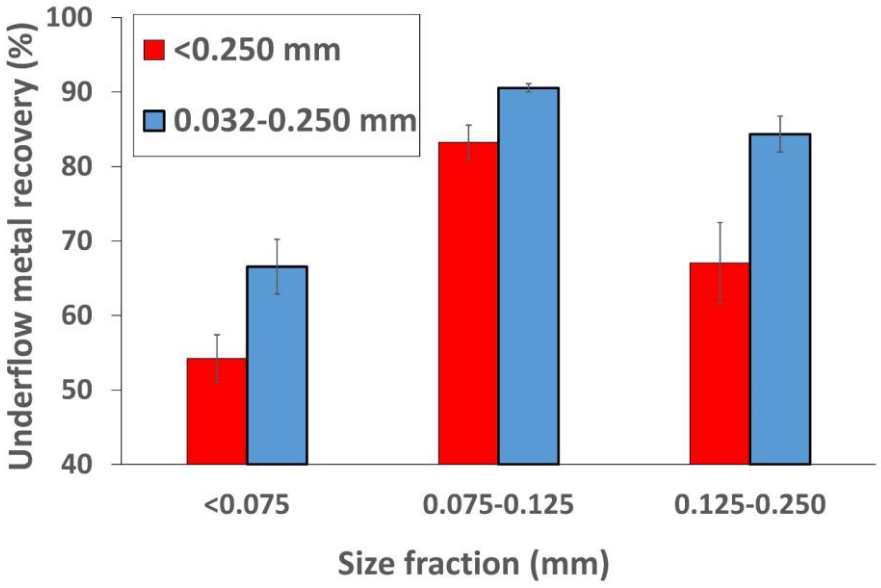

Figure 7. 2: Underflow metal recovery per size fraction for original (<0.250 mm) and modified (0.032–0.250 mm) WPCB flotation feeds at 14 wt.% solids.

As shown in **Figure 7. 2**, the modified feed (0.032–0.250 mm) improved metal recovery across all size fractions. This enhancement was most pronounced in the coarsest fraction (0.125–0.250 mm), where recovery increased from 67.05% for the original feed to 84.35% with the modified feed. The finest size fraction (<0.075 mm) also showed a marked improvement, with recovery rising from 54.23% to 66.55%. Overall metal recovery increased from 68.48% for the original feed to 83.64% for the modified feed, while overall separation efficiency improved from

DOI: 10.14750/ME.2026.030

42.66% to 54.78%. In addition to these overall and size-wise recovery improvements, **Figure 7. 3** illustrates the impact of the modified feed on the recovery of individual metal species. All metal species showed improved recovery, with notable gains for metals concentrated in both the coarse size fraction, such as copper, and the fine fraction, such as gold.

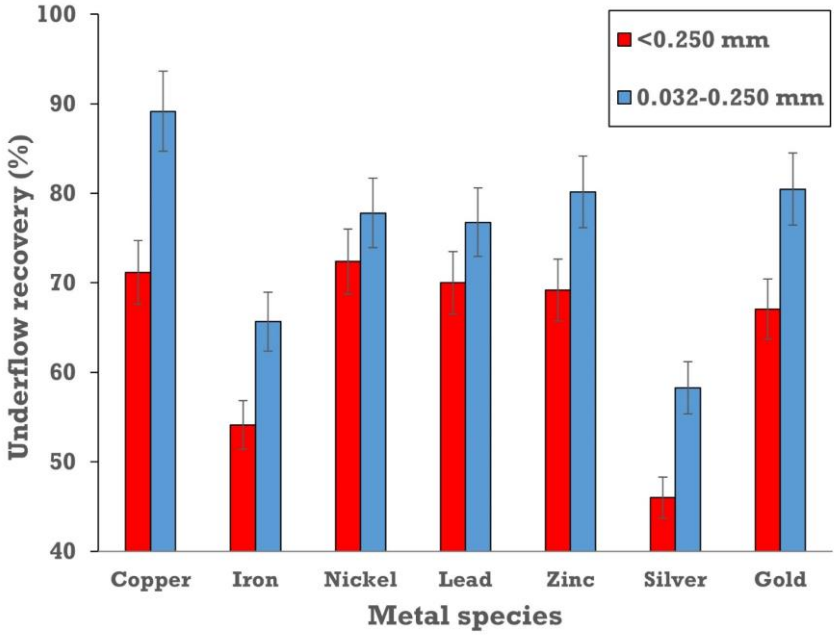

Figure 7. 3: Underflow recovery of individual metal species using original (<0.250 mm) and modified (0.032–0.250 mm) WPCB flotation feeds at 14 wt.% solids.

This enhancement results from rheological improvements achieved by removing the <0.032 mm fraction. As established in **Section 6.5**, metal losses under elevated solids concentrations in WPCB (14 wt.%) were primarily driven by mechanical entrapment associated with high slurry viscosity. The original feed exhibited an apparent viscosity of 16.00 mPa·s at 100 s^{-1}, which severely hindered flotation selectivity by promoting nonselective entrapment of metals in the froth. In contrast, the modified feed, with a reduced viscosity of 5.13 mPa·s, suppressed this mechanism, thereby improving the selective retention of metals in the underflow.

Despite these clear advantages in metal recovery, the flotation response in terms of overflow yield showed only marginal improvement. The overflow yield increased from 62.29% with the original feed to 66.05% with the modified feed, suggesting that nonmetal recovery to the overflow remained limited.

This modest gain contrasts with the expected response based on slurry viscosity. As shown in **Section 6.4.2**, high pulp viscosities impair cell hydrodynamics by reducing air dispersion and bubble mobility, which limits nonmetal separation. The viscosity reduction achieved with the

DOI: 10.14750/ME.2026.030

modified feed should, in principle, relieve this constraint. However, the limited increase in overflow yield suggests the involvement of other mechanisms.

Flotation tests were conducted under similar viscosity conditions: the modified feed at 14 wt.% (5.13 mPa·s) and the original feed at 10 wt.% (4.85 mPa·s). Despite comparable suspension rheology, the froth characteristics differed notably. As shown in **Figure 7. 4**, the froth from the modified feed had larger bubbles and a reduced volume, indicating bubble coalescence and diminished froth stability.

The decline in froth stability results from the absence of the <0.032 mm size fraction in the modified flotation feed. Particles in this range occupy the air–liquid interface and form a rigid film around bubbles, reducing coalescence and preserving froth volume. By restricting movement at the three-phase contact line, they maintain a higher bubble surface area and create a mechanical barrier that prevents thin film rupture [279, 280]. Similar findings by Aktas et al. [281] demonstrated that particles around 0.030-0.040 mm significantly enhanced froth stability at low air rates. In their absence, bubbles coalesce more readily, grow larger, and drain faster, explaining the larger bubbles and reduced froth volume observed with the modified feed.

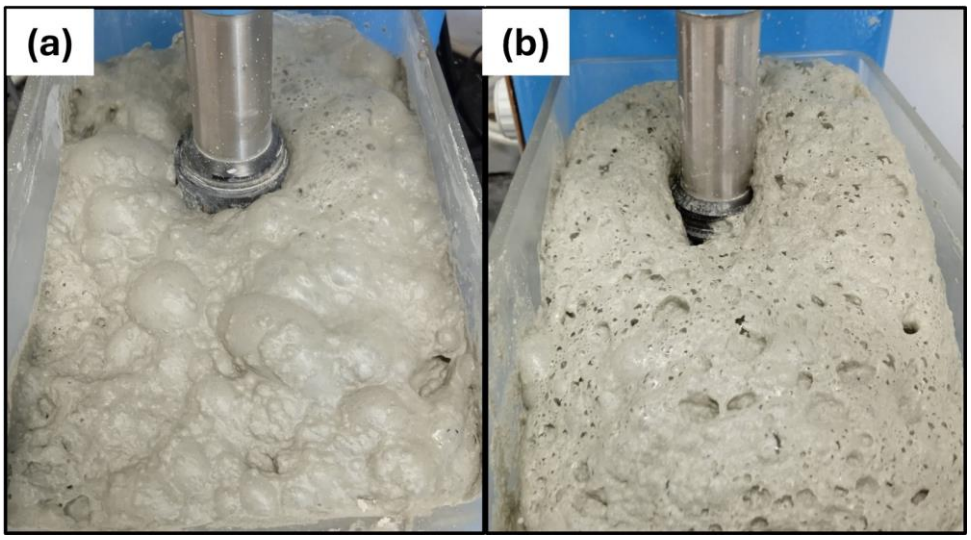

Figure 7. 4: Froth formation during the first minute of aeration for (a) modified (0.032–0.250 mm) feed at 14 wt.% solids and (b) original (<0.250 mm) feed at 10 wt.% solids.

These findings suggest that removing ultrafines from the flotation feed effectively mitigates pulp rheological challenges and improves metal recovery, but it also disrupts froth structure. This froth instability limits nonmetal rejection and caps separation efficiency, which, despite improvements, has plateaued at 54.78%. It is important to note that the separated <0.032 mm fraction, while exhibiting lower metal content, remains a viable flotation feed that could be processed independently under optimized conditions tailored to ultrafine flotation kinetics.

DOI: 10.14750/ME.2026.030

Increasing the frother dosage could theoretically restore froth stability; however, this adjustment involves trade-offs. Studies by Vidyadhar and Das [143] indicate that higher frother dosages may enhance froth stability but can also lead to increased metal losses to the overflow, undermining gains in underflow metal recovery. While removing ultrafine particles improves suspension rheology and metal recovery, its broader implications require careful consideration.

7.3. Chemical Pretreatment: Grinding Under Alkaline Conditions

7.3.1. Effect on functional groups in nonmetals of WPCB

The chemical transformations caused by alkaline conditions during grinding are essential for understanding process behavior. Alkaline media, whether introduced as dry NaOH powder or dissolved in water, can interact with the polymeric matrix of WPCB nonmetals, potentially altering chemistry and surface properties in ways that affect both grinding response and downstream flotation performance.

As shown in **Figure 7. 5**, the FTIR analysis of nonmetal samples from WPCBs revealed several characteristic peaks. The peaks at 1507 cm^{-1} and 1463 cm^{-1} correspond to C=C stretching and CH_3 bending modes typical of aromatic rings [152]. The peak at 1246 cm^{-1} indicates C-O stretching, while those at 1178 cm^{-1} and 1015 cm^{-1} represent C-O functionalities commonly found in organic materials, particularly those with ether linkages [151, 222, 282]. The overall spectrum indicates that the functional groups identified in the nonmetal samples closely match those typically found in epoxy resins, which dominate the polymeric content of WPCBs.

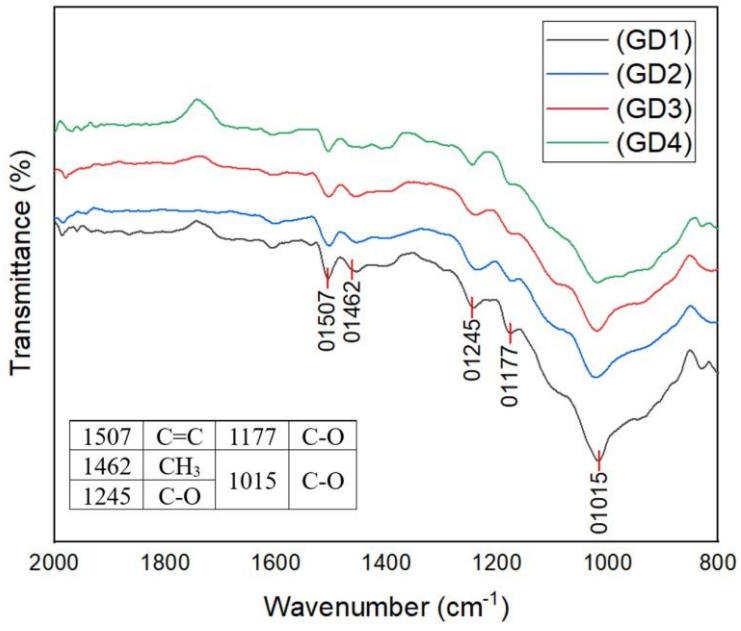

Figure 7. 5: FTIR spectra of WPCBS nonmetals following dry grinding under alkaline conditions.

DOI: 10.14750/ME.2026.030

The FTIR spectra in **Figure 7. 5** reveal distinct chemical transformations in the nonmetallic fraction of WPCBs following dry grinding under alkaline conditions. Comparing the spectra from the standard dry grinding condition (GD1) with those subjected to progressively higher alkaline dosages (GD2–GD4) shows clear variations in transmittance, particularly in regions associated with resin-based functional groups. Notably, bands related to aromatic structures, such as those linked to the benzene ring, exhibit increased transmittance under alkaline conditions. A prominent example is the peak at 1015 cm^{-1}, which rises steadily from 66.71% under GD1 to 74.37% (GD2), 81.72% (GD3), and peaks at 86.20% (GD4, 1 wt.% NaOH). These spectral shifts suggest a relative reduction in specific functional groups or a reorganization of the resin matrix, indicating that alkaline pretreatment facilitates chemical reactions that disrupt the polymer backbone.

This disruption likely involves the cleavage of ether bonds connecting benzene rings in the epoxy resin. This cleavage creates free bonds on the benzene rings, which readily adsorb hydroxyl groups (-OH) from the alkaline medium, leading to enhanced surface hydroxylation, an effect known to improve water–particle interaction [147]. These observations are not limited to dry grinding; as shown in **Figure 7. 6**, similar spectral shifts were also noted under wet alkaline grinding conditions. Notably, the transmittance at 1015 cm^{-1} increased with alkalinity, reaching 80.21% under GW6. Although this trend mirrors that observed in dry grinding, the lower maximum transmittance underscores the aqueous medium's influence on the extent of chemical transformation, reflecting differences in the reaction environment.

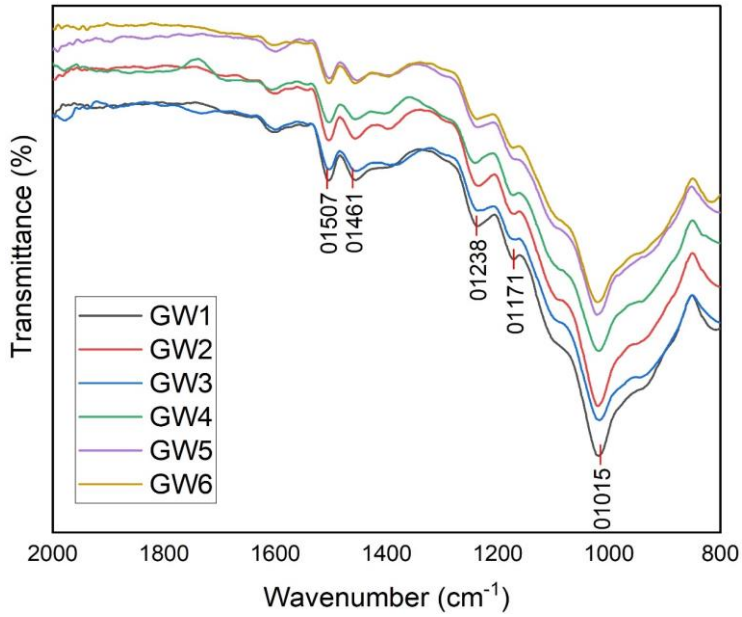

Figure 7. 6: FTIR spectra of WPCBS nonmetals following wet grinding under alkaline conditions.

DOI: 10.14750/ME.2026.030

Support for these structural changes comes from zeta potential measurements (**Figure 7. 7**), which show a progressive increase in negative surface charge under alkaline conditions. In standard dry grinding, the zeta potential measured –30 mV, while in dry grinding with 1 wt.% NaOH (GD4), it decreased to –41.64 mV. Likewise, in wet alkaline grinding at pH 12, the zeta potential shifted to –39.91 mV. This increase in negative charge aligns with the generation of negatively charged surface functional groups, such as newly formed hydroxyl groups. These findings highlight the role of grinding under alkaline conditions in inducing bulk chemical changes that have implications for surface behavior, promoting improved dispersion and flotation performance.

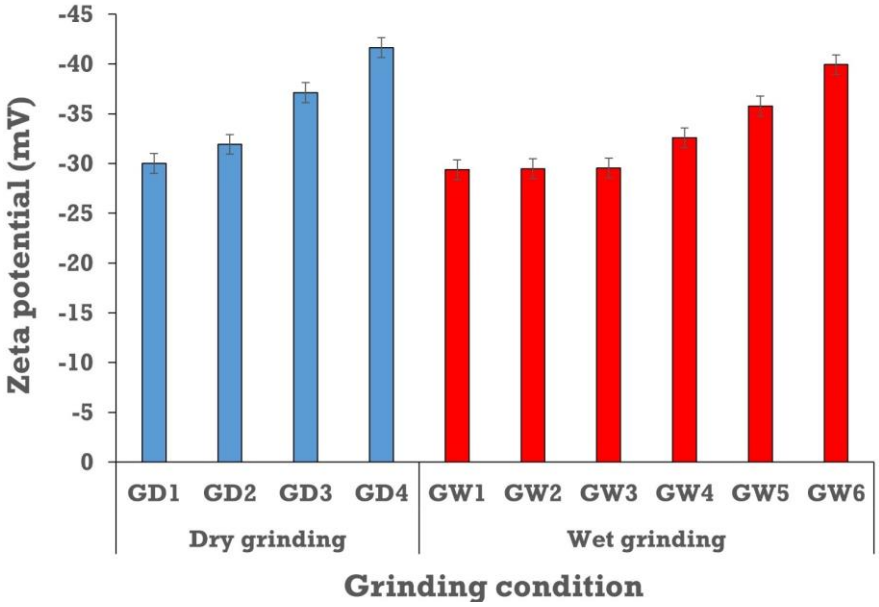

Figure 7. 7: Zeta potential of the WPCB nonmetallic fraction after wet and dry grinding under alkaline conditions.

Building on the observed chemical modifications in WPCB nonmetals, it is essential to consider how alkaline grinding mediates these transformations. The grinding process creates freshly fractured surfaces with increased chemical reactivity due to mechanically induced bond cleavage and elastoplastic stresses at the particle interface, resulting in unsaturated surface sites. These active surfaces stabilize through reactions with their environment, and when grinding occurs under specific chemical conditions, such as in an alkaline medium, the surface activity can enhance interactions, further influencing the material's surface chemistry [237, 283].

In wet grinding under alkaline conditions, the slurry was prepared using NaOH solutions adjusted to target pH levels (pH 8–12). The dissociation of NaOH in water releases ions that interact directly with the hydrophobic resinous components of nonmetal particles during

DOI: 10.14750/ME.2026.030

grinding. FTIR analysis of nonmetal fractions after wet grinding revealed immediate and complete shifts in the functional groups associated with these resins, indicating rapid chemical transformation. Notably, these spectral shifts were consistent when comparing samples analyzed immediately after grinding with those examined after the pre-flotation conditioning stage. As shown in **Figure 7. 8**, both sets of spectra differed from the baseline spectra of nonmetal fractions subjected to standard (non-alkaline) grinding. This observation strongly suggests that the chemical modifications induced by wet alkaline grinding were finalized during the grinding stage, with the conditioning stage introducing no further transformations.

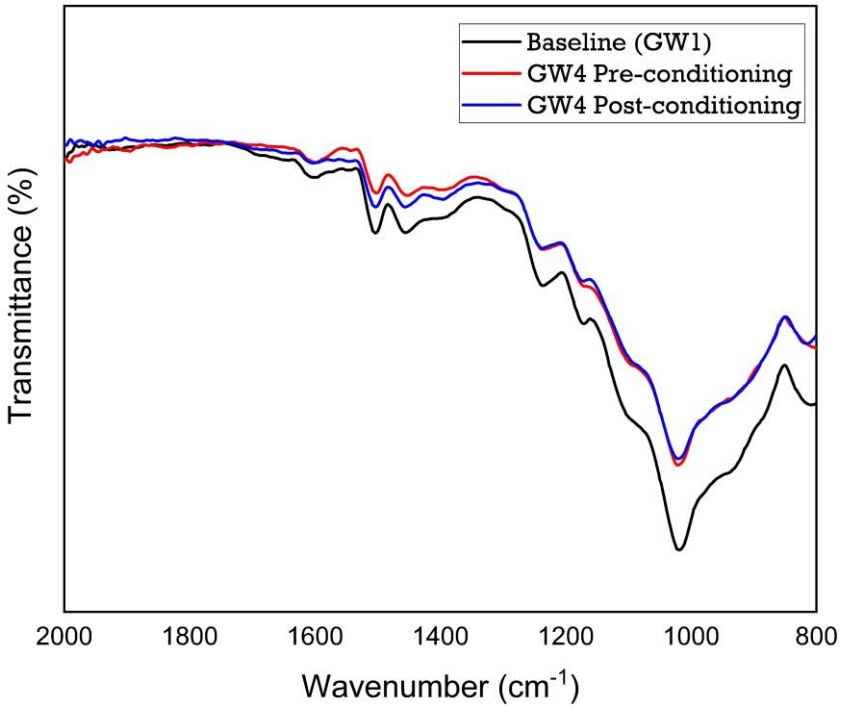

Figure 7. 8: FTIR spectra of nonmetal fractions post-wet grinding under alkaline conditions (pre- and post-conditioning stage).

The dry grinding approach under alkaline conditions revealed a distinct interaction pathway. NaOH was added in powder form at dosages of 0.1 wt.%, 0.5 wt.%, and 1 wt.%. Without an aqueous medium during grinding, the dissociation of NaOH and its interaction with the ground material were limited. Nonetheless, FTIR spectra of nonmetal fractions from dry grinding showed a transitional chemical modification pattern. Partial shifts in functional groups were observed after dry grinding, progressing to complete alignment only after the pre-flotation conditioning stage, as shown in **Figure 7. 9**. This gradual change may be attributed to the hygroscopic nature of NaOH, which can absorb ambient moisture, facilitating limited ionic dissociation and some reactivity with nonmetals. However, the final chemical alignment

DOI: 10.14750/ME.2026.030

occurred only during the pre-flotation conditioning stage, where the addition of water strengthened the interaction.

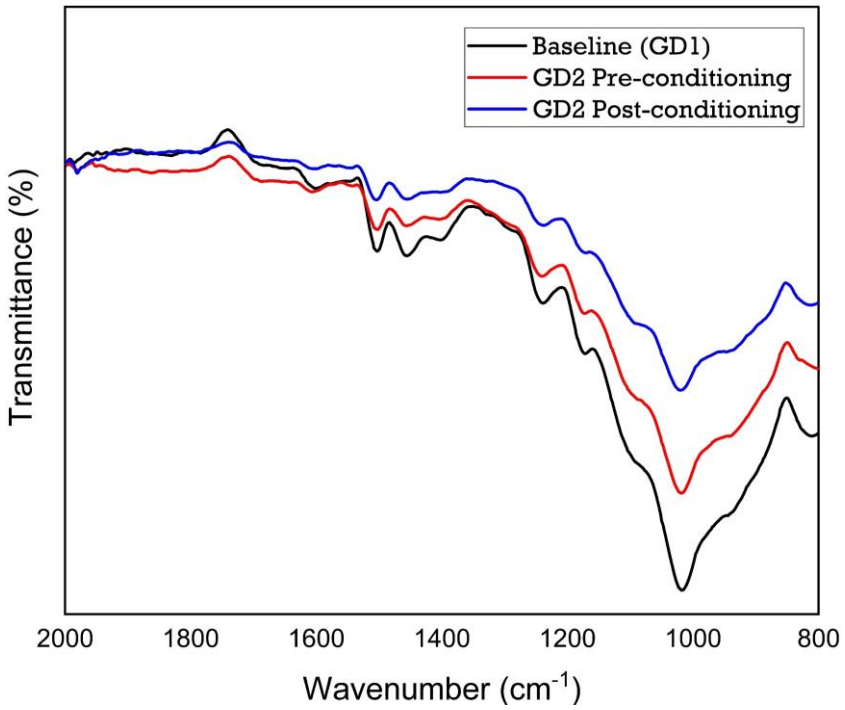

Figure 7. 9: FTIR spectra of nonmetal fractions post-dry grinding under alkaline conditions (pre- and post-conditioning stage).

The differences in chemical behavior between wet and dry grinding under alkaline conditions can be understood by examining pH dynamics during the pre-flotation conditioning phase. As summarized in **Table 7. 1**, wet grinding resulted in minimal pH elevation during conditioning, likely due to the small liquid volume used and the subsequent wet screening step, which may have moderated the pH. In contrast, dry grinding followed by conditioning led to a significant pH increase, enhancing the chemical interactions initiated during grinding and facilitating the final alignment of functional groups observed in the FTIR spectra.

Table 7. 1: pH variation during the pre-flotation conditioning stage following wet and dry grinding under different alkaline conditions.

Grinding condition	Designation	Conditioning stage pH level
Wet	GW2	7.9
	GW3	8.2
	GW4	8.2
	GW5	8.4
	GW6	8.9
Dry	GD2	9.7
	GD3	11.1
	GD4	12.4

DOI: 10.14750/ME.2026.030

These findings highlight the differences between wet and dry grinding in altering the chemistry of nonmetal fractions under alkaline conditions. In wet grinding, the immediate availability of a dissociated alkaline medium allows for rapid and complete chemical modifications during the grinding process. In contrast, dry grinding results in gradual changes, with initial modifications taking place during the grinding phase and further transformations occurring during the pre-flotation conditioning stage when water is introduced.

7.3.2. Effect on grinding efficiency

Building on the demonstrated chemical reactivity of WPCB nonmetals under alkaline grinding conditions, it is important to examine how these transformations might influence the mechanical aspects of grinding. Previous results (**4.3.1**) established that dry grinding achieved superior size reduction compared to wet grinding, primarily due to the differing behaviors of nonmetallic particles in each environment, particularly the aggregation tendencies of hydrophobic nonmetals in aqueous media.

Figure 7. 10 illustrates the effects of alkaline conditions on particle size characteristics during both dry and wet grinding, focusing on X_{80} and the mass percentage passing below 0.250 mm, the operational cut-off size for flotation feed. The X_{80} size during dry grinding (GD1–GD4) remained stable, showing minimal variation despite increasing NaOH dosage. Similarly, the production of the target size fraction (<0.250 mm) fluctuated only slightly, ranging from 68.92% to 70.81%. These results suggest that solid-phase NaOH has limited influence on breakage behavior and the resulting particle size distribution during dry grinding.

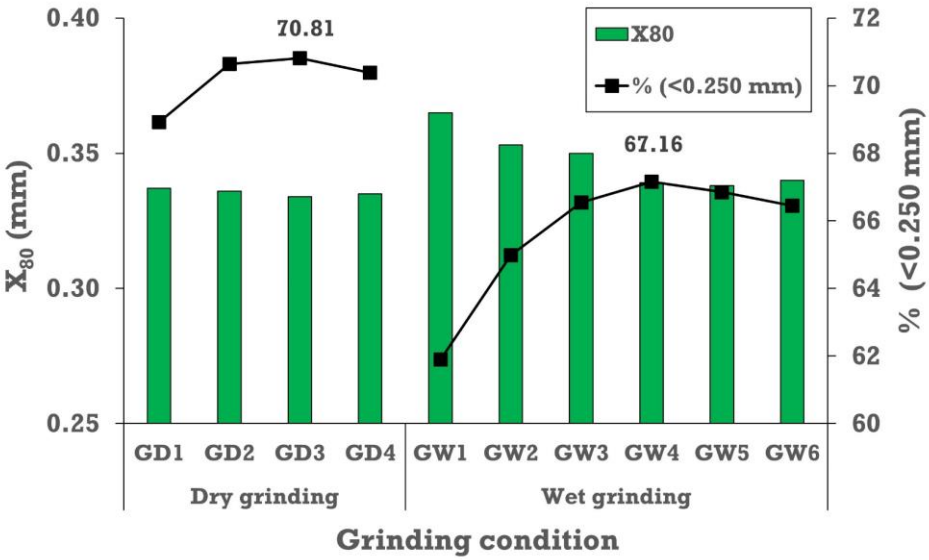

Figure 7. 10: Effect of alkaline conditions during dry and wet grinding on X_{80} and the mass percentage passing below 0.250 mm.

This observation aligns with our earlier findings on chemical interaction pathways under alkaline conditions. In dry grinding, solid-phase NaOH induces only partial shifts in functional groups, with significant chemical transformations occurring mainly after water is added during the pre-flotation conditioning stage. Unlike wet grinding, where the aqueous environment promotes particle aggregation and influences breakage behavior, dry grinding with solid-phase NaOH does not create conditions conducive to particle aggregation. Consequently, grinding efficiency remains largely unaffected by the alkaline additive in dry form.

In contrast, wet grinding responded clearly to alkaline pH adjustments. At neutral pH (GW1), the coarsest discharge was 0.356 mm, with only 61.90% of the product below the flotation feed cut-off size of 0.250 mm. However, as the pH increased from 8 to 10 (GW2–GW4), X_{80} consistently decreased from 0.353 mm to 0.339 mm, after which the particle size distribution stabilized at higher pH levels. Meanwhile, the proportion of material passing below 0.250 mm increased, peaking at 67.16% under GW4 (pH 10).

These results highlight that while alkaline conditions had limited influence during dry grinding, their impact on wet grinding was substantial. The observed increase in breakage efficiency with rising pH is likely driven by enhanced dispersion of nonmetals due to hydroxylation in alkaline conditions. This modification reduces hydrophobic attraction forces, promotes stronger water–particle interactions, minimizes aggregation, and improves flowability. Collectively, these changes shift the dominant breakage mechanism from bed-dominated particle stressing to more effective single- or multi-particle stressing, ultimately enhancing grinding performance.

7.3.3. Effect on flotation performance

Figure 7. 11 illustrates the effect of alkaline conditions during grinding on the reverse flotation performance of WPCBs at 14 wt.% pulp solids. The results emphasize the relationship between the grinding environment and flotation behavior, particularly the chemical transformation of nonmetallic components in alkaline conditions. As shown in the analysis of functional group changes in WPCB nonmetals, alkaline grinding alters their chemistry, enhancing hydrophilicity and dispersibility. These changes, resulting from NaOH addition in dry grinding or pH adjustment in wet grinding, influence the extent to which metals are retained in the underflow and nonmetals are rejected to the overflow, thereby affecting separation efficiency.

DOI: 10.14750/ME.2026.030

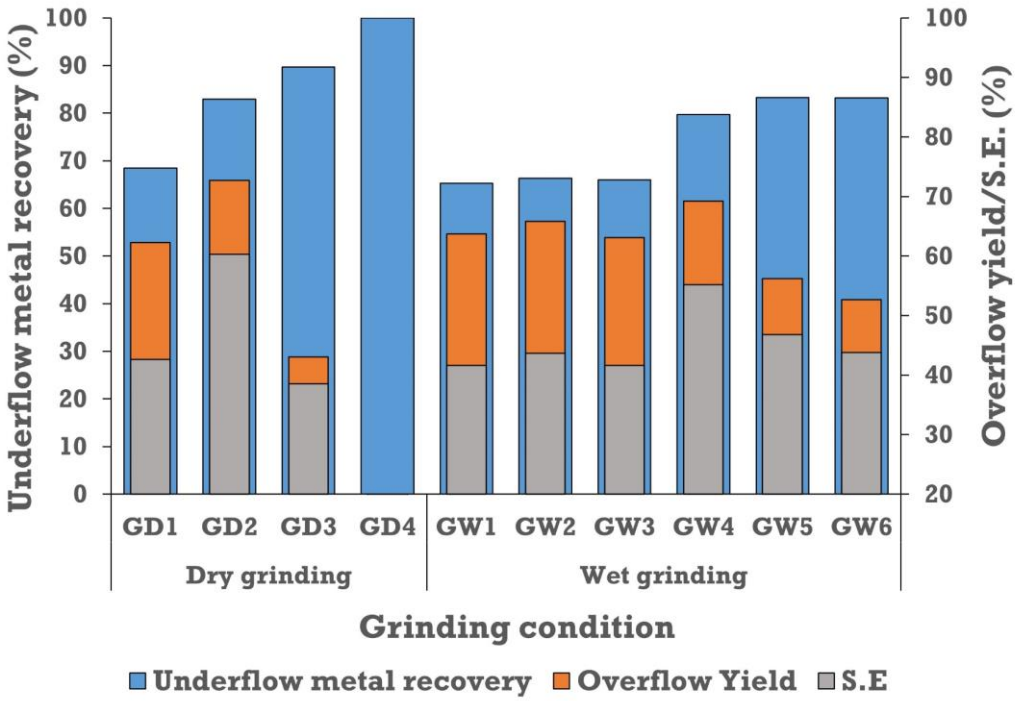

Figure 7. 11: Effect of dry and wet grinding under alkaline conditions on reverse flotation performance of WPCBs at 14 wt.% solids.

When 0.1 wt.% NaOH was added during grinding (GD2), both metrics improved substantially: the overflow yield rose to 72.71%, and metal recovery increased to 82.88%, indicating enhanced separation efficiency. This condition (GD2) represents the optimal balance between wetting nonmetals and effectively recovering metallic constituents. However, increasing the NaOH dosage to 0.5 wt.% (GD3) caused a sharp decline in overflow yield to 43.03%, while metal recovery continued to rise, reaching 89.67%. At this point, the separation process became increasingly nonselective, suggesting that excessive wetting of nonmetals hindered their rejection into the froth. Ultimately, under the most intense alkaline condition tested (1 wt.% NaOH, GD4), flotation separation collapsed entirely, with all content reporting to the underflow, indicating total depression of WPCB solids and the breakdown of froth-based selectivity.

In contrast, flotation behavior after wet alkaline grinding showed a more gradual and controlled response. Starting with the unadjusted baseline (GW1), flotation achieved an overflow yield of 63.71% and metal recovery of 65.27%. Incremental increases in slurry pH during grinding to 8, 9, and 10 (GW2–GW4) progressively enhanced flotation performance. Notably, GW4 (pH 10) reached a peak overflow yield of 69.19% and metal recovery of 79.69%, indicating an optimum in the wet alkaline environment. Further increases in pH to 11 and 12 (GW5–GW6) maintained metal recovery at approximately 83% but caused a marked decline in overflow

DOI: 10.14750/ME.2026.030

yield, reflecting the depression effects seen under dry grinding at higher alkalinity and indicating reduced separation efficiency due to excessive wetting of nonmetallic particles.

The response of specific metals to alkaline grinding revealed distinct behaviors and selectivity trends, as illustrated in **Figure 7. 12**, which shows metal-specific recovery percentages and enrichment ratios (ER, the ratio of the reverse flotation underflow metal content to the flotation feed metal content) for both dry (GD1–GD3) and wet (GW1–GW6) grinding conditions. Among the metals, copper exhibited the most favorable and consistent response. After dry grinding, recovery steadily increased from about 70% at GD1 to nearly 96% at GD3. Under wet conditions, copper recovery remained high, ranging from 70% to 90% across the pH spectrum. Notably, the ER for copper remained favorable throughout, peaking at approximately 3.5 in GD2 and 2.7 in GW4.

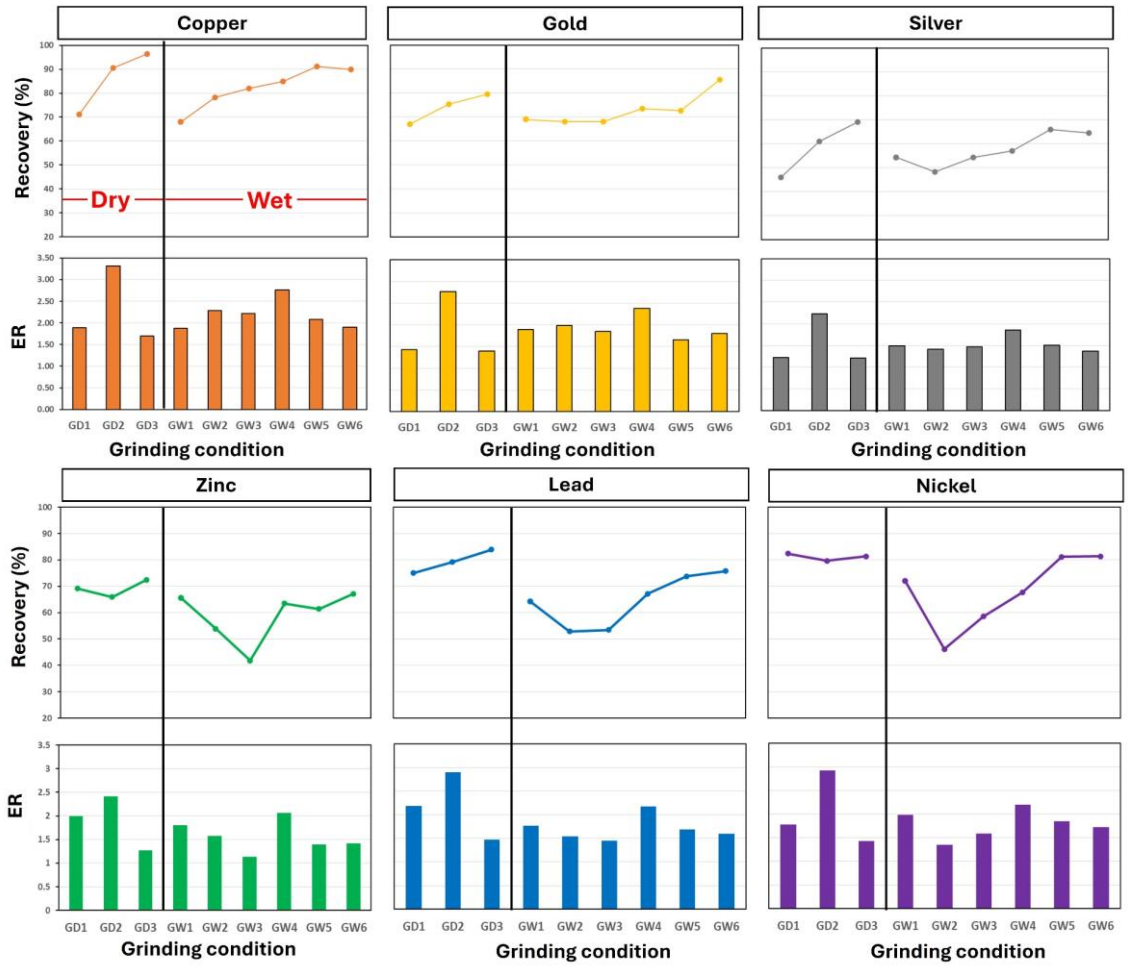

Figure 7. 12: Recovery and enrichment ratios of individual metals following dry and wet grinding under alkaline conditions.

Gold showed moderate improvement in recovery with dry alkaline grinding, increasing from 67% at GD1 to 80% at GD3. However, under wet grinding, significant enhancement was

observed only beyond pH 10. At GW4, gold recovery reached 73% with an ER of 2.38; at GW6 (pH 12), recovery increased further to 86%, although the ER declined to 1.81, indicating a trade-off between yield and grade at higher alkalinity. Silver exhibited the least favorable flotation performance. While alkaline grinding modestly improved its recovery to a maximum of 69% at GD3, this was accompanied by a sharp drop in ER to 1.20.

Zinc, lead, and nickel showed moderately positive responses under both dry and wet alkaline conditions. Recovery improvements were more pronounced under wet grinding at higher pH (GW4–GW6), while moderate NaOH addition in dry grinding also yielded incremental gains. The ER for zinc remained above unity across all conditions, with optimal ER observed at GD2 and GW4. Lead exhibited particularly strong selectivity following dry grinding with 0.1 wt.% NaOH (ER = 2.92), while nickel achieved its maximum enrichment under the same condition (ER = 2.90), indicating a favorable separation environment provided by GD2.

These trends suggest that enhanced flotation performance is closely linked to the hydroxylation of nonmetals during grinding in alkaline conditions. Hydroxylation-driven modifications promote a more dispersed pulp phase. As shown in the next section, these conditions significantly reduce the viscosity of the flotation suspension following GD2 grinding compared to GD1. This rheological improvement is particularly relevant for WPCB systems at 14 wt.% solids, where prior analysis has indicated that metal losses are predominantly driven by viscosity-induced mass-pull entrapment.

7.3.4. Effect on pulp rheology

Having established the chemical transformations induced by alkaline grinding on nonmetallic fractions and their effect on flotation performance, attention now shifts to the underlying rheological mechanisms driving these improvements. Rheological measurements of flotation feed suspensions derived from standard (GD1) and alkaline (GD2) grinding conditions are presented in **Figure 7. 13**.

The rheological characterization reveals that alkaline grinding (GD2) completely eliminates the yield stress found in suspensions after standard grinding. While the GD1 suspension exhibited a yield stress of 0.35 Pa, this resistance was absent in the GD2 suspension, indicating significantly reduced particle interactions and diminished aggregation tendencies. Furthermore, the apparent viscosity at a shear rate of 100 s^{-1} decreased from 16 mPa·s after GD1 to 6.75 mPa·s after GD2, representing a reduction of approximately 58%.

DOI: 10.14750/ME.2026.030

These rheological improvements directly align with the enhanced flotation performance observed earlier. The elimination of yield stress and the marked decrease in apparent viscosity reflect the chemical modifications identified through FTIR analysis. The improved wettability from hydroxylation weakens the interparticle hydrophobic forces that drive aggregate formation, leading to measurable reductions in viscosity and yield stress.

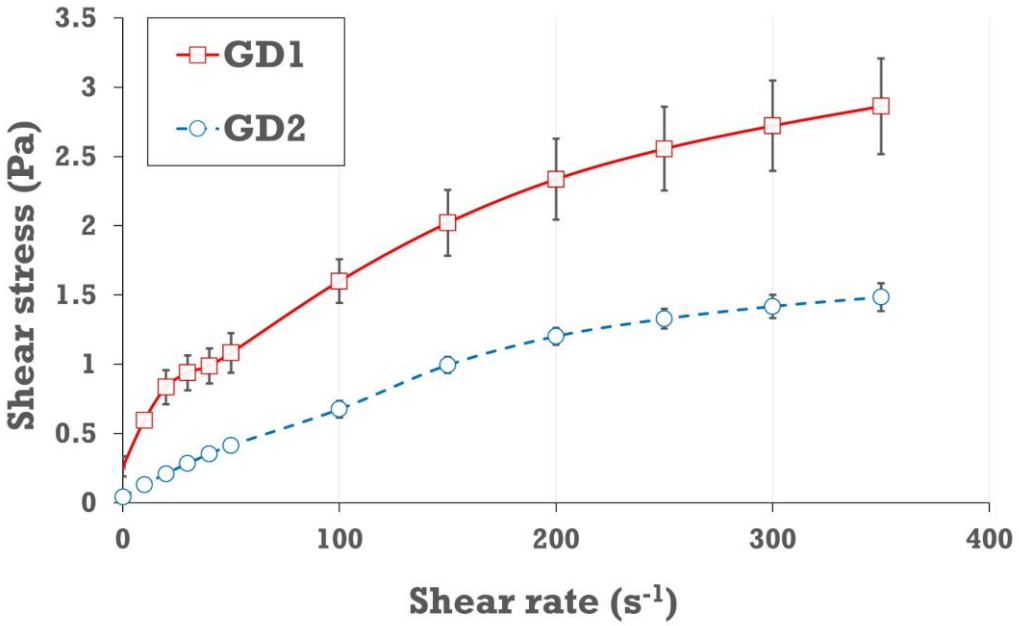

Figure 7. 13: Rheological behavior of WPCB flotation feed suspension at 14 wt.% solids following dry grinding under GD1 (standard grinding) and GD2 (alkaline grinding at 0.1% NaOH).

The rheological modifications induced by alkaline grinding have profound implications for flotation dynamics. The high-viscosity pulp observed after GD hinders air dispersion and impedes bubble transport within the flotation cell, reducing bubble-particle collision frequencies and degrading separation efficiency. By reducing viscosity, alkaline grinding enhances air dispersion and improves bubble-particle interactions, thereby promoting better separation efficiency. Additionally, lower viscosity aids particle settling by reducing drag force within the suspension, minimizing unintended mass pull entrapment, and improving metal recovery in the underflow product.

The relationship between rheological improvements and flotation efficiency becomes particularly evident when examining size-specific metal recovery, as illustrated in **Figure 7. 14**. Grinding under alkaline conditions (GD2) significantly improved metal recovery across all size fractions. This enhancement was most pronounced in the coarsest fraction (0.125–0.250 mm), where recovery increased from 67.05% following GD1 to 82.79% following GD2. The

DOI: 10.14750/ME.2026.030

finest size fraction (<0.075 mm) also showed notable improvement, with recovery rising from 54.23% to 69.28%. This differential response across size fractions helps explain the varying recovery rates and enrichment ratios observed among different metals. Metals concentrated in coarser size ranges are more sensitive to rheological drag and exhibit more pronounced improvements under conditions of reduced viscosity.

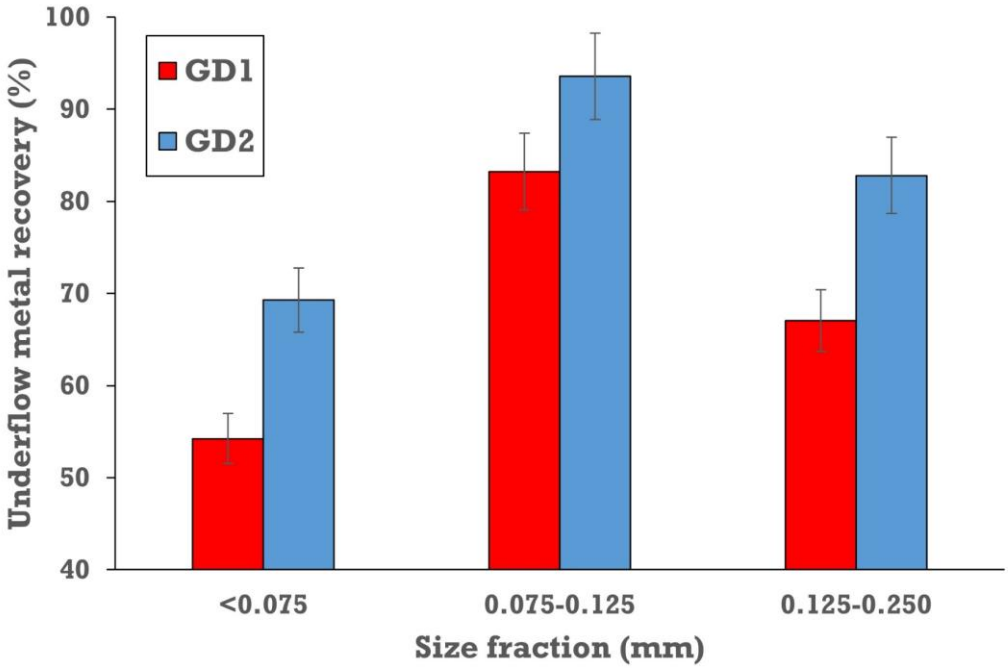

Figure 7. 14: Underflow metal recovery per size fraction following GD1 (standard grinding) and GD2 (alkaline grinding at 0.1% NaOH) at 14 wt.% solids.

An additional insight arises when comparing flotation performance following GD2 at 14 wt.% solids with that at the lower 10 wt.% solids concentration (see **Section 6.3**). Despite the GD2 suspension having similar or slightly higher viscosity than the 10 wt.% suspension (4.85 mPa·s), flotation performance was superior following GD2 treatment. Under identical cell hydrodynamic conditions, metal recovery following GD2 at 14 wt.% solids reached 82%, compared to an average of 72% for flotation at 10 wt.% solids.

This performance difference suggests that while rheological improvement is a primary mechanism, the benefits of alkaline grinding extend beyond mere viscosity reduction. As previously discussed, metallic particles in WPCBs are often coated with residual nonmetallic matter that imparts hydrophobic characteristics, making them susceptible to true flotation. Alkaline grinding likely helps break down these residues, restoring the intrinsic hydrophilic nature of the metallic surfaces. This "cleaning" effect enhances the selective retention of metals in the underflow, particularly for partially liberated or surface-contaminated particles.

Consequently, the superior flotation outcomes observed under GD2 can be attributed to the combined effects of rheological modification and improved metal surface properties, both promoted by the alkaline environment during grinding.

7.3.5. Alkaline grinding environment: process benefits and leaching considerations

Implementing alkaline conditions during the grinding stage marks a significant advancement in the reverse flotation processing of WPCBs. This method is particularly effective at WPCB-elevated solids concentrations, allowing efficient operation at 14 wt.% solids, a notable improvement over previously reported methods such as tannic acid dispersion (10 wt.% solids) or ultrasonic treatment (6 wt.% solids) by Han et al. [153] and Chen et al. [186], respectively. Additionally, grinding under alkaline conditions offers distinct advantages over the alkaline immersion technique described by Dai et al. [147]. While both approaches aim to enhance dispersion and mitigate rheological challenges in WPCB pulps, the grinding-integrated strategy provides a more industrially viable solution for continuous processes. It utilizes the generation of fresh, chemically active particle surfaces during comminution, promoting better interaction and favorable chemistry modifications without the extended retention times characteristic of immersion-based methods. This significantly streamlines the transition between grinding and flotation stages.

Beyond flotation performance, the alkaline nature of the grinding process necessitates careful consideration of potential metal leaching. To evaluate this, metal leachability was assessed under the optimal flotation conditions (GD2 and GW4) by analyzing supernatant liquids for dissolved metal ions. For wet grinding (GW4), the process liquid was separated via filtration immediately after grinding, while for dry grinding (GD2), it was collected post-flotation-conditioning following solid separation through filtration.

Chemical analysis revealed that neither approach resulted in detectable leaching of environmentally sensitive metals such as lead, zinc, or nickel, indicating that the mild alkaline conditions used do not pose leaching concerns for these elements. However, aluminum exhibited notable mobilization, particularly after wet grinding, with concentrations reaching 63 ppm compared to just 3 ppm under dry conditions. Minor increases in silicon and tin (2–5 ppm) were also observed, consistently higher in the wet grinding environment.

These findings suggest that while metal leaching is not a general concern under the tested alkaline conditions, specific elements such as aluminum may be susceptible to mobilization, particularly under prolonged exposure to alkaline media. The higher leaching observed in wet

grinding can be attributed to both enhanced NaOH dissociation in the aqueous medium and the extended contact duration between particles and the alkaline solution. In contrast, the dry grinding environment limits NaOH dissociation and involves only brief interaction during the flotation-conditioning stage, thereby minimizing metal solubilization.

Finally, this research points to a promising direction for future research. The complete depression of nonmetallic particles achieved at 1 wt.% NaOH under dry grinding conditions (GD4) opens the possibility of transitioning from a reverse to a direct flotation scheme. In this alternative approach, metals such as copper and gold, if rendered hydrophobic through suitable collectors, could be selectively floated into the froth product. This concept aligns with the approaches explored by Keleş et al. [86] and Burat et al. [180], offering an opportunity to enhance metal recovery while simplifying the overall separation strategy in WPCB processing.

7.4. Comparative Assessment of Pretreatment Approaches for WPCB Flotation

The preceding investigations have established that both physical and chemical pretreatment approaches effectively address the rheological challenges in WPCB flotation at WPCB-elevated solids concentrations. A direct comparison highlights their distinct advantages and limitations, providing a basis for process selection based on operational priorities (**Table 7. 2**).

At 14 wt.% solids, both approaches, the removal of ultrafines (<0.032 mm) and grinding under alkaline conditions (0.1 wt.% NaOH), achieve comparable improvements in metal recovery. However, the chemical pretreatment demonstrates superior nonmetal rejection, reflected in a higher overflow yield (72.71% versus 66.05%). This difference arises from their underlying mechanisms: physical removal reduces viscosity by eliminating ultrafine particles but compromises froth stability, while chemical modification enhances particle dispersion while maintaining the fractions that contribute to froth structure.

From an operational perspective, the approaches diverge in practical considerations. Physical pretreatment requires additional classification equipment, increasing capital costs but offering lower ongoing operational costs. However, the wide density range in WPCB particles may affect separation accuracy. Moreover, this step generates a fine stream that requires separate handling and may lead to metal losses. The chemical route, conversely, involves simpler implementation through reagent addition during grinding operations. However, it incurs ongoing reagent costs and requires pH control systems, which may increase operational complexity.

DOI: 10.14750/ME.2026.030

Table 7. 2: Comparative analysis of physical and chemical pretreatment (under GD2 grinding conditions) approaches for rheological control in WPCB flotation.

Parameter		Physical Approach (Ultrafine Removal)	Chemical Approach (Alkaline Grinding)
Performance at 14 wt.% solids	Metal recovery	83.64% (↑ from 68.48%)	82.88% (↑ from 68.48%)
	Overflow yield	66.05 % (↑ from 62.29%)	72.71% (↑ from 68.48%)
	S.E.	54.78% (↑ from 42.66%)	60.28% (↑ from 42.66%)
Rheological effects	Yield stress	Reduced to 0.13 Pa (from 0.35 Pa)	Eliminated
	Apparent viscosity	Reduced to 5.13 mPa·s (from 16 mPa·s)	Reduced to 6.75 mPa·s (from 16 mPa·s)
	Mechanism	Direct removal of viscosity-contributing fraction	Modification through hydroxylation
Froth characteristics	Stability	Reduced (larger bubbles, decreased volume)	Maintained
Operational considerations	Capital requirements	Higher (classification equipment)	Lower (reagent addition system)
	Operating costs	Lower ongoing costs	Higher (continuous reagent consumption)
	Additional streams	Yes (ultrafine fraction)	No
	Control requirements	Classification efficiency	Reagent dosing
Secondary benefits	Metal surface properties	No additional effect	Enhanced through surface cleaning
	Adaptability to feed variation	Lower (may require adjusting cut-point based on PSD)	Higher (consistent chemical effect)
Limiting factors	Primary limitation	Compromised froth stability	Narrow operating window between enhancement and depression

From an environmental standpoint, alkaline-assisted grinding generates process water with an elevated pH (~9.7) following the subsequent intense agitation conditioning stage. However, flotation performance optimization demonstrated that maximum separation efficiency is achieved at near-neutral pH (~7), necessitating pH adjustment prior to flotation. This requirement, driven by metallurgical imperatives, provides inherent pH control within the process flowsheet. Neutralization to pH 7 can be achieved through controlled acid addition or, more economically, through carbon dioxide as a pH regulator during the aeration phase of flotation. This process-integrated neutralization ensures that flotation operates under optimal chemical conditions while simultaneously conditioning effluent water for discharge or recirculation at environmentally benign pH levels. Consequently, process water exiting the flotation circuit is already near-neutral, eliminating the need for end-of-pipe neutralization infrastructure and minimizing the risk of alkaline effluent discharge. Moreover, leachability

DOI: 10.14750/ME.2026.030

assessments under these conditions confirmed that environmentally sensitive metals such as lead, zinc, and nickel remained below detection limits, demonstrating that the mild alkaline environment does not promote their dissolution. These results indicate that potential leaching is limited to a few amphoteric species and remains well within environmentally manageable thresholds.

To evaluate their robustness under more challenging conditions, rheological measurements were performed at 18 wt.% solids (**Figure 7. 15**). These results reveal the differing capacities of the two approaches to maintain flotation viability under higher solids loading.

The physical pretreatment demonstrates some benefits at 18 wt.% solids. Yield stress decreases from 0.97 Pa to 0.43 Pa, and apparent viscosity drops to 11.5 mPa·s, well below the 16 mPa·s threshold associated with effective flotation at 14 wt.% solids. Despite this favorable rheology, the approach suffers from compromised froth stability, which, along with yield stress, may limit separation efficiency. Therefore, while the suspension rheological properties improve, flotation performance does not necessarily follow.

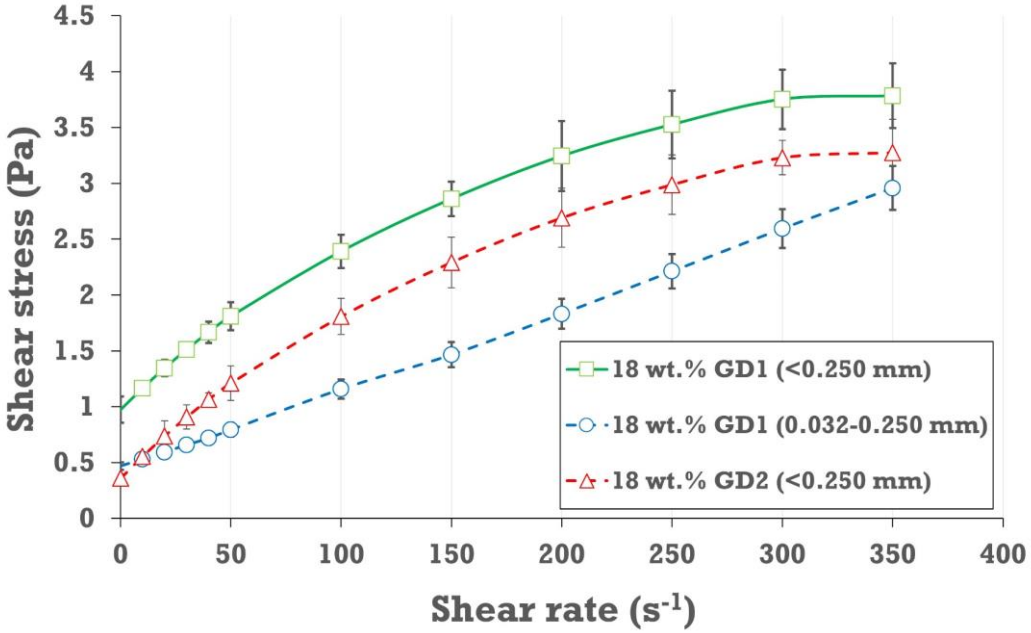

Figure 7. 15: Rheological behavior of WPCB flotation feed suspension at 18 wt.% solids following dry grinding under GD1 (<0.250 mm), physical pretreatment of modified feed (0.032–0.250 mm), and chemical pretreatment under GD2 grinding conditions (alkaline grinding at 0.1% NaOH).

In contrast, the chemically pretreated feed under GD2 conditions exhibits a more nuanced response. The yield stress disappears, while the apparent viscosity rises significantly to 18.1 mPa·s. This outcome suggests that surface hydroxylation, although effective at moderate solids

levels, is insufficient to counteract the dominant effects of particle crowding and hydrodynamic interaction at higher solids concentrations. Consequently, dispersion through surface chemistry fails to fully suppress viscosity buildup at this concentration. While increasing the NaOH dosage may further reduce interparticle attraction and lower viscosity, prior results (GD3 and GD4) showed that higher alkalinity leads to over-wetting of nonmetallic particles, depresses their hydrophobicity, and undermines flotation selectivity.

These findings indicate that both pretreatment approaches experience diminishing returns beyond 14 wt.% solids. The declining flotation results at 18 wt.% solids suggest a practical upper limit for solids concentration to maintain acceptable flotation performance and separation efficiency in WPCB processing.

Overall, both physical and chemical pretreatment strategies offer effective, yet limited, solutions for rheological control in WPCB flotation. The physical approach excels in reducing viscosity directly but compromises froth stability, while the chemical approach provides more comprehensive dispersion benefits within a narrower operating window.

7.5. Conclusions

The flotation performance of WPCBs at high pulp solid concentrations (14 wt.%) is hindered by unfavorable rheological conditions, characterized by high viscosity (16.0 mPa·s) and yield stress (0.35 Pa). These conditions impede metal recovery (68.48%) and nonmetal rejection (62.29% overflow yield). To enhance flotation at higher throughputs, two pretreatment strategies were examined. The physical approach involved removing ultrafine particles (<0.032 mm), which represent approximately 34% of the feed and have low metal content, akin to desliming practices in clay-rich ores. The chemical approach utilized alkaline grinding with solid NaOH in a dry environment (up to 1 wt.%) and controlled pH in wet conditions (up to pH 12). These strategies provide practical pathways for process optimization while offering insights into how pretreatment alters suspension behavior and flotation dynamics.

Removing ultrafine particles (<0.032 mm) effectively mitigated rheological constraints, reducing apparent viscosity by 68% (from 16.0 to 5.13 mPa·s) and yield stress by 63% (from 0.35 to 0.13 Pa). This pretreatment significantly improved metal recovery across all size fractions, with overall recovery increasing from 68.48% to 83.64%. The rheological improvement suppressed the mechanical entrapment of metals to the froth, confirming that ultrafines contribute disproportionately to flow resistance. However, the limited improvement in overflow yield (from 62.29% to 66.05%) revealed a trade-off: ultrafine removal

DOI: 10.14750/ME.2026.030

compromised froth stability, leading to bubble coalescence and reduced froth volume, which constrained separation efficiency to 54.78%. This limitation suggests that physical pretreatment must be balanced against potential disruptions to froth stability in industrial applications.

Chemical pretreatment through grinding under alkaline conditions demonstrated distinct performance patterns in dry and wet environments. While alkaline conditions had minimal impact on particle size reduction during dry grinding, increasing pH from 8 to 10 in wet grinding enhanced breakage efficiency, as the characteristic particle size X_{80} decreased from 0.35 to 0.33 mm and the proportion of particles smaller than 0.250 mm increased from 61.90 to 67.16 percent, indicating improved particle dispersion. Optimal flotation performance was achieved at 0.1 wt.% NaOH during dry grinding, with an overflow yield of 72.71% and metal recovery of 82.88%, and at pH 10 under wet grinding, where the corresponding values were 69.19% and 79.69%. This enhancement is attributed to alkaline conditions modifying nonmetal surface properties, promoting hydroxylation, eliminating yield stress, and reducing apparent viscosity by 58% (from 16.0 to 6.75 mPa·s). Alkaline grinding also provided surface-cleaning effects for metal particles by modifying residual hydrophobic coatings, further aiding metal recovery. However, excessive alkalinity led to over-wetting of nonmetals and a collapse in separation selectivity, indicating a narrow operational window for optimal performance.

In summary, both pretreatment strategies were effective at 14 wt.% solids during flotation, but their benefits diminished at higher solid loadings. While ultrafine removal maintained rheological improvement, its compromised froth stability limits flotation gains at 18 wt.%. Alkaline grinding provided better nonmetal rejection and dispersion at moderate dosages but struggled at higher viscosity without risking over-wetting of nonmetals. Ultimately, these strategies establish a practical upper limit for flotation concentration and underscore the importance of rheology management as a key factor in optimizing high-throughput WPCB processing.

DOI: 10.14750/ME.2026.030

Chapter 8: Conclusions and Future Work

8.1. Conclusions

The escalating generation of electronic waste, particularly waste printed circuit boards (WPCBs), poses a critical challenge to global resource sustainability amid dwindling natural reserves. This PhD dissertation aimed to advance the froth flotation process as an integral component of mechanical pretreatment for the efficient recovery of valuable metals from post-separation WPCB fractions, focusing on the relationship between grinding environments, pulp characteristics, and metallic particle flotation behavior to inform the development and optimization of an industrially scalable flotation process.

The investigation into mechanical processing demonstrated that stepwise comminution with staged physical separation effectively minimizes material losses and enables metal recovery at coarser fractions. However, economically significant metal values remain in the post-separation fraction, particularly in sizes below 1.0 mm. Chemical analysis confirmed substantial metal content across the post-separation size fractions, with the <0.5 mm fraction exhibiting the highest overall metal concentration at 3.93%. Economic assessment revealed that the selected fraction (<1 mm) holds approximately $6,701 per metric tonne in metals, with over 92% of this value attributed to gold despite its comparatively low concentration. These findings established the post-separation fraction as a high-value, metal-rich feed requiring further grinding to enhance liberation and prepare for froth flotation beneficiation.

A comparative analysis of grinding environments revealed clear differences in efficiency. Dry grinding produced finer particles (X_{80} = 0.33 mm compared to 0.37 mm for wet grinding) and yielded a higher percentage of the target size fraction <0.250 mm (69% vs. 60%). This difference was attributed to the hydrophobic nature of WPCB nonmetals, which promoted aggregation in wet conditions and reduced stress intensity during grinding. Despite these differences, both environments resulted in similar particle shape and liberation characteristics, as mechanical stresses during fracture remained unchanged between dry and wet conditions in a ball mill. Ground particles exhibited moderate elongation, angularity, and smooth surfaces, reflecting the laminated structure of WPCB. Liberation efficiency improved with decreasing particle size, reaching near-complete liberation below 0.075 mm, with variations across metals due to their structural roles in the WPCB matrix. Overall, dry grinding is preferred for flotation feed preparation, offering better size reduction and avoiding aggregation-related issues inherent in wet grinding.

DOI: 10.14750/ME.2026.030

Investigation into pulping challenges revealed that the hydrophobic nature of WPCB nonmetallic components, stemming from residual organic resins in manufacturing, creates two distinct pathways for flotation performance deterioration. Despite the WPCB flotation feed having a true density of 1.7 g/cm³, the nonpolar surfaces of these particles minimize water contact, triggering immediate aggregation upon water immersion and forming both dry and partially wetted surface aggregates. These aggregates represent the first pathway of metal loss, significantly impairing flotation performance by entrapping metallic particles, as confirmed through microscopic examination. The application of intense agitation as a pretreatment strategy demonstrated that dispersion effectiveness is highly dependent on energy input, with the aggregation index (AI) confirming optimal dispersion at moderate stirring (AI = 6.6% ± 2.6%). However, excessive agitation gave rise to the second pathway: fine hydrophobic particles stabilized air bubbles introduced by increased turbulence, creating a persistent foam layer at the pulp-air interface. Chemical analysis of this foam confirmed significant metal entrapment (e.g., 5.7 g/kg copper, 22.6 mg/kg gold), establishing foam formation as a critical but often-overlooked mechanism of unintended metal losses. Flotation performance followed these dispersion trends, with the highest separation efficiency (60%) achieved under optimal agitation conditions that balanced aggregate disruption while avoiding foam formation. These findings establish that controlled agitation effectively mitigates hydrophobic-driven pulping challenges, but excessive agitation triggers a secondary pathway of foam-mediated flotation losses, highlighting the dual role of hydrophobic interactions in WPCB processing systems.

Investigation into the reverse flotation dynamics of WPCBs revealed a complex interplay between process variables and separation performance. A consistent trade-off was observed between nonmetal rejection to the overflow and metallic particle retention in the underflow, rooted in the contrasting effects of these responses to flotation conditions. Statistical modeling clarified this relationship: the aeration rate exhibited a positive linear influence on overflow yield but a complex parabolic effect on metal recovery; impeller speed showed a quadratic relationship with overflow yield while negatively impacting recovery; and solids concentration emerged as the dominant factor, exerting a pronounced quadratic effect on overflow yield, peaking at moderate levels before declining, while demonstrating a strong negative linear relationship with metal recovery. Notably, analysis of individual metallic constituents revealed that reliance on total metal recovery metrics masks critical variations in flotation behavior. Copper, due to its high abundance, shaped the overall recovery pattern, while gold, a more economically critical but less abundant metal, responded differently, especially to changes in

solids concentration. These contrasting responses necessitate deliberate trade-offs in operational strategy, balancing economic value, recovery priorities, and process throughput.

The rheological investigation conclusively establishes pulp rheology as a critical, yet previously overlooked, process control parameter in the reverse flotation of WPCBs. As solids concentration increased, pulp behavior shifted from near-Newtonian at 6–10 wt.% to distinctly non-Newtonian at 14–18 wt.%, marked by sharp increases in apparent viscosity and measurable yield stress. These shifts, driven by hydrophobic interparticle attractions and the shape attributes of WPCB particles, directly influence flotation hydrodynamics, gas dispersion, and bubble-particle stability. Flotation performance mirrored these rheological transitions: overflow yield improved with rising viscosity up to 4.85 mPa·s at 10 wt.%, where medium thickening stabilized bubble–particle aggregates, but declined sharply beyond this threshold as high viscosity disrupted flow, confined turbulence, and impaired gas dispersion. This established 10 wt.% as the operational limit, balancing yield and manageable rheology.

Underflow metal recovery declined linearly with increasing solids concentration; however, its limited sensitivity compared to overflow yield indicated that rheology alone could not explain the loss trends. Size-based and kinetic analyses clarified the mechanisms: for 0.075–0.250 mm metals, overflow losses surged under high-viscosity conditions due to viscosity-enhanced mechanical entrapment, where hindered settling and pulp drag suspended particles into the froth. For <0.075 mm metals, high losses occurred even under dilute, low-viscosity conditions, driven by viscosity-independent mechanical entrapment via bulk-phase transport. Both mechanisms are mass-pull driven, nonselective, and distinct from true flotation or entrainment.

Targeted pretreatment effectively addressed the rheological constraints in WPCB flotation pulps under elevated solids concentrations. Physical pretreatment through ultrafine removal (<0.032 mm) from flotation feed shifted pulp toward near-Newtonian behavior and suppressed mass-pull metal entrapment. This increased overall metal recovery from 68.5% to 83.6%, although nonmetal rejection showed limited improvement, constrained by froth instability due to the absence of ultrafines. Grinding under alkaline conditions provided a more integrated chemical pretreatment. FTIR confirmed ether bond disruption and hydroxylation in nonmetals, promoting surface hydrophilicity and dispersion. These surface changes improved grinding behavior under wet conditions and positively influenced flotation performance. Optimal performance was achieved following dry grinding with 0.1 wt.% NaOH addition and wet grinding under pH 10, effectively balancing nonmetal wetting and metal recovery. These

improvements correlated with rheological changes, notably the complete elimination of yield stress and a 58% reduction in apparent viscosity. Flotation performance surpassed lower-solids benchmarks due to enhanced metal surface cleaning. However, excess alkalinity reversed these effects by over-wetting nonmetals. Leaching tests indicated minimal environmental risk, with aluminum being the only element mobilized under prolonged alkaline exposure.

Both pretreatment strategies effectively mitigate rheological challenges at 14 wt.% solids but differ in efficacy and practicality. Physical pretreatment offers straightforward viscosity reduction but compromises froth stability, while chemical modification provides broader dispersion benefits with over-wetting risks beyond optimal conditions. Operationally, physical pretreatment requires capital investment for classification equipment, whereas chemical pretreatment involves ongoing reagent costs and pH control. Both approaches establish ~14 wt.% as the practical upper limit for solids concentration and confirm rheology management as essential for enabling high-throughput WPCB flotation.

This dissertation approaches WPCB flotation as a multivariable optimization challenge in which recovery efficiency depends not on isolated process adjustments but on the integrated control of grinding, dispersion, and rheology. The findings reposition pulp rheology as a central constraint on flotation performance at high solids concentrations. By defining practical limits on solids loading, revealing loss mechanisms such as foam-driven and viscosity-induced entrapment, and evaluating targeted pretreatment strategies, this work establishes a framework for improving flotation selectivity and throughput. The results provide process-level insights and parameters that can guide the development of scalable, high-efficiency WPCB recovery processes consistent with circular economy objectives.

8.2. Future Work

Drawing from the findings of this dissertation, the following areas are recommended for future research:

1- This dissertation used a mixed WPCB feed representative of multiple manufacturing dates. As WPCB designs become more complex and metal content declines, focused studies on newer, single-source WPCBs (e.g., from mobile phones or laptops) are recommended. These studies should evaluate how evolving designs affect mechanical pretreatment efficiency and the metal content of the post-separation fraction intended for flotation.

2- Future work should investigate the influence of particle shape on flotation performance by applying and comparing alternative grinding methods for the post-separation fraction. In

particular, fine impact mills, known to promote the formation of more spherical metal particles, should be evaluated against conventional tumbling mills to determine how shape modification affects metal flotation behavior.

3- This dissertation proposed mechanisms for metal losses under the relatively high solids loadings characteristic of WPCB flotation; however, the behavior of liberated metals under lower solids loadings remains unclear. Future studies should apply appropriate entrainment or entrapment tracers to distinguish the different loss mechanisms. Considering the compositional heterogeneity of WPCBs, these tracers should be chemically distinct from existing components yet compatible with the broad physical density range of metals present.

4- Building on the demonstrated hydrophilic conversion of WPCB nonmetals through alkaline grinding, future research should examine whether surface coatings or residues on metals can influence their flotation response. Understanding these naturally occurring surface characteristics could clarify whether these features can be exploited or must be modified for improved selectivity. Further studies should also evaluate collector types and conditioning strategies that render or enhance metal hydrophobicity, enabling direct flotation schemes in which depressed nonmetals remain in the underflow and metals are recovered through a direct flotation circuit rather than a reverse-then-direct sequence.

5- To bridge the gap between laboratory findings and industrial application, pilot-scale testing of reverse flotation incorporating the identified pretreatment strategies is recommended. This should include the implementation of intense agitation as a dispersion pretreatment and the use of rheology modifiers to validate their combined effect on flotation performance in closed-circuit operation under industrially relevant solid concentrations and operating conditions.

6- Comprehensive economic and environmental assessments of direct metallurgical approaches and of flotation–integrated mechanical upgrading with the proposed pretreatment–flotation sequences should be conducted under realistic operating conditions. Such evaluations are essential to determine the technical and financial viability of these processes for industrial adoption.

DOI: 10.14750/ME.2026.030

Summary

Recent studies have broadened the scope of waste printed circuit board (WPCB) flotation by addressing parameter optimization, reagent selection, and surface modification. However, the technique remains limited to laboratory-scale investigations, with no industrial implementation achieved. This limitation highlights several unresolved knowledge gaps that hinder process advancement. For instance, the influence of the grinding environment on flotation feed preparation has not been quantified, and the effects of particle aggregation during pulp preparation are inadequately addressed. Additionally, the link between cell hydrodynamics, solids concentration, and separation efficiency is not well understood. The rheological behavior of WPCB pulps is not sufficiently characterized, although it poses both a processing constraint and a potential control variable. Furthermore, targeted pretreatment strategies that could mitigate these issues under industrially relevant conditions are currently lacking.

The aim of this PhD dissertation is to develop a comprehensive understanding of the factors that control the reverse flotation of WPCBs and to establish scientific and practical pathways for scalable, efficient processing. To achieve this aim, the identified research gaps were systematically addressed through investigations into grinding-induced feed modification, particle aggregation and dispersion in suspension, the influence of hydrodynamics and solids concentration on metal recovery dynamics, the rheological behavior of WPCB pulps, and the suitability of ultrafine removal and alkaline-assisted grinding as targeted pretreatment strategies.

The experimental work was structured into four sections:

1. Mechanical processing and controlled grinding of WPCBs were conducted to achieve selective liberation and prepare flotation feed with defined particle size distribution. The staged comminution was followed by multiple physical separation steps, after which the residual fraction was subjected to wet and dry ball milling. Characterization included particle size distribution, liberation degree, particle morphology, and chemical composition.
2. Particle aggregation and dispersion during pulping were examined through intense agitation preconditioning followed by reverse flotation tests. The impact of conditioning was quantified using post-conditioning wet sieving and a proposed aggregation index derived from changes in particle size distribution. Zeta potential measurements were utilized to characterize variations in surface potential, while

separation efficiency was assessed based on flotation products to evaluate overall performance.

3. Flotation performance and pulp properties were evaluated under varied hydrodynamic conditions and solids concentrations using a Box–Behnken design. The measurements included pulp rheology, water recovery, kinetic modeling of metal flotation, entrainment estimation, and hydrophobicity assessment through two-liquid phase testing.
4. Rheology-related processing constraints were addressed using ultrafine removal and alkaline-assisted grinding as pretreatment strategies. Their effects were evaluated through flotation performance under fixed hydrodynamic conditions, rheological measurements, FTIR analysis of nonmetallic phases, and quantification of potential metal leaching during alkaline treatment.

This dissertation establishes an integrated framework for understanding and optimizing the reverse flotation of WPCBs, treating the process as a multivariable system where separation efficiency relies on the combined control of the grinding environment, pulp dispersion, hydrodynamics, and rheology. The work identifies pulp rheology as a primary constraint at elevated solid concentrations, clarifies the mechanisms responsible for metal losses under viscous conditions, and establishes practical limits for stable operation. Additionally, it evaluates targeted pretreatment routes that can mitigate these constraints and enhance flotation selectivity and throughput.

In line with the main objectives of the dissertation, the following main findings are presented:

- It was established that the inherent hydrophobicity of WPCB nonmetallic particles controls their behavior from grinding through flotation, governing dispersion, rheology, and overall separation efficiency.
- It was revealed that dry grinding results in superior size reduction efficiency because hydrophobic interactions in wet grinding generate a rheology-dependent stress mechanism that suppresses breakage efficiency.
- It was proven that a stabilized foam layer formed under high turbulence constitutes a hydrophobicity-induced loss pathway, entrapping metallic particles and driving significant overflow losses during flotation.
- It was confirmed that agitation energy and duration determine the dispersion state of WPCB pulps; insufficient energy preserves aggregation, while excessive energy promotes foam formation, both of which impair flotation.

DOI: 10.14750/ME.2026.030

- It was revealed that copper and gold exhibit distinct and competing recovery responses to solids concentration in single-stage reverse flotation, requiring trade-off optimization.
- It was proven that high-solids flotation is constrained by rheological limits, where increased viscosity disrupts gas dispersion, aggregate stability, and froth mobility, reducing flotation performance.
- It was revealed that metallic particle losses to the overflow arise from viscosity-dependent and viscosity-independent mechanical entrapment mechanisms, affecting coarse-, intermediate-, and fine-sized metals in different ways.
- It was established that the removal of ultrafines mitigates rheological constraints and improves metal recovery at high solids concentration, although at the cost of reduced froth stability and lower nonmetal rejection.
- It was established that wet grinding under alkaline conditions promotes dispersion and improves grinding efficiency by chemically modifying nonmetallic surfaces, reducing hydrophobic attraction and particle aggregation.
- It was proved that grinding under alkaline conditions of controlled dosage enhances reverse flotation performance at elevated solids concentration by modifying pulp rheology and cleaning metallic surfaces.
- It was established that grinding under strong alkaline conditions induces chemical transformation of the WPCB resin matrix, rendering nonmetallic particles highly hydrophilic and enabling their effective depression, creating opportunities for direct flotation schemes.

The findings of this dissertation highlight several avenues for continued advancement of WPCB flotation, including investigations on single-source WPCB streams, the influence of particle shape through alternative grinding technologies, and clarification of metal loss mechanisms at lower solids loadings using dedicated tracers. Further work is warranted on direct flotation pathways and metal surface modification strategies. Pilot-scale validation of the proposed pretreatment–flotation approaches, supported by economic and environmental assessment, will be essential for translating the developed framework into an industrially viable process.

DOI: 10.14750/ME.2026.030

Acknowledgement

I would like to express my deepest gratitude to Prof. Ljudmilla Bokányi for her invaluable guidance, insightful advice, and continuous encouragement throughout the course of this work. I am also sincerely thankful to Dr. Ádám Rácz for his constructive feedback, technical expertise, and dedicated support, which greatly contributed to the completion of this work.

My appreciation extends to my colleagues working in the laboratory hall of the Institute for their assistance, cooperation, and good spirit during the experimental work. I am equally grateful to my friends for their intellectual companionship, stimulating discussions, and unwavering moral support, which made this journey both productive and enjoyable.

Above all, I owe my deepest thanks to my parents and family for their constant encouragement, patience, and unconditional support. Their belief in me has been my greatest source of strength throughout this endeavor.

List of Publications

1. Abbadi A, Bokányi L (2025) Flotation of comminuted waste printed circuit boards particles – A review. 233. https://doi.org/https://doi.org/10.1016/j.mineng.2025.109642

2. Abbadi A, Bokányi L (2024) Mitigating metal loss in waste printed circuit boards reverse flotation: The critical role of particle dispersion. 12:98–113. https://doi.org/10.33030/geosciences.2024.02.008

3. Abbadi A, Rácz Á, Bokányi L (2024) Exploring the comminution process of waste printed circuit boards in recycling: a review. J Mater Cycles Waste Manag 26:1326–1348. https://doi.org/10.1007/s10163-024-01945-3

4. Abbadi A, Mucsi G (2024) A review on complex utilization of mine tailings: Recovery of rare earth elements and residue valorization. J Environ Chem Eng 12:113118. https://doi.org/10.1016/j.jece.2024.113118

5. Abbadi A, Rácz Á, Luckeneder C, Bokányi L (2024) Comparative analysis of rod mills and ball mills: assessing impact on talc ore beneficiation efficiency. 18th Int Miner Process Symp, Eskişehir, Türkiye.

6. Abbadi AIH, Bokányi L (2022) Impact of flotation hydrodynamics on the recovery of fine talc lost in the tailings of conventional flotation process. Proc New Results Tech Earth Environ Sci, University of Miskolc, Faculty of Earth Sciences and Engineering, Miskolc-Egyetemváros, pp 363–377.

7. Abbadi A, Mádai V, Bokányi L (2022) Water quality change due to the mine backfilling and its possible response to talc flotation. Geosci Eng 10(15):5–19. https://doi.org/10.33030/geosciences.2022.15.005

References

1. Fazari J, Hossain MZ, Charpentier P (2024) A review on metal extraction from waste printed circuit boards (wPCBs). J Mater Sci 59:12257–12284. https://doi.org/10.1007/s10853-024-09941-6

2. Baldé CP, Kuehr R, Yamamoto T, et al (2024) Global E-waste Monitor 2024. Geneva/Bonn

3. Erkmen AN, Ulber R, Jüstel T, Altendorfner M (2025) Towards sustainable recycling of critical metals from e-waste: Bioleaching and phytomining. Resour Conserv Recycl 215:. https://doi.org/10.1016/j.resconrec.2024.108057

4. Tesfaye F, Lindberg D, Hamuyuni J (2017) Valuable metals and energy recovery from electronic waste streams. Miner Met Mater Ser 103–116. https://doi.org/10.1007/978-3-319-52192-3_11

5. Sahu S, Mohapatra M, Devi N (2022) Effective hydrometallurgical route for recovery of energy critical elements from E-wastes and future aspects. Mater Today Proc 67:1016–1023. https://doi.org/10.1016/j.matpr.2022.05.491

6. Pramila S, Fulekar MH, Bhawana P (2012) E-Waste- A Challenge for Tomorrow. Res J Recent Sci 1:86–93

7. Premalatha M, Tabassum-Abbasi, Abbasi T, Abbasi SA (2014) The generation, impact, and management of E-Waste: State of the art. Crit Rev Environ Sci Technol 44:1577–1678. https://doi.org/10.1080/10643389.2013.782171

8. Lecler MT, Zimmermann F, Silvente E, et al (2018) Improving the work environment in the fluorescent lamp recycling sector by optimizing mercury elimination. Waste Manag 76:250–260. https://doi.org/10.1016/j.wasman.2018.02.037

9. Oke EA, Potgieter H (2024) Recent chemical methods for metals recovery from printed circuit boards: A review. J Mater Cycles Waste Manag 26:1349–1368. https://doi.org/10.1007/s10163-024-01944-4

10. Kaya M (2016) Recovery of metals and nonmetals from electronic waste by physical and chemical recycling processes. Waste Manag 57:64–90. https://doi.org/10.1016/j.wasman.2016.08.004

11. Gautam S, Pandere V, Gautam A (2024) Debromination of Pyrolytic oil from waste printed circuit boards by catalytic thermo chemical reactions with Ca(OH)2 and ZSM-5. Biomass and Bioenergy 190:107382. https://doi.org/10.1016/j.biombioe.2024.107382

12. He H, Schwartz E, Ogunseitan OA, Schoenung JM (2024) Nanopowders from waste printed circuit boards: Review and evaluation from an alternatives assessment perspective. Resour Conserv Recycl 201:107327. https://doi.org/10.1016/j.resconrec.2023.107327

13. Xia D, Lee C, Charpentier NM, et al (2024) Drivers and Pathways for the Recovery of Critical Metals from Waste-Printed Circuit Boards

14. Mir S, Dhawan N (2022) A comprehensive review on the recycling of discarded printed circuit boards for resource recovery. Resour Conserv Recycl 178:106027. https://doi.org/10.1016/j.resconrec.2021.106027

15. Faraji F, Golmohammadzadeh R, Pickles CA (2022) Potential and current practices of recycling waste printed circuit boards: A review of the recent progress in pyrometallurgy. J Environ Manage 316:. https://doi.org/10.1016/j.jenvman.2022.115242

16. Wang Q, Zhang B, Yu S, et al (2020) Waste-Printed Circuit Board Recycling: Focusing on Preparing Polymer Composites and Geopolymers. ACS Omega 5:17850–17856. https://doi.org/10.1021/acsomega.0c01884

17. Chen T, Ma C, Wang B, et al (2024) Kinetics and debromination studies on the pyrolysis of waste printed circuit boards with the addition of copper and copper oxides. J Clean Prod 443:141141. https://doi.org/10.1016/j.jclepro.2024.141141

18. Kaya M (2019) Electronic Waste and Printed Circuit Board Recycling Technologies

19. Kar U, Nili S, Mends E, et al (2025) A review and environmental impact analysis on the current state of froth flotation on recycling of e-wastes. Resour Conserv Recycl 212:. https://doi.org/10.1016/j.resconrec.2024.107967

20. Kanta Das S, Ellamparuthy G, Kundu T, et al (2024) A comprehensive review of the mechanical separation of waste printed circuit boards. Process Saf Environ Prot 187:221–239. https://doi.org/10.1016/j.psep.2024.04.090

21. Fuerstenau MC, Han KN (2003) Principles of Mineral Processing. Society for Mining, Metallurgy and Exploration Incorporated.

22. Drzymała J (2007) Mineral processing: Foundations of theory and practice of minerallurgy, 1st ed. Wroclaw University of Technology.

23. Raichur AM, Wang XH, Parekh BK (2001) Estimation of surface free energy of pyrites by contact angle measurements. Miner Eng 14:65–75. https://doi.org/10.1016/S0892-6875(00)00160-6

24. Wills BA, Finch JA (2016) Wills' mineral processing technology, 8th ed. Elsevier Science Ltd.

25. Zhang X, Gu X, Han Y, et al (2021) Flotation of Iron Ores: A Review. Miner Process Extr Metall Rev 42:184–212. https://doi.org/10.1080/08827508.2019.1689494

26. Ogunniyi IO, Vermaak MKG (2009) Investigation of froth flotation for beneficiation of printed circuit board comminution fines. Miner Eng 22:378–385. https://doi.org/10.1016/j.mineng.2008.10.007

27. Gallegos-Acevedo PM, Espinoza-Cuadra J, Olivera-Ponce JM (2014) Conventional flotation techniques to separate metallic and nonmetallic fractions from waste printed circuit boards with particles nonconventional size. J Min Sci 50:974–981. https://doi.org/10.1134/S1062739114050172

28. Yao Y, Bai Q, He J, et al (2020) Reverse flotation efficiency and mechanism of various collectors for recycling waste printed circuit boards. Waste Manag 103:218–227. https://doi.org/10.1016/j.wasman.2019.12.030

29. Sarvar M, Salarirad MM, Shabani MA (2015) Characterization and mechanical separation of metals from computer Printed Circuit Boards (PCBs) based on mineral processing methods. Waste Manag 45:246–257. https://doi.org/10.1016/j.wasman.2015.06.020

30. Barnwal A, Mir S, Dhawan N (2020) Processing of Discarded Printed Circuit Board Fines via Flotation. J Sustain Metall 6:631–642. https://doi.org/10.1007/s40831-020-00304-4

31. Li C, Zeng L, Fu H, et al (2017) Mineralogical and chemical characteristics of the lead-zinc tailing and contaminated soil from the mine tailing pond in Hunan Province (China). Physicochem Probl Miner Process 53:1133–1147. https://doi.org/10.5277/ppmp170235

32. Yaashikaa PR, Priyanka B, Senthil Kumar P, et al (2022) A review on recent advancements in recovery of valuable and toxic metals from e-waste using bioleaching approach. Chemosphere 287:132230. https://doi.org/10.1016/j.chemosphere.2021.132230

33. Priyan MV, Annadurai R, Onyelowe KC, et al (2023) Recycling and sustainable applications of waste printed circuit board in concrete application and validation using response surface methodology. Sci Rep 13:1–19. https://doi.org/10.1038/s41598-023-43919-9

34. Jha R, Agrawal M, Jena A, et al (2024) A review on existing pre-treatment techniques of waste printed circuit boards. Can Metall Q 1–17. https://doi.org/10.1080/00084433.2024.2310348

35. Honarbari A, Cataldi P, Zych A, et al (2023) A Green Conformable Thermoformed Printed Circuit Board Sourced from Renewable Materials. ACS Appl Electron Mater 5:5050–5060. https://doi.org/10.1021/acsaelm.3c00799

36. Baldé CP, Angelo E D', Luda V, et al (2022) Global Transboundary E-waste Flows Monitor 2022. United Nations Inst Train Res 1–66

37. Shi Y, Huang Y, Tang Z, et al (2024) Copper recovery from waste printed circuit boards using a hybrid thermally regenerative battery system driven by low-grade waste heat. Chem Eng J 496:154115. https://doi.org/10.1016/j.cej.2024.154115

38. Oguchi M, Murakami S, Sakanakura H, et al (2011) A preliminary categorization of end-of-life electrical and electronic equipment as secondary metal resources. Waste Manag 31:2150–2160. https://doi.org/10.1016/j.wasman.2011.05.009

39. Yuan CY, Zhang HC, McKenna G, et al (2007) Experimental studies on cryogenic recycling of printed circuit board. Int J Adv Manuf Technol 34:657–666. https://doi.org/10.1007/s00170-006-0634-z

40. J. Goodship V. SA& H (2012) Waste electrical and electronic equipment (WEEE) handbook

41. Khandpur R (2011) Printed Circuit Boards: Design, Fabrication, and Assembly, 1st ed

42. Ambat R, Piotrowska K (2022) Materials and processes for electronic devices and components: how they contribute to corrosion reliability?

43. Clyde F. Coombs J (2001) Printed Circuits Handbook, Fifth Edit. McGRAW-HILL

44. Abbadi A, Rácz Á, Bokányi L (2024) Exploring the comminution process of waste printed circuit boards in recycling: a review. J Mater Cycles Waste Manag 26:1326–1348. https://doi.org/10.1007/s10163-024-01945-3

45. Robertson CT (2003) Printed Circit Board Designer's Reference: Basics. Prentice Hall PTR

46. R S Khandpur (2011) Printed Circuit Boards: Design, Fabrication, Assembly and Testing. McGraw-Hill

47. Coonrod J (2012) Different Copper Foils for Different Reasons

48. Li J, Shrivastava P, Gao Z, Zhang HC (2004) Printed circuit board recycling: A state-of-the-art survey. IEEE Trans Electron Packag Manuf 27:33–42. https://doi.org/10.1109/TEPM.2004.830501

49. Zhang S, Forssberg E (1997) Mechanical separation-oriented characterization of electronic scrap. Resour Conserv Recycl 21:247–269. https://doi.org/10.1016/S0921-3449(97)00039-6

50. Ogunniyi IO (2009) Investigation into Froth Flotation for The Beneficiation of Printed Circuit Board Comminution Fines. University of Pretoria

51. Kaya M (2019) Printed Circuit Boards (PCBs)

52. Hao J, Wang Y, Wu Y, Guo F (2020) Metal recovery from waste printed circuit boards: A review for current status and perspectives. Resour Conserv Recycl 157:104787. https://doi.org/10.1016/j.resconrec.2020.104787

53. Hino T, Agawa R, Moriya Y, et al (2009) Techniques to separate metal from waste printed circuit boards from discarded personal computers. J Mater Cycles Waste Manag 11:42–54. https://doi.org/10.1007/s10163-008-0218-0

54. Yamane LH, de Moraes VT, Espinosa DCR, Tenório JAS (2011) Recycling of WEEE: Characterization of spent printed circuit boards from mobile phones and computers. Waste Manag 31:2553–2558. https://doi.org/10.1016/j.wasman.2011.07.006

55. Ghosh B, Ghosh MK, Parhi P, et al (2015) Waste Printed Circuit Boards recycling: An extensive assessment of current status. J Clean Prod 94:5–19. https://doi.org/10.1016/j.jclepro.2015.02.024

56. Anić-Vučinić A, Bedeković G, Šarc R, Premur V (2020) Determining metal content in waste printed circuit boards and their electronic components. J Sustain Dev Energy, Water Environ Syst 8:590–602. https://doi.org/10.13044/j.sdewes.d7.0312

57. Holuszko ME, Kumar A, Espinosa DCR (2022) Electronic Waste: Recycling and Reprocessing for a Sustainable Future. Wiley

58. Arshadi M, Yaghmaei S, Mousavi SM (2018) Content evaluation of different waste PCBs to enhance basic metals recycling. Resour Conserv Recycl 139:298–306. https://doi.org/10.1016/j.resconrec.2018.08.013

59. Ogunniyi IO, Vermaak MKG, Groot DR (2009) Chemical composition and liberation characterization of printed circuit board comminution fines for beneficiation investigations. Waste Manag 29:2140–2146. https://doi.org/10.1016/j.wasman.2009.03.004

60. Bizzo WA, Figueiredo RA, Andrade VF De (2014) Characterization of printed circuit boards for metal and energy recovery after milling and mechanical separation. Materials (Basel) 7:4555–4566. https://doi.org/10.3390/ma7064555

61. Hagelüken C (2005) Recycling of electronic scrap at Umicore's integrated metals smelter and refinery. Proc - Eur Metall Conf EMC 2005 1:307–323

62. Ilyas S, Srivastava RR, Kim H, et al (2021) Circular bioeconomy and environmental benignness through microbial recycling of e-waste: A case study on copper and gold restoration. Waste Manag 121:175–185. https://doi.org/10.1016/j.wasman.2020.12.013

63. Akcil A, Erust C, Gahan CS ekha., et al (2015) Precious metal recovery from waste printed circuit boards using cyanide and non-cyanide lixiviants--A review. Waste Manag 45:258–271. https://doi.org/10.1016/j.wasman.2015.01.017

64. Wang X, Gaustad G (2012) Prioritizing material recovery for end-of-life printed circuit boards. Waste Manag 32:1903–1913. https://doi.org/10.1016/j.wasman.2012.05.005

65. Debnath B, Roychowdhury P, Kundu R (2016) Electronic Components (EC) Reuse and Recycling – A New Approach towards WEEE Management. Procedia Environ Sci 35:656–668. https://doi.org/10.1016/j.proenv.2016.07.060

66. Lee J, Kim Y, Lee J chun (2012) Disassembly and physical separation of electric/electronic components layered in printed circuit boards (PCB). J Hazard Mater 241–242:387–394. https://doi.org/10.1016/j.jhazmat.2012.09.053

67. Wu C, Awasthi AK, Qin W, et al (2022) Recycling value materials from waste PCBs focus on electronic components: Technologies, obstruction and prospects. J Environ Chem Eng 10:108516. https://doi.org/10.1016/j.jece.2022.108516

68. Kumari R, Samadder SR (2022) A critical review of the pre-processing and metals recovery methods from e-wastes. J Environ Manage 320:115887. https://doi.org/10.1016/j.jenvman.2022.115887

69. Chauhan G, Jadhao PR, Pant KK, Nigam KDP (2018) Novel technologies and conventional processes for recovery of metals from waste electrical and electronic equipment: Challenges & opportunities – A review. J Environ Chem Eng 6:1288–1304. https://doi.org/10.1016/j.jece.2018.01.032

70. Park S, Kim S, Han Y, Park J (2015) Apparatus for electronic component disassembly from printed circuit board assembly in e-wastes. Int J Miner Process 144:11–15. https://doi.org/10.1016/j.minpro.2015.09.013

71. Duan H, Hou K, Li J, Zhu X (2011) Examining the technology acceptance for dismantling of waste printed circuit boards in light of recycling and environmental concerns. J Environ Manage 92:392–399. https://doi.org/10.1016/j.jenvman.2010.10.057

72. Duan H, Zhu XN (2022) Recent advances in recovering technology for recycling gold from waste printed circuit boards: a review. Energy Sources, Part A Recover Util Environ Eff 44:1640–1659. https://doi.org/10.1080/15567036.2022.2056271

73. Wang F, Zhao Y, Zhang T, et al (2017) Metals recovery from dust derived from recycling line of waste printed circuit boards. J Clean Prod 165:452–457. https://doi.org/10.1016/j.jclepro.2017.07.112

74. Nekouei RK, Pahlevani F, Rajarao R, et al (2018) Two-step pre-processing enrichment of waste printed circuit boards: Mechanical milling and physical separation. J Clean Prod 184:1113–1124. https://doi.org/10.1016/j.jclepro.2018.02.250

75. Evangelopoulos P, Arato S, Persson H, et al (2019) Reduction of brominated flame retardants (BFRs) in plastics from waste electrical and electronic equipment (WEEE) by solvent extraction and the influence on their thermal decomposition. Waste Manag 94:165–171. https://doi.org/10.1016/j.wasman.2018.06.018

76. Lee H, Mishra B (2018) Selective recovery and separation of copper and iron from fine materials of electronic waste processing. Miner Eng 123:1–7. https://doi.org/10.1016/j.mineng.2018.04.021

77. Ventura E, Futuro A, Pinho SC, et al (2018) Physical and thermal processing of Waste Printed Circuit Boards aiming for the recovery of gold and copper. J Environ Manage 223:297–305. https://doi.org/10.1016/j.jenvman.2018.06.019

78. Kumar V, Lee JC, Jeong J, et al (2013) Novel physical separation process for eco-friendly recycling of rare and valuable metals from end-of-life DVD-PCBs. Sep Purif Technol 111:145–154. https://doi.org/10.1016/j.seppur.2013.03.039

79. Guo C, Wang H, Liang W, et al (2011) Liberation characteristic and physical separation of printed circuit board (PCB). Waste Manag 31:2161–2166. https://doi.org/10.1016/j.wasman.2011.05.011

80. Smith YR, Nagel JR, Rajamani RK (2019) Eddy current separation for recovery of non-ferrous metallic particles: A comprehensive review. Miner Eng 133:149–159. https://doi.org/10.1016/j.mineng.2018.12.025

81. Franke D, Suponik T, Nuckowski PM, et al (2020) Recovery of metals from printed circuit boards by means of electrostatic separation. Manag Syst Prod Eng 28:213–219. https://doi.org/10.2478/mspe-2020-0031

82. Niu B, Chen Z, Xu Z (2017) Recovery of Valuable Materials from Waste Tantalum Capacitors by Vacuum Pyrolysis Combined with Mechanical-Physical Separation. ACS Sustain Chem Eng 5:2639–2647. https://doi.org/10.1021/acssuschemeng.6b02988

83. Kumar A, Holuszko M, Espinosa DCR (2017) E-waste: An overview on generation, collection, legislation and recycling practices. Resour Conserv Recycl 122:32–42. https://doi.org/10.1016/j.resconrec.2017.01.018

84. Ning C, Lin CSK, Hui DCW, McKay G (2017) Waste Printed Circuit Board (PCB) Recycling Techniques. Top Curr Chem 375:1–36. https://doi.org/10.1007/s41061-017-0118-7

85. Vaughan J, Tungpalan K, Parbhakar-Fox A, et al (2021) Toward Closing a Loophole: Recovering Rare Earth Elements from Uranium Metallurgical Process Tailings. Adv Circ Econ LANTHANIDES 73:39–53. https://doi.org/10.1007/s11837-020-04451-7

86. Keleş B, İlkyaz Dinç N, Nur Dursun H, et al (2024) The effect of particle geometry (size & shape) on the recovery of gold and copper metallic particles from end-of-life random access memory cards by flotation. Waste Manag 179:66–76. https://doi.org/10.1016/j.wasman.2024.03.008

87. Hsu E, Barmak K, West AC, Park AHA (2019) Advancements in the treatment and processing of electronic waste with sustainability: A review of metal extraction and recovery technologies. Green Chem 21:919–936. https://doi.org/10.1039/c8gc03688h

88. Khaliq A, Rhamdhani MA, Brooks G, Masood S (2014) Metal extraction processes for

electronic waste and existing industrial routes: A review and Australian perspective. Resources 3:152–179. https://doi.org/10.3390/resources3010152

89. Abdelbasir SM, Hassan SSM, Kamel AH, El-Nasr RS (2018) Status of electronic waste recycling techniques: a review. Environ Sci Pollut Res 25:16533–16547. https://doi.org/10.1007/s11356-018-2136-6

90. Gulliani S, Volpe M, Messineo A, Volpe R (2023) Recovery of metals and valuable chemicals from waste electric and electronic materials: a critical review of existing technologies. RSC Sustain 1:1085–1108. https://doi.org/10.1039/d3su00034f

91. Vishwakarma A, Hait S (2024) E-Waste Valorization and Resource Recovery. In: Management of Electronic Waste: Resource Recovery, Technology and Regulation. pp 202–233

92. Cenci MP, Munchen DD, Mengue JC, Veit HM (2024) Metal Resources in Electronics: Trends, Opportunities and Challenges. In: Priya A (ed) Management of Electronic Waste: Resource Recovery, Technology and Regulation. Wiley, Hoboken, New Jersey

93. Jadhav U, Hocheng H (2015) Hydrometallurgical Recovery of Metals from Large Printed Circuit Board Pieces. Sci Rep 5:1–10. https://doi.org/10.1038/srep14574

94. Habashi F (2009) Recent trends in extractive metallurgy. J Min Metall Sect B Metall 45:1–13. https://doi.org/10.2298/JMMB0901001H

95. Tsydenova O, Bengtsson M (2011) Chemical hazards associated with treatment of waste electrical and electronic equipment. Waste Manag 31:45–58. https://doi.org/10.1016/j.wasman.2010.08.014

96. Ding Y, Zhang S, Liu B, et al (2019) Recovery of precious metals from electronic waste and spent catalysts: A review. Resour Conserv Recycl 141:284–298. https://doi.org/10.1016/j.resconrec.2018.10.041

97. Tuncuk A, Stazi V, Akcil A, et al (2012) Aqueous metal recovery techniques from e-scrap: Hydrometallurgy in recycling. Miner Eng 25:28–37. https://doi.org/10.1016/j.mineng.2011.09.019

98. Li H, Eksteen J, Oraby E (2018) Hydrometallurgical recovery of metals from waste printed circuit boards (WPCBs): Current status and perspectives – A review. Resour Conserv Recycl 139:122–139. https://doi.org/10.1016/j.resconrec.2018.08.007

99. Ashiq A, Kulkarni J, Vithanage M (2019) Hydrometallurgical recovery of metals from e-waste. Elsevier Inc.

100. Birloaga I, Vegliò F (2016) Study of multi-step hydrometallurgical methods to extract the valuable content of gold, silver and copper from waste printed circuit boards. J Environ Chem Eng 4:20–29. https://doi.org/10.1016/j.jece.2015.11.021

101. Becci A, Amato A, Fonti V, et al (2020) An innovative biotechnology for metal recovery from printed circuit boards. Resour Conserv Recycl 153:. https://doi.org/10.1016/j.resconrec.2019.104549

102. Zhang J, Peng Z, Wang J, et al (2024) Advanced Recovery Strategies for Metallic and Nonmetallic Fractions from Waste Printed Circuit Boards: A Comprehensive Review. Sep Purif Rev 54:37–59. https://doi.org/10.1080/15422119.2024.2358481

103. Trivedi A, Vishwakarma A, Saawarn B, et al (2022) Fungal biotechnology for urban mining of metals from waste printed circuit boards: A review. J Environ Manage 323:116133. https://doi.org/10.1016/j.jenvman.2022.116133

104. Faraji F, Golmohammadzadeh R, Rashchi F, Alimardani N (2018) Fungal bioleaching of WPCBs using Aspergillus niger: Observation, optimization and kinetics. J Environ Manage 217:775–787. https://doi.org/10.1016/j.jenvman.2018.04.043

105. Kumar A, Saini HS, Kumar S (2018) Bioleaching of Gold and Silver from Waste Printed Circuit Boards by Pseudomonas balearica SAE1 Isolated from an e-Waste Recycling Facility. Curr Microbiol 75:194–201. https://doi.org/10.1007/s00284-017-1365-0

106. Chen J, Tang D, Zhong S, et al (2020) The influence of micro-cracks on copper extraction by bioleaching. Hydrometallurgy 191:105243. https://doi.org/10.1016/j.hydromet.2019.105243

107. Udayakumar S, Razak MIBA, Ismail S (2022) Recovering valuable metals from Waste Printed Circuit Boards (WPCB): A short review. Mater Today Proc 66:3062–3070. https://doi.org/10.1016/j.matpr.2022.07.364

108. Anwer S, Panghal A, Majid I, Mallick S (2022) Urban mining: recovery of metals from printed circuit boards. Int J Environ Sci Technol 19:9731–9740. https://doi.org/10.1007/s13762-021-03662-y

109. Wang R, Xu Z (2014) Recycling of non-metallic fractions from waste electrical and electronic equipment (WEEE): A review. Waste Manag 34:1455–1469. https://doi.org/10.1016/j.wasman.2014.03.004

110. Zhang L, Xu Z (2016) A review of current progress of recycling technologies for metals from waste electrical and electronic equipment. J Clean Prod 127:19–36. https://doi.org/10.1016/j.jclepro.2016.04.004

111. Yang M, Liu H, Ye B, Qian W (2021) Recycling of printed circuit boards by abrasive waterjet cutting. Process Saf Environ Prot 148:805–812. https://doi.org/10.1016/j.psep.2021.01.052

112. Sander S, Schubert G, Jäckel HG (2004) The fundamentals of the comminution of metals in shredders of the swing-hammer type. Int J Miner Process 74:385–393. https://doi.org/10.1016/j.minpro.2004.07.038

113. Schubert G, Bernotat S (2004) Comminution of non-brittle materials. Int J Miner Process 74:19–30. https://doi.org/10.1016/j.minpro.2004.08.004

114. Quan C, Li A, Gao N (2012) Study on characteristics of printed circuit board liberation and its crushed products. Waste Manag Res 30:1178–1186. https://doi.org/10.1177/0734242X12457119

115. Duan C, Wen X, Shi C, et al (2009) Recovery of metals from waste printed circuit boards by a mechanical method using a water medium. J Hazard Mater 166:478–482. https://doi.org/10.1016/j.jhazmat.2008.11.060

116. Bachér J, Rintala L, Horttanainen M (2022) The effect of crusher type on printed circuit board assemblies' liberation and dust generation from waste mobile phones. Miner Eng 185:1–11. https://doi.org/10.1016/j.mineng.2022.107674

117. Martelo LM, Bastos MMSM, Soares HMVM (2024) Separation of the metallic and non-metallic fractions of waste printed circuit boards – A review focused on the organic swelling. Miner Eng 206:. https://doi.org/10.1016/j.mineng.2023.108529

118. Zhang S, Forssberg E (1999) Intelligent Liberation and classification of electronic scrap. Powder Technol 105:295–301. https://doi.org/10.1016/S0032-5910(99)00151-5

119. Duan C, Zhao Y, He J, Zhou N (2010) Research on liberation mechanism of the impact crushing waste printed circuit board. Adv Mater Res 113–116:730–734. https://doi.org/10.4028/www.scientific.net/AMR.113-116.730

120. Li J, Lu H, Guo J, et al (2007) Recycle technology for recovering resources and products from waste printed circuit boards. Environ Sci Technol 41:1995–2000. https://doi.org/10.1021/es0618245

121. Wen X, Duan C, Jiao H, et al (2005) Study on metals recovery from discarded printed circuit boards by physical methods. IEEE Int Symp Electron Environ 121–128. https://doi.org/10.1109/isee.2005.1437005

122. Tiwary CS, Kishore S, Vasireddi R, et al (2017) Electronic waste recycling via cryo-milling and nanoparticle beneficiation. Mater Today 20:67–73. https://doi.org/10.1016/j.mattod.2017.01.015

123. Li J, Xu Z, Zhou Y (2007) Application of corona discharge and electrostatic force to separate metals and nonmetals from crushed particles of waste printed circuit boards. J Electrostat 65:233–238. https://doi.org/10.1016/j.elstat.2006.08.004

124. Suponik T, Franke DM, Nuckowski PM, et al (2021) Impact of grinding of printed circuit boards on the efficiency of metal recovery by means of electrostatic separation. Minerals 11:1–21. https://doi.org/10.3390/min11030281

125. Yoo JM, Jeong J, Yoo K, et al (2009) Enrichment of the metallic components from waste printed circuit boards by a mechanical separation process using a stamp mill. Waste Manag 29:1132–1137. https://doi.org/10.1016/j.wasman.2008.06.035

126. Nie C chen, Shi S xiang, Lyu X jun, et al (2021) Settlement behavior and stratification of waste printed circuit boards particles in gravitational field. Resour Conserv Recycl 170:105615. https://doi.org/10.1016/j.resconrec.2021.105615

127. Dinç Nİ, Tosun AU, Baştürkcü E, et al (2022) Recovery of valuable metals from WPCB fines by centrifugal gravity separation and froth flotation. J Mater Cycles Waste Manag 24:224–236. https://doi.org/10.1007/s10163-021-01310-8

128. Tan Z, He Y, Xie W, et al (2011) Size distribution of wet crushed waste printed circuit boards. Min Sci Technol 21:359–363. https://doi.org/10.1016/j.mstc.2011.05.004

129. Eswaraiah C, Soni RK (2015) Milling and classification of printed circuit boards for material recycling. Part Sci Technol 33:659–665. https://doi.org/10.1080/02726351.2015.1020179

130. Nekouei RK, Pahlevani F, Rajarao R, et al (2018) Two-step pre-processing enrichment of waste printed circuit boards: Mechanical milling and physical separation. J Clean Prod 184:1113–1124. https://doi.org/10.1016/j.jclepro.2018.02.250

131. Silvas FPC, Jiménez Correa MM, Caldas MPK, et al (2015) Printed circuit board recycling: Physical processing and copper extraction by selective leaching. Waste

Manag 46:503–510. https://doi.org/10.1016/j.wasman.2015.08.030

132. Moraes VT de (2011) Recuperação de metais a partir do processamento mecânico e hidrometalúrgico de placas de circuito impresso de celulares obsoletos. Universidade de São Paulo

133. Yamane LH (2012) Recuperação de metais de placas de circuito impresso de computadores obsoletos através de processo biohidrometalúrgico. Universidade de São Paulo

134. Bachér J, Kaartinen T (2017) Liberation of Printed Circuit Assembly (PCA) and dust generation in relation to mobile phone design in a size reduction process. Waste Manag 60:609–617. https://doi.org/10.1016/j.wasman.2016.09.037

135. Wang F, Zhao Y, Zhang T, et al (2015) Mineralogical analysis of dust collected from typical recycling line of waste printed circuit boards. Waste Manag 43:434–441. https://doi.org/10.1016/j.wasman.2015.06.021

136. Kökkılıç O, Mohammadi-Jam S, Chu P, et al (2022) Separation of plastic wastes using froth flotation – An overview. Adv Colloid Interface Sci 308:. https://doi.org/10.1016/j.cis.2022.102769

137. Mohammadi-Jam S, Waters KE (2014) Inverse gas chromatography applications: A review. Adv Colloid Interface Sci 212:21–44. https://doi.org/10.1016/j.cis.2014.07.002

138. Mohammadi-Jam S, Burnett DJ, Waters KE (2014) Surface energy of minerals - Applications to flotation. Miner Eng 66:112–118. https://doi.org/10.1016/j.mineng.2014.05.002

139. Pita F, Castilho A (2017) Separation of plastics by froth flotation. The role of size, shape and density of the particles. Waste Manag 60:91–99. https://doi.org/10.1016/j.wasman.2016.07.041

140. Wang C qing, Wang H, Fu J gang, Liu Y nian (2015) Flotation separation of waste plastics for recycling-A review. Waste Manag 41:28–38. https://doi.org/10.1016/j.wasman.2015.03.027

141. Wang L, Peng Y, Runge K, Bradshaw D (2015) A review of entrainment: Mechanisms, contributing factors and modelling in flotation. Miner Eng 70:77–91. https://doi.org/10.1016/j.mineng.2014.09.003

142. Das A, Vidyadhar A, Mehrotra SP (2009) A novel flowsheet for the recovery of metal values from waste printed circuit boards. Resour Conserv Recycl 53:464–469. https://doi.org/10.1016/j.resconrec.2009.03.008

143. Vidyadhar A, Das A (2013) Enrichment implication of froth flotation kinetics in the separation and recovery of metal values from printed circuit boards. Sep Purif Technol 118:305–312. https://doi.org/10.1016/j.seppur.2013.07.027

144. nan Zhu X, Cui T, Li B, et al (2020) Metal recovery from waste printed circuit boards by flotation technology with non-ionic renewable collector. J Clean Prod 255:120289. https://doi.org/10.1016/j.jclepro.2020.120289

145. nan Zhu X, Ni Y, zhang Wang D, et al (2020) Effect of dissociation size on flotation behavior of waste printed circuit boards. J Clean Prod 265:121840. https://doi.org/10.1016/j.jclepro.2020.121840

146. chen Nie C, Zhang H, feng Qi X, et al (2021) Environment-friendly flotation technology of waste printed circuit boards assisted by pyrolysis pretreatment. Process Saf Environ Prot 152:58–65. https://doi.org/10.1016/j.psep.2021.05.040

147. Dai G, Han J, Duan C, et al (2021) Enhanced flotation efficiency of metal from waste printed circuit boards modified by alkaline immersion. Waste Manag 120:795–804. https://doi.org/10.1016/j.wasman.2020.11.002

148. Otsuki A, Gonçalves PP, Stieghorst C, Révay Z (2019) Non-destructive characterization of mechanically processed waste printed circuit boards: X-ray fluorescence spectroscopy and prompt gamma activation analysis. J Compos Sci 3:. https://doi.org/10.3390/jcs3020054

149. Wang H, Zhang Y, Wang C (2019) Surface modification and selective flotation of waste plastics for effective recycling——a review. Sep Purif Technol 226:75–94. https://doi.org/10.1016/j.seppur.2019.05.052

150. Sudheshwar A, Malinverno N, Hischier R, et al (2023) The need for design-for-recycling of paper-based printed electronics – a prospective comparison with printed circuit boards. Resour Conserv Recycl 189:106757. https://doi.org/10.1016/j.resconrec.2022.106757

151. Nie C chen, Jiang S qi, Li X guang, et al (2023) Surface characteristic driven in waste printed circuit boards flotation: Floatability mechanism of resin and glass fiber in non-metallic component. Process Saf Environ Prot 178:360–369. https://doi.org/10.1016/j.psep.2023.08.024

152. Kumar A, Holuszko ME, Janke T (2020) Examining the surface properties of waste printed circuit boards rejects using inverse gas chromatography. Resour Conserv Recycl 163:105093. https://doi.org/10.1016/j.resconrec.2020.105093

153. Han J, Duan C, Li G, et al (2018) The influence of waste printed circuit boards characteristics and nonmetal surface energy regulation on flotation. Waste Manag 80:81–88. https://doi.org/10.1016/j.wasman.2018.09.002

154. Flores-Campos R, Estrada-Ruiz RH, Velarde-Sánchez EJ (2017) Study of the physicochemical effects on the separation of the non-metallic fraction from printed circuit boards by inverse flotation. Waste Manag 69:400–406. https://doi.org/10.1016/j.wasman.2017.08.049

155. Chau TT, Bruckard WJ, Koh PTL, Nguyen A V. (2009) A review of factors that affect contact angle and implications for flotation practice. Adv Colloid Interface Sci 150:106–115. https://doi.org/10.1016/j.cis.2009.07.003

156. Bokányi L (1997) The Fundamentals of Metals Recycling by Flotation or Flotation Related Methods. In: Proceedings of the XX. Int. Mineral Proc. Congr., 21-26. Aachen – Germany, pp 227–236

157. Somlyai-Sipos L, Baumli P (2022) Wettability of Metals by Water. Metals (Basel) 12:. https://doi.org/10.3390/met12081274

158. Hornyák P (2010) Experimental investigation of wettability of pure copper and aluminium metals. Student research work, University of Miskolc. Supervisor: Bokányi L

159. Wang J, Wu M, Hou X (2022) Study on the influencing factors of spontaneous

wettability transition behaviour on metallic-based surfaces. Vacuum 200:111048. https://doi.org/10.1016/j.vacuum.2022.111048

160. Ogunniyi IO, Vermaak MKG (2009) Froth Flotation for Beneficiation of Printed Circuit Boards Comminution Fines : An Overview. Miner Process Extr Metall Rev An Int J 101–121. https://doi.org/http://dx.doi.org/10.1080/08827500802333123

161. Bokányi L (2006) Effect of CuSO4 on surface properties and recycling flotation of copper and lead. In: XXIII Int. Miner. Process. Congr. 3. Istambul, pp 2147–2151

162. Janishar Anzoom S, Bournival G, Ata S (2024) Coarse particle flotation: A review. Miner Eng 206:108499. https://doi.org/10.1016/j.mineng.2023.108499

163. Kumar V, chun Lee J, Jeong J, et al (2015) Recycling of printed circuit boards (PCBs) to generate enriched rare metal concentrate. J Ind Eng Chem 21:805–813. https://doi.org/10.1016/j.jiec.2014.04.016

164. Zhu X nan, Nie C chen, Zhang H, et al (2019) Recovery of high-grade copper from waste printed circuit boards by mechanical-grinding assisted flotation. J Clean Prod 232:1251–1256. https://doi.org/10.1016/j.jclepro.2019.06.063

165. Nie C chen, Shi S xiang, Zhu X nan, et al (2022) Enhanced cleaner flotation behavior of non-metallic particles in waste printed circuit boards: From the perspective of particle size. Waste Manag 153:167–177. https://doi.org/10.1016/j.wasman.2022.08.028

166. Ellamparuthy G, Angadi SI, Rao DS, et al (2021) Separation and characterization studies of end-of-life mobile printed circuit boards. Part Sci Technol 39:467–474. https://doi.org/10.1080/02726351.2020.1756547

167. He J, Duan C (2017) Recovery of metallic concentrations from waste printed circuit boards via reverse floatation. Waste Manag 60:618–628. https://doi.org/10.1016/j.wasman.2016.11.019

168. Zhu X nan, Zhang L ye, Dong S ling, et al (2020) Mechanical activation to enhance the natural floatability of waste printed circuit boards. Waste Manag 109:222–230. https://doi.org/10.1016/j.wasman.2020.05.008

169. Ma G, Xia W, Xie G (2018) Effect of particle shape on the flotation kinetics of fine coking coal. J Clean Prod 195:470–475. https://doi.org/10.1016/j.jclepro.2018.05.230

170. Wen B, Xia W (2017) Effect of particle shape on coal flotation. Energy Sources, Part A Recover Util Environ Eff 39:1390–1394. https://doi.org/10.1080/15567036.2017.1332697

171. Wiese J, Becker M, Yorath G, O'Connor C (2015) An investigation into the relationship between particle shape and entrainment. Miner Eng 83:211–216. https://doi.org/10.1016/j.mineng.2015.09.012

172. Wiese JG, O'Connor CT (2016) An investigation into the relative role of particle size, particle shape and froth behaviour on the entrainment of chromite. Int J Miner Process 156:127–133. https://doi.org/10.1016/j.minpro.2016.06.005

173. Xia W (2017) Role of particle shape in the floatability of mineral particle: An overview of recent advances. Powder Technol 317:104–116. https://doi.org/10.1016/j.powtec.2017.04.050

174. Wang L, Peng Y, Runge K (2016) Entrainment in froth flotation: The degree of entrainment and its contributing factors. Powder Technol 288:202–211. https://doi.org/10.1016/j.powtec.2015.10.049

175. Muleller S, Llewellin EW, Mader HM (2010) The rheology of suspensions of solid particles. In: Proceedings of the Royal Society A: Mathematical, Physical and Engineering Sciences. pp 1201–1228

176. Wang L, Li C (2020) A Brief Review of Pulp and Froth Rheology in Mineral Flotation. J Chem 2020:. https://doi.org/10.1155/2020/3894542

177. Mallampati SR, Lee BH, Mitoma Y, Simion C (2018) Sustainable recovery of precious metals from end-of-life vehicles shredder residue by a novel hybrid ball-milling and nanoparticles enabled froth flotation process. J Clean Prod 171:66–75. https://doi.org/10.1016/j.jclepro.2017.09.279

178. Das SK, Ellamparuthy G, Kundu T, et al (2021) Critical analysis of metallic and non-metallic fractions in the flotation of waste printed circuit boards. Powder Technol 389:450–459. https://doi.org/10.1016/j.powtec.2021.05.061

179. Keleş B, İlkyaz Dinç N, Nur Dursun H, et al (2024) The effect of particle geometry (size & shape) on the recovery of gold and copper metallic particles from end-of-life random access memory cards by flotation. Waste Manag 179:66–76. https://doi.org/10.1016/j.wasman.2024.03.008

180. Burat F, Dinç Nİ, Dursun HN, Ulusoy U (2023) The Role of Particle Size and Shape on the Recovery of Copper from Different Electrical and Electronic Equipment Waste. Minerals 13:. https://doi.org/10.3390/min13070847

181. Luo X, Feng B, Wong C, et al (2016) The critical importance of pulp concentration on the flotation of galena from a low grade lead-zinc ore. J Mater Res Technol 5:131–135. https://doi.org/10.1016/j.jmrt.2015.10.002

182. Alsafasfeh A, Alagha L (2017) Recovery of phosphate minerals from plant tailings using direct froth flotation. Minerals 7:. https://doi.org/10.3390/min7080145

183. Runge K, Tabosa E, Crosbie R, McMaster J (2012) Effect of flotation feed density on the operation of a flotation cell. Hobart, Australia

184. Dehghani F (2022) Investigating impact of pulp density on flotation. University of Alaska Fairbanks

185. Bakker CW, Meyer CJ, Deglon DA (2009) Numerical modelling of non-Newtonian slurry in a mechanical flotation cell. Miner Eng 22:944–950. https://doi.org/10.1016/j.mineng.2009.03.016

186. Chen L, He J, Zhu L, et al (2023) Efficient recovery of valuable metals from waste printed circuit boards via ultrasound-enhanced flotation. Process Saf Environ Prot 169:869–878. https://doi.org/10.1016/j.psep.2022.11.046

187. Cheng G, Liu JT, Ma LQ, et al (2014) Study on energy consumption in fine coal flotation. Int J Coal Prep Util 34:38–48. https://doi.org/10.1080/19392699.2013.843530

188. Wang D, Liu Q (2021) Hydrodynamics of froth flotation and its effects on fine and ultrafine mineral particle flotation: A literature review. Miner Eng 173:107220.

https://doi.org/10.1016/j.mineng.2021.107220

189. Nesset JE, Hernandez-aguilar JR, Acuna C, et al (2006) Some gas dispersion characteristics of mechanical flotation machines. 19:807–815. https://doi.org/10.1016/j.mineng.2005.09.045

190. Safari M, Harris M, Deglon D, et al (2016) The effect of energy input on flotation kinetics. Int J Miner Process 156:108–115. https://doi.org/10.1016/j.minpro.2016.05.008

191. Firouzi M, Nguyen A V., Hashemabadi SH (2011) The effect of microhydrodynamics on bubble-particle collision interaction. Miner Eng 24:973–986. https://doi.org/10.1016/j.mineng.2011.04.005

192. Censori M, La Marca F, Carvalho MT (2016) Separation of plastics: The importance of kinetics knowledge in the evaluation of froth flotation. Waste Manag 54:39–43. https://doi.org/10.1016/j.wasman.2016.05.021

193. Carvalho T, Ferreira C, Santos LR, Paiva C (2012) Optimization of Froth Flotation Procedure for Poly(ethylene terephthalate) Recycling Industry M. Polym Eng Sci 1–10. https://doi.org/10.1002/pen.22058

194. Thanh Truc NT, Lee C, Lee B, Mallampati SR (2015) Separation of Hazardous Brominated Plastics from Waste Plastics by Froth Flotation after Surface Modification with Mild Heat-Treatment. Int J Chem Mol Eng 9:1309–1312

195. Fuerstenau DW, Pradip, Herrera-Urbina R (1992) The surface chemistry of bastnaesite, barite and calcite in aqueous carbonate solutions. Colloids and Surfaces 68:95–102. https://doi.org/10.1016/0166-6622(92)80150-Z

196. Manono M, Corin K, Wiese J (2018) Perspectives from literature on the influence of inorganic electrolytes present in plant water on flotation performance. Physicochem Probl Miner Process 54:1191–1214. https://doi.org/10.5277/ppmp18157

197. Estrada-Ruiz RH, Flores-Campos R, Gámez-Altamirano HA, Velarde-Sánchez EJ (2016) Separation of the metallic and non-metallic fraction from printed circuit boards employing green technology. J Hazard Mater 311:91–99. https://doi.org/10.1016/j.jhazmat.2016.02.061

198. nan Zhu X, chen Nie C, Zhang H, et al (2019) Recovery of metals in waste printed circuit boards by flotation technology with soap collector prepared by waste oil through saponification. Waste Manag 89:21–26. https://doi.org/10.1016/j.wasman.2019.03.061

199. Ata S (2012) Phenomena in the froth phase of flotation - A review. Int J Miner Process 102–103:1–12. https://doi.org/10.1016/j.minpro.2011.09.008

200. Drzymala J, Kowalczuk PB (2018) Classification of flotation frothers. Minerals 8:. https://doi.org/10.3390/min8020053

201. Otsuki A, Bryant G (2015) Characterization of the interactions within fine particle mixtures in highly concentrated suspensions for advanced particle processing. Adv Colloid Interface Sci 226:37–43. https://doi.org/10.1016/j.cis.2015.07.005

202. Sajjad M, Otsuki A (2022) Correlation between Flotation and Rheology of Fine Particle Suspensions. Metals (Basel) 12:1–31. https://doi.org/10.3390/met12020270

203. Yang S, Wu Y, Chai W, Cao Y (2023) Effect of energy input on surface properties and dispersion of diaspore and kaolinite in flotation process. Chem Eng Process - Process Intensif 192:109518. https://doi.org/10.1016/j.cep.2023.109518

204. Xie L, Wang J, Lu Q, et al (2021) Surface interaction mechanisms in mineral flotation: Fundamentals, measurements, and perspectives. Adv Colloid Interface Sci 295:102491. https://doi.org/10.1016/j.cis.2021.102491

205. Miettinen T, Ralston J, Fornasiero D (2010) The limits of fine particle flotation. Miner Eng 23:420–437. https://doi.org/10.1016/j.mineng.2009.12.006

206. Bremmell KE, Fornasiero D, Ralston J (2005) Pentlandite-lizardite interactions and implications for their separation by flotation. Colloids Surfaces A Physicochem Eng Asp 252:207–212. https://doi.org/10.1016/j.colsurfa.2004.10.100

207. Zhang S, Yang Y, Wang D, et al (2024) Influence of Particle Size on Flotation Separation of Ilmenite and Forsterite. Minerals 14:. https://doi.org/10.3390/min14101041

208. Jeldres RI, Uribe L, Cisternas LA, et al (2019) The effect of clay minerals on the process of flotation of copper ores - A critical review. Appl Clay Sci 170:57–69. https://doi.org/10.1016/j.clay.2019.01.013

209. Wang C qing, Wang H, Gu G hua, et al (2015) Interfacial interactions between plastic particles in plastics flotation. Waste Manag 46:56–61. https://doi.org/10.1016/j.wasman.2015.08.041

210. Wang C, Sun R, Xing B (2021) Copper recovery from waste printed circuit boards by the flotation-leaching process optimized using response surface methodology. J Air Waste Manag Assoc 71:1483–1491. https://doi.org/10.1080/10962247.2021.1874568

211. Zhu X nan, Ni Y, Wang D zhang, et al (2020) Effect of dissociation size on flotation behavior of waste printed circuit boards. J Clean Prod 265:121840. https://doi.org/10.1016/j.jclepro.2020.121840

212. Franke DM, Suponik T, Nuckowski PM, Dubaj J (2021) Evaluation of the Efficiency of Metal Recovery from Printed Circuit Boards using Gravity Processes. Physicochem Probl Miner Process 57:63–77. https://doi.org/10.37190/PPMP/138471

213. Yu Y, Cheng G, Ma L, et al (2017) Effect of agitation on the interaction of coal and kaolinite in flotation. Powder Technol 313:122–128. https://doi.org/10.1016/j.powtec.2017.03.002

214. Yu Y, Ma L, Wu L, et al (2017) The role of surface cleaning in high intensity conditioning. Powder Technol 319:26–33. https://doi.org/10.1016/j.powtec.2017.06.048

215. Yamaguchi A, Okano H, Sumitomo S, et al (2021) Effect of impeller and gas stirring on agglomeration behavior of polydisperse fine particles in liquid. ISIJ Int 61:1775–1783. https://doi.org/10.2355/isijinternational.ISIJINT-2020-688

216. Li C, Runge K, Shi F, Farrokhpay S (2016) Effect of flotation froth properties on froth rheology. Powder Technol 294:55–65. https://doi.org/10.1016/j.powtec.2016.02.018

217. Farrokhpay S (2012) The importance of rheology in mineral flotation: A review. Miner Eng 36–38:272–278. https://doi.org/10.1016/j.mineng.2012.05.009

218. Cruz N, Peng Y (2016) Rheology measurements for flotation slurries with high clay contents – A critical review. Miner Eng 98:137–150. https://doi.org/10.1016/j.mineng.2016.08.011

219. Bu X, Ma G, Peng Y, et al (2022) Grinding kinetics of coal in wet ball-milling using the Taguchi method. Int J Coal Prep Util 42:369–388. https://doi.org/10.1080/19392699.2019.1603147

220. Gonçalves PP, Otsuki A (2019) Determination of liberation degree of mechanically processed waste printed circuit boards by using the digital microscope and SEM-EDS analysis. Electron 8:. https://doi.org/10.3390/electronics8101202

221. Gouvêa Junior JT, Chipakwe V, de Salles Leal Filho L, Chehreh Chelgani S (2023) Biodegradable ether amines for reverse cationic flotation separation of ultrafine quartz from magnetite. Sci Rep 13:1–16. https://doi.org/10.1038/s41598-023-47807-0

222. Nie C chen, Jiang S qi, Li X guang, et al (2023) Eco-friendly approach for enhancing the floatability of non-metallic components in waste printed circuit boards: Adding gutter oil during dry grinding. Waste Manag 172:71–79. https://doi.org/10.1016/j.wasman.2023.09.006

223. Brezani I Flotation kinetics - equation fitting. https://www.mathworks.com/matlabcentral/fileexchange/28583-flotation-kinetics-equation-fitting. Accessed 30 Jul 2024

224. Otsuki A, Dodbiba G, Fujita T (2018) Two-liquid flotation for separating mixtures of ultra-fine rare earth fluorescent powders for material recycling—a review. Colloids and Interfaces 2:1–31. https://doi.org/10.3390/colloids2010007

225. Kocabağ D, Güler T (2007) Two-liquid flotation of sulphides: An electrochemical approach. Miner Eng 20:1246–1254. https://doi.org/10.1016/j.mineng.2007.05.005

226. Nykänen VPS, Braga AS, Pinto TCS, et al (2020) True flotation versus entrainment in reverse cationic flotation for the concentration of iron ore at industrial scale. Miner Process Extr Metall Rev 41:11–21. https://doi.org/10.1080/08827508.2018.1514298

227. Huu D, Heitkam S, Kupka N, et al (2018) Froth properties and entrainment in lab-scale flotation : A case of carbonaceous sedimentary phosphate ore. Chem Eng Res Des 142:100–110. https://doi.org/10.1016/j.cherd.2018.11.036

228. Ross VE (1989) Determination of the contributions by true flotation and entrainment during the flotation process. In: International Colloquium: Developments in Froth Flotation. Southern African Institute of Mining and Metallurgy, Gordon's Bay, South Africa.

229. Otsuki A, Gonçalves PP, Leroy E (2019) Selective milling and elemental assay of printed circuit board particles for their recycling purpose. Metals (Basel) 9:. https://doi.org/10.3390/met9080899

230. Koyanaka S, Endoh S, Ohya H (2006) Effect of impact velocity control on selective grinding of waste printed circuit boards. Adv Powder Technol 17:113–126. https://doi.org/10.1163/156855206775123467

231. Yan G, Guo J, Zhu G, et al (2020) Liberation enhancement and copper enrichment improvement for waste printed circuit boards by heating pretreatment. Waste Manag 106:145–154. https://doi.org/10.1016/j.wasman.2020.03.023

232. Duan CL, Diao ZJ, Zhao YM, Huang W (2015) Liberation of valuable materials in waste printed circuit boards by high-voltage electrical pulses. Miner Eng 70:170–177. https://doi.org/10.1016/j.mineng.2014.09.018

233. Cui H, Anderson C (2020) Hydrometallurgical treatment of waste printed circuit boards: Bromine leaching. Metals (Basel) 10:1–18. https://doi.org/10.3390/met10040462

234. Daily Metal Prices. https://www.dailymetalprice.com/. Accessed 1 Mar 2025

235. Alves dos Santos N, Galery R (2018) Modelling flotation per size liberation class – Part 2 – Evaluating flotation per class. Miner Eng 129:24–36. https://doi.org/10.1016/j.mineng.2018.09.013

236. Runge KC, Frausto JJ, Lisso MM, et al (2024) Importance of considering classification and liberation when optimising comminution and flotation. Miner Eng 209:108612. https://doi.org/10.1016/j.mineng.2024.108612

237. Tanhua A, Peltoniemi M, Kallio R, et al (2022) The effects of dry grinding and chemical conditioning during grinding on the flotation response of a Cu-Zn sulphide ore and a spodumene pegmatite silicate ore. Miner Eng 189:. https://doi.org/10.1016/j.mineng.2022.107865

238. Pereira L, Kupka N, Huu Hoang D, et al (2023) On the impact of grinding conditions in the flotation of semi-soluble salt-type mineral-containing ores driven by surface or particle geometry effects? Int J Min Sci Technol 33:855–872. https://doi.org/10.1016/j.ijmst.2023.03.007

239. Ogonowski S, Wołosiewicz-Głab M, Ogonowski Z, et al (2018) Comparison of wet and dry grinding in electromagnetic mill. Minerals 8:1–19. https://doi.org/10.3390/min8040138

240. Routray S, Swain R (2019) Effect of Chemical Additives on Reduction in Mill Power During Continuous Grinding of Chromite Overburden Materials in a Tumbling Mill: A Case Study. J Inst Eng Ser D 100:123–128. https://doi.org/10.1007/s40033-018-0170-7

241. Chipakwe V, Semsari P, Karlkvist T, et al (2020) A comparative study on the effect of chemical additives on dry grinding of magnetite ore. South African J Chem Eng 34:135–141. https://doi.org/10.1016/j.sajce.2020.07.011

242. Bu X, Chen Y, Ma G, et al (2020) Wet and dry grinding of coal in a laboratory-scale ball mill: Particle-size distributions. Powder Technol 359:305–313. https://doi.org/10.1016/j.powtec.2019.09.062

243. Zhao R, Han Y, He M, Li Y (2017) Grinding kinetics of quartz and chlorite in wet ball milling. Powder Technol 305:418–425. https://doi.org/10.1016/j.powtec.2016.07.050

244. Burmeister C, Titscher L, Breitung-Faes S, Kwade A (2018) Dry grinding in planetary ball mills: Evaluation of a stressing model. Adv Powder Technol 29:191–201. https://doi.org/10.1016/j.apt.2017.11.001

245. Kwade A (1999) Determination of the most important grinding mechanism in stirred media mills by calculating stress intensity and stress number. Powder Technol 105:382–388. https://doi.org/10.1016/S0032-5910(99)00162-X

246. Huang T, Zhu J, Huang X, et al (2022) Assessment of precious metals positioning in waste printed circuit boards and the economic benefits of recycling. Waste Manag 139:105–115. https://doi.org/10.1016/j.wasman.2021.12.030

247. Barnwal A, Dhawan N (2020) Recovery of copper values from discarded random access memory cards via fluidization and thermal exposure. J Clean Prod 256:120516. https://doi.org/10.1016/j.jclepro.2020.120516

248. Bilesan MR, Makarova I, Wickman B, Repo E (2021) Efficient separation of precious metals from computer waste printed circuit boards by hydrocyclone and dilution-gravity methods. J Clean Prod 286:. https://doi.org/10.1016/j.jclepro.2020.125505

249. Van Oss CJ (2003) Long-range and short-range mechanisms of hydrophobic attraction and hydrophilic repulsion in specific and aspecific interactions. J Mol Recognit 16:177–190. https://doi.org/10.1002/jmr.618

250. Vanderbruggen A, Sygusch J, Rudolph M, Serna-Guerrero R (2021) A contribution to understanding the flotation behavior of lithium metal oxides and spheroidized graphite for lithium-ion battery recycling. Colloids Surfaces A Physicochem Eng Asp 626:127111. https://doi.org/10.1016/j.colsurfa.2021.127111

251. Vanderbruggen A, Salces A, Ferreira A, et al (2022) Improving Separation Efficiency in End-of-Life Lithium-Ion Batteries Flotation Using Attrition Pre-Treatment. Minerals 12:. https://doi.org/10.3390/min12010072

252. Patil DP, Andrews JRG, Uhlherr PHT (2001) Shear flocculation-kinetics of floc coalescence and breakage. Int J Miner Process 61:171–188. https://doi.org/10.1016/S0301-7516(00)00036-3

253. SUN W, DENG M jiao, HU Y hua (2009) Fine particle aggregating and flotation behavior induced by high intensity conditioning of a CO2 saturation slurry. Min Sci Technol 19:483–488. https://doi.org/10.1016/S1674-5264(09)60090-9

254. Forbes E (2011) Shear, selective and temperature responsive flocculation: A comparison of fine particle flotation techniques. Int J Miner Process 99:1–10. https://doi.org/10.1016/j.minpro.2011.02.001

255. Yang B, Song S (2014) Hydrophobic agglomeration of mineral fines in aqueous suspensions and its application in flotation: A review. Surf Rev Lett 21:1–7. https://doi.org/10.1142/S0218625X14300032

256. Shen Z, Zhang Q (2022) Hydrophobic agglomeration behavior of rhodochrosite fines Co-induced by oleic acid and shearing. Sep Purif Technol 282:120115. https://doi.org/10.1016/j.seppur.2021.120115

257. Yi H, Zhao Y, Rao F, Song S (2018) Hydrophobic agglomeration of talc fines in aqueous suspensions. Colloids Surfaces A Physicochem Eng Asp 538:327–332. https://doi.org/10.1016/j.colsurfa.2017.11.017

258. Yangshuai Q, Yongfu Y, Lingyan Z, et al (2017) Dispersion and agglomeration mechanism of flaky graphite particles in aqueous solution. J Dispers Sci Technol 38:796–800. https://doi.org/10.1080/01932691.2016.1198703

259. Pease JD, Curry DC, Young MF (2006) Designing flotation circuits for high fines recovery. Miner Eng 19:831–840. https://doi.org/10.1016/j.mineng.2005.09.056

260. Schubert H (2008) On the optimization of hydrodynamics in fine particle flotation. Miner Eng 21:930–936. https://doi.org/10.1016/j.mineng.2008.02.012

261. Nasab ME, Dashti A (2014) Investigation of the effects of hydrodynamic parameters on the flotation recovery of coal particles. Int J Coal Prep Util 34:260–275. https://doi.org/10.1080/19392699.2013.879293

262. Anzoom SJ, Tripathy SK, Sahu L, et al (2020) Influence of impeller speed and cell volume on coal flotation performance in a self-aerating flotation machine. Adv Powder Technol 31:4053–4063. https://doi.org/10.1016/j.apt.2020.08.008

263. Ralston J, Fornasiero D, Grano S, et al (2007) Reducing uncertainty in mineral flotation-flotation rate constant prediction for particles in an operating plant ore. Int J Miner Process 84:89–98. https://doi.org/10.1016/j.minpro.2006.08.010

264. Genovese DB (2012) Shear rheology of hard-sphere, dispersed, and aggregated suspensions, and filler-matrix composites. Adv Colloid Interface Sci 171–172:1–16. https://doi.org/10.1016/j.cis.2011.12.005

265. Zhang M, Peng Y (2015) Effect of clay minerals on pulp rheology and the flotation of copper and gold minerals. Miner Eng 70:8–13. https://doi.org/10.1016/j.mineng.2014.08.014

266. Cruz N, Peng Y, Wightman E, Xu N (2015) The interaction of clay minerals with gypsum and its effects on copper-gold flotation. Miner Eng 77:121–130. https://doi.org/10.1016/j.mineng.2015.03.010

267. Xu D, Ametov I, Grano SR (2011) Detachment of coarse particles from oscillating bubbles-The effect of particle contact angle, shape and medium viscosity. Int J Miner Process 101:50–57. https://doi.org/10.1016/j.minpro.2011.07.003

268. Forbes E, Davey KJ, Smith L (2014) Decoupling rehology and slime coatings effect on the natural flotability of chalcopyrite in a clay-rich flotation pulp. Miner Eng 56:136–144. https://doi.org/10.1016/j.mineng.2013.11.012

269. Patra P, Bhambhani T, Nagaraj DR, Somasundaran P (2012) Impact of pulp rheological behavior on selective separation of Ni minerals from fibrous serpentine ores. Colloids Surfaces A Physicochem Eng Asp 411:24–26. https://doi.org/10.1016/j.colsurfa.2012.06.037

270. Gao Y, Zhang G, Wang M, Liu D (2018) The critical role of pulp density on flotation separation of nickel-copper sulfide from fine serpentine. Minerals 8:. https://doi.org/10.3390/min8080317

271. Wang Y, Lauten RA, Peng Y (2016) The effect of biopolymer dispersants on copper flotation in the presence of kaolinite. Miner Eng 96–97:123–129. https://doi.org/10.1016/j.mineng.2016.05.010

272. Young CA (2019) SME Mineral Processing and Extractive Metallurgy Handbook. Society for Mining, Metallurgy & Exploration

273. Farrokhpay S, Ndlovu B, Bradshaw D (2018) Behavior of talc and mica in copper ore flotation. Appl Clay Sci 160:270–275. https://doi.org/10.1016/j.clay.2018.02.011

274. Chen X, Hadde E, Liu S, Peng Y (2017) The effect of amorphous silica on pulp rheology and copper flotation. Miner Eng 113:41–46.

https://doi.org/10.1016/j.mineng.2017.08.001

275. Otsuki A, Mensbruge LD La, King A, et al (2020) Non-destructive characterization of mechanically processed waste printed circuit boards - particle liberation analysis. Waste Manag 102:510–519. https://doi.org/10.1016/j.wasman.2019.11.006

276. Saisinchai S (2014) Separation of PVC from PET/PVC mixtures using flotation by calcium lignosulfonate depressant. Eng J 18:45–53. https://doi.org/10.4186/ej.2014.18.1.45

277. Wang CQ, Wang H, Liu YN (2015) Separation of polyethylene terephthalate from municipal waste plastics by froth flotation for recycling industry. Waste Manag 35:42–47. https://doi.org/10.1016/j.wasman.2014.09.025

278. Zhou Z, Scales PJ, Boger D V. (2001) Chemical and physical control of the rheology of concentrated metal oxide suspensions. Chem Eng Sci 56:2901–2920. https://doi.org/10.1016/S0009-2509(00)00473-5

279. Rahman RM, Ata S, Jameson GJ (2012) The effect of flotation variables on the recovery of different particle size fractions in the froth and the pulp. Int J Miner Process 106–109:70–77. https://doi.org/10.1016/j.minpro.2012.03.001

280. Liang L, Li Z, Peng Y, et al (2015) Influence of coal particles on froth stability and flotation performance. Miner Eng 81:96–102. https://doi.org/10.1016/j.mineng.2015.07.004

281. Aktas Z, Cilliers JJ, Banford AW (2008) Dynamic froth stability: Particle size, airflow rate and conditioning time effects. Int J Miner Process 87:65–71. https://doi.org/10.1016/j.minpro.2008.02.001

282. Chen Y, Zhang Y, Yang J, et al (2018) Improving bromine fixation in co-pyrolysis of non-metallic fractions of waste printed circuit boards with Bayer red mud. Sci Total Environ 639:1553–1559. https://doi.org/10.1016/j.scitotenv.2018.05.269

283. Sasikumar C, Srikanth S, Kumar R, et al (2011) Where does the energy go in high energy milling? Front Mechanochemistry Mech Alloy 240–246

284. Koyanaka S, Ohya H, Lee JC, et al (2000) Impact Milling of Printed Circuit Board Waste for Resource Recycling and Evaluation of Liberation using Heavy Medium Separation. KONA Powder Part J 18:194–199. https://doi.org/10.14356/kona.2000025

285. Koyanaka S, Endoh S, Ohya H, Iwata H (1997) Particle shape of copper milled by swing-hammer-type impact mill. Powder Technol 90:135–140. https://doi.org/10.1016/S0032-5910(96)03213-5

286. Zhang ZY, Zhang FS, Yao TQ (2017) An environmentally friendly ball milling process for recovery of valuable metals from e-waste scraps. Waste Manag 68:490–497. https://doi.org/10.1016/j.wasman.2017.07.029

287. Touze S, Guignot S, Hubau A, et al (2020) Sampling waste printed circuit boards: Achieving the right combination between particle size and sample mass to measure metal content. Waste Manag 118:380–390. https://doi.org/10.1016/j.wasman.2020.08.054

288. Saleh AM (2010) A study on the performance of second order models and two phase models in iron ore flotation. Physicochem Probl Miner Process 44:215–230

DOI: 10.14750/ME.2026.030

289. Da Silva C, Peces M, Faundez M, et al (2022) Gamma distribution function to understand anaerobic digestion kinetics: Kinetic constants are not constant. Chemosphere 306:135579. https://doi.org/10.1016/j.chemosphere.2022.135579

DOI: 10.14750/ME.2026.030

Appendix I Supplementary Information from the Literature Review

A.1 WPCB Recycling Process Evaluation

Table A. 1: Summary of advantages and limitations of WPCB recycling processes.

Recycling processes	Advantages	Limitations
Mechanical	Effective separation of metals from nonmetals	The liberation of metals and nonmetals at different size fractions
	Preserves integrity of nonmetallic fractions	Challenges in recovering metals from comminution fines
	Enhances extraction efficiency of downstream metallurgical processes	Metal losses during dust generation
	Simplicity and relatively low initial investment	Process optimization and complementary approaches needed for effectiveness
Pyrometallurgical	Versatile processing regardless of WPCB size, shape, or composition	High initial capital investment
	High throughput suitable for large-scale industrial applications	High energy consumption and operational costs
	Organic content partially serves as reducing agent/fuel, lowering energy need	Significant slag generation trapping valuable metals
	Established commercial technology with proven efficiency for precious metals	Releases hazardous emissions (e.g., heavy metals, dioxins,).
		Requires emission control systems and additional refining steps
Hydrometallurgical	High metal recovery efficiency With superior selectivity	Large chemical consumption
	Better process control and predictability	Generation of hazardous liquid and solid waste
	Lower energy requirements and operating temperature	Time-consuming due to slow leaching kinetics
	No slag formation and low emissions	Significant investment in waste treatment infrastructure
Biometallurgical	Environmentally friendly with lower energy consumption	Slow recovery kinetics and long processing times
	Cost-effective with minimal capital investment.	Sensitive to environmental factors (e.g., temperature, water purity).
	Selective metal extraction with minimal hazardous waste	Scalability to industrial levels remains a challenge.
	Generates weaker organic acids, easier to treat than inorganic acids	Challenges in treating high pulp density input.

DOI: 10.14750/ME.2026.030

A.2 Mechanical Comminution Techniques for WPCB

Table A. 2: Summary of conventional mechanical comminution methods used for WPCB pretreatment before the beneficiation stage.

Source	WPCB Feed	Comminution Machinery	Internal Sieve Opening (mm)	D_{50}[d] (mm)	Reported Liberation Size (mm)	Liberation Grade
[125]	Collection[a]	Shredder Stamp mill	10	1.15	-	< 60%
[284]	Bare Boards	Cutting mill High speed hammer mill	1	0.120	–0.100	80 to 90%
[285]	PWB scrap	Cutting mill Swing-hammer mill	1	0.150	-	-
[286]	Collection	Cutting mill Ball mill	-	-	-	-
[59]	Collection	Hammer mill	0.5	-	–0.075	99.48%
[167]	Collection	Impact crusher Ball mill	3	0.10	–0.250	81%
[116]	PCB-MP[b]	Cutting mill/Hammer mill	-	28.6/20.5	-	58/77%
[54]	PCB-PC[c] PCB-MP	Hammer mill	4	0.850	-	-
[29]	PCB-PC	Hammer mill Disc mill	7	3	–0.59	<50%

[a] Refers to a wide collection of WPCBs from different devices with different manufacturing dates; [b] Refers to printed circuit boards from Mobile Phones; [c] Refers to printed circuit boards from personal computers;
[d] Refers to the size at which 50% of the sample's mass is finer;

DOI: 10.14750/ME.2026.030

Appendix II Supplementary Details for Materials and Methods

B.1 Specifications and Operating Conditions of Separation Equipment

The first separation stage employed a cross-belt magnetic separator with the following specifications: a 350 mm sender belt width, an adjustable gap between the belt and magnet ranging from 20 to 140 mm, magnet dimensions of 200 × 310 mm, a magnetic flux density of 0.5 Tesla, a 1.1 kW conveyor belt drive motor, and a maximum belt speed of 1 m/s. The next stage employed an Eriez HDECS eddy current separator, featuring 7 pairs of rare earth magnets. The separator was operated at a drum speed of 1600 rpm and a belt speed of 0.5 m/s. The final stage utilized an Eriez Magnetics electrostatic drum separator, operated at a drum speed of 30 rpm and an applied voltage of 20 kV. The electrode was positioned 50 mm from the drum, and the separation splitter was set at an angle of approximately 80°.

B.2 Grinding Time Selection

To determine an appropriate grinding duration for preparing the WPCB flotation feed, a preliminary dry grinding progression test was conducted using batch tumbling mill runs at 15, 30, 60, and 180 minutes.

Table B. 1: Cumulative particle size distribution of WPCB post-separation fractions at varying grinding times (dry grinding).

Sieve opening size (mm)	Cumulative passing (%)				
	Feed	Grinding time (min)			
		15	30	60	180
0.5	63.97	77.97	81.38	93.69	98.92
0.25	40.92	50.77	53.96	68.92	76.26
0.125	20.72	33.98	37.32	45.12	54.33
0.075	13.43	20.95	27.27	33.85	45.0

The median particle size (X_{50}) of the ground material was used as the primary indicator for size reduction effectiveness. The feed material prior to grinding had an X_{50} of 0.35 mm, which established the baseline for evaluating grinding performance. After 15 minutes of grinding, the X_{50} decreased to 0.25 mm. A further reduction to 0.22 mm was observed at 30 minutes, still indicating limited size reduction relative to the feed. However, after 60 minutes, a substantial shift in particle size occurred, with X_{50} reaching 0.15 mm—representing a clear increase in

breakage efficiency. Extending grinding to 180 minutes resulted in X_{50} dropping to 0.10 mm, but with diminishing returns in terms of useful breakage and a notable increase in fines generation. Specifically, the material fraction below 0.075 mm rose from 21% at 15 minutes to 27% at 30 minutes, 34% at 60 minutes, and peaked at 45% at 180 minutes. This increase in fines at prolonged grinding durations is attributed to secondary breakage, which disproportionately affects particles already within the target size range, generating fines that negatively impact downstream separation processes. The choice of 60 minutes was thus based on achieving a significant improvement in size reduction over the initial feed, while avoiding the excessive secondary breakage evident at 180 minutes.

B.3 Liberation Degree Assessment

For size fractions larger than 2 mm, the methodology proposed by Sarvar et al. [29] was applied based on visual inspection and assessment. The procedure involved quartering the sample into smaller subsamples, which were then evenly spread across an A3 paper. Half of the spread subsample was examined to identify the different material types.

For size fractions smaller than 2 mm, the degree of liberation was assessed following the methodology proposed by Gonçalves et al. [220]. For the size fractions (1.0–2.0, 0.5–1.0, 0.25–0.5, 0.125-0.25 and 0.075-0.125 mm), a digital optical microscope (ZEISS Axio Imager) was utilized. Representative samples from each size fraction were carefully placed in a glass Petri dish, ensuring an even distribution to prevent particle overlapping. In cases where particle dispersion was insufficient, manual separation using a wooden spatula was performed to enhance visibility and improve the accuracy of liberation and association assessments. For the size fraction below 0.075 mm, scanning electron microscopy (SEM) and energy dispersive spectrometry (EDS) (Jeol JXA 8600) were used. Approximately 0.2 g of representative sample was mounted on aluminum SEM stubs using conductive carbon tape.

B.4 Sample Preparation for ICP-OES Analysis

Given the inherent variability in the quantitative determination of metals in WPCBs, as highlighted by Touze et al. [287], the accuracy of ICP-OES results is strongly influenced by sample preparation conditions, including particle size and mass. Their study demonstrated that larger particle sizes and smaller sample masses lead to higher relative standard deviations, consistent with Gy's sampling theory developed for ore analysis. To minimize analytical uncertainty and achieve a margin of error below 10%, Touze et al. [287] recommended sample

DOI: 10.14750/ME.2026.030

preparation involving particle sizes below 0.2 mm and a sample digestion mass of 5 g for elements such as copper, iron, lead, zinc, and nickel.

In accordance with this recommendation, any sample fraction larger than 0.25 mm was subjected to additional grinding to achieve the appropriate size for chemical analysis. Furthermore, prior to digestion, all samples were sequentially divided using a rotary splitter to ensure representative subsampling and improve analytical accuracy.

B.5 Kinetic Model Parameters and Assumptions

In the equations, R represents the percent recovery at time t. RI is the ultimate, maximum recovery in the case of prolonged flotation ($t = \infty$). k is the flotation rate constant (min^{-1}). In the case of the Kelsall model, θ represents the fraction of flotation components with a slow rate constant. k_f and k_s are the rate constants for fast and slow components, respectively. This model uses two rate terms instead of one and assumes an ultimate fractional recovery of 1.0, omitting an explicit ultimate recovery parameter. If k_s approaches 0, θ indicates the unrecovered fraction, making (1 - θ) equivalent to ultimate recovery, thus simplifying the model to two parameters [288]. For the Gamma distribution model, λ (min) and P (−) are the characteristic constants of the Gamma distribution. When the Gamma distribution parameters are determined, the expected value of the rate constant (k) can be calculated by P/λ [289].

B.6 Entrainment Contribution Estimation Using Ross Method

This method makes the assumption that the concentration of entrained particles in the froth and concentrate is the same as the concentration of specific species in the pulp. Based on this, the recovery by entrainment can be calculated by taking the mass of water recovered in the froth and multiplying it by the concentration of that species solids in the pulp at that time point:

$$m_E(t) = m_w(t)C(t) \qquad \textbf{Eq. (B. 1)}$$

Where $m_E(t)$ represents the mass in grams of species i recovered by entrainment at time t. $m_W(t)$ stands for the mass in grams of water recovered in the concentrate at time t. C(t) is the concentration in g per g of water of species i in the slurry at time t.

This approach assesses both entrainment and true flotation contributions through a single flotation test. The mass balance is as follows:

$$R_i(t) = F_i(t) + E_i(t) \qquad \textbf{Eq. (B. 2)}$$

DOI: 10.14750/ME.2026.030

Where $R_i(t)$ refers to the total recovery of species i at time t, encompassing both true flotation and entrainment. $F_i(t)$ represents the portion of $R_i(t)$ attributable to true flotation of species i at time t. $E_i(t)$ denotes the portion of $R_i(t)$ attributable to entrainment of species i at time t.

DOI: 10.14750/ME.2026.030

Appendix III Experimental Documentation and Notes

C.1 Sample preparation for visual liberation assessment following 1st comminution stage

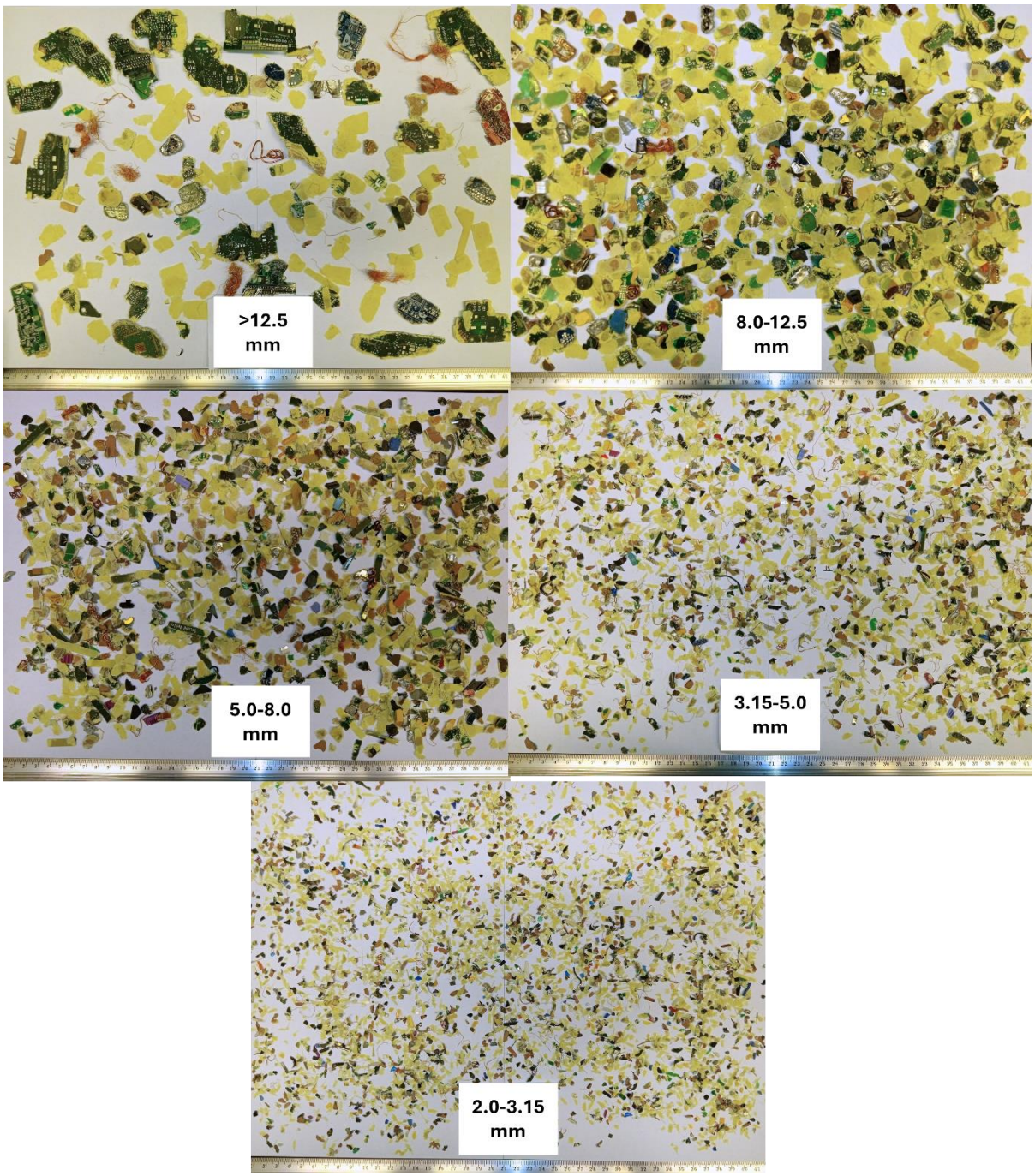

Figure C. 1: Size fractions obtained after the first stage of WPCB comminution. For fractions larger than 2 mm, material classification involved quartering the sample, spreading a subsample over an A3 sheet, and visually identifying material types from half of the area to ensure representativeness.

DOI: 10.14750/ME.2026.030

C.2 Metal-nonmetal locking following 2nd comminution stage

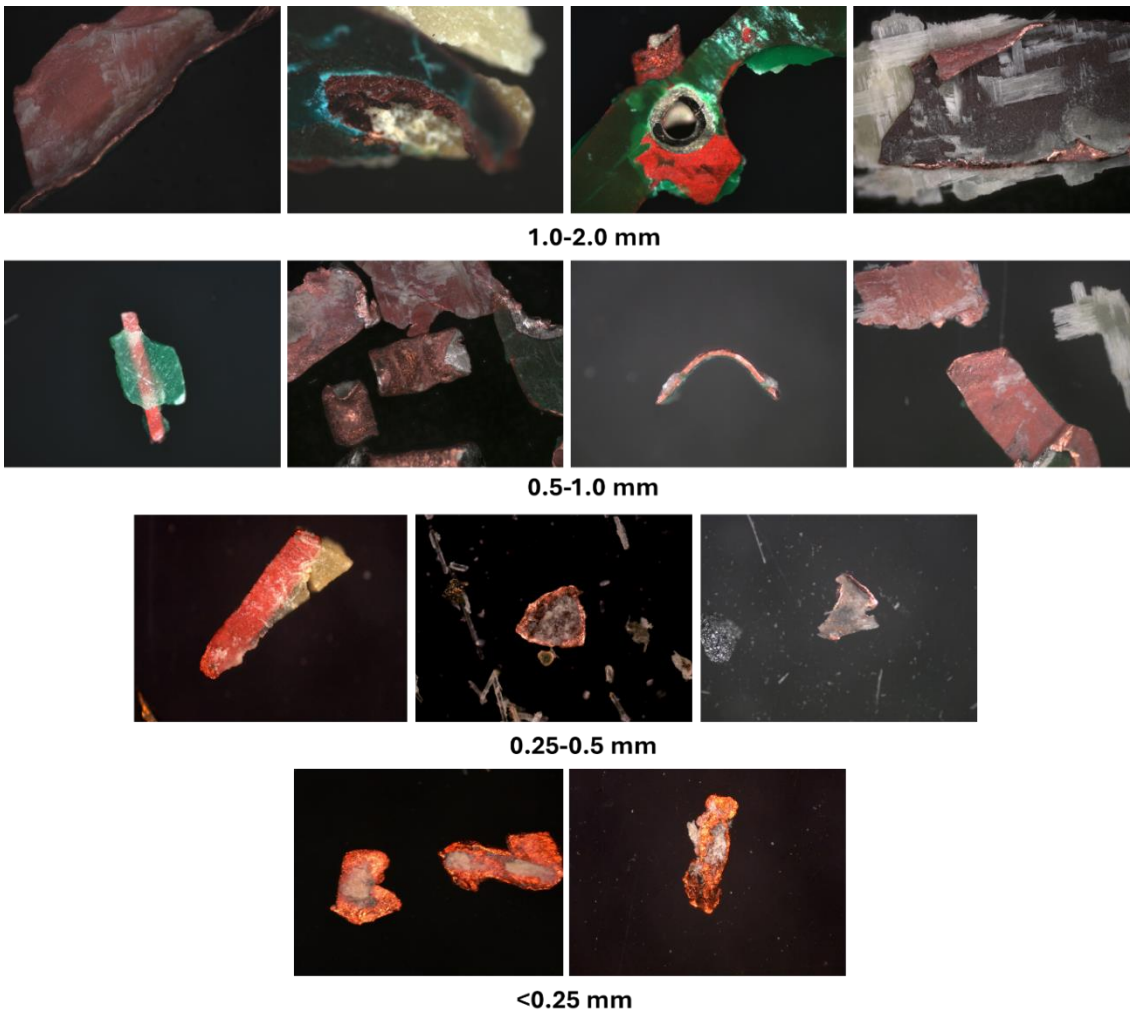

Figure C. 2: Images acquired using a digital microscope (20× magnification) showing representative examples of metal–nonmetal intergrowth and locking in WPCB particles after the second stage of comminution, across different size fractions.

DOI: 10.14750/ME.2026.030

C.3 SEM-EDS elemental mapping

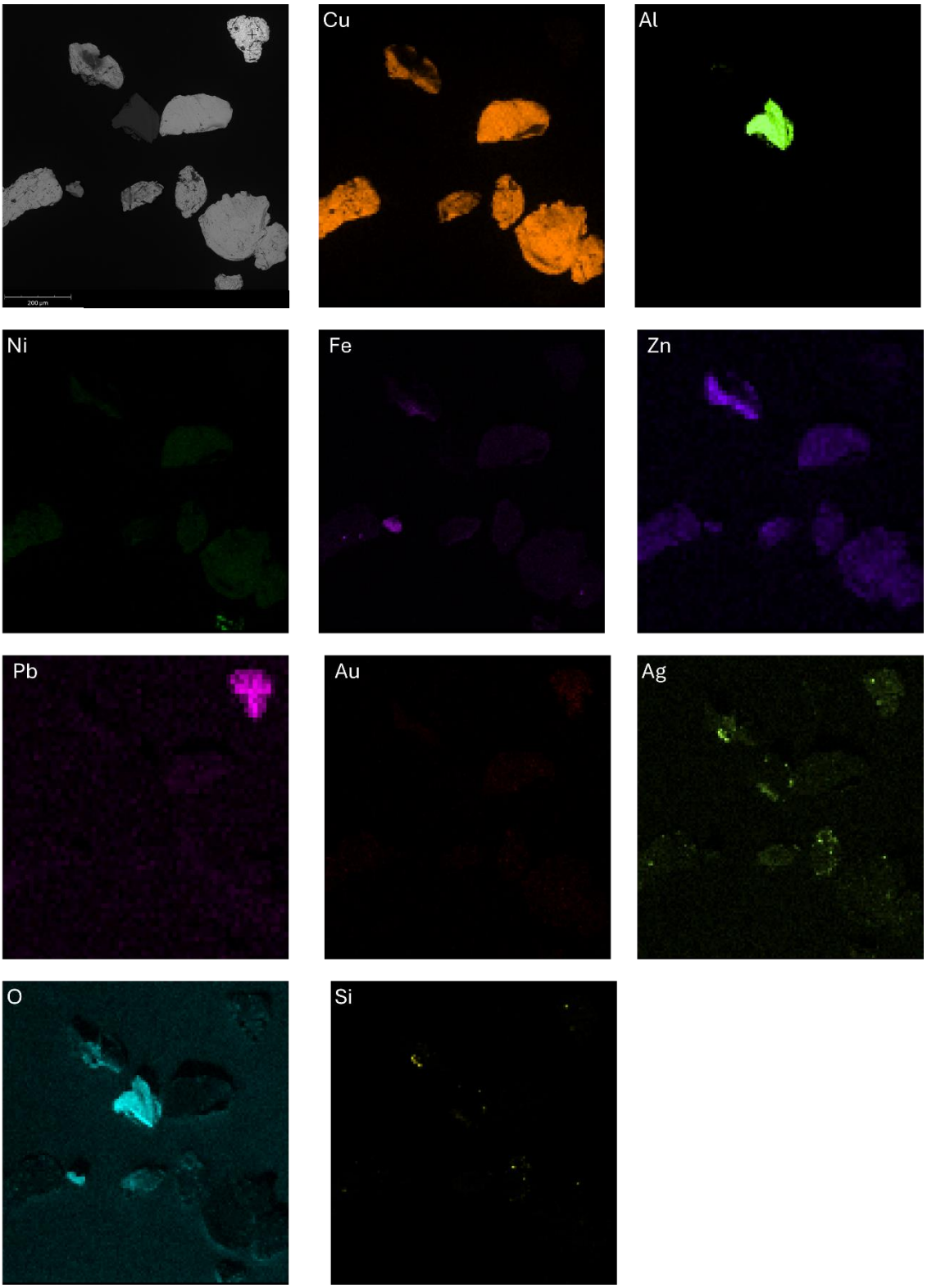

Figure C. 3: SEM-EDS elemental mapping of a WPCB sample in the 0.075–0.125 mm size fraction (300× magnification), showing the spatial distribution of discrete metals. Copper and aluminum appear as distinct localized particles, while silver exhibits a more diffuse distribution across multiple regions.

DOI: 10.14750/ME.2026.030

C.4 Particle aggregation during wet sieve analysis

Figure C. 4: Particle aggregation during wet sieve analysis following intense agitation pretreatment at 500 rpm stirring speed.

C.5 Reduced Regression Models

$$Overflow\ Yield\ (\%) = -590.23 + 0.885N - 14.98Qa + 9.32X + 0.014NQa - 0.0003N^2 - 0.449X^2 \quad \text{Eq. (C. 1)}$$

$$Underflow\ Metal\ Recovery\ (\%) = +118.1 - 0.032N + 16.98Qa - 1.11X - 5.50Qa^2 \quad \text{Eq. (C. 2)}$$

$$Water\ Recovery\ (\%) = -21.11 + 0.011N + 2.67Qa + 1.66X \quad \text{Eq. (C. 3)}$$

where N, Qa, and X correspond to impeller speed (rpm), aeration rate (1/L), solids concentration (wt.%), while the interaction terms NQa illustrate the relationships between the variables. The squares of each factor are noted as N^2, Qa^2, and X^2, respectively.

DOI: 10.14750/ME.2026.030

C.6 Standard deviation of the estimate

The losses of metals to overflow per size fraction were used for flotation kinetic analysis. Experimental data were fitted to four different kinetic models: Classical, Klimpel, Kelsall, and Gamma. While all models achieved high correlation coefficients ($R^2 > 0.99$), further evaluation based on the standard deviation of the estimate (Sr) revealed notable differences in model performance across particle sizes and flotation conditions.

As illustrated in **Figure C. 5**, no single model consistently provided the best fit to the experimental data. The Classical model exhibited the poorest agreement, particularly for the fine size, where it consistently showed the highest Sr values across most tests. In contrast, the Klimpel, Kelsall, and Gamma models displayed relatively better agreement, although their performance varied with flotation conditions. Given the absence of a clearly superior model, the Klimpel model was selected for subsequent kinetic analyses, offering a practical compromise between accuracy and simplicity. The Gamma model was excluded due to its tendency to predict unrealistic ultimate losses of 100%, while the Kelsall model, despite its versatility, lacks an ultimate recovery parameter, complicating direct comparisons.

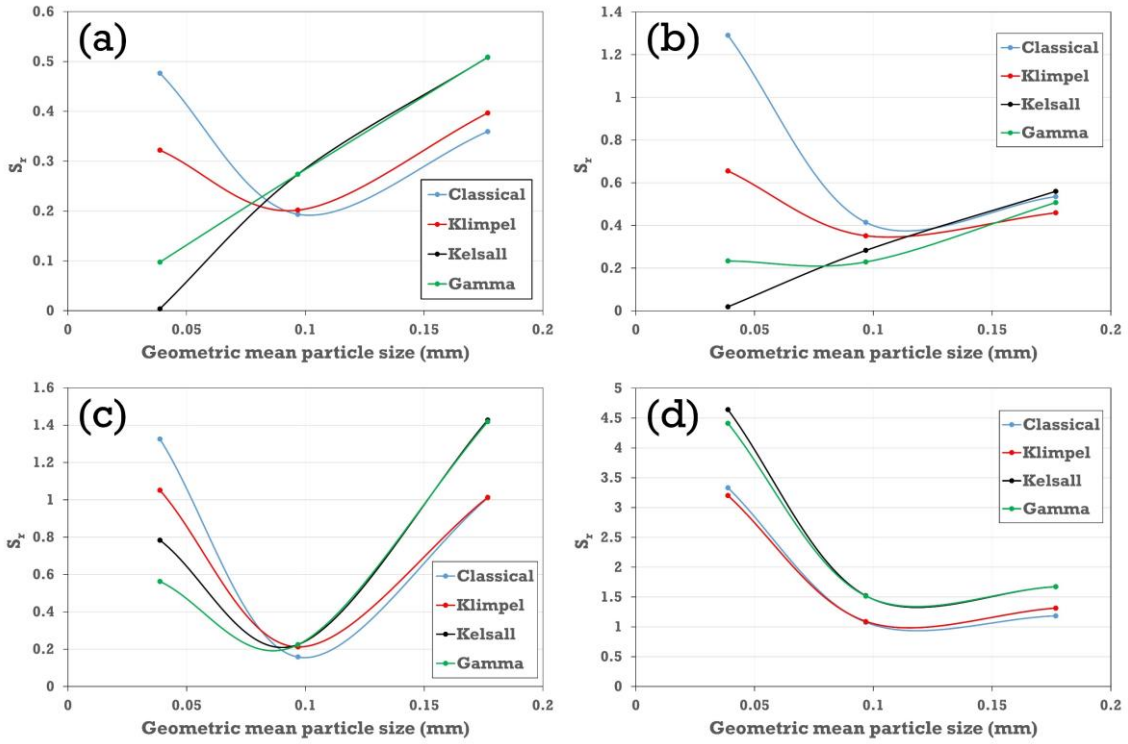

Figure C. 5: Standard deviation of the estimate (Sr) as a result of model fitting. (a) Run #1, (b) Run #3, (c) Run #12, (d) Run #14. Lines are used to connect data points solely for visual clarity.

DOI: 10.14750/ME.2026.030

C.7 Two liquid flotation

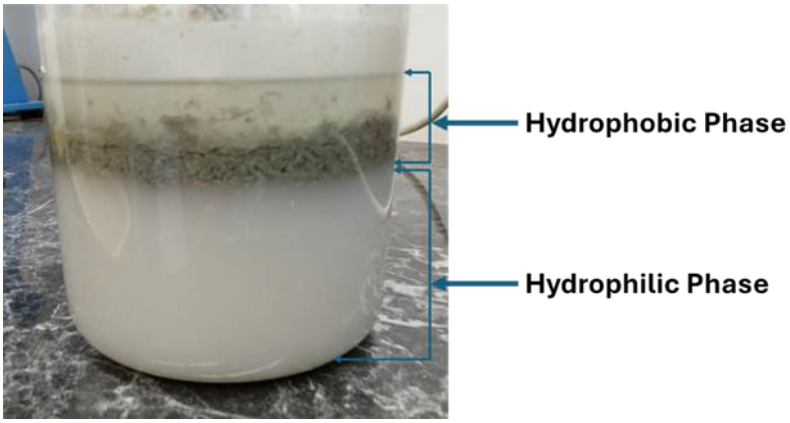

Figure C. 6: Stratification of phases during the settling period in a two-liquid flotation experiment.

DOI: 10.14750/ME.2026.030

Appendix IV Experiment Raw Results

D.1 WPCB Mechanical Processing and Grinding

Table D. 1: Chemical analysis results (mg/kg) of post-separation size fractions used in Table 4.2.

Size fraction (mm)	Mass distribution (%)	Ag	Cu	Fe	Ni	Pb	Zn	Au
1-2	28.18	<0.1	3000	650	900	5000	4600	<0.1
0.5-1	25.87	100	19000	4000	3000	1000	3000	16
<0.5	45.94	255	25000	6000	2000	1000	5000	85

Table D. 2: Sample ImageJ shape factor analysis data for metallic particles in flotation feed (<0.25 mm) used in Table 4.5.

Size fraction: 0.125-0.250 mm							
#	Circularity	Aspect Ratio	Solidity	#	Circularity	Aspect Ratio	Solidity
1	0.688	1.456	0.933	11	0.443	3.189	0.892
2	0.762	1.196	0.951	12	0.513	1.474	0.938
3	0.378	2.653	0.822	13	0.043	3.771	0.55
4	0.734	1.286	0.941	14	0.325	1.58	0.868
5	0.147	2.087	0.595	15	0.512	1.774	0.94
6	0.653	2.209	0.947	16	0.286	1.556	0.933
7	0.142	1.564	0.61	17	0.207	1.17	0.836
8	0.213	5.384	0.548	18	0.101	1.904	0.704
9	0.151	4.989	0.422	19	0.455	2.141	0.903
10	0.498	1.725	0.9	20	0.716	1.264	0.973
Size fraction: 0.075-0.125 mm							
1	0.537	1.219	0.935	11	0.644	1.401	0.949
2	0.325	2.224	0.837	12	0.318	2.671	0.814
3	0.564	1.413	0.947	13	0.557	1.27	0.894
4	0.489	1.753	0.921	14	0.408	2.461	0.846
5	0.562	1.578	0.937	15	0.401	3.277	0.862
6	0.519	1.722	0.858	16	0.311	2.448	0.798
7	0.411	2.216	0.917	17	0.701	1.397	0.945
8	0.505	1.542	0.873	18	0.477	1.45	0.861
9	0.619	1.59	0.963	19	0.414	2.108	0.918
10	0.069	1.9	0.474	20	0.374	1.797	0.811
Size fraction: <0.075 mm							
1	0.101	4.872	0.536	11	0.281	1.235	0.783
2	0.418	1.619	0.898	12	0.354	1.737	0.869
3	0.329	4.171	0.864	13	0.031	9.506	0.518
4	0.678	1.615	0.95	14	0.677	1.736	0.927
5	0.401	1.752	0.825	15	0.374	3.516	0.82
6	0.436	2.058	0.867	16	0.713	1.475	0.955
7	0.641	1.468	0.943	17	0.357	1.885	0.882
8	0.54	1.772	0.923	18	0.751	1.568	0.984
9	0.391	1.608	0.853	19	0.567	1.358	0.835
10	0.623	1.892	0.919	20	0.694	1.715	0.931

DOI: 10.14750/ME.2026.030

D.2 Aggregation/Dispersion Challenges and the Role of Intense Agitation

Table D. 3: Particle size distribution of WPCB flotation feed from dry sieving (reference) and post-agitation wet sieving at varying stirring speeds (data for Figure 5.5).

		Size fraction (mm)			Total
		<0.075	0.075-0.125	>0.250	(g)
Trial 1	Reference	47.99	21.40	30.32	99.71
	500 rpm	36.65	7.41	54.82	98.88
	1000 rpm	39.53	12.70	47.06	99.29
	1500 rpm	46.12	17.22	35.73	99.07
	2000 rpm	37.96	9.40	50.84	98.20
Trial 2	Reference	46.80	22.25	30.78	99.84
	500 rpm	40.31	8.50	50.33	99.14
	1000 rpm	36.35	10.16	53.08	99.58
	1500 rpm	48.50	19.27	31.60	99.36
	2000 rpm	35.09	13.38	49.26	97.73
Trial 3	Reference	47.70	22.18	29.89	99.78
	500 rpm	33.27	5.55	60.55	99.37
	1000 rpm	42.43	14.08	43.13	99.64
	1500 rpm	44.96	16.20	37.74	98.91
	2000 rpm	32.81	10.21	54.55	97.57

Table D. 4: Flotation product weights after intense agitation pretreatment at varying stirring speeds, contributing to Figures 5.11 and 5.12.

	Agitation	Flotation Yield (g)		Total
	(rpm)	Overflow	Underflow	(g)
Trial 1	500	80.95	18.22	99.17
	1000	79.53	19.92	99.45
	1500	75.62	24.00	99.62
	2000	83.25	15.80	99.05
Trial 2	500	82.48	16.35	98.83
	1000	83.24	16.12	99.36
	1500	77.62	21.62	99.24
	2000	79.11	18.75	97.86

DOI: 10.14750/ME.2026.030

Table D. 5: Chemical analysis results (mg/kg) of flotation products following intense agitation pretreatment at varying stirring speeds.

Flotation Exp.		Ag	Cu	Fe	Ni	Pb	Zn	Au
500 rpm	Overflow	105	12200	4200	570	445	810	15.7
	Underflow	500	70600	7750	2350	960	5070	62.8
1000 rpm	Overflow	135	10320	3680	680	460	1360	34.2
	Underflow	680	72950	13800	3955	1840	7080	118.2
1500 rpm	Overflow	96	4400	2887	500	255	834	32
	Underflow	384	82800	10800	4152	2064	8592	144
2000 rpm	Overflow	142	4949	6440	672	357	1036	51.7
	Underflow	342	58380	8304	5616	3120	9792	98.9

- Metal mass in product

$$Metal\ mass\ (g) = \left(\frac{Assayed\ concentration\ \left(\frac{mg}{kg}\right)}{1000} \right) \times\ Mass\ of\ Product\ (kg) \quad \text{Eq. (D. 1)}$$

- Metal content (grade) in each product

$$Metal\ content\ (\%) = \left(\frac{Mass\ of\ metal\ in\ Product\ (g)}{Total\ mass\ of\ Product\ (g)} \right) \times 100 \quad \text{Eq. (D. 2)}$$

- Metal recovery

$$Recovery\ (\%) = \left(\frac{Mass\ of\ metal\ in\ product\ (g)}{Mass\ of\ metal\ in\ Feed\ (g)} \right) \times 100 \quad \text{Eq. (D. 3)}$$

D.3 Reverse Flotation: Rheology and Metal Recovery

Table D. 6: Flotation product weights and water recovery data from Box–Behnken experimental design

Run	Flotation Yield (g)		Water recovery (g)	Run	Flotation Yield (g)		Water recovery (g)
	Overflow	Underflow			Overflow	Underflow	
1	33.79	26.08	76.08	11	79.50	20.39	193.4
2	37.90	21.89	81.57	12	82.61	57.10	221.54
3	42.69	17.22	120.20	13	90.06	49.42	172.31
4	38.05	21.73	92.40	14	102.08	37.56	249.36
5	64.39	35.54	116.56	15	95.47	44.31	257.36
6	70.77	29.05	153.15				
7	74.47	25.36	160.01				
8	73.64	26.32	162.48				
9	73.32	26.42	153.01				
10	65.77	33.85	131.68				
11	79.50	20.39	193.4				

DOI: 10.14750/ME.2026.030

Table D. 7: Chemical analysis results (mg/kg) of flotation products from Box–Behnken experimental design.

Flotation Exp.		Metal content (mg/kg)						
		Ag	Cu	Fe	Ni	Pb	Zn	Au
Run 1	Overflow	151	3180	3800	415	212	755	14.9
	Underflow	375	61800	8540	2075	900	3740	73.4
Run 2	Overflow	165	6460	7120	685	385	1340	17
	Underflow	330	65880	8840	2585	1105	4630	89.7
Run 3	Overflow	179	7235	3950	730	375	1460	12.6
	Underflow	215	79380	7300	3230	1265	5340	70.1
Run 4	Overflow	160	8175	5045	480	248	1000	16.3
	Underflow	398	66045	7546	2320	1065	3975	74.6
Run 5	Overflow	125	3800	7300	790	420	1720	20.6
	Underflow	335	60200	13700	3250	1190	5800	102
Run 6	Overflow	141	6600	7480	760	410	1200	25
	Underflow	310	42000	15910	2620	1310	5080	89.9
Run 7	Overflow	147	6075	5325	655	350	1210	14.2
	Underflow	442	83250	10050	3590	1780	6620	75
Run 8	Overflow	154	7120	5680	730	360	648	17.9
	Underflow	450	76000	14510	2528	1155	6300	90.3
Run 9	Overflow	161	7270	4560	528	258	952	17
	Underflow	407	87285	8290	2435	1194	5400	100.5
Run 10	Overflow	116	7910	6040	615	335	1160	21.7
	Underflow	215	71400	6965	1945	995	3665	97.1
Run 11	Overflow	180	8830	6750	740	375	1410	19
	Underflow	570	82800	12550	3660	1675	6145	85.8
Run 12	Overflow	185	7490	4330	465	235	810	13.1
	Underflow	300	53950	10000	2290	1094	4270	99
Run 13	Overflow	180	8460	5500	510	280	1025	16
	Underflow	325	58240	8000	2720	1270	4920	107
Run 14	Overflow	180	10600	6900	780	395	1742	12.5
	Underflow	610	64600	10380	3468	1547	5372	56.6
Run 15	Overflow	165	11920	5500	540	270	1250	15
	Underflow	345	61200	7560	2590	1270	4010	61.5

DOI: 10.14750/ME.2026.030

Table D. 8: Overflow yield with time for flotation tests (Runs 1, 3, 12, and 14 from Box–Behnken design) used for size-by-size analysis in Section 6.5.

	Size fraction (mm)	Overflow yield (g)				Underflow (g)		Size fraction (mm)	Overflow yield (g)				Underflow (g)
		0.5 min	1 min	2 min	4 min				0.5 min	1 min	2 min	4 min	
Run 1 (1)	0.125-0.250	2.82	1.33	1.62	1.70	9.41	Run 3 (1)	0.125-0.250	2.48	2.96	4.39	2.56	4.42
	0.075-0.250	2.14	0.93	1.31	1.26	3.29		0.075-0.250	1.51	1.39	1.57	1.01	3.32
	<0.075	3.83	3.43	6.88	4.87	14.89		<0.075	9.00	5.20	7.27	4.63	7.78
	Total	8.79	5.69	9.81	7.83	27.59		Total	12.99	9.55	13.23	8.2	15.52
Run 1 (2)	0.125-0.250	2.96	1.92	2.04	2.19	7.69	Run 3 (2)	0.125-0.250	3.22	3.55	2.78	1.81	5.37
	0.075-0.250	2.36	1.11	1.22	1.05	2.98		0.075-0.250	0.96	1.74	1.00	0.87	4.21
	<0.075	4.06	3.92	7.14	4.69	13.96		<0.075	9.48	4.25	5.89	5.00	9.33
	Total	9.38	6.95	10.4	7.93	24.63		Total	13.66	9.54	9.67	7.68	18.91
	Size fraction (mm)	Overflow yield (g)				Underflow (g)		Size fraction (mm)	Overflow yield (g)				Underflow (g)
		0.5 min	1 min	2 min	4 min				0.5 min	1 min	2 min	4 min	
Run 12 (1)	0.125-0.250	10.45	6.42	4.81	4.31	13.90	Run 14 (1)	0.125-0.250	9.87	4.37	5.71	6.50	12.90
	0.075-0.250	5.64	2.70	1.78	1.36	9.41		0.075-0.250	3.90	2.25	3.15	2.00	8.44
	<0.075	13.07	8.70	11.45	20.38	25.31		<0.075	20.83	9.63	15.80	19.02	13.60
	Total	29.16	17.82	18.04	26.05	48.62		Total	34.6	16.25	24.66	27.52	34.94
Run 12 (2)	0.125-0.250	9.53	4.34	4.56	5.76	15.05	Run 14 (2)	0.125-0.250	8.12	6.24	5.32	8.59	10.47
	0.075-0.250	3.20	3.09	2.57	1.68	10.13		0.075-0.250	5.28	3.14	3.03	2.52	6.78
	<0.075	15.29	9.17	10.50	16.74	28.07		<0.075	23.41	11.66	14.63	17.71	10.31
	Total	28.02	16.6	17.63	24.18	53.25		Total	36.81	21.04	22.98	28.82	27.56

Table D. 9: Water recovery with time for WPCB flotation tests (Runs 1, 3, 12, and 14 from Box–Behnken design).

	Water Recovery (g)				Total (g)
	0.5 min	1 min	2 min	4 min	
Run 1 (1)	26.26	14.18	15.64	17.79	73.87
Run 1 (2)	30.42	17.20	16.92	19.54	84.08
Run 3 (1)	44.30	16.17	29.85	22.10	112.42
Run 3 (2)	50.55	16.61	38.07	22.19	127.42
Run 12 (1)	72.38	45.34	46.55	46.42	210.69
Run 12 (2)	65.60	39.12	41.60	50.91	197.23
Run 14 (1)	108.90	45.68	53.31	54.11	262.0
Run 14 (2)	99.12	57.26	41.86	47.16	245.40

DOI: 10.14750/ME.2026.030

Table D. 10: Chemical analysis results (mg/kg) of flotation products from Runs 1, 3, 12, and 14 (Box–Behnken design) used for size-by-size analysis in Section 6.5.

		Run 1: 0.125-0.250 mm									Run 3: 0.125-0.250 mm						
		Ag	Cu	Fe	Ni	Pb	Zn	Au			Ag	Cu	Fe	Ni	Pb	Zn	Au
Overflow	0.5 min	80	4490	1750	3000	160	820	2.1	Overflow	0.5 min	350	21365	7400	1145	565	3280	11.6
	1 min	176	11210	3600	730	335	1860	6.0		1 min	170	10165	3270	610	305	1635	5.2
	2 min	176	12675	3900	710	380	1760	5.6		2 min	145	11600	3805	590	330	1595	9.9
	4 min	106	7640	2250	400	225	1040	6.1		4 min	270	18870	6660	990	585	2770	11.2
Underflow		449	103270	7470	2535	1200	6360	27.6	Underflow		790	169195	14590	4290	1965	10725	56.7
		Run 1: 0.075-0.125 mm									Run 3: 0.075-0.125 mm						
		Ag	Cu	Fe	Ni	Pb	Zn	Au			Ag	Cu	Fe	Ni	Pb	Zn	Au
Overflow	0.5 min	9	205	320	50	30	64	0.8	Overflow	0.5 min	170	1580	6155	900	460	1120	15.7
	1 min	40	905	1410	240	120	295	3.8		1 min	95	2150	2870	470	220	555	9.5
	2 min	30	640	1075	160	85	210	3.5		2 min	100	2410	4600	650	320	740	15.1
	4 min	21	420	685	110	60	135	1.6		4 min	165	2520	9585	1085	600	1150	19.9
Underflow		945	65200	26220	7180	3465	8720	149.2	Underflow		795	48760	22800	6275	2900	6995	154.5
		Run 1: <0.075 mm									Run 3: <0.075 mm						
		Ag	Cu	Fe	Ni	Pb	Zn	Au			Ag	Cu	Fe	Ni	Pb	Zn	Au
Overflow	0.5 min	50	265	3025	230	110	300	5.6	Overflow	0.5 min	105	527	6200	385	195	585	14.9
	1 min	26	215	1860	150	65	190	4.0		1 min	95	630	5900	445	185	650	12.2
	2 min	14	90	980	70	40	95	2.9		2 min	65	415	4360	280	150	415	13.0
	4 min	22	140	1465	94	48	125	2.7		4 min	70	465	6290	290	175	500	13.8
Underflow		185	4080	9480	1240	575	1610	48.9	Underflow		280	7215	12210	1760	785	2590	90.0

DOI: 10.14750/ME.2026.030

Table D. 10: Continue

		Run 12: 0.125-0.250 mm									Run 14: 0.125-0.250 mm						
		Ag	Cu	Fe	Ni	Pb	Zn	Au			Ag	Cu	Fe	Ni	Pb	Zn	Au
Overflow	0.5 min	165	13510	5385	795	415	2020	9.7	Overflow	0.5 min	785	39485	11630	1865	945	4030	24.9
	1 min	80	8960	1835	325	175	825	5.7		1 min	625	43775	10670	1885	825	4060	16.9
	2 min	245	28680	8130	1175	660	3020	15.5		2 min	775	50815	13520	2545	1255	5095	24.7
	4 min	200	13745	5235	665	390	1750	5.3		4 min	370	17735	5995	1010	560	2000	15.8
Underflow		430	158940	8935	2900	1430	7165	32.1	Underflow		315	144675	3465	1880	890	5590	32.6
		Run 12: 0.075-0.125 mm									Run 14: 0.075-0.125 mm						
		Ag	Cu	Fe	Ni	Pb	Zn	Au			Ag	Cu	Fe	Ni	Pb	Zn	Au
Overflow	0.5 min	65	1685	3340	445	235	500	11.5	Overflow	0.5 min	275	5090	7950	1190	570	1180	29.4
	1 min	100	4185	4435	670	335	840	16.2		1 min	120	3025	3750	680	270	650	12.0
	2 min	165	5105	7730	1070	585	1215	25.6		2 min	255	5490	7780	1205	600	1175	35.6
	4 min	145	4030	8960	1020	630	1175	45.3		4 min	110	2780	5015	550	335	630	16.8
Underflow		580	52400	22000	5200	2600	5800	121.0	Underflow		630	50195	18250	4370	2000	5441	131.7
		Run 12: <0.075 mm									Run 14: <0.075 mm						
		Ag	Cu	Fe	Ni	Pb	Zn	Au			Ag	Cu	Fe	Ni	Pb	Zn	Au
Overflow	0.5 min	90	780	6900	370	210	570	22.8	Overflow	0.5 min	245	1210	12150	820	425	970	34.6
	1 min	50	600	4380	270	120	420	10.7		1 min	155	1300	6955	560	260	690	21.0
	2 min	60	770	6125	390	195	585	17.2		2 min	220	1320	10115	755	345	825	27.7
	4 min	20	190	1850	105	65	145	7.5		4 min	55	260	2900	165	100	205	12.1
Underflow		240	8280	15480	1740	840	2550	76.8	Underflow		335	15130	12150	2390	1145	3970	152.9

DOI: 10.14750/ME.2026.030

D.4 Mitigating Rheological Challenges in the Flotation of WPCB

Table D. 11: Size-by-size flotation product weights (at 14 wt.% solids) for modified feed (0.032–0.250 mm) after ultrafine removal.

	Size fraction (mm)	Overflow (g)	Underflow (g)
Trial 1	0.125-0.250	25.0	14.60
	0.075-0.250	9.15	11.55
	<0.075	57.18	20.73
	Total	91.33	46.88
Trial 2	0.125-0.250	25.07	14.36
	0.075-0.250	8.96	10.30
	<0.075	58.18	18.46
	Total	92.21	43.12

Table D. 12: Chemical analysis results (mg/kg) of flotation products (at 14 wt.% solids) by size from modified feed (0.032–0.250 mm) after ultrafine removal.

	0.125-0.250 mm						
	Ag	Cu	Fe	Ni	Pb	Zn	Au
Overflow	215	12035	4125	755	370	1595	8.1
Underflow	625	151220	10355	3380	1565	9155	44.7
	0.075-0.125 mm						
	Ag	Cu	Fe	Ni	Pb	Zn	Au
Overflow	145	3060	5320	855	380	880	18.2
Underflow	590	45275	21050	5175	2265	6470	130.7
	0.032-0.075 mm						
	Ag	Cu	Fe	Ni	Pb	Zn	Au
Overflow	55	330	3380	250	120	295	10.0
Underflow	250	6210	12805	1655	775	2560	82.2

DOI: 10.14750/ME.2026.030

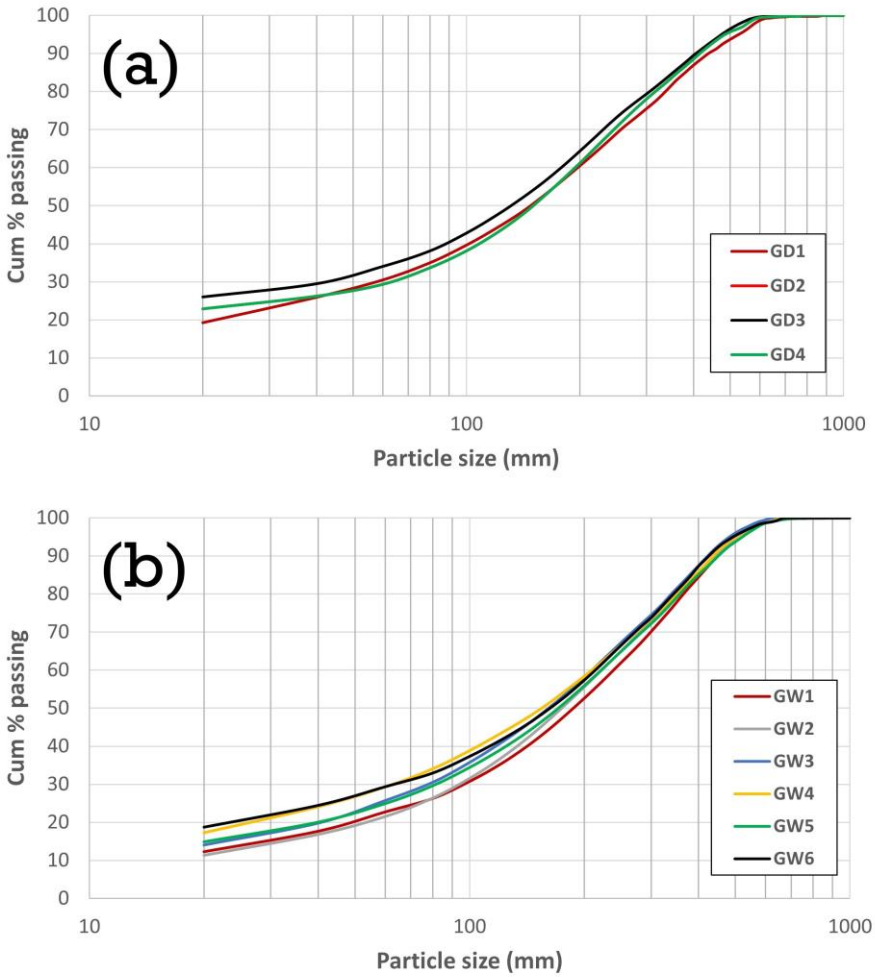

Figure D. 1: Particle size distribution curves after alkaline grinding under (a) dry and (b) wet conditions (Supporting Figure 7.10).

Table D. 13: Size-by-size flotation product weights at 14 wt.% solids after dry grinding with varying NaOH dosages (0.1 wt.% - 1 wt.%).

Desig.	Size fraction (mm)	Overflow (g)	Underflow (g)	Desig.	Size fraction (mm)	Overflow (g)	Underflow (g)
GD1(1)	0.125-0.250	20.14	19.63	GD2(2)	0.125-0.250	25.23	14.25
	0.075-0.250	7.47	13.35		0.075-0.250	10.49	8.06
	<0.075	59.15	19.58		<0.075	65.99	12.03
	Total	86.77	52.55		Total	101.71	34.34
GD1(2)	0.125-0.250	19.74	20.19	GD3(1)	0.125-0.250	13.76	25.84
	0.075-0.250	8.34	10.56		0.075-0.250	6.21	14.58
	<0.075	61.99	16.76		<0.075	39.66	38.54
	Total	90.07	47.50		Total	59.63	78.95
GD2(1)	0.125-0.250	24.18	15.48	GD3(2)	0.125-0.250	15.61	22.36
	0.075-0.250	11.48	9.34		0.075-0.250	7.04	12.62
	<0.075	65.27	13.05		<0.075	45.00	33.36
	Total	100.93	37.88		Total	67.65	68.34

DOI: 10.14750/ME.2026.030

Table D. 14: Size-by-size flotation product weights at 14 wt.% solids after wet grinding under varying pH levels (pH 7–12).

Desig.	Size fraction (mm)	Overflow (g)	Underflow (g)	Desig.	Size fraction (mm)	Overflow (g)	Underflow (g)
GW1(1)	0.125-0.250	20.56	18.68	GW4(1)	0.125-0.250	20.78	18.54
	0.075-0.250	8.05	12.55		0.075-0.250	11.71	8.93
	<0.075	58.89	18.61		<0.075	62.72	14.93
	Total	87.51	49.83		Total	95.22	42.39
GW1(2)	0.125-0.250	19.57	19.66	GW4(2)	0.125-0.250	20.81	17.71
	0.075-0.250	7.67	13.19		0.075-0.250	11.73	8.53
	<0.075	56.06	20.59		<0.075	62.80	14.26
	Total	83.30	53.44		Total	95.33	40.51
GW2(1)	0.125-0.250	20.51	19.29	GW5(1)	0.125-0.250	15.68	23.87
	0.075-0.250	10.08	10.81		0.075-0.250	7.61	13.15
	<0.075	61.08	17.52		<0.075	54.44	23.66
	Total	91.67	47.62		Total	77.73	60.67
GW2(2)	0.125-0.250	19.46	20.07	GW5(2)	0.125-0.250	16.61	21.38
	0.075-0.250	9.57	11.25		0.075-0.250	8.06	11.78
	<0.075	57.96	18.23		<0.075	57.68	21.19
	Total	86.99	49.55		Total	82.35	54.36
GW3(1)	0.125-0.250	19.63	19.81	GW6(1)	0.125-0.250	10.13	29.38
	0.075-0.250	10.10	10.61		0.075-0.250	10.00	10.74
	<0.075	57.37	20.53		<0.075	52.73	25.32
	Total	87.10	50.95		Total	72.87	65.44
GW3(2)	0.125-0.250	20.86	18.16	GW6(2)	0.125-0.250	9.39	30.26
	0.075-0.250	10.74	9.72		0.075-0.250	9.45	11.16
	<0.075	60.53	18.36		<0.075	49.83	26.31
	Total	92.13	46.25		Total	68.67	67.73

DOI: 10.14750/ME.2026.030

Table D. 15: Chemical analysis results (mg/kg) of flotation products (at 14 wt.% solids) by size after dry grinding with varying NaOH dosages.

	GD1: 0.125-0.250 mm						
	Ag	Cu	Fe	Ni	Pb	Zn	Au
Overflow	380	34880	4605	305	165	1265	25.7
Underflow	75	77490	3945	1760	745	3245	13.7

	GD1: 0.075-0.125 mm						
	Ag	Cu	Fe	Ni	Pb	Zn	Au
Overflow	265	15685	4725	480	410	1175	27.2
Underflow	440	45410	8195	4335	1065	4295	53.5

	GD1: <0.075 mm						
	Ag	Cu	Fe	Ni	Pb	Zn	Au
Overflow	185	1615	3440	305	140	560	10.6
Underflow	510	7065	10425	1910	795	1560	89.9

	GD3: 0.125-0.250 mm						
	Ag	Cu	Fe	Ni	Pb	Zn	Au
Overflow	90	4490	6370	485	220	1570	15.3
Underflow	125	97030	3115	985	680	2550	9.8

	GD3: 0.075-0.125 mm						
	Ag	Cu	Fe	Ni	Pb	Zn	Au
Overflow	145	2905	5175	365	200	1865	13.2
Underflow	315	60510	10290	2530	1255	3560	65.1

	GD3: <0.075 mm						
	Ag	Cu	Fe	Ni	Pb	Zn	Au
Overflow	75	1410	4110	330	135	800	8.8
Underflow	90	4810	6925	875	370	1390	34.1

	GD2: 0.125-0.250 mm						
	Ag	Cu	Fe	Ni	Pb	Zn	Au
Overflow	45	8720	6225	520	230	1965	15.4
Underflow	95	119700	5965	2185	925	4350	20.4

	GD2: 0.075-0.125 mm						
	Ag	Cu	Fe	Ni	Pb	Zn	Au
Overflow	80	2285	2515	280	120	1020	7.5
Underflow	170	85980	12450	5800	2170	6085	70.3

	GD2: <0.075 mm						
	Ag	Cu	Fe	Ni	Pb	Zn	Au
Overflow	45	940	2270	275	105	475	6.4
Underflow	365	16675	20625	3455	1395	3875	131.1

DOI: 10.14750/ME.2026.030

Table D. 16: Chemical analysis results (mg/kg) of flotation products (at 14 wt.% solids) by size after wet grinding with varying pH levels.

	GW1: 0.125-0.250 mm								GW2: 0.125-0.250 mm						
	Ag	Cu	Fe	Ni	Pb	Zn	Au		Ag	Cu	Fe	Ni	Pb	Zn	Au
Overflow	235	41335	5280	365	295	1615	21.9	Overflow	335	10700	2360	1960	825	3100	29.9
Underflow	295	101710	3825	1500	630	4265	11.8								
	GW1: 0.075-0.125 mm								GW2: 0.075-0.125 mm						
	Ag	Cu	Fe	Ni	Pb	Zn	Au		Ag	Cu	Fe	Ni	Pb	Zn	Au
Overflow	510	34595	7340	715	590	1950	30.1	Overflow	95	7700	2960	215	285	1090	3.7
Underflow	395	41095	7610	2505	985	3135	41.9								
	GW1: <0.075 mm								GW2: <0.075 mm						
	Ag	Cu	Fe	Ni	Pb	Zn	Au		Ag	Cu	Fe	Ni	Pb	Zn	Au
Overflow	125	2240	3720	425	195	720	6.9	Overflow	200	7050	9170	870	765	2210	14.1
								Total underflow	390	55000	8970	1720	1570	5140	68.1
	GW3: 0.125-0.250 mm								GW4: 0.125-0.250 mm						
	Ag	Cu	Fe	Ni	Pb	Zn	Au		Ag	Cu	Fe	Ni	Pb	Zn	Au
Overflow	55	6290	2925	165	250	1330	6.7	Overflow	130	18470	6560	380	545	2900	14.9
								Underflow	120	126015	25200	1125	460	5970	12.7
	GW3: 0.075-0.125 mm								GW4: 0.075-0.125 mm						
	Ag	Cu	Fe	Ni	Pb	Zn	Au		Ag	Cu	Fe	Ni	Pb	Zn	Au
Overflow	100	5420	3165	175	295	1245	4.8	Overflow	100	6030	2705	215	265	920	8.1
								Underflow	325	82155	10770	1595	1550	2310	98.5
	GW3: <0.075 mm								GW4: <0.075 mm						
	Ag	Cu	Fe	Ni	Pb	Zn	Au		Ag	Cu	Fe	Ni	Pb	Zn	Au
Overflow	195	7045	12330	875	810	2725	21.6	Overflow	51	1780	1470	245	170	475	10.5
Total underflow	315	51935	6790	1530	1225	2750	59.8	Underflow	290	7795	16705	1280	1930	2940	122.2

Note: Due to sampling error, the underflow chemical analysis for GW2 and GW3 was performed on the bulk sample and is represented as "Total underflow" in this table, rather than size-by-size.

DOI: 10.14750/ME.2026.030

Table D. 16: Continue

	GW5: 0.125-0.250 mm								GW6: 0.125-0.250 mm						
	Ag	Cu	Fe	Ni	Pb	Zn	Au		Ag	Cu	Fe	Ni	Pb	Zn	Au
Overflow	140	9240	4515	285	215	2255	28.7	Overflow	80	15420	4420	315	345	2470	18.4
Underflow	235	83985	2390	1020	455	2225	12.1	Underflow	15	63830	2030	790	390	1765	8.3
	GW5: 0.075-0.125 mm								GW6: 0.075-0.125 mm						
	Ag	Cu	Fe	Ni	Pb	Zn	Au		Ag	Cu	Fe	Ni	Pb	Zn	Au
Overflow	100	5760	3390	200	190	1260	7.6	Overflow	125	5570	2605	220	185	1000	7.8
Underflow	295	46665	10915	3280	1395	4215	69.0	Underflow	445	64280	14775	4285	1565	4635	84.9
	GW5: <0.075 mm								GW6: <0.075 mm						
	Ag	Cu	Fe	Ni	Pb	Zn	Au		Ag	Cu	Fe	Ni	Pb	Zn	Au
Overflow	70	1585	3565	265	175	730	10.0	Overflow	95	1925	4345	380	210	780	9.5
Underflow	145	10410	4945	875	485	1105	68.0	Underflow	300	9330	11430	1630	935	2145	134.6